UNIVERSITY OF TROMSØ UIT

FACULTY OF SCIENCE AND TECHNOLOGY
DEPARTMENT OF PHYSICS AND TECHNOLOGY

On the relation between type-II ion outflow and naturally enhanced ion acoustic lines in the polar ionosphere

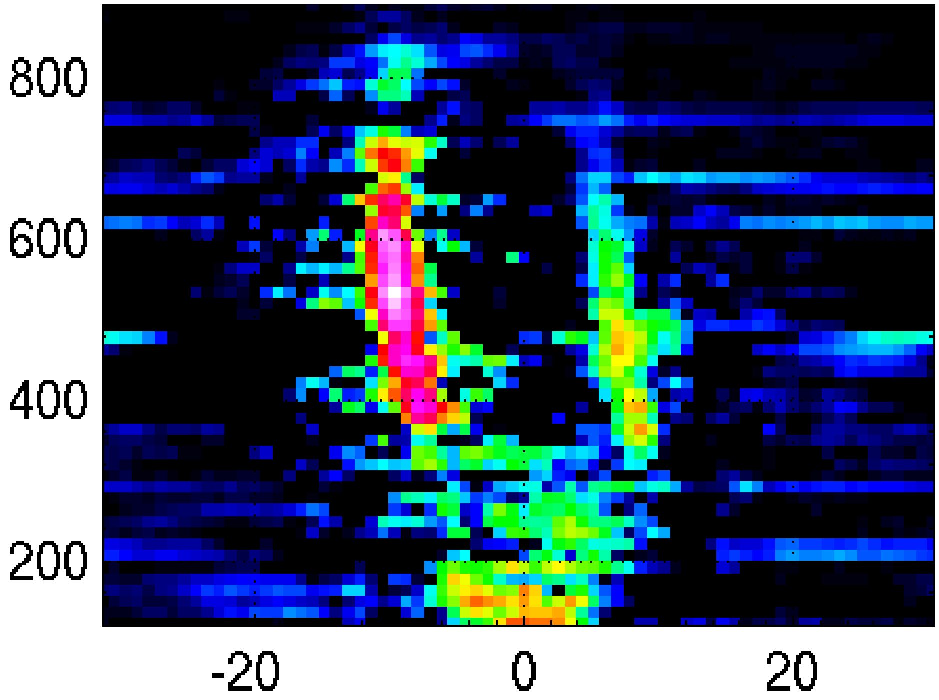

Massimo Di Loreto

FYS-3900 Master’s Thesis in Physics

December 2013

Felix, qui potuit rerum cognoscere causas

Fortunate is (s)he, who was able to know the causes of things

Publius Vergilius Maro (Georgicon, II, 490)

Contents

Abstract

Many authors think that ion outflows and naturally enhanced ion acoustic lines (NEIALs) are correlated. In this work we investigated the relation between type-II ion outflows and NEIALs. Currently, several ion outflows acceleration mechanisms and NEIALs generation theories have been proposed. In the first part of this thesis we review the most important works regarding these two processes. In the second part we present the results of our analysis, together with some unexpected events which were not previously described in the literature.

We searched for ion outflow in the data taken from the 42 m fixed antenna of the EISCAT Svalbard radar, then we checked the incoherent scatter spectra in order to confirm the occurrence of NEIAL events. Afterwards, we removed the data dumps affected by NEIALs and performed a second analysis employing the software GUISDAP 8.7. Finally, we used a Matlab script which we wrote to plot field aligned ion velocities, electron densities, ion and electron temperatures, temperature ratio and ion fluxes in order to: (1) investigate the starting altitude of both NEIALs and outflows; (2) obtain information about the NEIALs' generation theories, if they are compatible with our observations and at which altitude range they can be valid.

We found some recurring situations for the NEIAL occurrence: particle precipitation and ion outflows are usually involved for events above 300 km, while the few NEIAL events below 200 km that we observed seem to be not always correlated with particle precipitation and not embedded in ion outflows. Our results suggest that each of the three NEIAL generation theories might prevail during its favorite conditions.

1. Introduction

1.1. Overview

In this thesis we will discuss the relation between naturally enhanced ion acoustic lines (often referred as NEIALs) and ion outflows, specifically type-II ion outflows.

NEIALs are enhancement in one or both ion shoulders of the power spectra received by incoherent scatter radars. They are usually observed between 150 and 1000 km altitude and are thought to be due to instabilities occurring in the ionosphere.

Ion outflows are strong upflows of ion particles which provide a significant source of plasma for the magnetosphere. They are mostly made of H^+ and O^+ ions, but contributions from He^+ and O^{++} have been observed (*Lockwood et al.*, 1985). In this work we will focus on the outflows observed in the polar region, albeit they have been observed in mid-latitude areas as well (*Yeh and Foster*, 1990).

In chapter 1 we will describe the physical environment where these events occur. Therefore we will discuss the Sun-Earth system, looking at the particles journey from the Sun to the Earth's upper atmosphere. This flux of plasma is known as *solar wind*. When the particles interact with the Earth's magnetic field, many phenomena can occur, e.g. auroras, particle precipitation, ring currents and so on. NEIALs and ion outflows are processes that are strongly related to this interaction. They occur mostly in the ionosphere, so we will give a brief overview about its principal characteristics, with an eye to the peculiarities of the polar ionosphere. This is in fact a fundamental environment for the Sun-Earth interactions, since it has open magnetic field lines which, in particular conditions, can let the particles enter into the ionosphere and lower regions of atmosphere, acting in practice as a "highway" for the solar particles, which can overcome the barrier formed by the particular shape of the Earth's magnetic field. Finally, we will briefly discuss the ionospheric currents.

In chapter 2 we will first describe the difference between polar wind and auroral ion outflow, then we will discuss them in more detail, focusing on auroral ion outflows which are a central topic of this thesis. We will give a short summary of the observational evidences of the outflows and characterize the two different types known today. This is an important point, since NEIALs are observed mostly during one of the two outflow types. Finally we will discuss some of the theories proposed to explain their acceleration mechanisms.

The following chapter 3 is dedicated to naturally enhanced ion acoustic lines. After a short introduction, we presented a summary of the most relevant observations of the last 25 years, trying to describe morphological characteristics, unusual spectral shapes, statistical analysis, correlations with other processes and other relevant features of NEIALs.

Afterward we will describe the three most important theories about their generation mechanisms, highlighting strengths and weaknesses of each.

In chapter 4 we discuss the basics of incoherent scatter theory and techniques and introduce the EISCAT radar system. We will then briefly describe the ionospheric parameters which can be measured by the EISCAT radars and the parameters which can be derived from the measured ones.

In chapter 5 we will describe our analysis methods, the software used and the possible issues related to our approach. We made a case study type of work, so we will discuss each case separately. We will try to relate our results to NEIALs and outflow theories and we will compare our results with previous studies. We will finally highlight odd cases, where we observed particular features which could be important for future studies.

Finally chapter 6 contains the conclusions of our work, together with the possibilities for future studies to better understand the relation between NEIALs and ion outflows.

In Appendix A we tried to develop a method based on an idea of Prof. Björn Gustavsson, aimed to identify NEIALs using the decay of electron density over time. We basically assumed that after a NEIAL occurs, the electron density undergoes a sort of shutoff. We investigated if the exponential decay of electron density could aid us in identifying the presence of NEIALs.

In Appendix B we will list the Matlab routines, scripts and other customized code we wrote in order to extrapolate and analyze data from the raw files.

1.2. The Sun-Earth system

The Sun is an average G-type main sequence star whose emission spectrum can be described with a good approximation by a Planck radiation law:

$$B_\nu = \frac{2h\nu^3}{c^2}\frac{1}{\exp\left(\frac{h\nu}{k_B T}\right)-1} \tag{1.2.1}$$

The most important part of the spectrum as far as is concerned our work is the extra ultra violet region (EUV) between 0.01 and 0.1 µm, since it is the radiation responsible for the formation of the ionosphere through the photoionization process (*Brekke*, 2012).

The emission of UV and X-ray radiation is often connected with sunspots, which in turn are correlated to magnetic activity on Earth. Sunspots number varies periodically on an average interval of 11.1 years. While the existence of a correlation between solar activity and weather is not definitely proved to date, a close correlation between variation in the sunspots number and variation of the Earth's geomagnetic field is accepted among scientific community. These variations of the Earth's field are due to currents in the ionosphere, which we will treat in the next section (*Brekke*, 2012).

Beside sunspots, other phenomena occurs on the Sun, e.g. solar flares (powerful explosions in the solar atmosphere above sunspots that sends burst of energetic particles into space) and coronal mass ejections (CME), which represent an important form of mass release from the Sun, with large CME containing as much as 10^{16} g of plasma moving away from the Sun at speed as high as $1000\,\mathrm{km\,s^{-1}}$ (*Schunk and Nagy*, 2004).

Thus, the Sun emits not only electromagnetic radiation but also particles. These charged particles forms the *solar wind*, which flows from the Sun to the most remote areas of the Solar system. The magnetic fields can be carried out by the particles from the Sun through interplanetary space in a “frozen-in” manner. We will not go into details here, but suffice to say that the “frozen-in” field concept means that where the plasma has a high electrical conductivity (due to its collisionless nature), it can carry the magnetic field along as a “glue” in the plasma. The solar magnetic field carried by the solar wind forms the *interplanetary magnetic field* (IMF).

The solar wind will then stream out from the rotating Sun and it will move in spirals in a similar fashion to the water from a spinning nozzle of a garden hose, hence the name *garden hose effect*. However the magnetic field lines do not emanate only from the ecliptic plane, but from any latitude of the Sun. This means that the resulting structure of the magnetic field is fairly complex and actually resembles the skirt of a ballerina. This “ballerina skirt” structure, called *heliospheric current sheet* and depicted in Fig. 1.2.1, is one of the biggest continuous structure of the entire Solar System. The magnetic fields on the opposite sides of the heliospheric current sheet have opposite polarity and as the different folds of the skirt drape the various objects in the solar system, they are exposed to different IMF polarities. This has an evident effect on the currents in the Earth’s atmosphere.

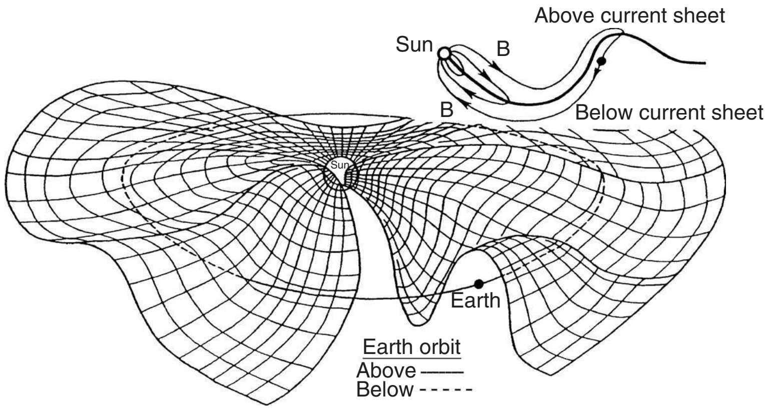

Figure 1.2.1.: Heliospheric current sheet. As the Sun rotates, its magnetic field twists into a Parker spiral, a form of an Archimedean spiral, as it extends through the solar system. The inset at the top-right of the figure shows the opposite directions of the magnetic field on the two sides of the current sheet. [from *Schunk and Nagy* (2004)]

After the particles leave the Sun with an average velocity of 400 km/s, they flow through the space and reach the Earth magnetic field after a trip lasting several hours. Like most of the planets in the Solar System, the Earth has a magnetic field resembling, to a very good approximation, a dipole. Since collisionless plasmas cannot flow across magnetic fields, the Earth’s field acts as a hard obstacle, deflecting the flow around the Earth, which in turn warps the magnetic field lines like showed in Fig. 1.2.2.

When the supersonic solar wind hits the Earth’s magnetic field a *bow shock* is formed, which heats and decelerates the particles (*Schunk and Nagy*, 2004). The heated solar wind is then accelerated again as it moves past the Earth. The thin layer (around 100 km) that separates the magnetized solar plasma from that confined by the Earth's magnetic field is called *magnetopause* and its location is the result of the balance between dynamic pressure of the solar wind and the compressed geomagnetic field. The extensive current flowing along the magnetopause acts to separate the solar wind field from the geomagnetic field. The region where the geomagnetic field dominates is known as the *magnetosphere*. The *plasmasphere* is the region of the Earth's magnetosphere consisting of low energy (cool) plasma. The outer boundary of the plasmasphere is called *plasmapause*. It corotates with our planet at about four Earth radii and it is characterized by a sharp decrease of electron and ion density.

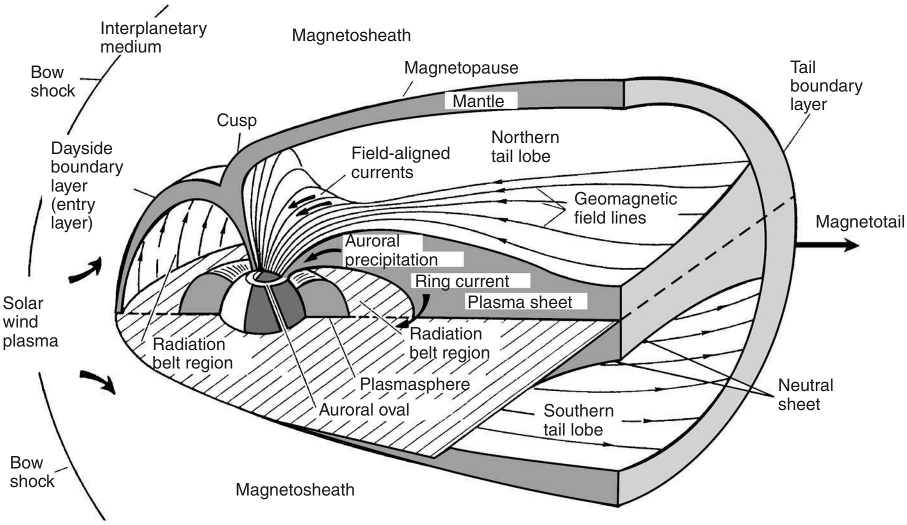

Figure 1.2.2.: Diagram showing the various regions of the Earh magnetosphere. [from *Schunk and Nagy* (2004)]

Direct incoming of solar wind plasma into the atmosphere is possible on the dayside near the polar cusp (Fig. 1.2.2). This process occurs with a higher probability when the IMF and the geomagnetic field have opposite directions, that is, when it is observed a southward IMF. Solar wind particles can also reach the tail of the magnetosphere and then populate the plasma sheet region. Particles in the plasma sheet can enter the Earth's upper atmosphere on the nightside along specific magnetic lines, which at low altitudes converge in a region narrow in latitude, but extended around the Earth. This region is called *auroral oval* (see Fig. 1.2.2) and it is present both in northern and southern hemisphere, and is typical not only of the Earth but also of other planets in the Solar System (*Brekke*, 2012). Its name is of course related to the possibility to observe, from places which are located within the auroral ovals, the northern lights, a spectacular phenomenon caused by the interaction of solar wind particles with the atoms of upper atmosphere around 100 km altitude.

1.3. Ionosphere

Overview

Fig. 1.3.1 shows the various regions of Earth's atmosphere, together with the temperature altitude profile and some important physical processes occuring in 0-600 km altitude range. In this work we are mostly interested in the ionosphere which, as the name suggests, is the ionized portion of the upper atmosphere. It extends from about 60 to 1000 km altitude, albeit the intensity of solar radiation plays an important role in producing and sustaining ionization. As we mentioned, the main source for the ionosphere is the photoionization of neutral molecules via solar EUV and soft X-ray radiation, although other processes can be of importance (e.g. cosmic rays, especially at night). Together with chemical reactions with neutrals and recombination with electrons, diffusion and transport processes take place, strongly influenced by the Earth's magnetic field.

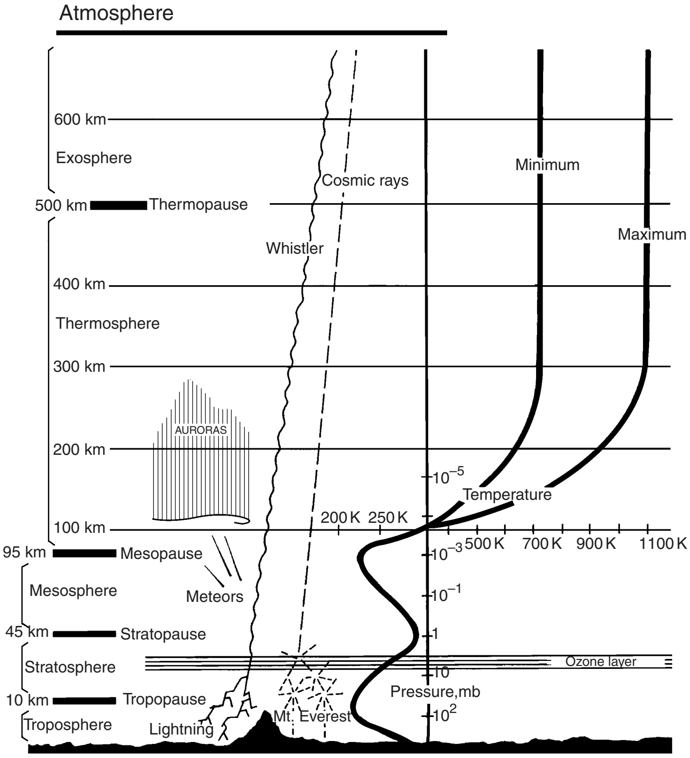

Figure 1.3.1.: Earth atmosphere together with several phenomena of interest. The dark solid curves show atmospheric temperature profiles for solar maximum and minimum conditions. [from *Schunk and Nagy* (2004)]

The electron density variation with altitude determines the structure of the ionosphere, which is divided in several layers, or regions (Fig. 1.3.2), which are usually identified as (*Schunk and Nagy*, 2004):

- *D-region* (60-100 km). The chemical processes are the most important, therefore this region is sometimes referred as C-region due to its complicated chemistry. Molecular ions are the most abundant and N_2, O_2 and O are the most abundant neutral species. In the D region there are both positive and negative ions.

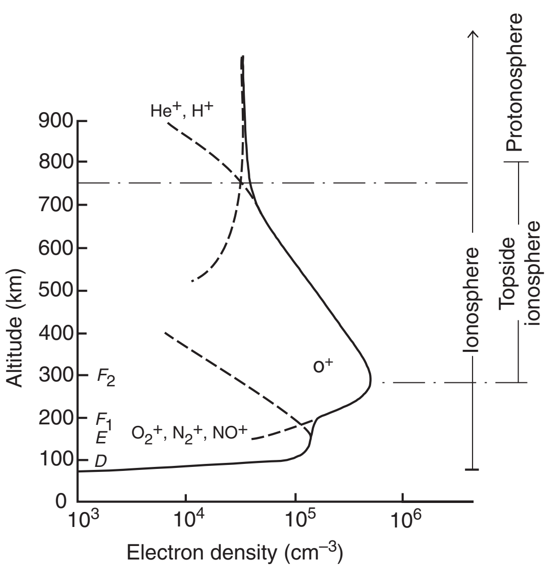

Figure 1.3.2.: Density profiles for several ionospheric ions. Different ionospheric regions are also indicated. Note that this figure is relative to a mid-latitude ionosphere. The polar ionosphere has in fact different profiles, especially for the O^+. [from *Schunk and Nagy* (2004)]

- *E-region* (100-150 km). Its name stems from the fact that it was initially observed that this region was able to reflect electric fields. The chemical reactions are still very important but not as complicated as in the D region. The major ions are NO^+ and O_2^+. The ion density[1] is about $10^{11}\,m^{-3}$, while the neutral density is about $10^{17}\,m^{-3}$, therefore the plasma is weakly ionized. Northern lights occurs in this region. There exist observations of NEIALs at 146 km, at the boundary between E-region and the above F-region (see *Rietveld et al.* 1991).
- *F-region* (150-350 km). It is often subdivided in *F1* and *F2* regions. At lower latitudes O^+ is the dominant ion species up to 300 km, then above 300 km H^+ becomes more and more abundant. In the polar ionosphere, however, O^+may dominate up to 600 km and higher, depending on magnetospheric and solar conditions. The maximum electron density usually occurs around 300 km, in the F2 region, as a result of balance between plasma transport and chemical loss processes. The electron density is about $10^{12}\,m^{-3}$ and the neutral density is about $10^{14}\,m^{-3}$, hence the plasma is partially ionized, and collisions between the different charged particles and between the charged particle and neutrals must be taken into account. A lot of NEIAL events occur in the upper part of this region.
- *Topside ionosphere* (350-1000 km). Although the neutrals still outnumber the ions, the plasma can safely be assumed fully ionized and only collisions between charged particles need to be considered. In the polar ionosphere, the dominant species are O^+ and H^+ and, to a lesser extent, He^+; their exact concentration depends on solar conditions and temperatures (*Banks and Kockarts*, 1973). The most of NEIAL events occurs in this region, together with strong ion outflows.

---

[1] Albeit it is widely referred as "density", this is actually a *number density*, that is, the number of particles per cubic meter.

The temperature of the ionosphere is essentially controlled by the absorption of UV solar radiation. Since the electrons have a larger mobility and heat conductivity, their temperature becomes higher than the ion temperature, reaching easily 2000 K at about 250 km altitude. The ions interact by collisions more strongly with the neutral gas and much of their excess energy is transferred to neutral gas. Therefore the ion temperature is mostly equal to that of the neutrals up to 300 km. Above this altitude, where ion-neutral collisions are less and less frequent, we can assume $T_e > T_i > T_n$. Due to the strong dependence on solar radiation, the ion and electron temperatures varies strongly with time of the day, season and solar activity (*Brekke*, 2012).

Currents in the ionosphere

The magnetosphere-ionosphere-atmosphere system at high latitudes is strongly coupled via several mechanisms, e.g. electric fields, particle precipitation and field aligned currents (*Brekke*, 2012 and *Schunk and Nagy*, 2004).

The convection electric field has origin in the solar wind and IMF. The latter penetrates the magnetopause and connects with the geomagnetic field in a circular region called *polar cap*. The connection between ionosphere and magnetosphere is held by *open field lines*, along which charged particles can penetrate in the lower layers of atmosphere. Note that field lines in the auroral oval are closed, but they are nevertheless stretched in the magnetospheric tail (see Fig. 1.3.3).

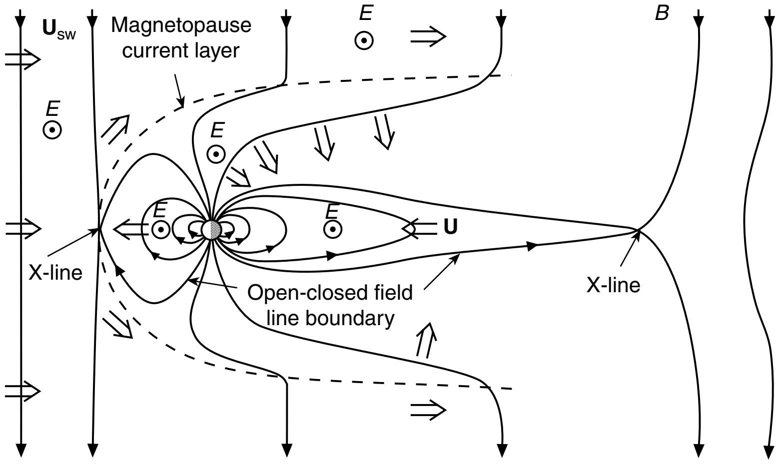

Figure 1.3.3.: Schematic view of Earth magnetosphere. On the left there is the solar wind flowing, carrying a southward IMF. The X-line are the lines interested by the reconnection process. The electric field points from dawn to dusk. North is up. [from *Schunk and Nagy* (2004)]

Now, since the solar wind is a highly conducting, collisionless and magnetized plasma, it can be described to the lowest order by the MHD equations, where the electric field in the solar wind is governed by the equation $\mathbf{E} = -\mathbf{u_{sw}} \times \mathbf{B}$ (where $\mathbf{u_{sw}}$ is the solar wind velocity vector). This electric field, visible in Fig. 1.3.3, is of course always perpendicular to $\mathbf{B}$ and it is mapped at ionospheric altitudes along the highly conductive geomagnetic field lines. Fig. 1.3.4 shows the fields and currents in the vicinity of the Earth. The mapped electric field on the polar cap implies that the charges on the polar cap boundary (positive on the right and negative on the left of Fig. 1.3.4) act to induce electric fields on nearby closed lines that are of opposite direction to the mapped electric field in the polar cap. On the field lines that separate these opposite electric fields, field aligned currents flow between the ionosphere and the magnetosphere. These currents are known as *Birkeland currents*, in honor of the famous Norwegian physicist Kristian Birkeland (1867-1917). The precipitating electrons are responsible for the upward Birkeland current, while the associated upflowing electrons of ionospheric origin are responsible for the downward Birkeland current. The current system is then closed by horizontal currents, as depicted in Fig. 1.3.4.

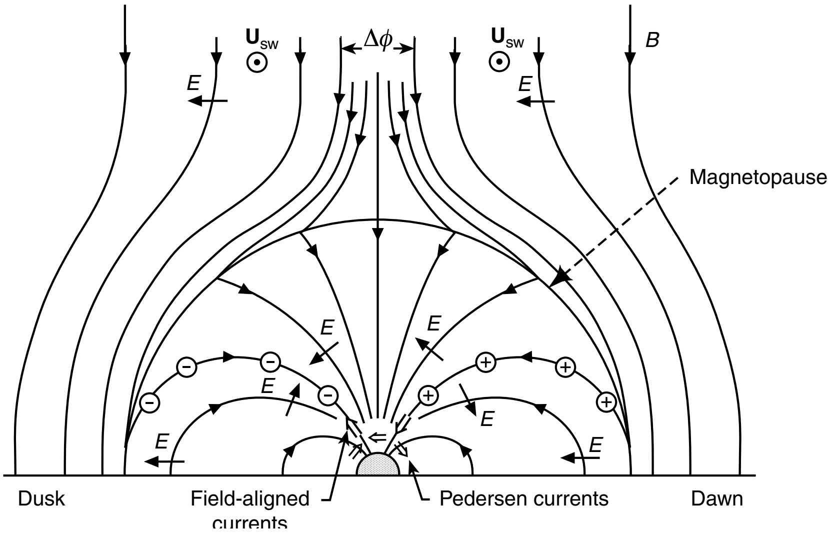

Figure 1.3.4.: Electric and magnetic fields in the vicinity of the Earth. The Sun is in front of the observer and the solar wind is flowing toward the observer. The north is at the top. [from *Schunk and Nagy* (2004)]

The field aligned currents are concentrated in two regions that encircle the geomagnetic pole (Fig. 1.3.5). In the poleward Region-1 currents flow into ionosphere in the dawn side and away from the ionosphere on the dusk side. In the equatorward Region-2 currents flow away from the ionosphere on the dawn side and into the ionosphere on the dusk side.

When the IMF is northward, an additional current exists in the polar cap, called *NBZ current*, (Northward B_z), due to its dependence on the B_z component of the IMF. The intensity of the NBZ current is directly proportional to B_z; it has been observed that, when the NBZ current is present, the Region 1 and 2 currents are still existing, but with a diminished intensity.

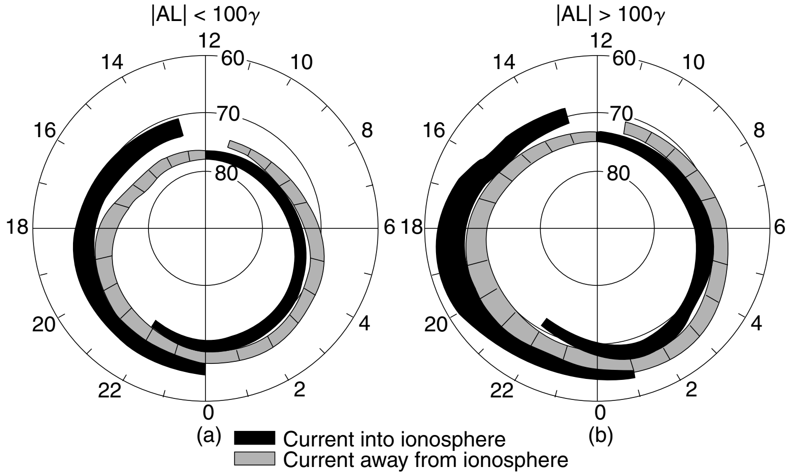

Figure 1.3.5.: Distribution in Region-1 and Region-2 of field aligned (Birkeland) currents for (a) quiet conditions and (b) active periods. [from *Schunk and Nagy* (2004)]

2. Ion outflows

2.1. Overview

During the past forty years, we have got an increasing knowledge regarding the many physical processes occurring in the Earth's atmosphere. Among them, ion outflows play an important part, e.g. for their role as ions suppliers of the magnetosphere and their probable connection with the natural enhanced ion acoustic lines (NEIALs).

There exists several outflow processes, and it is possible to group them into two general categories: *bulk ion outflows* and *ion energization processes*. We can summarize their characteristics (*Yau and André*, 1997):

- Bulk ion outflows : low energies (usually a few eV) and bulk ion velocities, where all the ions acquire energy. Typical bulk ion outflows are the polar wind and the auroral outflow, which is also referred as thermal ion upflow (TIU);
- Ion energization processes: higher energies where the energization can affect only a fraction of the ions. Typical ion energization processes include upwelling ions, ion beams, ion conics and transversely accelerated ions (TAI).

In this work we will focus on the auroral outflow, so when we use the term "ion outflow" we actually mean *bulk auroral ion outflow*.

In this chapter we will look at the basic characteristics of the different bulk ion outflows processes, the possible explanations of their acceleration mechanisms and their relation with NEIALs.

The existence of bulk ion outflow was first theorized by *Block and Fälthammar* (1968). The first observation of magnetic field-aligned bulk ion outflow is reported by *Shelley et al.* (1972). They have been also observed in the polar regions using the incoherent scatter technique by means of the EISCAT radar systems (*Wahlund et al.*, 1992b and reference therein).

As described by *Schunk* (2000), enhancements in the ion temperature T_i and electron temperature T_e lead to increasing pressures (due to $P = nkT$) which in turn create plasma upwellings from the F region. In non-auroral regions this flow is basically an ambipolar flow. Usually, plasma pressures together with ambipolar electric fields are sufficient to describe the upwelling of the lighter ions (H^+ and He^+) and this is in fact the basic mechanism explaining the generation of the classical polar wind. However, heavier ions require higher energies which cannot be supplied by pressure gradient and ambipolar electric field alone; the O^+ions, for example, require about 10 eV to escape the ionosphere.

We will now discuss briefly the polar wind and then we will concentrate on the auroral ion outflow. Note, however, that some of these processes tend to overlap, so it is not always possible to fully categorize an event.

2.2. Polar wind

Studies from the 1960s confirmed the possibility, for light ions such as H^+ and He^+, to escape the Earth's gravitational attraction (see e.g. *Bates and Patterson*, 1962). The explanation is provided by the thermal evaporation theory: due to the lower pressure in the tail with respect to the ionosphere, light ions can escape along the magnetic field lines. At first, it was believed that the ions velocity should be comparable with their thermal speed, but after successive studies and measurements it was clear that velocity becomes supersonic at relatively high altitudes. The term "polar wind" was coined by *Axford* (1968) to describe the supersonic ion flow at collisionless altitudes, in analogy to the solar wind.

The characteristics of topside ionosphere are dependent, among other things, on the geomagnetic latitude. Satellite measurements have shown that at higher latitudes it is possible to observe some peculiar effects. As pointed out in *Banks and Kockarts* (1973) the most important anomalies in the polar ionosphere are:

1. O^+ is the most abundant ion component up to 4000 Km at these latitudes, whereas on lower geomagnetic latitudes the principal component is H^+.
2. The polar nighttime electron densities are very small (down to $3 \times 10^7\,\mathrm{m}^{-3}$ at 3000 km)
3. Above 2000 km a change in ion composition from H^+ to O^+ occurs near a magnetic latitude of 60° as one progresses poleward.
4. Large-scale upward fluxes of H^+ have been observed outside the plasmapause.

Satellite observations have shown that, outside the plasmapause boundary, much lower densities are found. In Fig. 2.2.1 it is shown the sharp decrease of H^+ density. The O^+ density, on the other hand, is not affected by such a large decrease and hence it is the dominant ionic constituent in polar regions. The density is shown as a function of the parameter L, which is defined as $L = r_0/R_e$ where R_e is the Earth radius and r_0 is the distance from the Earth center at which a given field line hits the equatorial plane. For a place on Earth with magnetic latitude λ_m and where $r = R_e$, the magnetic field line through that place reaches the equatorial plane at a distance $r_0 = \frac{R_e}{\cos^2 \lambda_m}$ (*Brekke*, 2012).

Successive studies helped to identify the phenomenon known as *classical polar wind*, which is caused by an ambipolar outflow and, as we can read in *Schunk and Nagy* (2004), goes through four different transformations as it flows up:

1. from chemical to diffusion dominated;
2. from subsonic to supersonic flow;
3. from collisional to collisionless regime;
4. from O^+ to H^+ions.

Other accelerating forces include plasma pressure gradients, magnetic mirror force and $\mathbf{E} \times \mathbf{B}$ convection; decelerating forces include gravitation and ion-neutral collision (*André and Yau*, 1997).

The presence of electric fields causes a horizontal motion in the form of convections in and out of typical structures as the polar cap and nocturnal auroral oval. This effect is important because the timescale of the upflow is comparable with the timescale of the flow

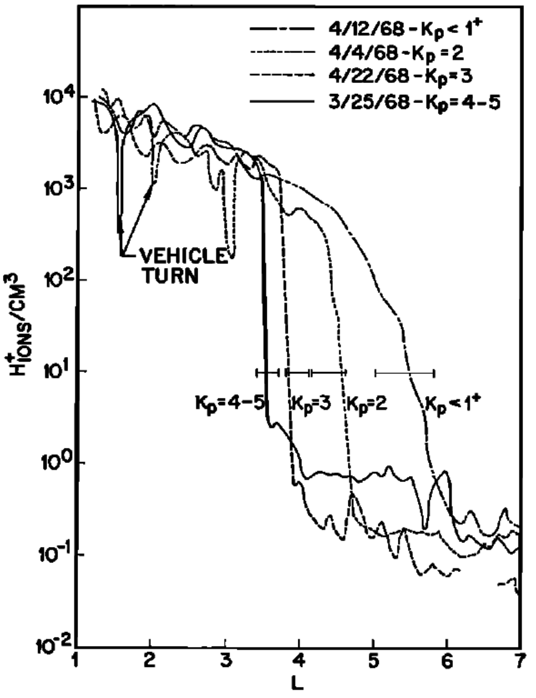

Figure 2.2.1.: H^+ density as a function of L for different levels of magnetic activities K_p. [from *Chappell et al.* (1970)]

across the polar cap, which means that the local conditions are always changing. Hence a lot of complications can arise in modeling the polar wind and this is the reason why several mathematical approaches are used in its theoretical description, e.g. hydrodynamic, hydromagnetic, generalized transport and kinetic.

The hydrodynamic approach has shown that H^+ outflow affects both $H^+$and O^+ temperatures. It was shown that as the H^+ velocity increases the O^+ temperatures decreases. This happens because the increase in H^+ velocity is related to a decrease in its density and hence the O^+ ions will be more coupled to the relatively colder neutrals, which will cause the decrease of O^+ temperature.

Regarding the H^+ temperature, its behavior is complicated by the contribution to the thermal balance from e.g. convection and frictional heating. However, the general trend is that, due to frictional heating, H^+ temperature increases as its velocity increases, since H^+ is moving faster and faster in a gravitationally bounded O^+. Note, however, that this is strictly true only for subsonic velocities.

Another important peculiarity of the polar wind is the H^+ flux limiting character, as it can be clearly see in Fig.2.2.2. Here the H^+ flux is proportional to the H^+ and O^+ densities until it reaches asymptotic values. The process behind this behavior is the exchange reaction $O^+ + H \longleftrightarrow O + H^+$, which limits the H^+ production and, since the escape rate is dependent upon the production, we get the limiting flux.

Similar solutions have been found also for He^+. In addition, several other processes exist in the polar wind, however their in-depth treatment is beyond the scope of this work.

It is important to note that there are several restrictions to all of this. First of all the above

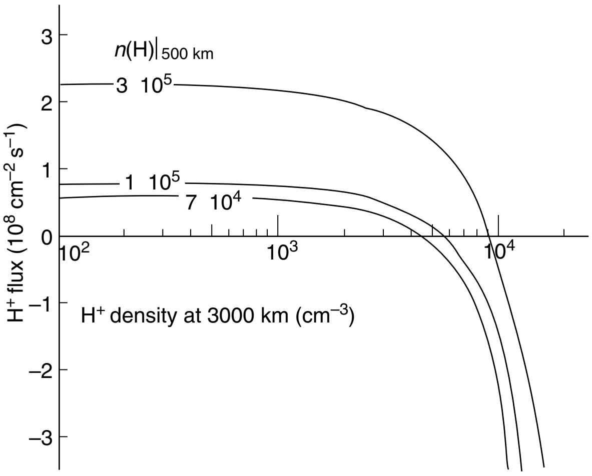

Figure 2.2.2.: The H^+ escape flux for different boundary densities and neutral hydrogen densities. [from *Schunk and Nagy* (2004)]

results are valid only if O^+ ions are gravitationally bounded. If O^+ is energized we have an O^+ outflow at lower altitudes which will cause a decrease in its density and hence will affect the H^+ flow.

In addition we need a collision-dominated environment. A rough relation to check if and where this is true is: $u_i \ll H_i \nu_i$ (u_i is the ion velocity, H_i is the scale height and ν_i the ion-ion collision frequency); basically the ionosphere is collisionless up to 1500 km for H^+ and up to 3000 km for O^+ and He^+ (*Schunk and Nagy*, 2004).

The last assumption we need is a steady-state situation, which greatly simplifies the models, even though the polar wind is very rarely in a steady state. To overcome this difficulty, 3-D time-dependent simulations of polar wind have been used, which gave several interesting results. Among them (see *Schunk and Nagy* (2004) for an in-depth treatment):

1. Plasma convection through the auroral oval and regions of high electric fields produces transient O^+ upflows and downflows.
2. O^+ upflows usually occur in the auroral oval at all local times and downflows occur in the polar cap. However, if there is an increasing magnetic activity, O^+ upflows can occur in the polar cap. Generally the O^+ upflows are stronger where both T_e and T_i are high.
3. During strong magnetic activity, O^+ can be the dominant ion up to 9000 km.

These polar wind simulations represent the classical polar wind, which is due to thermal processes in the lower ionosphere. However there can be other processes affecting the polar wind which are not included in the classical picture, e.g.

1. escaping photoelectrons, which may provide additional acceleration at about 7000 km since they drag the thermal ions with them.
2. cusp ion beams and conics can destabilize the polar wind when they pass through it at high altitudes, resulting in a wave-particle interaction which modifies velocities and fluxes.

3. anomalous resistivity on auroral field lines can affect the polar wind as the plasma convects through the nocturnal auroral oval

In this case the polar wind is usually referred as *non-classical polar wind*. Fig. 2.2.3 shows the non-classical processes that can affect the polar wind.

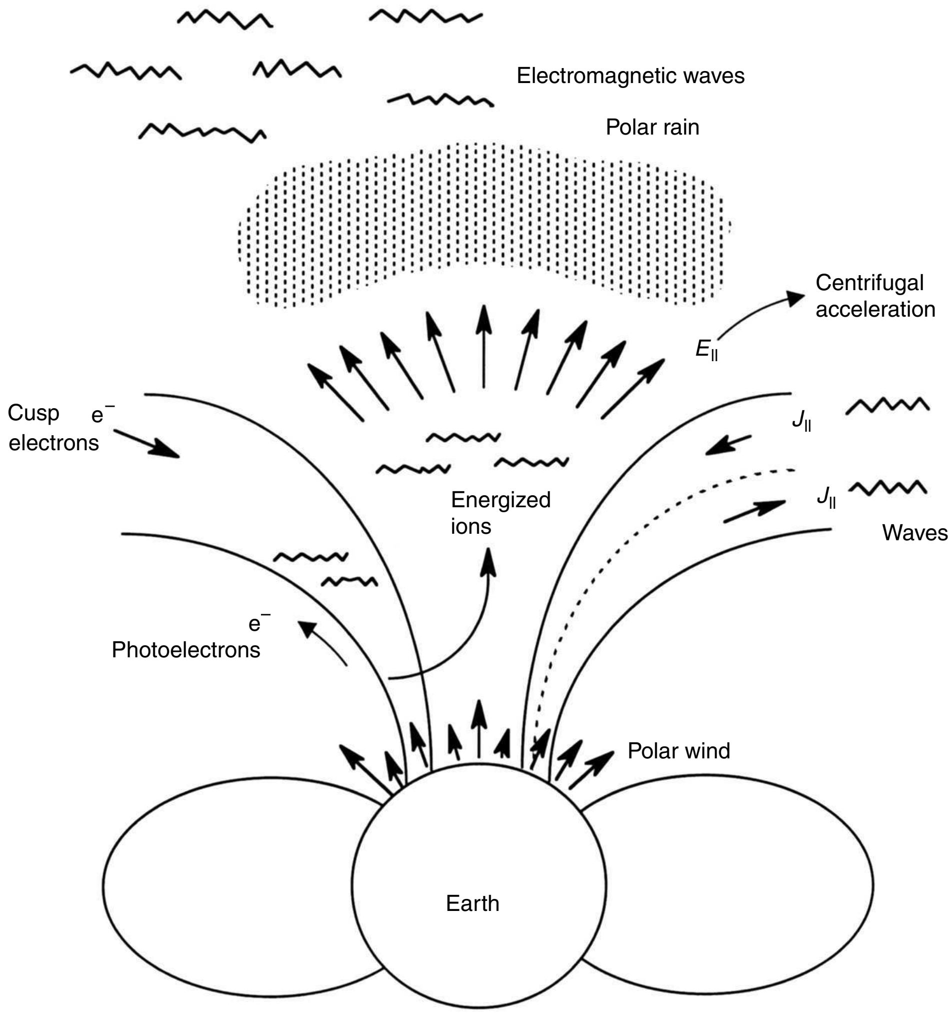

Figure 2.2.3.: Main non-classical processes affecting the polar wind. [from *Schunk and Nagy* (2004)]

2.3. Auroral ion outflow

Observations have shown that there are several ion species involved in ion outflows, albeit the most important are H^+ and O^+. Apart from the polar wind, in its classical and non-classical occurrence, the other important bulk process is the auroral ion outflow, which consists mainly of O^+ ions, with sometimes a NO^+ component and with an H^+ component less than 10% below 900 km. The bulk ion auroral outflows are observed on a wide range of altitudes, usually from 350 to 1500 km, but it is possible to find them even at lower altitudes (see, for example, *Rietveld et al.*, 1991, *Forme et al.*, 1995 and *Ogawa et al.*, 2011). The ions usually reach a velocity of 1500 m s^{-1} between 900 and 1500 km.

Flux can be as high as $10^{14}\,\mathrm{m^{-2}s^{-1}}$. As showed by *Ogawa et al.* (2009), they are highly correlated with the solar wind density and the IMF B_y component, but they occur less frequently when the geomagnetic activity index (K_P), solar wind velocity and negative (southward) IMF B_z component are high.

The most evident difference between polar wind and auroral ion outflow is that the latter will not usually push ions outside of the ionosphere, unless further energizations occurs at higher altitudes. This is because the heavier ions such as O^+ cannot easily escape gravity. In addition, the flux is always subsonic, whereas the polar wind is supersonic above a certain altitude. The ions that do not reach the escape velocity will fall down in the lower altitude ionosphere.

The bulk ion auroral outflows are thermal processes. When the energies are much higher the velocity distribution of the particles deviates from a maxwellian and non-thermal processes (e.g. ion beams and ion conics) take place.

Statistical studies on outflows can be find in *Endo et al.* (2000). They determined the MLT distribution and K_P dependence of ion upflow and downflow events using the EISCAT VHF radar in Tromsø. We can summarize their findings:

1. Ion outflow and downflow events can be observed at any MLT, both in dayside and nightside, and for any K_P.
2. Upflow and downflows are more common in the nightside.
3. Upflow events are usually more common than downflow events (except around midnight), irrespective of K_P values.
4. Occurrence frequencies of both upflows and downflows are directly proportional to K_P level, however the occurrence frequencies of the downflows seem to stop after a certain level (Fig. 2.3.1), probably due to the fact that for higher K_P the upflowing ions can get energies high enough to escape gravity and therefore they will not fall back on Earth.

There exist two different classes of auroral ion outflow, type-I and type-II, which were identified by *Wahlund et al.* (1992b).

The type-I ion outflow is characterized by an enhanced and anisotropic ion temperature T_i with $T_{i_\perp} > T_{i_\parallel}$ and a low electron density, especially below 300 km. The temperature anisotropy is due to large (usually above $50\,\mathrm{mV\,m^{-1}}$) perpendicular electric fields causing strong frictional heating (*Løvhaug and Flå*, 1986) and the low electron density is due to a lack of auroral particle precipitation. Fig. 2.3.2 shows a good example of type I ion outflow. We are now going to discuss this figure in more detail, since this type of color plot is widely use in this work (e.g. in chapter 5). Panel 1 shows the electron density, useful to check, for instance, the presence of particle precipitation. Panel 2 shows the electron temperature, which in this particular case was not homogeneously enhanced for the entire ion upflow event, while the ion temperature (Panel 3) was clearly enhanced at about 1800 and 2030 UT. Panel 4 shows the ion velocity (positive means ions drifting away from the Earth) and it was fundamental in this work to identify ion outflows to analyze. Finally Panel 5 give us some information about the radar settings, e.g. system temperature, elevation and azimuth. The last two are useful, for instance, to check if the

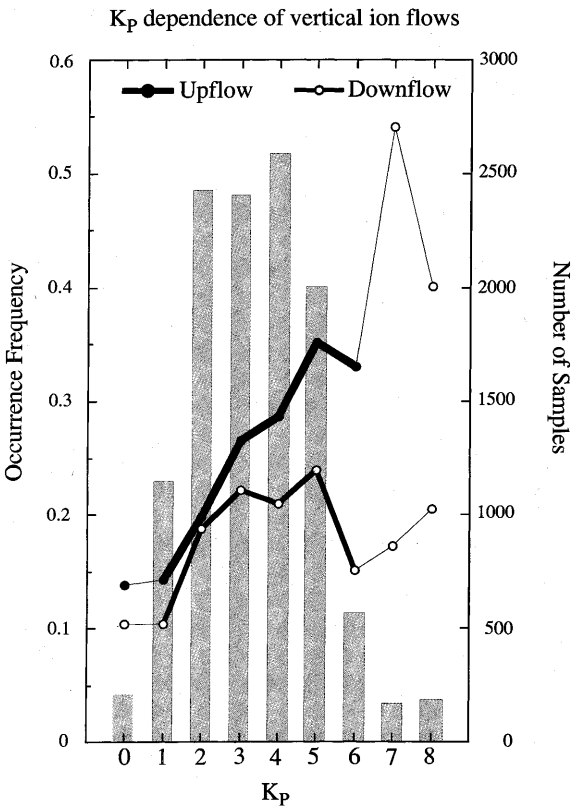

Figure 2.3.1.: K_P dependence of ion upflow and downflow for every MLT. Note how the downflow occurrence do not increase at high K_P values (from *Endo et al.*, 2000)

antenna was pointed field aligned or if the experiment was a multiposition one (i.e. the antenna switched between 2 or more different positions at regular time intervals)

Since the 1970s it was theoretically clear that non-Maxwellian distributions can develop if strong electric and magnetic crossed fields are present in collisional plasma (see, for example, the in-depth review of *St-Maurice and Schunk*, 1979). In the case of the ionosphere F region, if the ion-neutral collision frequency is less than ion cyclotron frequency and if the $\mathbf{E} \times \mathbf{B}$ drift is larger than neutral thermal velocity, it will then result in a toroidal-shape distribution in velocity space.

The basic mechanism explaining the ion (and neutral) temperature enhancement is the Joule heating effect, which is responsible for the energy transfer between ions and neutrals and can also be seen as a manifestation of the magnetosphere-ionosphere coupling, since it is one of the mechanisms whereby the energy originated in the solar wind is released in the Earth's atmosphere (*Davies et al.*, 1997).

The type-II ion outflow (Fig. 2.3.3) is characterized by an enhanced electron temperature (as high as 6000 K), a fairly high electron density but a not affected ion temperature, which enforce the idea that the acceleration mechanisms of type-I and type-II are, at least partly, different, since the lack of high ion temperatures is in fact in contrast with the Joule heating mechanism proposed for type-I outflows.

Nevertheless there exist several attempts to explain the generation mechanisms of type-II outflows; most of the authors agrees on some responsibility of field aligned electric field for the ion outflow generation and acceleration. There are however some controversy about the source of the field aligned electric field: many studies propose the soft electron particle precipitation as a source for the field aligned electric field (e.g. *Horwitz and Moore*, 1997; *Burchill et al.*, 2010), while others proved that, at least in some cases, the soft electrons are not a good explanation for the observed ion outflow (e.g. *Kagan and St.-Maurice*, 2005).

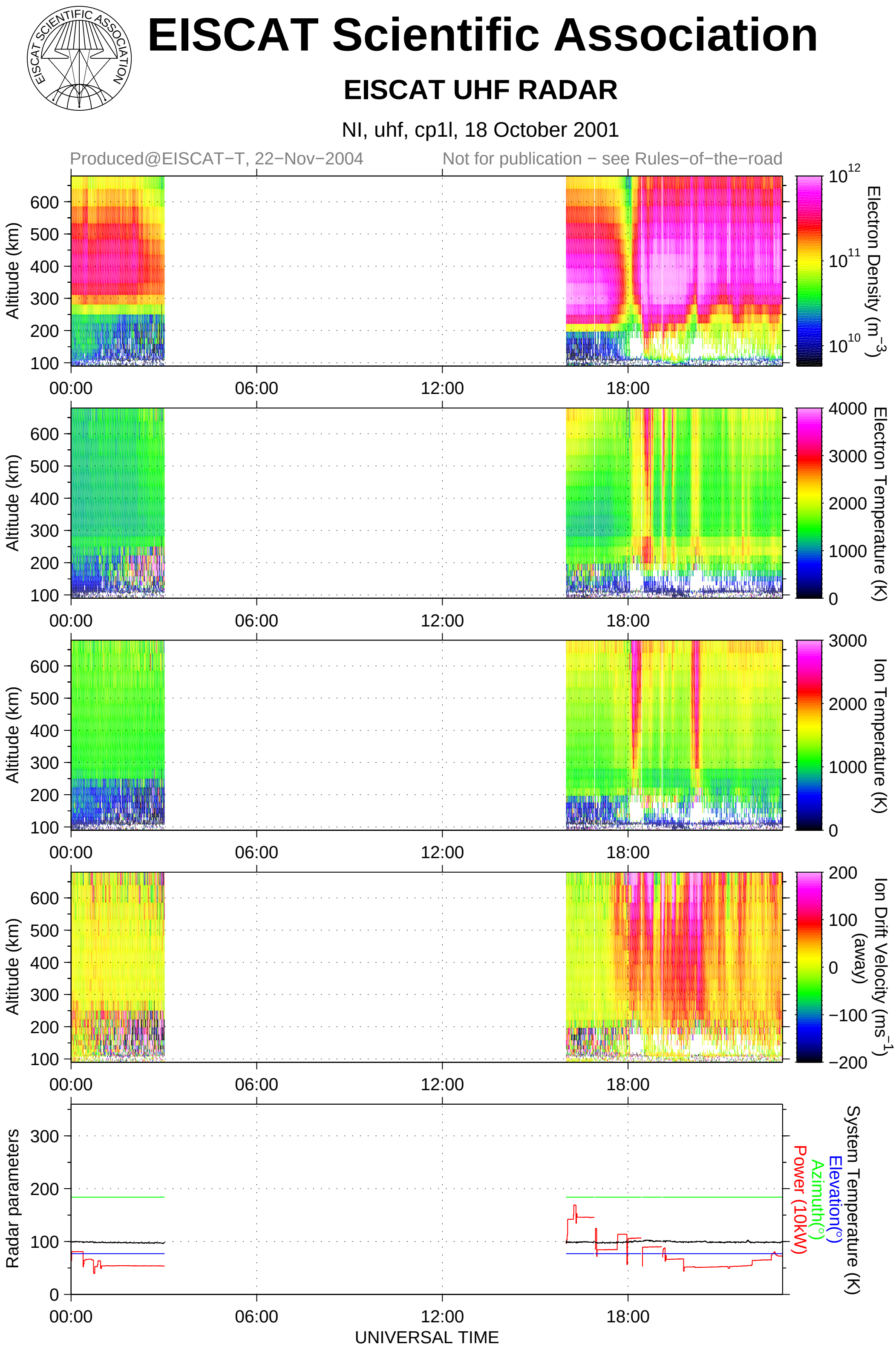

Figure 2.3.2.: Example of type-I ion upflow occurring on 18 October 2001. Note the enhanced ion temperature around 18:00 and 20:30 UT where the ion temperature exceeded the electron temperature. [from *EISCAT Scientific Association* (2013)]

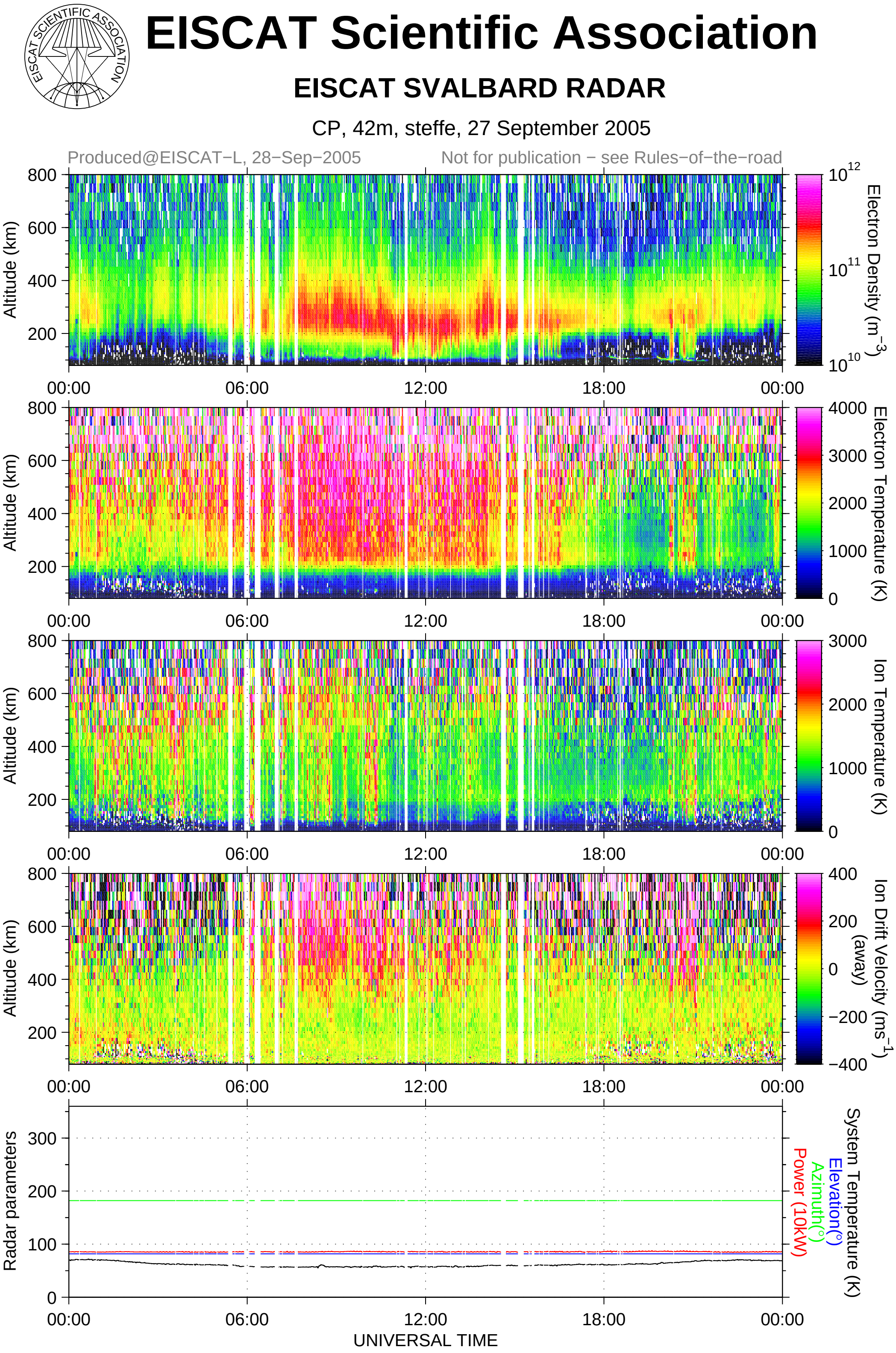

Figure 2.3.3.: Example of type-II ion upflow occurring between 07:00 and 12:00 UT on 27 September 2005. Note the enhanced electron temperature during this period while the ion temperature remained mostly unaffected and always lower in magnitude than electron temperature. A weaker and shorter type-II outflow is also visible around 21:00 UT. [from *EISCAT Scientific Association* (2013)]

2.4. Acceleration mechanisms

The acceleration mechanisms of the ion outflows are not yet fully understood. Several theories have been proposed in the last thirty years, but so far none of them is able to provide a complete description of the acceleration process. The most common and recurring in literature (see e.g. *Burchill et al.*, 2010) are:

1. Frictional heating
2. Soft electron precipitation
3. Anisotropic ion heating of plasma waves
4. Precipitation of heavy ions from the ring current
5. High frequency turbulence affecting electrons

We will now give a brief overview of these different theories.

2.4.1. Frictional heating

Loranc and St. Maurice (1994) investigated the effect of ion frictional heating in ion upflows developing a time-dependent gyro-kinetic model of the high latitude F region response to frictional heating. The kinetic model gave them quantitatively different results with respect to the fluid model, and they argue that the differences could not be due to the limitations of the kinetic model they used, but rather that they may be linked to the limitations of the fluid equations themselves. The reason lies in the assumptions made about velocity distributions: the transport equation in the fluid model is built on the assumption of zeroth-order maxwellian or bi-maxwellian distribution, whereas *Loranc and St. Maurice* (1994) obtained some very large departures from maxwellian ion velocity distributions.

They simulated the passage of a convecting flux tube through a spatially localized frictional heating region by specifying the exobase parallel and perpendicular temperature under different conditions (standard conditions, short duration heating, slow heating and cooling, elevated electron temperature, small temperature increase and large temperature increase) and under several assumptions about plasma components, exobase structure, collisions, polarization fields.

As we mentioned, they used a kinetic model, where the single component O^+ plasma is described by the ion guiding center motion and electrons follows a Boltzmann distribution.

They considered the neutral exobase to form a discontinuous boundary between the weakly ionized and the fully ionized plasma, which means that in the model the plasma changes discontinuously from weakly to fully ionized across an altitude near the neutral exobase, which was placed arbitrarily at 500 km.

In addition they omitted the effects of ion-ion collisions and chemistry, which is usually a fair assumption if the streams are equal or higher than $3000\,\mathrm{m\,s^{-1}}$ for 400 km altitude and ion densities not higher than $10^{11}\,\mathrm{m^{-3}}$; and this is indeed the case in the work of *Loranc and St. Maurice* (1994).

They also assumed that the ion distribution function below the exobase (and hence in the collisional regime) could be approximated by a bi-maxwellian distribution function. Albeit it was observed that non-maxwellian distortions are an intrinsic part of frictional heating, they argued that in the parallel direction and for their particular study a maxwellian distribution was reasonable.

We can summarize their findings:

1. Their model responded to the frictional heating with transient ion parallel velocities higher than $3000\,\mathrm{m\,s^{-1}}$, temperatures higher than $10\,000\,\mathrm{K}$ and as high as $20\,000\,\mathrm{K}$ and fluxes higher than $10^{15}\,\mathrm{m^2\,s^{-1}}$.
2. In all case studied, the largest parallel fluxes were produced near the exobase.
3. In contrast to the parallel flux, the parallel velocity and temperature initially increased with altitude.
4. Well after heating ceased, large parallel temperature and downward velocities and fluxes developed as the flux returned to diffusive equilibrium.
5. After the heating ceased, the maximum downward parallel velocities are comparable in magnitude to the maximum upward velocities but the maximum parallel temperatures were much less than the maximum temperatures during the heating phase.

Loranc and St. Maurice (1994) observed that their model requires substantial electron temperature enhancements and ion-neutral frictional heating to reproduce the largest observed ion fluxes. However, there is an important difference between their conclusions and the results from the fluid model: the upward ion parallel velocities and fluxes produced by fluid models are significantly smaller than those produced by their kinetic model.

2.4.2. Soft electron precipitation

A review of the soft auroral electron precipitation role in the subject of the outflow acceleration can be found in *Horwitz and Moore* (1997). They discuss the effects of soft electron (i.e. with an energy below 0.5 keV) precipitation on high latitude F region ionospheric upflows. Such electron precipitation can occur particularly during northward IMF conditions (*Makita et al.*, 1988).

Liu et al. (1995), in order to study the effect of soft-particle precipitation and frictional heating on the ion outflow, made use of the so-called Field Line Interhemispheric Plasma (FLIP) model. They included the effects of electron precipitation and ion frictional heating using measurements from HILAT and DE-2 satellites as inputs for the model. Results indicated that the combined effects of soft electron precipitation and ion frictional heating are the principal drivers of ion outflows. In particular the upflows can be attributed to the precipitation-induced abrupt ionization and thermal electron heating and subsequent plasma expansion, while the ion temperature variations can be attributed to variations in frictional heating. Fig. 2.4.1 shows indeed that the soft-electron precipitation is sufficient to explain the peak upflow velocities at an altitude of 700 km whereas the frictional heating are of secondary importance in the driving of ionospheric upflow despite their importance for the ion temperatures.

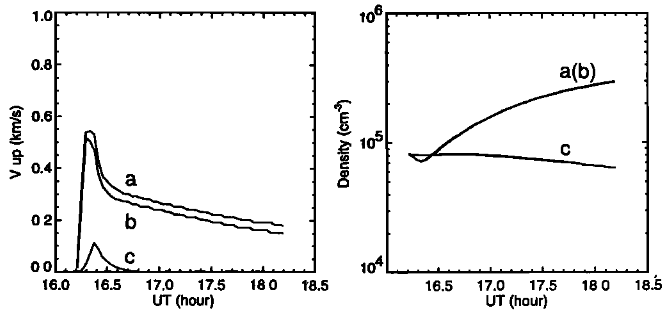

Figure 2.4.1.: Evolution of the upflow velocity (left) and O^+ density (right) at an altitude of 700 km including: (a) electron precipitation and frictional heating; (b) only electron precipitation; (c) only frictional heating. [from *Liu et al.* (1995)]

Caton et al. (1996) employed the same ionospheric plasma transport model as *Liu et al.* (1995) but used measurements from EISCAT radar as input. In the $200 - 900$ km altitude range they used a precipitating electron energy flux equal to 1 erg $\mathrm{cm}^{-1}\,\mathrm{m}^{-2}$ with an average energy of 100 eV, a convection speed equal to $1200\,\mathrm{m\,s}^{-1}$ and a downward magnetospheric electron heat flux of $1.1 \times 10^{10}\,\mathrm{eV\,cm}^{-1}\,\mathrm{m}^{-2}$ to match the temperature gradient observed.

They turned on and off these inputs individually to study their impact on the altitude profiles. As it can be seen in Fig. 2.4.2 the soft-electron (< 1 keV) precipitation has a dominant role in the production of ionospheric outflows.

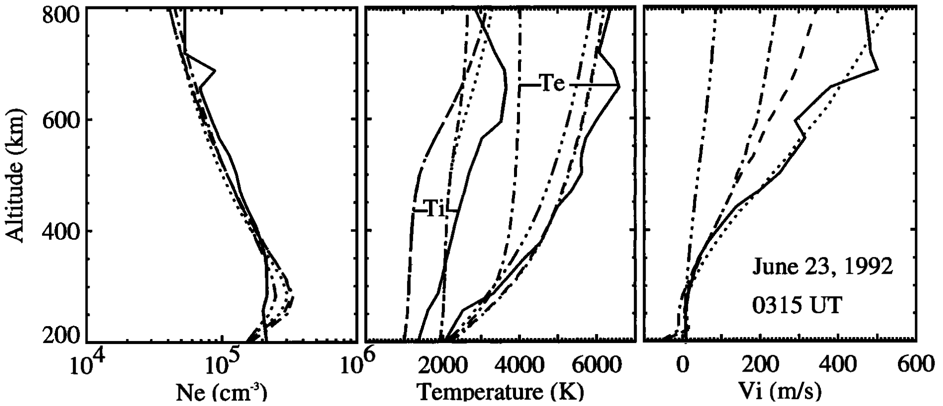

Figure 2.4.2.: EISCAT measurement (solid lines) together with model results including all three input parameters (dotted line). Dashed line: only convection is off; dash-dot-dot-dot-dash line: only precipitation off; dash-dot-dash line: only the topside eat flux is off. [from *Caton et al.* (1996)]

It should be note, however, that a convection velocity equal to $1200\,\mathrm{m\,s}^{-1}$ could give rise to non-Maxwellian (e.g. toroidal) ion distributions and this can in turn cause uncertainties in the interpreted temperatures, leading to inaccuracies in the derived radar profiles (see *Davies et al.*, 1995).

Statistical studies have been conducted by *Seo et al.* (1997) using measurements from DE-2 satellite in the $850 - 900$ km altitude range for precipitating soft (≤ 1 keV) electrons. They examined 1137 independent samples (resulting from seven satellite passes) of field aligned ion flow velocities, fluxes, Mach numbers, densities, ion and electron temperatures, soft electron energy fluxes and soft electron average energies. In this data set the ion velocity range was $500 - 1500\,\mathrm{m\,s^{-1}}$ and they slightly restricted the soft electron energy range to $0 - 2\,\mathrm{erg\,cm^{-2}\,s^{-1}}$.

Fig. 2.4.3 shows the good correlations ($r = 0.97$) between electron temperatures and ion upflow velocities (a) and fluxes (b). This result can be compared to Fig. 2.4.4, where instead the correlation is between ion temperatures and ion upflow velocities (a) and fluxes (b); this time the correlation coefficient is a bit lower ($r = 0.91$ between ion temperatures and ion velocities and $r = 0.94$ for ion temperatures and ion fluxes). These results suggest that the ambipolar electric field associated with enhanced electron temperatures (as heated by both direct collisions with the precipitating electrons as well as downward magnetospheric heat fluxes) could have an important role in the driving of ionospheric upflow. Similar results were obtained by *Keating et al.* (1990).

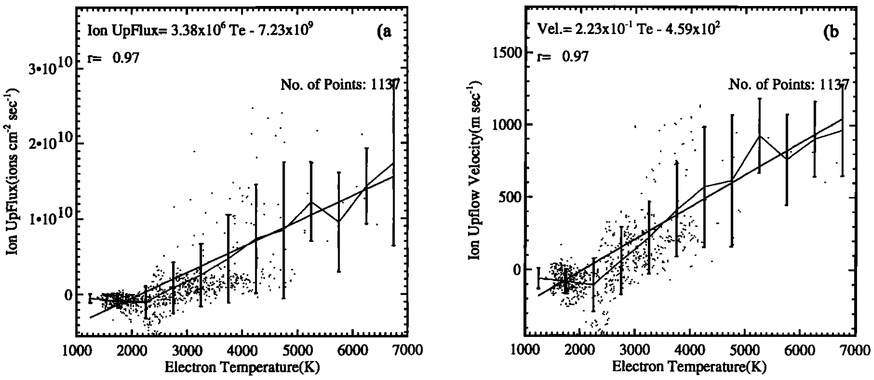

Figure 2.4.3.: (a) correlation between electron temperature and ion outflow fluxes; (b) correlation between electron temperature and ion outflow velocities. [from *Seo et al.* (1997)]

Another interesting feature observed by *Seo et al.* (1997) is the anticorrelation of electron temperatures and ion temperatures with the average energies of the precipitating soft electrons (see Fig. 2.4.5). From this figure is also evident that: large upflows ($\geq 5 \times 10^9\,\mathrm{ions\,cm^{-2}\,s}$) are only observed during periods of very soft ($\leq 80\,\mathrm{eV}$ average energy) electron precipitation (panel a); the occurrence frequency peaked at low average energies (20 eV) and there is a drastic decrease above 50 eV (panel b); upward velocities exceeding $500\,\mathrm{m\,s^{-1}}$ were only observed for electron precipitation average energies below 80 eV and there is a reduction in upward velocity with increasing average electron precipitation energy (panel c).

Burchill et al. (2010) employed the Cusp-2002 sounding rocket to retrieve information on thermal ion upflow in proximity to the dayside cusp at altitudes between 640 and 768 km. They found significant correlation between upflow and precipitating magnetosheath electron energy flux and a weak correlation between ion upflow and wave power in the VLF band. A summary of their observation:

1. There is a positive correlation ($r = 0.62$) between the magnitude of the ion upflow and the logarithm of the precipitating magnetosheath electron energy flux when the fluxes are greater than about 1×10^{10} and less than $3 \times 10^{11}\,\mathrm{eV\,cm^{-2}\,s^{-1}}$ (Fig. 2.4.6).
2. Ion upflow is not observed for electron energy fluxes less than about $10^{10}\,\mathrm{eV\,cm^{-2}\,s^{-1}}$ (Fig. 2.4.6).

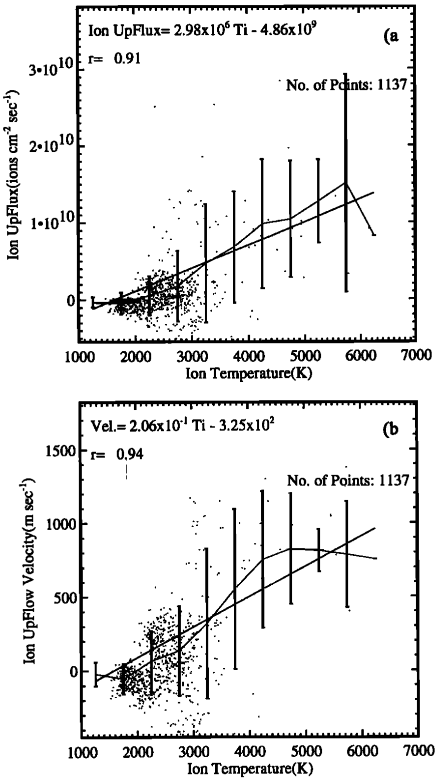

Figure 2.4.4.: (a) correlation between ion temperature and ion outflow fluxes; (b) correlation between ion temperature and ion outflow velocities. [from *Seo et al.* (1997)]

3. Ion upflow is not correlated with convection electric fields greater than 70 mV m^{-1}. There is, however, a slightly negative correlation ($r = -0.38$) between ion upflow and convection electric fields for magnitudes less than about 70 mV m^{-1}. One possible explanation provided by *Burchill et al.* (2010) is that the electron precipitation leads to enhanced ionospheric conductivity and therefore weaker electric fields (Fig. 2.4.7).
4. Ion upflow correlates weakly with wave power in the VLF ($r = 0.33$) and BBELF ($r = 0.27$) bands.
5. There are positive correlations between ion upflow and the parallel ($r = 0.81$) and perpendicular ($r = 0.70$) ion temperatures (Fig. 2.4.8).
6. Observations of ion downflows at the downstream edges of the upflow regions can be indicative of a return to equilibrium outside the electron precipitation regions.

2.4.3. Anisotropic ion heating by plasma waves

Ganguli et al. (1994) investigated the possible importance of shear-driven processes in particle energization and ionospheric dynamics.

When thermal ion upflows are located in the convective flow reversal region, the convective parallel velocity is usually small but spatial gradients can be large, which imply that

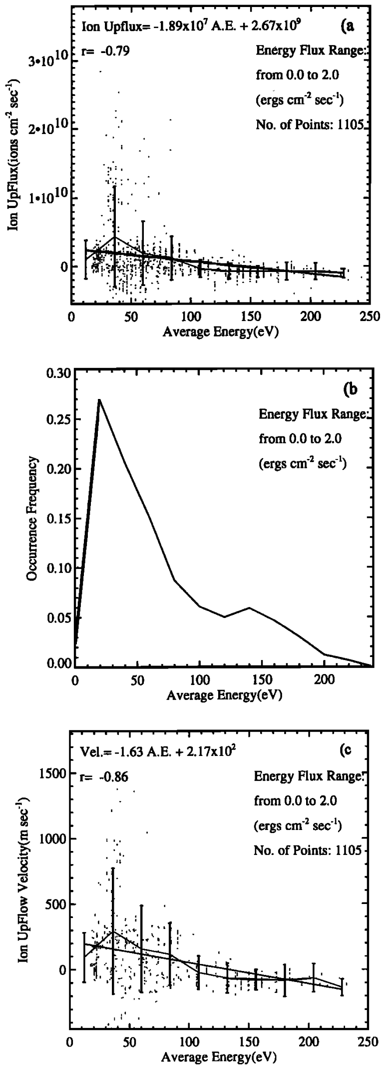

Figure 2.4.5.: (a) ion fluxes versus soft electron precipitation average energy; (b) occurrence histogram distribution of soft electron preciptation average energies; (c) ion fluxes versus soft electron preciptation average energy. [from *Seo et al.* (1997)]

the Joule heating effect is small. Therefore the high level of ion heating observed (few eV or more) cannot be explained by the classical Joule heating alone but requires additional heating source (e.g. plasma waves).

As investigated by *Tsunoda et al.* (1989), there is a strong correlation between ion heating and shear in the convective velocities, which suggest an important role of velocity shears. *Ganguli et al.* (1994) provided additional evidence for this correlation using measurement from the DE-2 satellite. Fig. 2.4.9 shows a nice example of the good correlation of ion upflow with the shear in the large-convective flow.

Assuming an ideal ionosphere (only two species, no collisions), they investigated some of the possible microinstabilities that can be triggered by the velocity shear and followed their non-linear evolution. They found that a small amount of velocity shear in the transverse flow can be sufficient to excite large-scale Kelvin-Helmholtz mode. Then they used a particle-in-cell (PIC) code to investigate the non-linear evolution of these low frequency

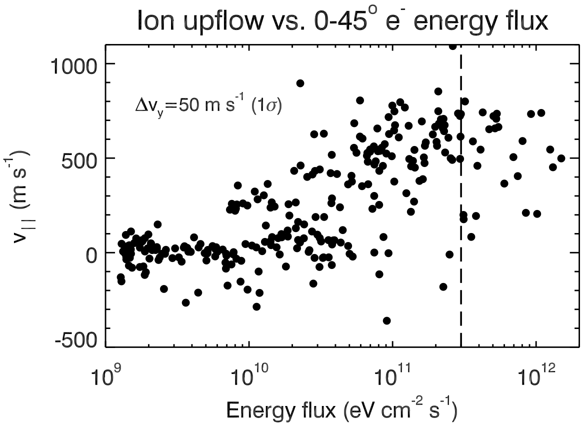

Figure 2.4.6.: Ion upflow versus 0° – 45° electron energy flux. The vertical dashed line represents the electron energy flux threshold at which the spacecraft potential begins to significantly affect the upflow measurement. [from *Burchill et al.* (2010)]

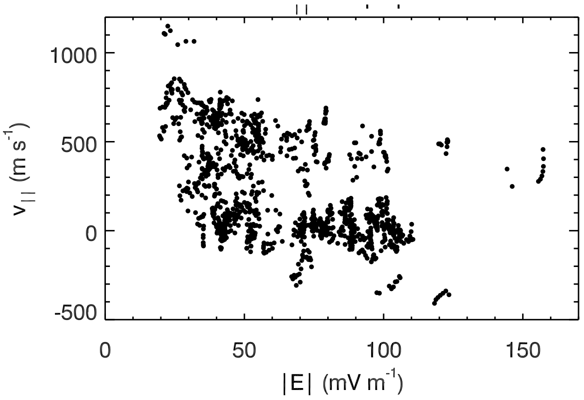

Figure 2.4.7.: Relationship between ion upflow and magnitude of convection electric field. [from *Burchill et al.* (2010)]

waves and found that they can steepen (i.e. formation of small-scale size density structures) and give rise to regions of strongly sheared flows. These stressed regions may then seed plasma waves (microinstabilities) in the range of ion cyclotron to lower hybrid frequencies (Fig.2.4.10), which are potential source of ion heating. Fig.2.4.11 summarizes this scenario.

However, they also note that their model is still incomplete, since:

- the PIC code does not include collisions and hence cannot be applicable to very low altitudes;
- they have not evaluated microscopic contributions from another class of shear driven instabilities, such as the inhomogeneous energy density driven instability (IEDDI), can potentially energize the ions more efficiently;
- the viscosity model needs further refinements.

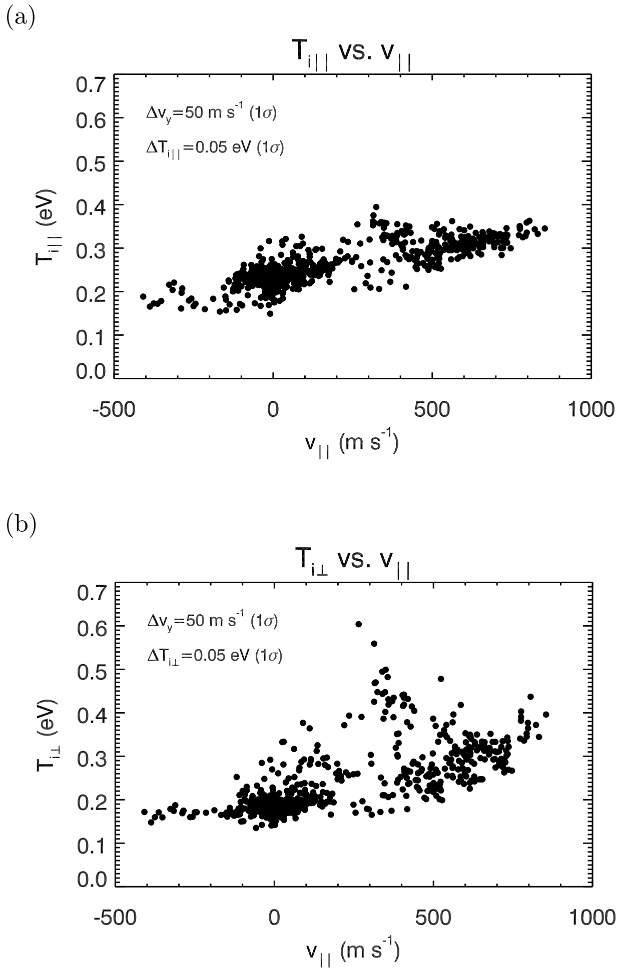

Figure 2.4.8.: (a) ion parallel temperature versus ion field-aligned velocity; (a) ion perpendicular temperature versus ion field-aligned velocity. [from *Burchill et al.* (2010)]

2.4.4. Precipitation of heavy ions from the ring current

Yeh and Foster (1990) presented an analysis of a 3-hour outflow event at mid-latitude observed by the Millston Hill incoherent scatter radar during a strong magnetic storm. The bulk ion speed increased with altitude above 600 km and at times exceeded 3000 m s^{-1} at 1000 km altitude. The observations were made during an interval of strong frictional ion heating at adjacent latitudes and intense local heavy ion precipitation from the storm-inflated ring current.

In their paper *Yeh and Foster* (1990) examined two possible mechanisms to explain the ion outflow:

- heavy ion ring current precipitation
- frictional ion heating

They found that intense O^+ production (200 ions cm^{-3} s^{-1}) and upward acceleration (between 5 and 10 m s^{-2}) of ion bulk motion took place between altitudes of 600-800 km. An explanation of these features can involve a mechanism suggested by *Torr et al.* (1974) in which intense precipitating O^+ at mid-latitude during magnetic storms can produce large

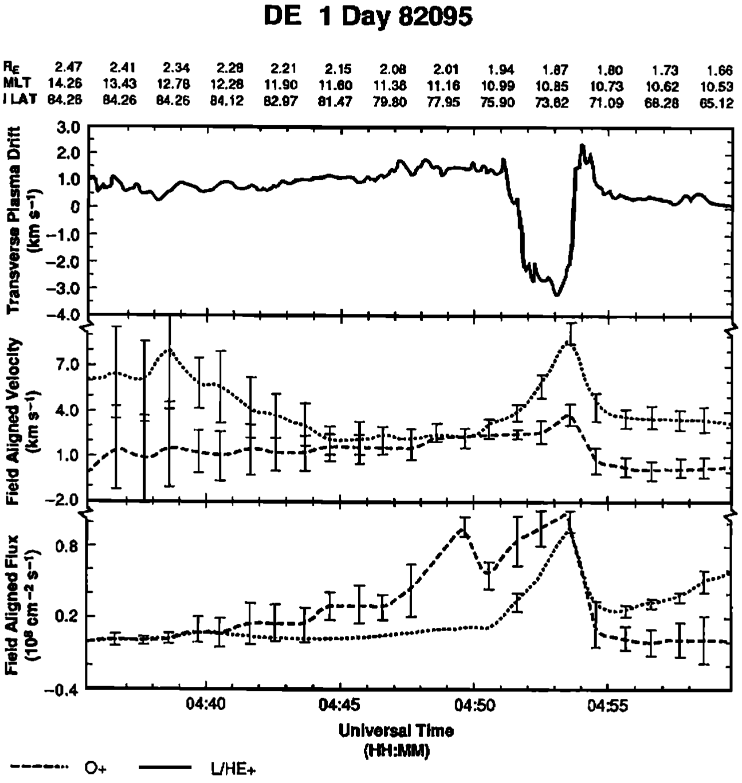

Figure 2.4.9.: Ion bulk parameters derived using DCE values from the short wire (z) antenna on DE-1 spacecraft. [from *Ganguli et al.* (1994)]

fluxes of back-splash energetic O^+ moving upwards from the topside ionosphere. They argue that the newly produced O^+ can account for sufficient momentum to explain the acceleration of the bulk ion motion with increasing altitude.

A second possible theory is based on the fact that upward O^+ velocities larger than $2000\,\mathrm{m\,s^{-1}}$ can develop in several hundred seconds on flux tubes subjected to ion temperatures of $5000\,\mathrm{K}$ in the collisional F region. Since large convection velocities and evidence for strong frictional heating were observed immediately poleward of Millstone Hill, *Yeh and Foster* (1990) suggested that the ion outflow they observed occurred on flux tubes which had recently exited from a region of strong frictional heating.

2.4.5. High frequency turbulence affecting electrons

Kagan and St.-Maurice (2005) noticed that an explanation based on a field aligned electric field alone would disagree with the momentum balance. Therefore they introduced the electron energy balance in the system, finding the consistency with the field aligned electric field explanation, but with the additional presence of electron scattering due to a high frequency turbulence.

They analyzed the three most probable explanations for a high electron temperature, namely:

- soft electron precipitation, which is not possible because the temperature increases above the F-peak and above the layer where electrons deposit their energy

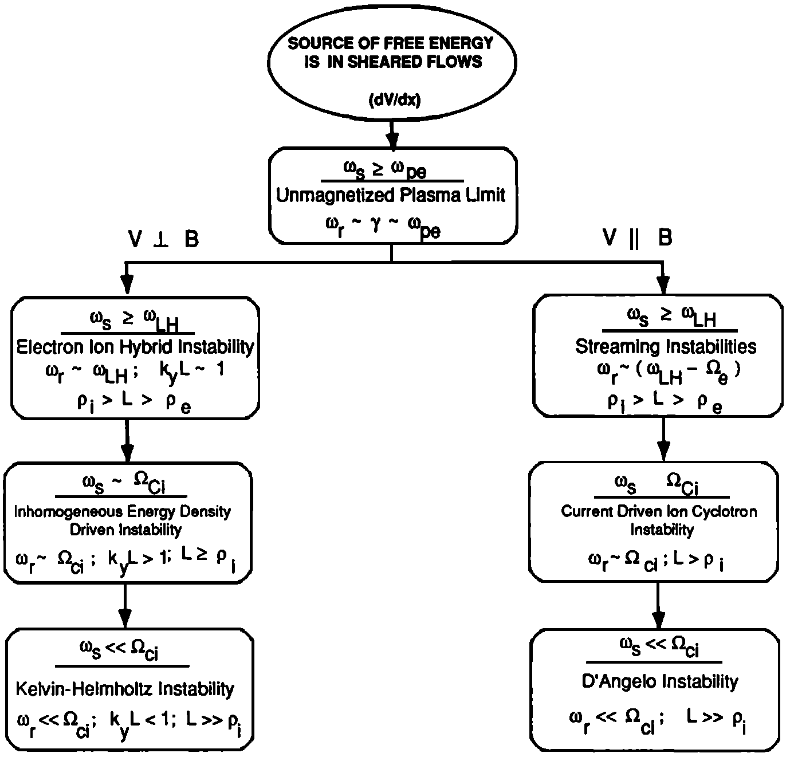

Figure 2.4.10.: A hierarchy of some of the microinstabilities that can be triggered by velocity shear. [from *Ganguli et al.* (1994)]

- heat conduction from above, which cannot be an explanation because the vertical temperature gradients are too small to account for the observed temperatures
- friction between electrons and ions in presence of acceleration by a field aligned electric field, which can be a possible explanation, but needed further analysis

They used a steady-state quasi-neutral two-fluid model based on ion and electron momentum and electron energy balance equations, obtaining the surprising result that ions should go down above 750 km, which means that this model is not good enough to account for ion acceleration in the topside ionosphere. The possible explanations analyzed by *Kagan and St.-Maurice* (2005) are:

- the existence of a third species in the system (i.e. precipitating and super-thermal electrons)
- high frequency turbulence, able to scatter electrons without affecting the ions

In order to solve this problem they introduced the electron energy balance equation, which allowed them to derive the field aligned electric field (provided the field aligned velocity is known and the gravity effects on electrons are neglected).

The numerical results state that only the turbulent scattering can be a good explanation. Using their words: “We reach the surprising conclusion that, in the end, rather large, km/s, ion outflows can be achieved with just a little bit of quasi-stationary turbulence to slow down the electrons, and with a rather modest field-aligned electric field (in comparison with the regular ambipolar field) to accelerate the charged particles”.

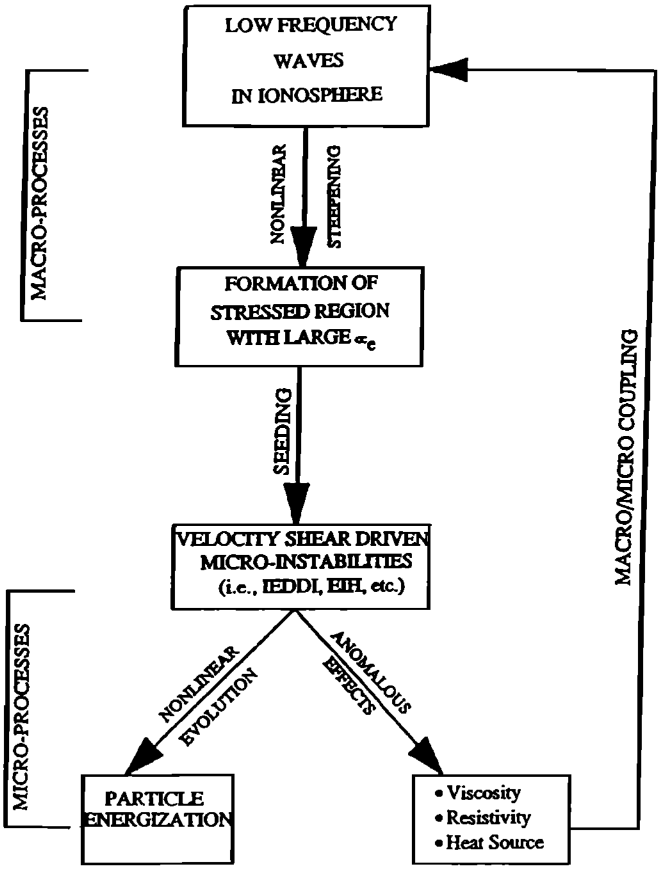

Figure 2.4.11.: A schematic view of the ion energization process. [from *Ganguli et al.* (1994)]

Regarding the possible origin of the field aligned electric field, *Kagan and St.-Maurice* (2005) recall that thermal ion upflow of type-II are often accompanied by an auroral arc moving southward, as observed for example by *Wahlund et al.* (1992b). This motion is caused by an $\mathbf{E} \times \mathbf{B}$ drift, as shown in Fig.2.4.12. However, since there is an upward current sheet, there should be a magnetic perturbation perpendicular to the current vector, due to the Ampère's law $\nabla \times \mathbf{B} = \mu_0 \mathbf{J}$. This perturbation tilts the Earth magnetic field towards east, which implies that the perpendicular westward electric field is tilted downward. But since the total electric field must point in the west direction, it is necessary to have an electric field pointing upward, which is exactly the field aligned electric field we are searching, responsible for the acceleration of the particles: the ions will go upward and the electrons downward, while the presence of turbulence will slow the electrons, which in turn will enhance ions motion. Electrons are then heated, partly due to friction and mostly due to heat advection. This process produces the enhanced electron temperature observed in type-II ion outflows.

It is important to notice that the outflow described by *Kagan and St.-Maurice* (2005) was of the type without enhanced ion acoustic lines. They speculate about the connection between NEIALs and high frequency turbulence, citing the work of *Forme* (1993) about the decay of Langmuir turbulence as the origin of NEIALs. In addition, since it is possible that higher field aligned electric field are triggered along the arcs, a stronger counter-streaming of electrons can occur, thus generating topside current instabilities, as described by *Kindel and Kennel* (1971). These current instabilities could eventually cause the destabilization of the ion acoustic lines leading to the observed NEIALs during type-II ion outflows.

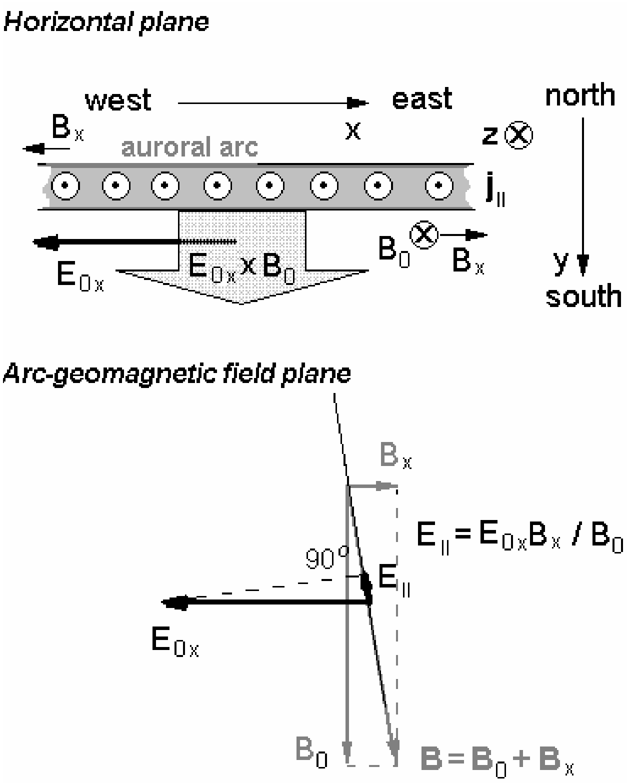

Figure 2.4.12.: Formation of the field aligned electric field. $\mathbf{j}_{||}$ is the upward parallel current; $\mathbf{B_0}$ is the Earth magnetic field; $\mathbf{B_x}$ the perturbation magnetic field; $\mathbf{E_{0x}}$ is the component of the electric field driving the arc to the south; $\mathbf{E}_{||}$ is the field aligned electric field. Note that proportions of $\mathbf{B_x}$ and hence $\mathbf{E}_{||}$ are exaggerated.

3. Naturally enhanced ion acoustic lines

3.1. Overview

Enhancements in the ion acoustic shoulders of the incoherent scatter spectrum were initially predicted by *Rosenbluth and Rostoker* (1962). But, for nearly thirty years, the enhancements of the ion acoustic lines observed by several radar facilities were dismissed as an effect due to satellites passing in front of the radar beam. Eventually it was shown by *Foster et al.* (1988) that some of these enhancements have a physical origin.

Afterwards, many authors reported observation of the so-called *naturally enhanced ion acoustic lines* (NEIALs). We will put emphasis on the observations conducted in the polar region, since we have used exclusively EISCAT data in this work.

Fig. 3.1.1 shows the differences between the ion part of a standard incoherent scatter spectrum (a) and the same spectrum during a NEIAL event (b). It is useful to briefly describe this figure, since we will extensively use it when discussing our results. The most important elements for our analysis are the upper left panel, which shows the power received by the instrument as a function of time, and the bottom left panel, which shows the ion part of the incoherent scatter spectrum intensity profile at each altitude.

We call *downshifted* line the one on the negative part of the spectrum (i.e. on the left) and *upshifted* line the one on the positive part (i.e. on the right). The terms “down” and “up” are referred to the fact that the frequency receive is respectively lower or higher than the frequency transmitted, due to the Doppler effect. In other branches of physics downshifted and upshifted are called respectively *redshifted* and *blueshifted*. Usually at least one of the ion lines is enhanced, and it is common to observe a changing behavior with respect to altitude, e.g. an enhanced downshifted line at low altitudes and an enhanced upshifted line at higher altitudes (see, for instance, *Lunde et al.*, 2007).

Several theories have been proposed as a possible explanation of this phenomenon. However, at present none of them is able to fully explain the quite complex generation mechanisms of the NEIALs. Currently the most accredited theories in the literature are:

1. current-driven instabilities, involved intense field-aligned current densities, first proposed by *Collis et al.* (1991) and *Rietveld et al.* (1991) and based on the studies of *Kindel and Kennel* (1971);
2. ion-ion two stream instabilities, first proposed by *Wahlund et al.* (1992a);
3. parametric decay of Langmuir waves, proposed initially by *Forme* (1993), and then updated by *Forme* (1999).

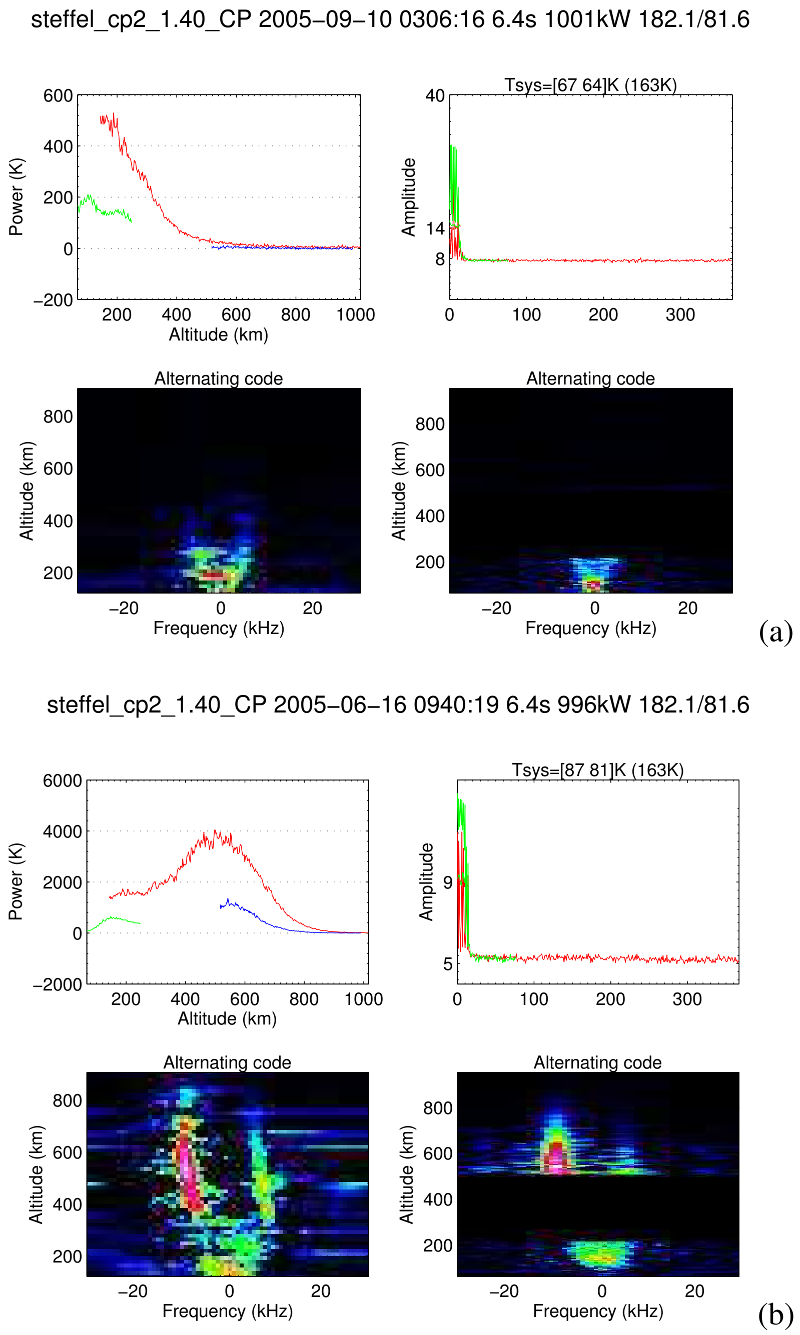

Figure 3.1.1.: (a) Standard incoherent scatter spectra on a quiet day; (b) Incoherent scatter spectra during a NEIAL event. Note the “bump” in the spectral power, corresponding to the altitude where enhanced acoustic echoes are occurring.

NEIALs are usually related to ion outflow events. Many authors believe that the two phenomena are closely working together, but so far there is no definitive conclusion on the inner mechanisms of both of these processes and hence how they can actually be linked to each other. In this work we tried to give new information about their relation.

On a side note, it is interesting to keep in mind that ion-acoustic enhancements can be observed also when the radar beam is perpendicular to the geomagnetic field in the E region (see e.g. *Foster and Erickson*, 2000). In this case the generation mechanism is thought to be the Farley-Buneman instability (*Farley*, 1963; *Buneman*, 1963), which can grow when the $\mathbf{E} \times \mathbf{B}$ drift exceeds approximately 400 m s^{-1} (*Sedgemore-Schulthess and St.-Maurice*, 2001). In this work we treated exclusively field-aligned ion-acoustic enhancement, which, as we mentioned, have not yet a satisfying theory to explain their generation.

3.2. Observations

Collis et al. (1991) used data (10 seconds dumps) from the EISCAT UHF and VHF radars in Tromsø and a meridian-scanning photometer in Kilpisjärvi, 90 km at south-est of EISCAT, together with all-sky TV images. They observed enhancements in ion acoustic lines associated with the 630 nm red aurora, specifically they observed NEIALs just before and just after a red arc crossed the field-line where the radar beam was pointing (see Fig. 3.2.1). This implies down-streaming electrons equatorward of the maximum luminosity and upward streaming electrons on the poleward side.

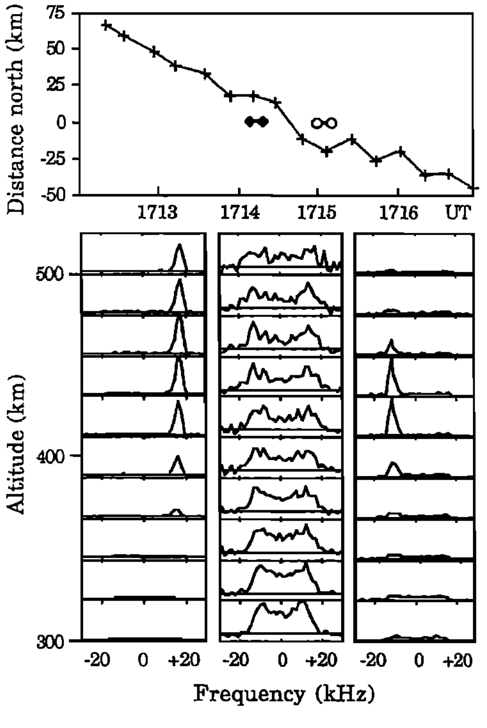

Figure 3.2.1.: (Upper panel) Location of maximum 630 nm intensity from the scanning photometer with respect to NEIALs (black dot is upshifted, white dot is downshifted); (Lower panels) Radar spectra: upshifted line (left), downshifted line (right), normal spectra (center). [from *Collis et al.* (1991)]

The incoherent scatter theory predicts that an asymmetry should develop if there is a relative drift between the electrons and the ions (see *Rosenbluth and Rostoker*, 1962). *Collis et al.* (1991) tried to estimate the field-aligned current (FAC) by fitting for the electron drift speed. They found very large FAC densities (several $mA\,m^{-2}$ while they are usually measured in $\mu A\,m^{-2}$) and an electron drift speed less than $0.3v_{th}$ (where v_{th} is the electron thermal velocity). According to *Kindel and Kennel* (1971), the value of $0.3v_{th}$ is approximately the threshold speed for the growth of the ion-acoustic instability when the temperature ratio T_e/T_i is approximately 3. *Collis et al.* (1991) argued that an instability can develop for higher drift speeds but in such a case, where one should also observe higher spectral asymmetries, their technique cannot be applied. They also cannot obtain fits if both ion-acoustic shoulders are enhanced. This can be due to the presence of FACs flowing in opposite direction, occurring either simultaneously or at different times, since NEIALs can be very short living and the integration time was fairly long 10 s.

In addition, they also note that more extreme conditions were required to see effects in the UHF (933 MHz) measurements with respect to the VHF (224 MHz); this feature was studied in detail by other authors (*Cabrit et al.* 1996).

Rietveld et al. (1991) used the EISCAT radar with the antenna pointing along the magnetic field to obtain information on NEIALs in the 138-587 km altitude range. They observed back-scatter power enhanced more than one order of magnitude with the ion-acoustic enhancements appearing typically in two height regions:

- the boundary between E and F region, with a mean height of 168 km and the upshifted line usually enhanced but without a simultaneous enhancement of both upshifted and downshifted lines;
- the topside ionosphere, with a mean height of 450 km and often an occurring switching in the enhancement from the upshifted to the downshifted line. Sometimes both shoulders were enhanced in the same 10-seconds data dump, implying that these kind of spectra cannot be of an artificial (i.e. satellites) source.

They found that these enhancements are usually associated with disturbed magnetic conditions, auroral electron precipitation and red aurora in the F region. The electron temperatures were usually high (which can imply a type-II ion outflow occurring) with a temperature ratio T_e/T_i approximately between 2 and 3, similar to what *Collis et al.* (1991) found. The horizontal electric field was not very large, but could exhibit spatial and/or temporal variations during the echoes. They found that the ion outflows associated with the NEIALs started at an average altitude of 350 km. The duration of the NEIALs burst was estimated varying from less than a second to several tens of seconds.

Regarding the source of NEIALs, they also argue, as *Collis et al.* (1991) did, that huge thermal electron fluxes of more than $1\,\mathrm{mA\,m^{-2}}$ are required to trigger the enhancements. They suggest that parallel electric fields are created in the ionosphere by field-aligned flows of soft electrons which deposit their energy in the horizontally poor conducting F region and that these fields produce the thermal flows responsible for the onset of the instability.

Wahlund et al. (1992b) (see also chapter 2) registered the presence of spurious enhanced ion acoustic shoulders in their data during a type-II ion outflow. They discussed the possible effects of plasma turbulence, namely that the turbulence may produce anomalous resistivity which in turn could produce enhanced field-aligned electric fields, provided that field-aligned currents exist. Such an enhanced field-aligned electric field may then accelerate ions and contribute to the observed ion outflows.

The first categorization of NEIALs was made by *Forme et al.* (1995). Using both UHF and VHF EISCAT data, they found that the observations can be separated in two types depending on the physical conditions (see Fig. 3.2.2):

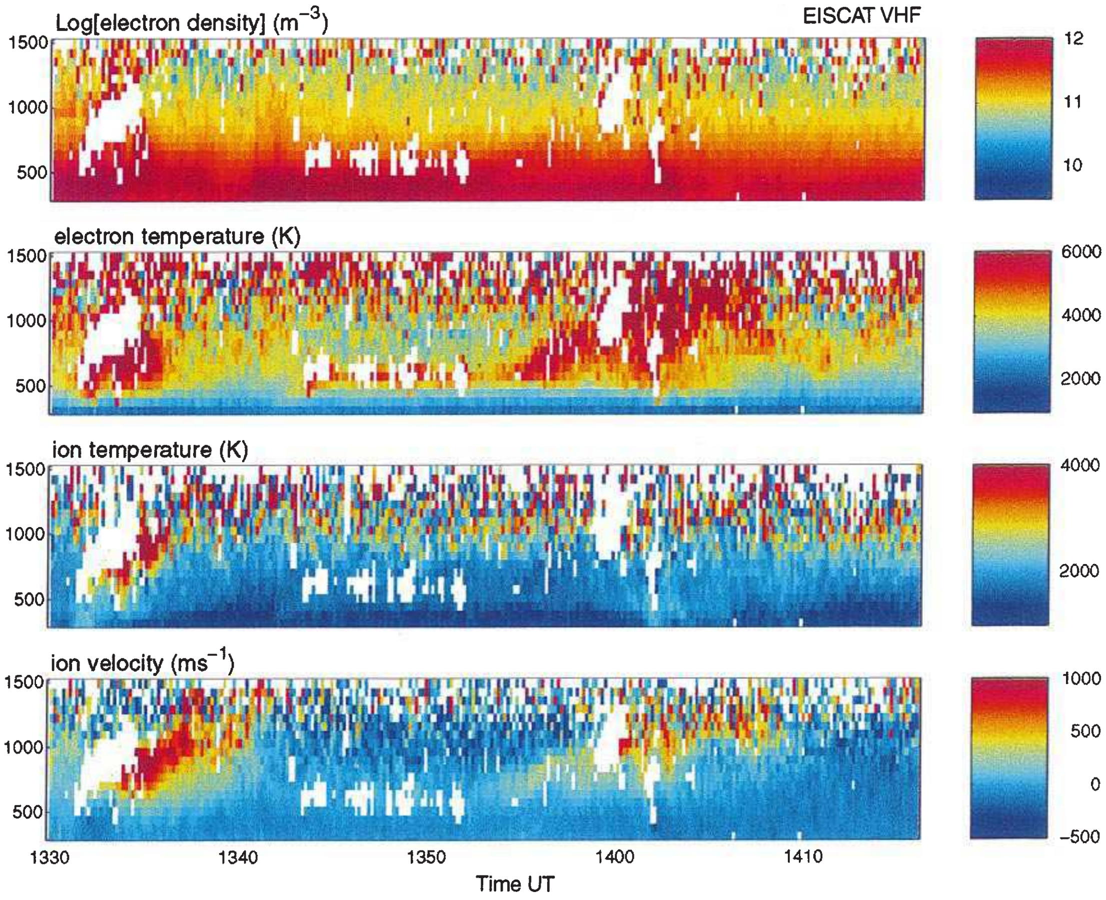

Figure 3.2.2.: EISCAT color plot showing the two different type of NEIALs observed by *Forme et al.* (1995). The events occurring around 1330 UT and 1400 UT are type-A enhancement; the events occurring between 1340 UT and 1350 UT are not associated to any ion upflow and are thought to be type-B NEIALs. [from *Forme et al.* (1995)]

- Type-A: related to strongly enhanced electron temperatures (6000-8000 K), ion outflows with large vertical velocities, an altitude extent of 300-700 km and auroral arcs and precipitating particles of 100 eV to 10 keV; the spectra are strongly asymmetric and usually the downshifted line is enhanced. These characteristics lead us to think that the outflows involved in their occurrence are the type-II.
- Type-B: corresponds to slightly enhanced electron temperatures, no ion outflow, spatial extents of 100-200 km and an apparent lack of soft particle precipitation (i.e. with average energies less than 1 keV). The electron heating is more localized and less pronounced then type-A. In this case the spectra are less asymmetric with the upshifted line mostly enhanced.

Unfortunately in our study we did not find any NEIAL belonging to the type-B category, and since it also seems that they are not abundant in the literature, they are perhaps a rare event.

Like *Collis et al.* (1991), they found that NEIALs are more likely observable with the VHF than UHF radar, probably due to a wavelength dependency effect. In addition they found in some data an enhanced central peak; however, they are unsure about its geophysical origin, since such spikes can be produced by a residual DC offset in the receiving system. One of the interesting conclusions of their work is that both the heat source and the ion acceleration regions were localized within the turbulent regions, which imply that a great effort is needed to obtain reliable data due to the non-maxwellian nature of the NEIALs spectra.

An interferometric technique was employed by *Grydeland et al.* (2003) and *Grydeland et al.* (2004) in order to greatly increase the data resolution. Indeed, they managed to get a 0.2 seconds resolution, whereas with the usual incoherent scatter observations one can achieve 10 or 6 seconds resolution for each dump. They were hence able to get very interesting information about NEIALs and their fine structure, namely:

- simultaneously radar and optical observations show that NEIALs occurrence is associated with finely structured aurora.
- presence of filamentary structures of the order of 100 km long, aligned with the Earth's magnetic field, with scale size in the perpendicular direction of the order of few hundred meters. This is within an order of magnitude of the smaller scale sizes observed in optical aurora.
- when the enhancements in ion-acoustic lines occur simultaneously on the same data dump, the two peaks are due to scattering from the same volume so that spatial averaging can not be the cause of simultaneous upshifted and downshifted lines.
- the simultaneous upshifted and downshifted enhancements are not caused by temporal averaging. This is evident in Fig. 3.2.3 where the almost continuous behavior of each curve implies that the time resolution is sufficient for resolving the scattering structure.

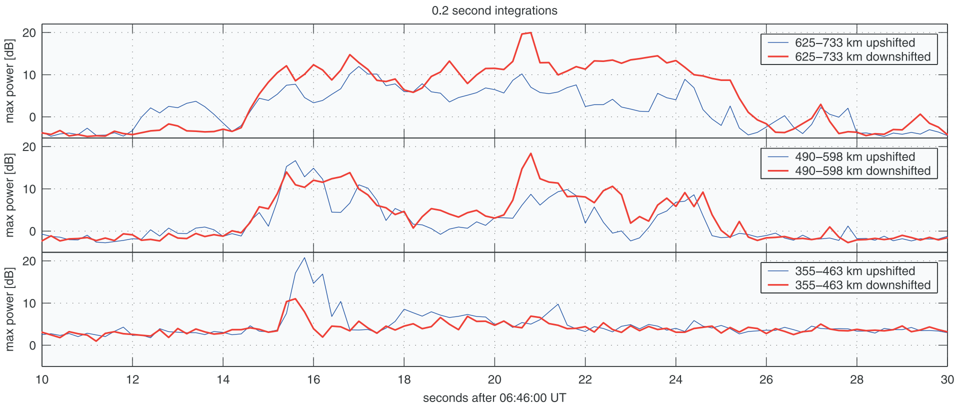

Figure 3.2.3.: Received power as a function of time for three different altitude ranges. The smooth profile means that the resolution in time is good enough. Note how the upshifted line is enhanced at lower altitudes, whereas the downshifted line is enhanced at higher altitudes. [from *Grydeland et al.* (2003)]

The last two points have a great importance in assessing the validity of the NEIALs generation theories and we will make use of such conclusions later on.

Michell et al. (2009) and *Michell and Samara* (2010) managed to get an integration time as short as 12 ms, using the Poker Flat Incoherent Scatter Radar (PFISR) located in Alaska.

Their results are in good agreement with *Grydeland et al.* (2003): they found simultaneously enhanced ion acoustic lines at short time scales and confirmed that NEIALs are a prompt event associated with fine scale auroral structure and occurring on the boundary of auroral luminous features. However, they also reported that for most of the cases the ion acoustic lines were not simultaneously enhanced; on the contrary, in our work, we observed many simultaneous enhancements in our data set, which are likely due to the time averaging of ~6 s in our data dumps.

Several statistical studies have been conducted on NEIALs data. *Rietveld et al.* (1996) analyzed the observations made in the period 1987-1993 with the UHF radar in Tromsø (CP-1 experiment, mostly 10 seconds dumps). They found a correlation between the annual occurrence of enhanced ion acoustic echoes and sunspot numbers (Fig.3.2.4). This was somewhat expected since auroral activity, which is associated with enhanced acoustic echoes, is known to be correlated with the solar activity. They also found a lack of NEIALs in the morning hours and a maximum occurrence between 12-24 UT time period. This probably reflects the times when the auroral oval is above Tromsø, which is most likely in the evening. Regarding the seasonal dependence, *Rietveld et al.* (1996) found no significant variation over the year in their data. It should be noted, however, that *Ogawa et al.* (2011) found an evident seasonal dependence in their data, both in ion outflow and NEIALs occurrence frequencies. We will talk about this later on.

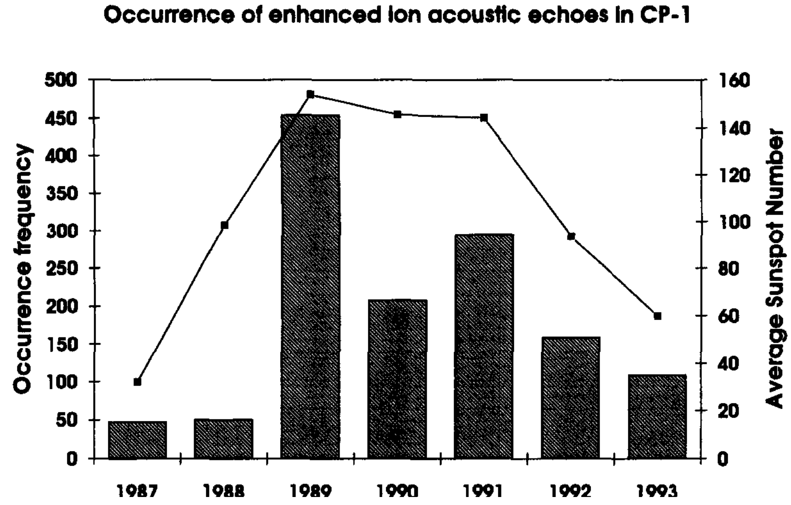

Figure 3.2.4.: Histogram showing the occurrence of NEIALs in the UHF data (bars) together with the average sunspot number (points). It is evident a certain amount of correlation between the two physical phenomena. [from *Rietveld et al.* (1996)]

As other studies pointed out, most of the NEIAL events lasts less than 10 seconds, hence shorter integration time are needed to better characterize them. The interferometric technique employed by *Grydeland et al.* (2003) can overcome this difficulty. *Rietveld et al.* (1996) found also a predominance of the downshifted lines above 300 km, together with cases where both shoulders were enhanced, whereas no recorded cases of such double enhancement were found below 300 km. Below 250 km the upshifted shoulder is more often enhanced, as already found by *Rietveld et al.* (1991) and others. However, differently from *Rietveld et al.* (1991), they found that low altitude NEIALs are much rarer than previously suggested.

The subject of the cross section's wavelength dependence during NEIAL events was studied in detail by *Cabrit et al.* (1996) using both VHF and UHF EISCAT radars. They found a difference of more than 2 orders of magnitude in the back-scattering cross section at 224 MHz (VHF) and 933 MHz (UHF). This discrepancy cannot be explained by normal thermal ionospheric density fluctuation, hence they argue that the observed difference is due to anomalous echoes caused by low-energy particle precipitation. They analyzed two possible explanations: (1) spatial localization and (2) k vector dependence.

They excluded the possibility of k vector dependence due to finite Debye length, since it is very small and cannot account for the observed back scattering cross sections. They also excluded satellites passing by a side-lobe of the antenna because the echoes comes from many gates whereas only a few gates are usually affected by satellites.

They argue that a scattering by a local density enhancement is, from a geophysical point of view, very unlikely to occur. Scattering from an anomalous echo could be a realistic explanation, since many physical conditions characterizing NEIALs are the same as in the observations made by *Cabrit et al.* (1996): discrete arc produced by low-energy electrons, high altitude electron temperature increase and a strong perpendicular electric field at one edge of the arc. However it is unlikely that during a time interval of 50 s the occurrence of enhanced back-scatter in the VHF beam can always be explained by the unfortunate spatial geometry of an extremely sharp localization of anomalous echoes.

That is why they focused on the k dependence in instability models and in the Langmuir parametric model which, as we shall see, is a strong candidate for the NEIALs generation mechanisms.

One of the most comprehensive statistical studies on NEIALs and outflows have been done by *Ogawa et al.* (2011). They analyzed about 78000 field-aligned profiles obtained from EISCAT Svalbard radar (ESR) between March 2007 and February 2008. They found nearly 1500 NEIALs in the ESR data at altitudes between 100 and 500 km. It is interesting to look at the NEIALs and outflows distribution (Fig. 3.2.5), where we can see that the annual occurrence frequencies of NEIALs and outflows are anticorrelated, despite it is believed that NEIALs happen mostly when we have an outflow event.

NEIALs occurrence is however correlated with ion flux, which is higher in summer than in winter due to the higher electron density during summer months. The observed NEIAL occurrence frequencies could also mean that NEIALs can occur when there is no significant ion upflow. However, as Fig. 3.2.6 shows, NEIALs at high altitudes are usually shifted in frequency like being embedded in the outflows, so it is unlikely that a large fraction of summer F region NEIALs occur without outflow. One possible explanation provided by *Ogawa et al.* (2011) is that ion-acoustic lines are enhanced at wavelengths near the ESR wavelength for relatively high electron densities but rather away from the ESR wavelength for low densities.

On the subject of relation between NEIALs and upflows it is useful to look at the work of *Forme and Fontaine* (1999) where they tried to evaluate electron temperature and ion velocity inside the turbulence, which is usually not feasible due to the non-maxwellian nature of the velocity distribution during NEIALs events.

The method they used to estimate the electron temperature is based on the fact that the ion acoustic frequency and the Doppler shift are not modified by the enhanced ion acoustic

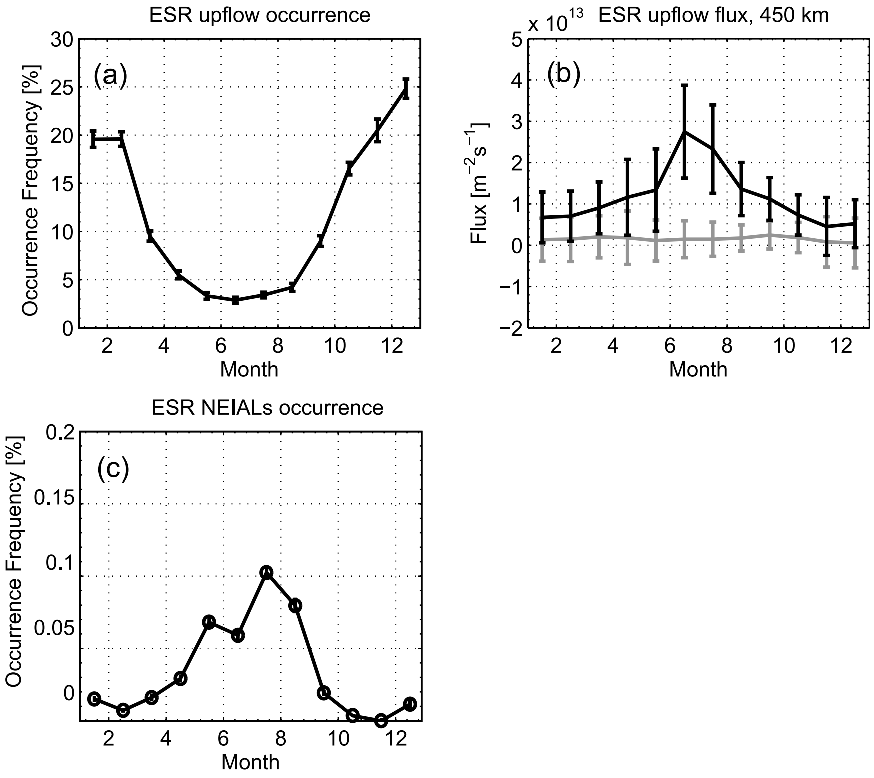

Figure 3.2.5.: Monthly variation of: (a) occurrence frequency of ion outflows; (b) upward ion flux at 450 km altitude where the gray line indicated the average flux of all data (upflow, downflow and no flow events); (c) occurrence frequency of NEIALs in the F region. Note that only data taken between 0700 and 1700 MLT were used for (a) and (b). [from *Ogawa et al.* (2011)]

fluctuation. They found the electron temperature to be as high as 11 000 K and the field aligned velocity equal to 1300 m s^{-1} at an altitude of 800 km. Having these values allowed them to use the vertical ion momentum equation to get information on the ion outflow. The results show that a large electron temperature gradient (of the order of 0.02 K m^{-1}) can increase the ambipolar electric field, leading to large ion upflow.

3.3. Generation theories

As we mentioned, there are currently three candidate theories to explain the generation mechanisms of the NEIALs. If one takes in consideration the results of *Grydeland et al.* (2003), *Michell et al.* (2009) and *Michell and Samara* (2010), could then be tempted to think that the parametric decay of Langmuir waves can be the one that better suits observations. In fact, these authors showed that on very short timescales (as low as 12 ms in *Michell and Samara*, 2010) both ion acoustic lines can be enhanced simultaneously. However, the current driven instability is not compatible with this observation unless the currents change direction on very short time scales, while the ion-ion two stream instability needs very large ion drifts to explain the simultaneous enhancements. Nevertheless, as we shall see, many issues are still present, particularly at lower altitudes, where the soft particle precipitation (less than 500 eV) cannot have a primary role as required by the

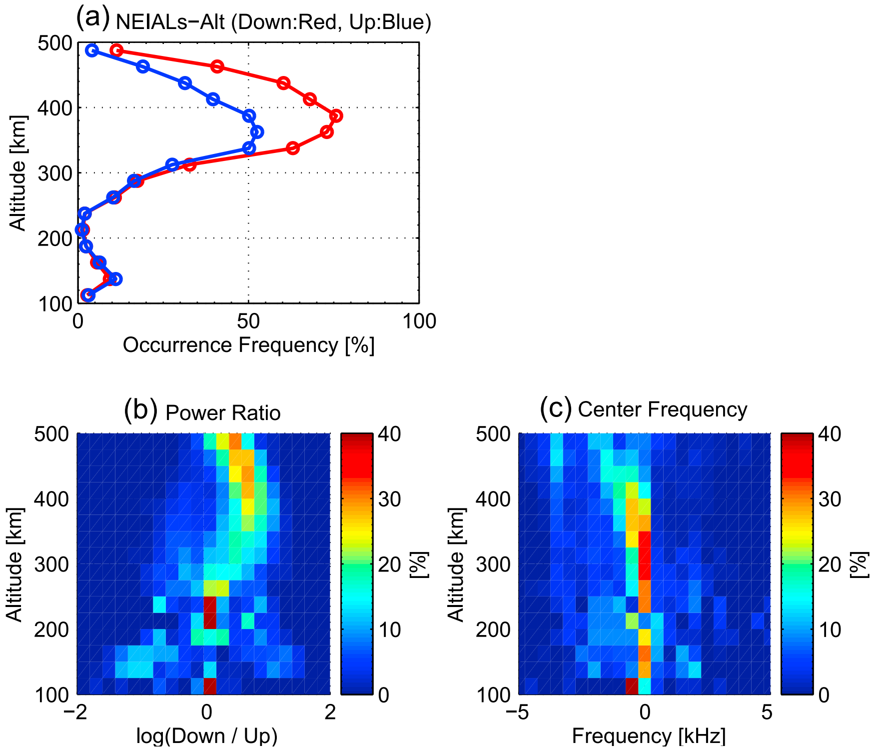

Figure 3.2.6.: (a) occurrence frequency of NEIALs at several altitudes. Note how the downshifted line (red) is mostly enhanced at high altitudes with respect to the upshifted line (blue); (b) Power ratio of the downshifted line to the upshifted line showing how at high altitudes the downshifted line has usually a larger power then the upshifted line; (c) Center frequency between the downshifted and upshifted peak at various altitudes. The shifting towards negative frequency with increasing altitude means probably that most of the NEIALs are embedded in the outflow events. [from *Ogawa et al.* (2011)]

Langmuir decay theory, since most particles in this energy range are simply too weak to reach the lower regions of the atmosphere.

In the following we will try to shed some light on these three possible explanations, namely intense field-aligned current densities, ion-ion two stream instability and parametric decay of Langmuir waves.

3.3.1. Current driven instability

Rietveld et al. (1991) discussed the possible mechanisms underlying the observation of intense ion-acoustic enhancements observed with the EISCAT radar. They argue that, in order to develop an asymmetry in the ion-acoustic lines, it is required that electrons drift at a speed which is a detectable fraction of their own thermal speed. When an asymmetry is present in the spectra, it is possible that the plasma reaches conditions for the destabilization of ion-acoustic waves, which they believe is due to a two-stream instability between ions and electrons. Fig.3.3.1 shows that the spectrum associated with currents from energetic beam electrons is the same as would be obtained without any parallel current, which means that the ion acoustic peak is produced not by large fluxes of a small number of energetic electrons, but by a displacement in the thermal electron distribution function. As stated by *Kindel and Kennel* (1971), it is easier to reach an instability for the ion acoustic line when the temperature ratio T_e/T_i is higher, and it is customary to consider a temperature ratio of ~3 as a threshold to set the instability.

The weak point of this theory is the fact that the field aligned currents implied are huge, i.e. ~1 mA m^2, which was one order of magnitude higher than the largest currents measured at the time. However, more recently, *Neubert and Christiansen* (2003), employing the Ørsted satellite, observed high density small scale field aligned currents, which reached 1 mA m^2 during very disturbed conditions throughout the auroral oval and especially in the cusp and in the pre-noon cusp.

Rietveld et al. (1991) described what possible physical mechanisms can lead to such instability. The general idea is based on charge conservation arguments. Parallel currents carried by soft particles of about 500 eV will collide with neutrals and be stopped around 200 km altitude. But the total current divergence has to be zero. Therefore, if the Pedersen conductivity, which is perpendicular to the magnetic field, is too small at the altitude where the soft electrons are stopped, current continuity will force the thermal electrons to carry the field aligned current that was originally carried by the beam electrons. In this scenario, parallel electric fields will be only generated in the regions where the beam electrons become collisional and the current dissipates.

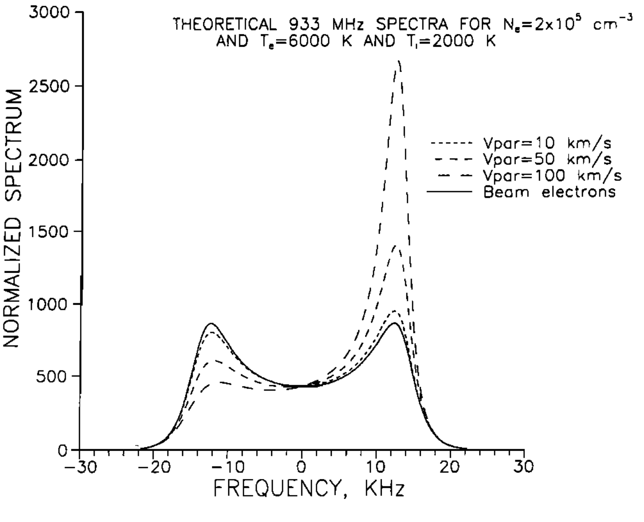

Figure 3.3.1.: Theoretical incoherent scatter spectra with the upshifted ion acoustic line enhanced. The solid curve represents the spectra obtained when the same current as was carried by thermal electrons moving at 100 km/s is carried by 1% of the electrons (in the KeV energy range). Note how this spectra is basically the same as would be obtained without any parallel current. [from *Rietveld et al.* (1991)]

As shown in Fig. 3.3.2 electrons are mostly moving downward at lower altitudes whereas they tend to move upward at higher altitudes. Since in their data there is no indication of ion flow with a magnitude comparable to the electron thermal speed, *Rietveld et al.* (1991) conclude that there must be an electric field reversal together with the current bursts (the ions are in fact not moving together with the electrons).

They argue that if we assume that an electric field due to negative charges accumulation is present in the region of current divergence and this field is actually responsible for the acceleration of thermal electrons, than we have to conclude that there has to be an ambient electric field implicitly assumed to be present according to this model. This ambient field

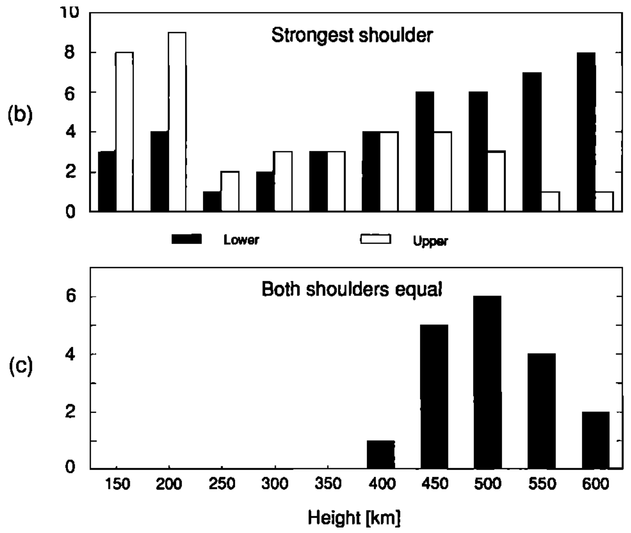

Figure 3.3.2.: (Top panel) Distribution of enhanced spectra according to whether the upper (upshifted) shoulder (representing downgoing electrons) or the lower (downshifted) shoulder (representing upgoing electrons) is enhanced; (Bottom panel) Distribution of spectra where both shoulders are equally enhanced. [from *Rietveld et al.* (1991)]

is responsible for canceling the field produced above the charged layer by the divergence in the beam electron current. This is illustrated in Fig. 3.3.3. Basically there is an ambient electric field ($E_{\|}^{AMBIENT}$ in the figure) between the magnetosphere and ionosphere and when the beam electrons are stopped at F region heights, they produce an electric field that tends to cancel the ambient field above the deposition layer and to amplify it below this altitude. However, since a perfect balance is very unlikely, together with the beam electrons there would be a parallel field, even at the altitudes where the beam travels with no interaction with the surroundings.

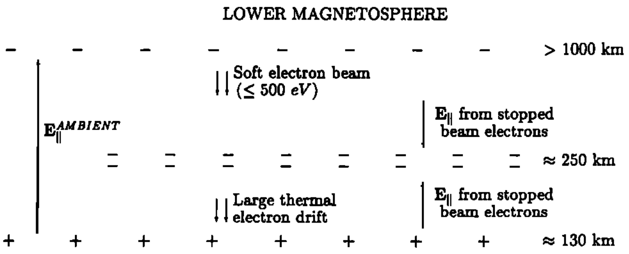

Figure 3.3.3.: Diagram illustrating the various electric fields interacting with the beam electrons when low horizontal conductivities are present. [from *Rietveld et al.* (1991)]

Rietveld et al. (1991) notes that one very important consequence of having thermal electrons carrying the excess currents is that they can generate plasma instabilities, whereas beam electrons carrying similar currents can only generate weak large scale waves, such as Bernstein waves (see *Laqua* (2007) for an in-depth review). This is due to the fact that currents carried by thermal electrons are much more unstable than currents carried by beam electrons. This can have many consequences, e.g. instabilities generated by thermal electrons are not produced exactly perpendicular to the magnetic field; once short-scale wave parallel electric fields are produced, they are the cause for the scattering of electrons trying to move along the magnetic field in response to the large scale electric fields. One direct effect of this is that the parallel conductivity $\sigma_{\|}$ has to decrease, while the perpendicular conductivity increases slightly. However, since the product $J_{\|} = \sigma_{\|} E_{\|}$ has to stay constant, the parallel electric field must increase when the conductivity goes down. This can greatly affect the ion motion. This is clear if we consider that the equation of motion implies that $q_j E_{\|}/m_j \cong \nu_j v_{\|_j}$. Since the collision frequency is almost equal for ions and electrons, the most important factor affecting the velocity $v_{\|_j}$ is the mass m_j, and we know that the ratio m_i/m_e is about 10^4 for a population formed mostly by oxygen ions. So, if the ions are moving with a velocity of $100\,\mathrm{m\,s^{-1}}$, this would normally imply electron drifts of the order of $100\text{-}1000\,\mathrm{km\,s^{-1}}$, enough to destabilize the ion acoustic waves and produce effects on the incoherent spectra. However, if we assume that anomalous conductivities are produced by the very fact that substantial thermal electron currents are present, then the same velocity of $100\,\mathrm{m\,s^{-1}}$ would correspond to an electron drift of $1\text{-}10\,\mathrm{km\,s^{-1}}$ and the effect on ion acoustic spectra would be almost impossible to observe. *Rietveld et al.* (1991) argue that what we see could be only the “tip of the iceberg”, meaning that there are probably many situations where smaller but important thermal field-aligned electron drifts exist without being detected by incoherent scatter radars.

Forme et al. (1993) developed a model to calculate electron and ion temperatures when current driven instabilities occur. They discussed three types of instabilities (see Fig. 3.3.4): the Buneman instability, which arises when $v_{d,e} > 1.8 v_{th,e}$; the ion acoustic instability, for which an approximate threshold condition on the drift velocity is $v_{d,e} > T_i T_e^{-1} v_{th,e}$; the ion cyclotron instability, which has the least stringent threshold, where $v_{d,e} > 15 T_i T_e^{-1} v_{th,i}$ ($v_{d,e}$ is the electron drift velocity, $v_{th,e}$ and $v_{th,i}$ are respectively the thermal electron and ion velocity).

Among their results:

- the three instabilities lead to strongly enhanced electron temperatures, with electron heating rates bigger for the Buneman and ion acoustic instabilities then ion cyclotron instability;
- the ion heating rates are of the same order for the ion acoustic and ion cyclotron instabilities, while the ion heating rate in the Buneman instability is not affected by the turbulence;
- the different heating rates affects temporal evolution of temperatures: after 2 s $T_e/T_i \approx 20$ for the Buneman instability, $T_e/T_i \approx 4$ for the ion acoustic instability and $T_e/T_i \approx 1$ for the ion cyclotron instability.

Fig. 3.3.5 shows the temperature profiles for the ion acoustic instability, between 300 km and 3000 km altitude. They argue that it seems difficult to explain the observations by e.g. *Wahlund et al.* (1992b), *Collis et al.* (1991) and *Rietveld et al.* (1991), since they present high temperatures at relatively low altitudes of 140-1500 km. Assuming a current density of $1000\,\mu\mathrm{A\,m^{-2}}$, as proposed by *Collis et al.* (1991) and *Rietveld et al.* (1991), could have indeed triggered the ion acoustic instability at 800 km altitude, but also lead to unrealistically high electron temperatures.

The temperatures estimated by *Forme et al.* (1993) are indeed very high, however, we must remember that the incoherent scattering technique becomes unreliable during NEIALs events and that, as *Forme and Fontaine* (1999) have shown, the temperature inside the

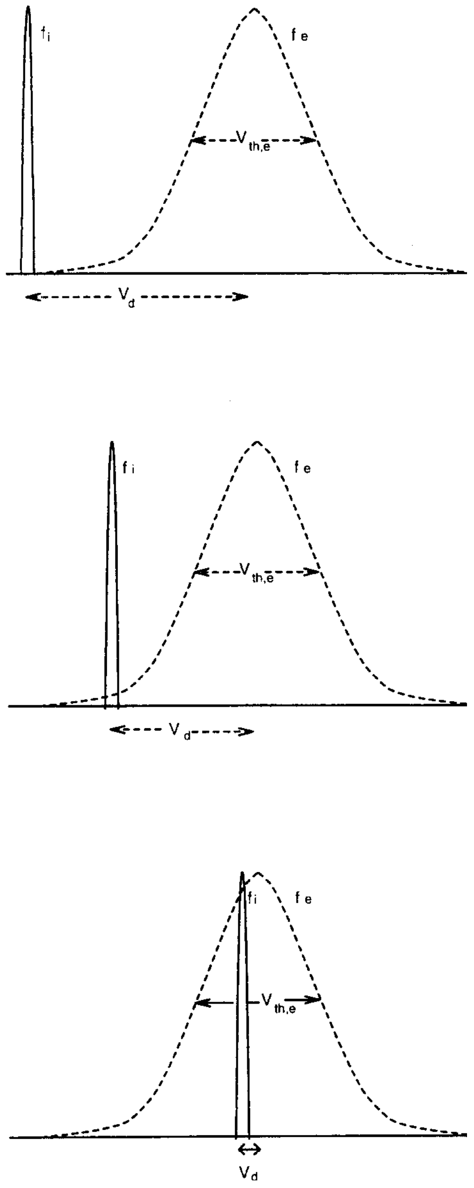

Figure 3.3.4.: Ion and electron distribution function for (a) Buneman instability; (b) ion acoustic instability; (c) ion cyclotron instability. f_e (dashed line) is the electron distribution function, f_i (solid line) is the ion distribution function, $v_{th,e}$ is the electron thermal velocity and v_d is the drift velocity. [from *Forme et al.* (1993)]

turbulent regions can become very high, even though the techniques to extrapolate parameters inside the turbulence are not very accurate.

3.3.2. Ion-ion two stream instability

The ion-ion two stream instability theory was first proposed by *Wahlund et al.* (1992a). They argue that this kind of instability is the source of enhanced ion acoustic spectra, since the enhanced ion acoustic lines are often observed together with ion outflows, auroral arcs, topside electron temperature enhancements (as high as 8000 K), soft particle

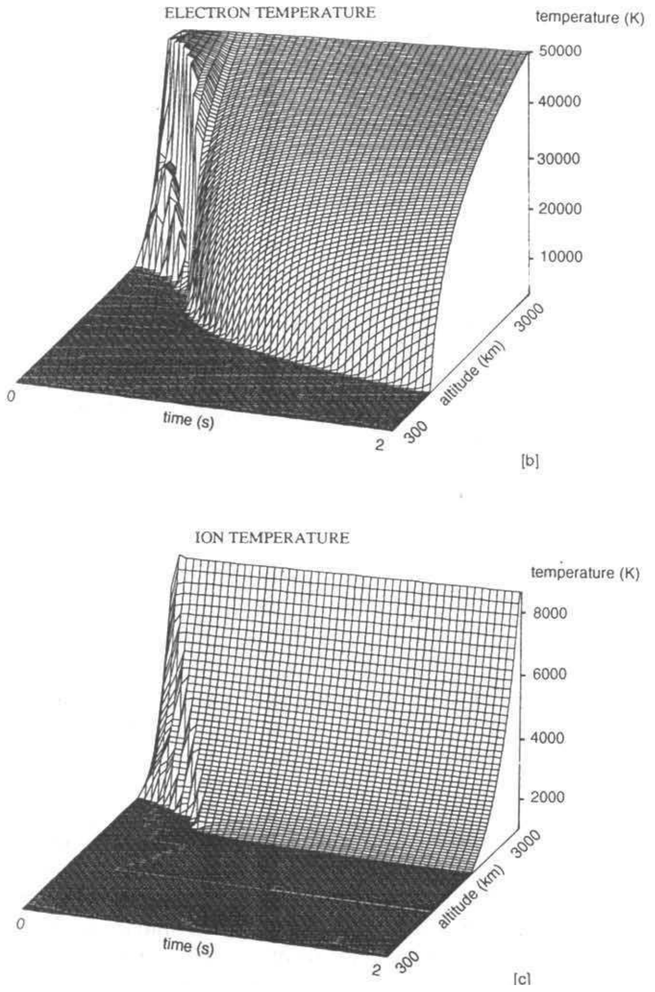

Figure 3.3.5.: Electron temperature (b) and ion temperature (c) profiles for the ion acoustic instability, with a current density of $30\,\mu\mathrm{A\,m}^{-2}$ between 300 and 3000 km altitude and within 2 s from the onset of instability. [from *Forme et al.* (1993)]

precipitation ($\sim 500\,\mathrm{eV}$) and this conditions are favorable for triggering the ion-ion two steam instability.

The ion-ion two steam instability occurs due to a relative drift between two ion species, e.g. $\mathrm{H}^+ - \mathrm{O}^+$ or $\mathrm{NO}^+ - \mathrm{O}^+$, of which the latter would be more common at lower altitudes, if the higher collision frequency would not prevent it. The $\mathrm{H}^+ - \mathrm{O}^+$ two-stream instability is usually developed when $T_e/T_i \geq 3$ and for ion drift velocities of the order of the ion thermal speed.

Wahlund et al. (1992a) used the linear theory to describe their explanation and assumed that each plasma component had a drifting maxwellian distribution, since most non-maxwellian distributions can be approximated by a sum of drifting maxwellians. This approach gave good results, even though it could not reproduce the spectral enhancement of the central peak, a feature observed by some authors, e.g. *Rietveld et al.* (1991).

Wahlund et al. (1992a) first assumed an ion composition of 5% H^+ and 95% O^+, a temperature ratio $T_e/T_i = 10$, and several velocities ratio (v_d/v_{th}, where v_d is the drift velocity and v_{th} is the thermal velocity). Fig. 3.3.6 shows the simulation results. They argue that the initial acceleration may be due to a non-ambipolar quasi-static electric field. When the instability is triggered, the ion acoustic turbulence will in turn create an enhanced anomalous resistivity which, if field aligned currents are present, can enhance the parallel electric field (due to $J_{\parallel} = \eta^{-1} E_{\parallel}$, where $\eta = 1/\sigma$ is the resistivity and σ is the conductivity) and give ions an additional acceleration. It is important to note that for large ion drifts (i.e. where $v_d / v_{th} \geq 4$) both ion acoustic shoulders can be enhanced.

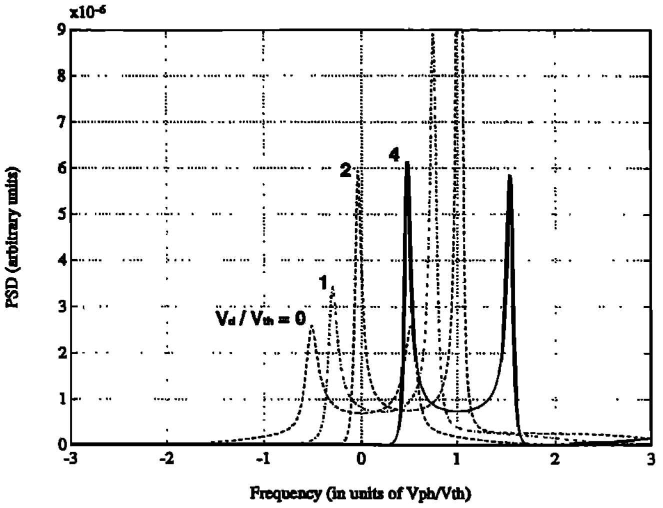

Figure 3.3.6.: Ion acoustic spectra produced in a plasma made of H^+ (5%) and O^+ (95%) with $N_e = 1 \times 10^{11}\,\mathrm{m}^{-3}$, $T_e = 1\,\mathrm{eV}$, $T_i = 0.1\,\mathrm{eV}$ and for different velocity drifts. Significant asymmetrical enhancement are already visible when velocity drifts is around the thermal velocity of ions. [from *Wahlund et al.* (1992a)]

The biggest advantages of the ion-ion two stream instability theory against the current driven ion acoustic instability theory, which needs a drift between electrons and ions, is that the theory proposed by *Wahlund et al.* (1992a) does not need huge currents and can explain situations where both the ion acoustic shoulders are enhanced, albeit, as we mentioned, very large ion drifts are needed to enhance both lines simultaneously. The latter is an important point, since we know now (see *Grydeland et al.*, 2003 and *Michell et al.*, 2009) that simultaneously enhanced upshifted and downshifted ion acoustic lines are not caused by temporal or spatial averaging, bur are thought to be a real physical phenomenon.

St.-Maurice et al. (1996) showed that, while this mechanism can work above 400km, it cannot be in action lower down where charged particles collide with neutrals, hence it cannot explain the observation of NEIALs at lower altitudes (below 200 km), which are presents e.g. in *Rietveld et al.* (1991), *Lunde et al.* (2007), *Ogawa et al.* (2011) and in our work as well.

However, as one moves up in the F region, electrons collide mostly with ions above 225 km, while the ions collide increasingly less frequently with the neutrals. This means that, in the presence of a parallel electric field, the electron velocity is limited by the ions, while the ion velocity increases steadily with altitude as their collision frequency decreases. Since ions having different masses will have different velocities as they move up, *St.-Maurice et al.* (1996) think that an instability could be produced by a mixture of relative ion and electron drifts.

Another issue pointed out by *St.-Maurice et al.* (1996) is that, since relative drift between ion species must be of the order of thermal speed of one of the species in order to achieve instability, the total ion velocity distribution would be double-humped. They calculated that this would require relative drifts along the magnetic field lines of the order of 1 km s^{-1} for a typical ionosphere below 500 km and if this drift arise from parallel electric fields, the field would be so large that an instability produced by the relative drift between ions and electrons (as the one proposed by *Collis et al.*, 1991 and *Rietveld et al.*, 1991) would be already present and in control of nonlinear processes (*Sedgemore-Schulthess and St.-Maurice*, 2001).

3.3.3. Parametric decay of Langmuir waves

A different approach to understand the generation mechanisms of NEIALs was employed by *Forme* (1993). Instead of basing their theory on intense streaming of thermal particles, they suggested that the ion acoustic fluctuation can be due to the decay of a beam generated Langmuir wave into ion acoustic waves on the scheme $L \to L' + S$ where L is the "pump" Langmuir wave, L' is the back-scattered Langmuir wave and S is the produced ion acoustic wave.

They assumed an electron beam moving through a stationary background plasma. The total distribution of electron and ions is then a "bump-on-tail" distribution, which, as *Tsytovich* (1967) have shown, is unstable to the beam instability. There exists two analytical forms of beam instability, the so-called "reactive" (or "resistive") and the "kinetic" form; both are actually two limiting versions of the beam instability. *Forme* (1993) used the kinetic form, since the reactive model requires a mono-energetic beam, which is unlikely to happen in the upper ionosphere.

The most important type of nonlinear interaction responsible for parametric instabilities is the three-waves interaction, where an initial Langmuir wave with frequency ω^l and wave vector $\mathbf{k^l}$ causes the growth of another Langmuir wave with frequency $\omega^{l'}$ and wave vector $\mathbf{k^{l'}}$ and the growth of an ion acoustic wave with frequency ω^s and wave vector $\mathbf{k^s}$. The three waves are characterized at the threshold by the following relations, which stems from the fact that wave energy and momentum must be conserved (see also *Chen*, 1984):

$$\omega^l = \omega^{l'} + \omega^s \qquad \mathbf{k^l} = \mathbf{k^{l'}} + \mathbf{k^s} \tag{3.3.1}$$

Weakly turbulent mode coupling cannot in fact proceed directly from one electron plasma oscillation to two other plasma oscillations. Weak turbulence can, however, proceed if energy is put into another mode that would decay at a moderate rate, e.g. the ion acoustic mode, especially if $T_e/T_i \gg 1$ (*Chen*, 1984 and *Sedgemore-Schulthess and St.-Maurice*, 2001). Note that the high temperature ratio is typical of type-II outflow events, which, as far as we know, are more likely to be associated with NEIALs.

A way to better visualize the process is to look at the $\omega - k$ diagram in Fig. 3.3.7 (from *Sedgemore-Schulthess and St.-Maurice*, 2001, adapted from *Chen*, 1984). The upper parabolic trace in figure is the wavelength dependence of electron Langmuir waves, which is $\omega_l^2 = \omega_p^2 + 3k_l^2 v_e^2$ (where v_e is the electron thermal velocity; we used subscripts to avoid a burdening in notation). The lower trace is one possible ion acoustic mode, with $\omega_s = k_s c_s$ (where $c_s = [(3T_i + T_e)/m_i]^{0.5}$ is the ion-acoustic speed with temperatures given in electron-volt).

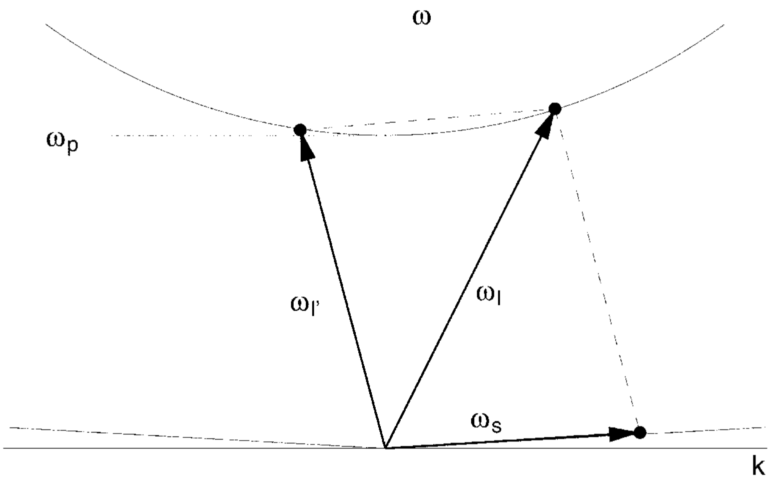

Figure 3.3.7.: Parallelogram construction on an $\omega - k$ diagram for a Langmuir decay instability. ω_p indicates the plasma frequency. The upper curve is the electron plasma wave's dispersion relation. The straight lines represent the ion acoustic wave's dispersion relation. [from *Sedgemore-Schulthess and St.-Maurice* (2001), adapted from *Chen* (1984)]

We can see how the Langmuir wave (ω^l, $\mathbf{k^l}$) can decay into a backward moving Langmuir wave ($\omega^{l'}$, $\mathbf{k^{l'}}$) and an ion acoustic wave (ω^s, $\mathbf{k^s}$) The parallelogram is the consequence of the constrain in eq. (3.3.1). The vector (ω^s, $\mathbf{k^s}$) must lie on the ion curve. Note that the initial Langmuir wave cannot decay into two other Langmuir waves, because there is no way to make the difference vector (ω^l, $\mathbf{k^l}$)-($\omega^{l'}$, $\mathbf{k^{l'}}$) lie on the electron curve.

It is also possible to determine the threshold electric field magnitude E_{th} needed to trigger the decay (see *Fejer*, 1979):

$$\varepsilon_0 E_{th}^2 = 4 n_0 K_B T_i (\nu_{ie}/\omega_p) B^{-1} \tag{3.3.2}$$

where $\varepsilon_0 = 8.854 \times 10^{-12}$ F/m is the permittivity of free space, n_0 is the background electron density, $K_B = 8.617\,\mathrm{eV\,K^{-1}}$ is the Boltzmann constant, T_i is the ion temperature, ν_{ie} is the ion-electron collision frequency, ω_p is the plasma frequency and B is (in this case) a numerical value ($B \simeq 0.58$).

Forme (1993) proceeded to evaluate the parameters for which the decay $L \rightarrow L' + S$ occurs. They assumed a background electron density $n_0 \approx 10^{11} - 10^{12}\,\mathrm{m^{-3}}$ and a temperature ratio $T_e/T_i \approx 3$. Fig.3.3.8 shows the beam parameters they estimated for a standard ionosphere situation.

They estimate the electron beam velocity to be:

$$v_b \approx \frac{\omega_p}{\frac{\omega_s}{2c_s} + \frac{\omega_p c_s}{3v_e^2}} \tag{3.3.3}$$

This gives, for the initial parameters they used, a numerical value in the interval $10^6\,\mathrm{m\,s^{-1}}$ to $10^7\,\mathrm{m\,s^{-1}}$, which correspond to beam energies of a few tens of eV (for UHF) to a a few

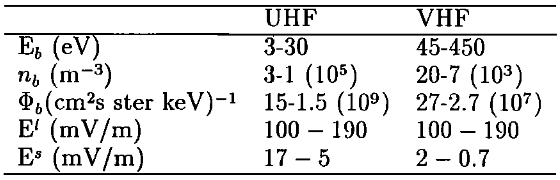

	UHF	VHF
E_b (eV)	3-30	45-450
n_b (m^{-3})	3-1 (10^5)	20-7 (10^3)
Φ_b(cm^2s ster keV)$^{-1}$	15-1.5 (10^9)	27-2.7 (10^7)
E^l (mV/m)	$100-190$	$100-190$
E^s (mV/m)	$17-5$	$2-0.7$

Figure 3.3.8.: Beam parameters and electric fields of Langmuir (E^l) an ion acoustic (E^s) waves for background electron densities of $n_0 \approx 10^{11} - 10^{12}\,\mathrm{m}^{-3}$. The value of E^s is probably overestimated by one or two orders of magnitude, since the calculation did not take in account the ion acoustic damping. [from *Forme* (1993)]

hundreds of eV (for VHF). These soft electron precipitation energies are indeed usually associated with the NEIALs.

They finally estimated the beam density critical value as:

$$\frac{n_b}{n_0} > \frac{20T_i\nu_{ei}}{m_e v_b^2 \omega_p} \tag{3.3.4}$$

where ν_{ei} is the electron-ion collision frequency.

Unfortunately the shape of precipitating electrons distribution function is not obtainable by means of incoherent scatter radars. It is, however, commonly measured by rockets and satellites (see e.g. *Robinson et al.*, 1987).

Some characteristics of enhanced ion acoustic fluctuations observed by incoherent scatter radars are not explained with this decay model. For example precipitating electrons enhance preferentially downgoing Langmuir waves which, in this model, decay in upgoing Langmuir waves and downgoing ion acoustic waves. However, several authors (e.g. *Ogawa et al.*, 2011 and *Lunde et al.*, 2007) have shown that, above $200-300\,\mathrm{km}$, ion acoustic waves propagate mostly upward. *Forme* (1993) argued that only upward propagating Langmuir waves due to low energy counter-streaming electrons may explain this, implying that upward propagating ion acoustic waves would correspond to more intense fluxes of upgoing than downgoing electrons. They argued also that such low energy electrons, of which the observation was reported by e.g. *Fung and Hoffman* (1991), may be of a different origins, namely back-scattered and secondary electrons or photoelectrons.

In a subsequent article (*Forme*, 1999), they extended the Langmuir decay theory to better explain the evidence of mostly enhanced downshifted lines at higher altitudes. Basically what they did is to allow the newly produced Langmuir wave to cascade into a downshifted ion acoustic wave and a second upshifted Langmuir wave. Schematically:

$$L \to L' + S \tag{3.3.5}$$

$$L' \to L'' + S' \tag{3.3.6}$$

They showed that for a given beam number density, the beam energy or the background density is important to trigger either the left or the right ion line. A large energy spread of the beam or low electron collision frequencies can explain the simultaneous observation of enhanced left and right shoulders. This theory can therefore overcome the difficulties to explain the observational features listed by *Forme* (1993) and be a strong candidate to explain a large number of NEIAL observations.

3.4. Summary

As we saw there is no predominant theory able to explain all the NEIALs observational features. A good summary on this topic can be read in *Sedgemore-Schulthess and St.-Maurice* (2001).

The direct excitation of unstable ion acoustic wave is characteristic of the plasma stream instability theories, namely the current driven and the ion-ion two stream instabilities.

Direct excitation theories are able to explain many observed features. For example the sharp cut-off in electrons precipitation can create intense parallel electric fields which cause large drifts in thermal electron population (as it occurs in the current driven instability theory). This could be the reason why the simultaneous optical and radar observations have all located enhanced radar spectra on the edge of precipitation regions instead of in the middle of an auroral arc. In addition, we know that the instability threshold due to an electron drift decreases when the electron temperature is enhanced, hence, as the observations point out, NEIALs are often observed together with electron temperature enhancements. The wavelength dependence can be explained by a two stream instability as well, since it is driven more easily at longer wavelengths, and this is very well confirmed by observations.

The current driven instability requires very high parallel electric fields, which in turn means huge parallel current densities; however, currents of such intensity are not so often observed, although, as *Neubert and Christiansen* (2003) have shown, it is possible to measure these high currents, especially in the pre-noon cusp.

On the other hand, the ion-ion two stream instability can produce both upshifted and downshifted enhanced ion acoustic lines and does not need huge currents to occur. But it has difficulties in explaining enhancements in ion acoustic lines enhancements occurring at low altitudes (below 200 km), which seem to be not so common, although have been observed in numerous occasions and are thought to have a geophysical origin.

The theory of Langmuir decay is an indirect excitation model, since it requires the decay of a Langmuir wave in order to generate an ion acoustic wave. It does not require huge parallel current densities, can explain the simultaneous occurrence of both downshifted and upshifted lines at the same altitude and can also give a good explanation for the cut-off in the scattered power with decreasing altitude. However, the theory of Langmuir decay needs precipitating electrons as the trigger mechanism, which makes difficult to explain the observations of enhanced ion acoustic waves on the edge of precipitation structures.

Mishin and Fiala (1995) proposed a cross between these theories. They have suggested that Langmuir turbulence could heat the electrons and dramatically decrease the threshold for a streaming instability. However the electron temperature would be very high, and, although we cannot get precise values inside the instability regions, this huge enhancement in the electron temperature would be unlikely to occur.

We can try to propose a way to let the theories fit together. At higher altitudes (above 200-250 km) the dominant theories could be the parametric decay of Langmuir waves and the ion-ion two-stream instability. The parametric decay can in fact explain the occurrence of simultaneously upshifted and downshifted enhanced ion lines which are often observed at these altitudes, while the ion-ion instability can be valid only above 400 km (as discussed by *St.-Maurice et al.*, 1996). At lower altitudes the current driven instability could be the dominant one, especially below 250 km. We know that this theory is not able to explain simultaneously enhanced ion lines, but usually they are not observed at this low altitude. Still, the current driven instability needs very high current densities, which are not often observed, albeit they are not anymore discarded as impossible to occur. For instance, in the case shown in Fig. 3.4.1, all of the three theories could be acting to produce the enhancement in ion acoustic lines.

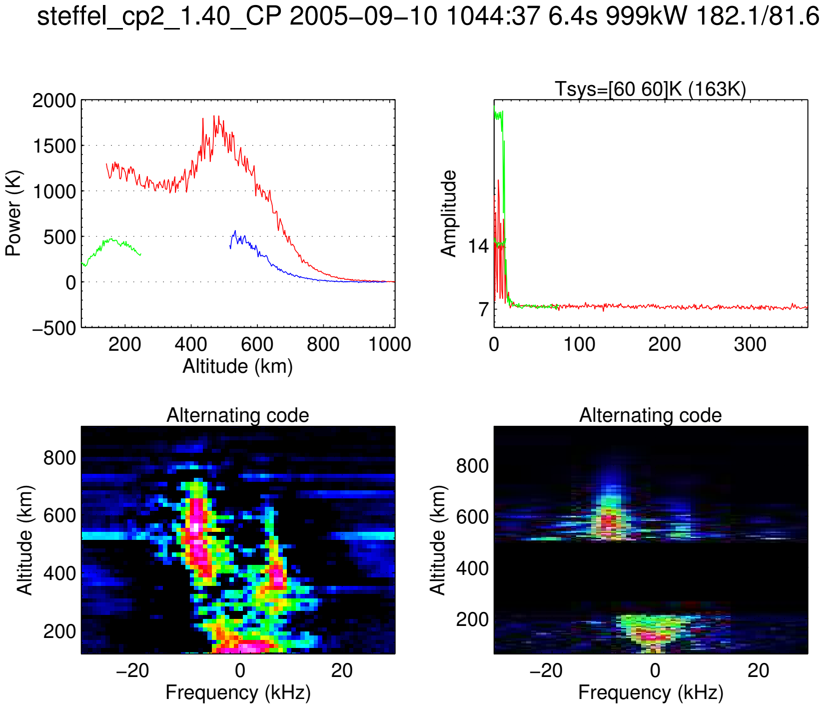

Figure 3.4.1.: NEIAL spectra showing the possibility for the three theories to act together: at lower altitudes (around 200 km) could dominate current driven instability. Further up around 400 km the parametric decay of Langmuir waves can explain the simultaneous enhancement of both ion lines. The ion-ion instability could explain the NEIAL around 600 km.

4. Incoherent scatter theory and the EISCAT system

4.1. Incoherent scatter

4.1.1. Theory of incoherent scatter

When spatial fluctuations are present in a medium, waves cannot propagate unperturbed through it since energy will be scattered by the refractive index variations into other directions. In the ionosphere these fluctuations are caused by the fact that the plasma consists of charged discreet particles which, when they move through the plasma, will excite electron density fluctuations which in turn can be detected by electromagnetic wave scattering. This kind of scattering is called *incoherent scattering* (see e.g. the review by *Hagfors*, 1995).

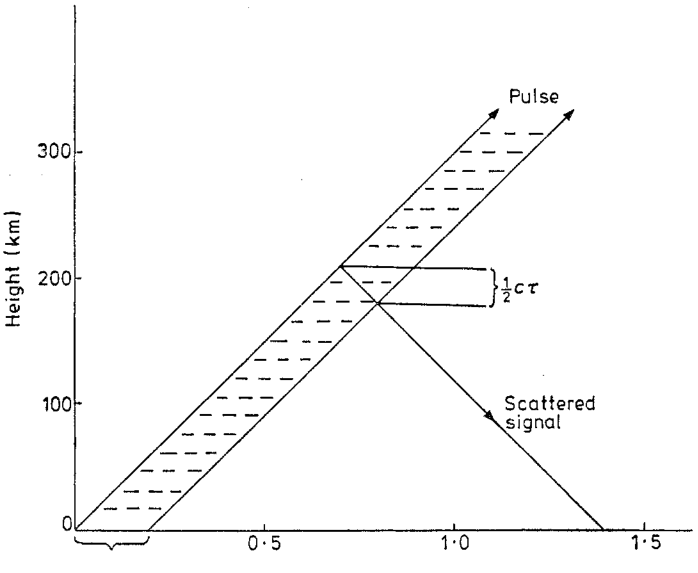

Figure 4.1.1.: Incoherent scatter experiment setting. A pulse of the order of 10^6 W is sent up in the ionosphere and then reflected and received back by the radar antenna. The received signal is of the order of 10^{-17} W. The height resolution is related to the pulse length and it is equal to $0.5c\tau$, where c is the speed of light and τ is the pulse length. [from *Beynon and Williams* (1978)]

Fig.4.1.1 schematically shows an incoherent scatter radar experiment, where an high power electromagnetic wave is transmitted into the ionosphere. Electrons which are hit by the wave are accelerated and hence emit electromagnetic radiation, which is received by the radar as a weak, scattered signal coming from these electrons. The ions are practically not participating to the scattered signal, since their large mass prevents them from being accelerated by the incoming radiation.

The scattered radiation contains also other frequencies, in addition to the radar frequency. This is due to the Doppler broadening of the signal, which is caused by the thermal motion of the particles. In addition there can also be a Doppler shift due to the collective motion of the particles species.

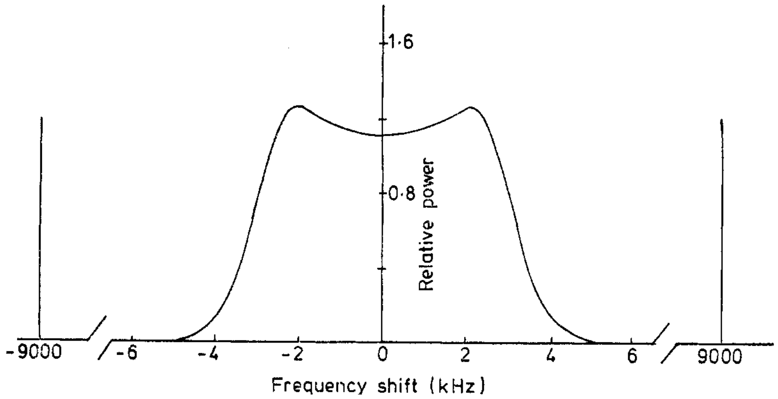

Figure 4.1.2.: Typical shape of the incoherent scatter power spectrum from the ionospheric F region. [from *Beynon and Williams* (1978)]

Fig. 4.1.2 shows a typical power density spectrum received by an incoherent scatter radar. The information are extracted from this spectrum or, equivalently, from the auto-correlation function of the received signal, which is the Fourier transform of the power density spectrum (due to the Wiener-Khinchin theorem). The central part is shaped by the two broadened ion acoustic lines and the two lines on the side are the plasma lines. It is important to note that the figure in not in scale, since the ion lines frequency is of the order of KHz, whereas the plasma lines frequency is of the order of MHz.

Now we will briefly describe the physics behind the incoherent scatter spectrum, starting with the definition of some useful quantities. Our references are *Bjørnå* (2005) and our own notes.

The *Debye length* is a measure of the sphere of influence of a test charged particle placed in a plasma. It is defined for electrons and ions, respectively as:

$$\lambda_e = \sqrt{\frac{\varepsilon_0 k_B T_e}{n_0 e^2}} \qquad \lambda_i = \sqrt{\frac{\varepsilon_0 k_B T_i}{n_0 e^2}} \tag{4.1.1}$$

The total Debye length is hence written as:

$$\frac{1}{\lambda_D^2} \equiv \frac{1}{\lambda_e^2} + \frac{1}{\lambda_i^2} \tag{4.1.2}$$

For distances $r \gg \lambda_D$ the shielding cloud around the test particle will cancel its effects. The Debye length in the ionosphere is of the order of 10^{-3} m.

The *electron plasma frequency* is defined as:

$$\omega_{pe} = \sqrt{\frac{n_e e^2}{m_e \varepsilon_0}} \tag{4.1.3}$$

It represent the frequency at which the electrons oscillate when responding to the electric fields built up when the plasma is slightly perturbed locally. The electric fields are built up in order to restore the charge neutrality and pull the particles back to the original position. But, because of their inertia, particles will overshoot and oscillations occur. These are high frequency oscillations (of the order of MHz) and the ions are too massive to have time to respond. These oscillation are called *electron plasma oscillation* or *Langmuir oscillations*. Note that the electron plasma frequency is proportional to the square root of electron density.

However, if one takes into account the thermal motion of the particles ($v_{th,e} = \sqrt{k_B T_e / m_e}$) the perturbation will propagate through the plasma and the result is a high frequency *electron plasma wave*. In this case we can write the dispersion relation as:

$$\omega = \omega_{pe}\sqrt{1 + 3k^2\lambda_e^2} \tag{4.1.4}$$

where $k = |\mathbf{k}|$ is the wave vector magnitude.

Different types of waves in the plasma have different dispersion relations. A dispersion relation has the form:

$$\varepsilon(\mathbf{k}, \omega) = 0 \tag{4.1.5}$$

where $\varepsilon(\mathbf{k}, \omega)$ is the *dispersion function*.

The *ion acoustic waves* are low frequency waves, where the ions have time to respond to the propagation. They are described, if a fluid model of the plasma is used, by the following dispersion relation:

$$\omega = kC_s \tag{4.1.6}$$

where C_s is the ion acoustic speed:

$$C_s = \sqrt{\left(\frac{\gamma_e k_B T_e + \gamma_i k_B T_i}{m_i}\right)} \tag{4.1.7}$$

where γ_e and γ_i are the ratio of specific heats (C_p/C_V) for electrons and ions respectively and k_B is the Boltzmann constant (not to be confused with the wave vector magnitude k).

However, the fluid model cannot describe some feature of the plasma, namely the *Landau damping*. In order to study such phenomena, we need the kinetic theory, in which a central element is the *distribution function* $f = f(\mathbf{r}, \mathbf{v}, t)$ for each particle species. For a uniform, isotropic and stationary plasma f is a function only of the velocity magnitude: $f = f(v)$. Perhaps the most important distribution function with this property is the Maxwellian, which in the one-dimensional case is:

$$f_M(v_x) = \sqrt{\frac{m}{2\pi k_B T}} \exp\left[\frac{-(v_x - v_d)^2}{2v_{th}^2}\right] \tag{4.1.8}$$

In kinetic theory the wave frequency and the dispersion function are complex quantities and can then be written as:

$$\omega = \omega_r + \imath\omega_i \qquad \varepsilon = \varepsilon_r + \imath\varepsilon_i \tag{4.1.9}$$

where the first factor represents the oscillation in time at frequency ω_r and the second factor represent a growth if $\omega_i > 0$ or a damping of the oscillation if $\omega_i < 0$. This damping is called *Landau damping*.

For the ion acoustic waves the kinetic theory gives, when the damping is weak ($|\omega_i| \ll \omega_r$):

$$\omega_r = \frac{kC_s}{1 + k^2\lambda_e^2} \tag{4.1.10}$$

and ω_i will be proportional to $-\omega_r \left(T_e/T_i\right)^{3/2} \exp\left[-T_e/T_i\right]$. The condition $|\omega_i| \ll \omega_r$ is equivalent to $T_e \gg T_i$. In this case we have $C_s \approx \sqrt{k_B T_e/m_i}$ and hence ω_r will be determined by the electron temperature (the electron thermal motion) and the ion mass (the ion inertia). For ion acoustic waves the damping depends on the temperature ratio T_e/T_i (the larger the ratio the stronger the damping) and it will determine the shape of ion line in the incoherent scatter spectrum.

For the sake of completeness we report here the mathematical expression for the power spectrum (*Bjørnå*, 2005):

$$S(\mathbf{k},\omega) = C\frac{n_e}{k}\left\{ f_e\left(\frac{\omega}{k}\right)\left|1 + \frac{Z_e(\mathbf{k},\omega)}{\varepsilon(\mathbf{k},\omega)}\right|^2 + f_i\left(\frac{\omega}{k}\right)\left|\frac{Z_i(\mathbf{k},\omega)}{\varepsilon(\mathbf{k},\omega)}\right|^2 \right\} \tag{4.1.11}$$

where C is a numerical constant, f_i and f_e are the electrons and ions velocity distribution functions (in the direction of the magnetic field), $\varepsilon(\mathbf{k},\omega)$ is the complex dispersion function and $\varepsilon = 1 - Z_e - Z_i$, where Z_e and Z_i are integrals containing the respectively the electrons and ions distribution functions.

4.1.2. Parameters measured by incoherent scattering

Many parameters can be directly measured by the incoherent scattering, while others can be derived. We will now give a brief description of them. A thoroughly review can be found in e.g. *Beynon and Williams* (1978).

Electron density

Electron density is basically proportional to the area of the incoherent scatter spectrum. This means that it is proportional to the scattered power and to the temperature ratio T_e/T_i and it can be determined by measuring these two quantities. Another independent way to get it is using Faraday rotation, for which one needs to know the magnetic flux density and the angle between the path of the signal and the magnetic field lines.

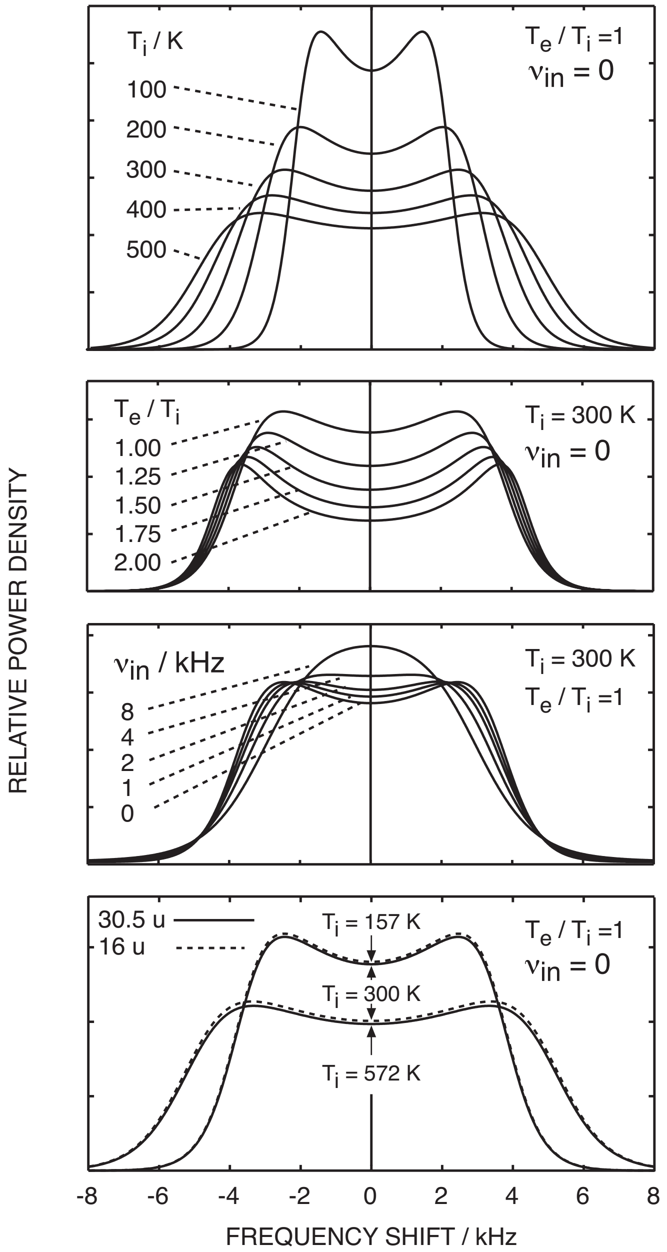

Figure 4.1.3.: Shape of incoherent scatter spectra depending on several ionospheric parameters. [from *Nygrén* (1996)]

Temperature ratio T_e/T_i

When $T_e \gg T_i$ is not strictly satisfied, the ion acoustic waves are more strongly damped, which means that the two ion acoustic lines with peaks at $\omega \approx \pm kC_s$ are broadened and merge into one broad double-humped line, as it shows Fig. 4.1.3.

The sharpness of the shoulders and the depth of the valley between them are dependent on the damping and hence are a measure of the temperature ratio T_e/T_i.

Ion mass

When $T_e \gg T_i$ we can write eq. 4.1.7 as $C_s \approx \sqrt{k_B T_e / m_i}$. This velocity is then proportional to the broadening of the ion acoustic shoulders, and from the latter is hence possible to estimate the mass of the ions.

Plasma velocity

If there is a bulk movement of the plasma the spectrum as a whole is Doppler shifted. By measuring the mean Doppler shift of the scattered spectrum the component of plasma velocity in the mirror direction can be determined (see Fig.4.1.4). However a great precision is required, since for the usual ionospheric conditions and radar configuration the Doppler shifted frequency differs from the "zero frequency" often by less then 0.5% It is also important to note that with a typical back-scattering configuration is impossible to obtain a vector velocity, but only the velocity component along the radar beam. This is of course due to the fact that the velocity component perpendicular to the line of sight has a zero Doppler shift.

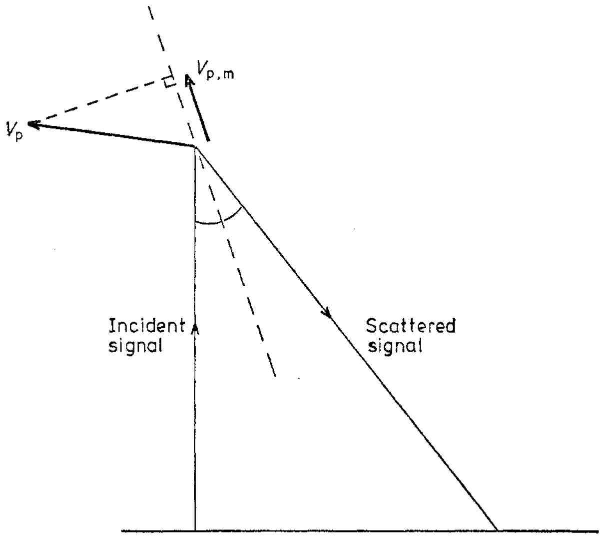

Figure 4.1.4.: The mirror direction in a bi-static configuration, showing the component of plasma drift velocity measured in such a system. [from *Beynon and Williams* (1978)]

Other parameters

In particular conditions it is possible to measure also ion neutral collision frequency, electric current density and the spectrum of supra-thermal electrons.

In addition, from the parameters measured directly, several others can be estimated:

- electric field
- ionospheric conductivities (Hall and Pedersen conductivities)
- neutral wind velocity
- neutral temperature

- downward flux of heat from the exosphere

See *Beynon and Williams* (1978) for a complete discussion of the parameters that can be derived by the incoherent scatter spectrum.

4.2. The EISCAT facility

The EISCAT (**E**uropean **I**ncoherent **Scat**ter) Scientific Association conducts research on the lower, middle and upper polar atmosphere and ionosphere using incoherent scatter radars. There are two radars in Northern Scandinavia (Ramfjordmoen, near Tromsø, in Norway) and one on Svalbard (Norway). At the Ramfjordmoen facility it operates an ionospheric heater as well. Additional receiver stations are located in Sodankylä (Finland) and Kiruna (Sweden).

The UHF radar (Ramfjordmoen) operates at 931 MHz with a peak transmitter power over 2 MW and a 32 m, fully steerable parabolic dish antennas. In Ramfjordmoen there are the transmitter and one receiver, while two other receivers are located in Sodankylä and Kiruna. This allows tri-static measurements to be made.

The VHF radar (Ramfjordmoen) operates at 224 MHz with a peak transmitting power of 2×1.5 MW and a 120 m $\times 40$ m parabolic cylinder antenna, composed of four sectors. It can be steered in the meridional plane from vertical to 60° north of the zenith.

The EISCAT Svalbard radar (ESR) is located near Longyearbyen in the Svalbard archipelago, it operates at 500 MHz with a peak transmitter power of 1 MW. There are two antennas, one fully steerable paraboloid of 32 m diameter and one fixed field aligned antenna of 42 m diameter.

In Tab. 4.1 and Tab. 4.2 are respectively summarized the geographic positions and some technical characteristics of the EISCAT facilities.

Location	Tromsø	Kiruna	Sodankylä	Longyearbyen
Geographic Latitude	69°35’11” N	67°51’38” N	67°21’49” N	78°09’11” N
Geographic Longitude	19°13’38” E	20°26’07” E	26°37’37” E	16°01’44” E
Altitude	86.28 m	417.62 m	197.03 m	445 m

Table 4.1.: Geographical coordinates of EISCAT facilities. [from *EISCAT Scientific Association*, 2013]

Location	Tromsø	Tromsø	Longyearbyen
Band	VHF	UHF	UHF
Transmitter frequencies	222.8 - 225.4 MHz	926.6 - 930.5 MHz	498 - 502 MHz
Transmitter	1 klyostron	2 klyostrons	-
Peak power	1.6 MW	2 MW	1 MW
Average power	200 kW	250 kW	250 kW
Pulse duration	1 µs-2 ms	1 µs-2 ms	0.5 µs-2 ms
Minimum inter-pulse	1 ms	1 ms	0.1 ms
Receiver frequencies	214.3 - 234.7 MHz	921.0 - 933.5 MHz	485 - 515 MHz

Table 4.2.: Some technical characteristics of EISCAT radars transmitters. [from *EISCAT Scientific Association*, 2013]

5. Results

As we mentioned in the introductory chapter, we are mostly interested in discussing the relation between type-II ion outflows and naturally enhanced ion acoustic lines. There are basically three physical parameters to take into account:

- Ion velocity, useful to investigate the starting altitude of the outflow when the NEIAL event occurs, employing for instance a velocity altitude profile. An ion velocity profile over time is useful to understand the ion outflow behavior with and without the NEIAL event.
- Electron density, that in turn gives important information about the particle precipitation, which is thought to play a role both in ion outflow and NEIAL events. It is useful to plot both the F region and the E region electron density over time in order to identify soft and hard particle precipitation, respectively.
- Temperatures, which are important to assess the typology of the outflow the possible the heating mechanisms during the events. In addition, they are useful to identify "mixed" situations, e.g. type-II ion outflows with the ion temperature slightly enhanced. Temperature ratio is useful to investigate both the ion outflow typology and the thresholds for instabilities to occur.

5.1. Results: Introduction

The analysis of EISCAT data followed a standard procedure:

1. Search for ion outflows (preferably type-II) looking at EISCAT auto-generated color plots on the Madrigal database at `http://www.eiscat.com/madrigal/`. We usually searched for field aligned experiments, so we looked mostly at data obtained by the ESR 42m antenna.
2. Manual search for naturally enhanced ion acoustic lines looking at the real time graph (RTG) using the `remtg`[1] Matlab routine, which we customized in order to download the RTGs to our PC. Unfortunately, we were not able to analyze some data due to the lack of a working RTG definition file in the database. We downloaded all of the raw data we used from the EISCAT database at:
`http://www.eiscat.com/rtg/rtg.cgi`.
3. Analysis of data dumps near (during, before and/or after) NEIALs events. We defined a *NEIAL event* as an event where enhanced acoustic lines were clearly visible in one or more consecutive data dumps. We know that this is not necessarily an

---

[1] for further information, check `http://www.eiscat.com/rtg/remtg.html`

exact definition, since we can actually have separated NEIAL events during 6 s (see *Michell et al.*, 2009); nevertheless, we believe that this is a good operative definition in our case study scenario. To get reliable parameters, we manually removed the dumps containing NEIALs from the chosen data set, since they can alter the incoherent scatter analysis results. In some case it was necessary to remove also dumps containing satellites passes, since the software's automatic check function was not 100% reliable. The software used to extract parameters was `Guisdap 8.7`, which can be found at:
`http://www.eiscat.com/groups/Documentation/UserGuides/GUISDAP`.

4. Analysis of parameters and plotting. We used a Matlab routine written by us in order to derive additional parameters (e.g. electron temperature and particle flux), to remove data with errors considered too large and to plot several figures, like ion velocity, temperatures and electron density, both as altitude profiles and time varying quantities at a fixed altitude. Further information on this routine, together with the source code, can be found in Appendix B.

We tried to follow a standard procedure to get comparable results along different experiment types and conditions. First of all we usually tried to find a relation between the NEIALs and the outflow starting altitude; in order to do this, we plotted the ion velocity altitude profiles just before the NEIAL occurrence. The issue is that in order to get reliable values, we need to integrate for at least 60 s, more often 120 s. Hence we run the risk to smooth out any peculiarities occurring just before the NEIAL. For example, a sudden increment in ion velocity occurring 10 s before the NEIAL will be heavily smoothed out with a 120 s integration. However, as we shall see, useful information can still be obtained.

Together with the ion velocity altitude profile, we evaluated the electron and ion temperatures, the temperature ratio T_e/T_i, the flux and the electron density. We wrote a function to evaluate also the parallel (i.e. field aligned) electric field, but the values we got had very large errors, so we did not include any plot with it.

Afterwards we plotted values as a function of time. In this regard, the electron density is very interesting since it can tell us something about the particle precipitation which, as we have seen in chapter 3, is correlated with NEIAL events. Again, we have the usual problem about the integration time, i.e. an integration time of 120 s can easily smooth out a sudden parameter increase near the NEIAL occurrence. We tried to lower down the integration time, as *Rietveld et al.* (1991) did, but we did not succeed due to very large errors. We could, however, get good results, albeit the relatively long integration time.

The temperature time variation is important as well. In some cases we found an interesting anti-correlation between electron and ion temperature, to which we could not give a satisfactory physical explanation, even though we tend to exclude technical errors. The cause of this behavior can be related to the the temperature measurements; we discuss a possible explanation in sec. 5.4.

Through many hours of analysis, we found “odd” cases here and there. Some of them were not isolated cases, so we report here any unexpected observational feature we found in the data. One of the most interesting is a sort of “slow-growing” NEIAL event, where, instead of a sudden increase in power, we observed a smooth growing in time, lasting as much as 20 seconds. In other cases we observe very weak ion acoustic lines, especially at altitudes above 400 km. These "failed NEIALs" have inhomogeneous enhancements, which appear like weak spots in the spectrum. Since the presence of weak enhancement in the ion acoustic lines is clear, these cases cannot be easily discarded as noise.

We chose to divide the result in two parts: the first part is made of standard field aligned experiments with a fixed field aligned antenna; the second one is related to the *Steffe CP-2* experiment, which was set in such a way to have the radar on for one minute and off for the successive one minute. The reason why we included some of the observations here is that this particular setting presents interesting features, namely very powerful NEIALs with long duration. In addition, they were suited to our analysis due to the large signal-to-noise ratio.

Note: all the times are given in Universal Time (UT), in the form "hhmm:ss". All parameters are evaluated field aligned, unless specified. In addition, the white periods in the color plots are due to the radar transmitter being off, thus no analysis was performed during these time intervals. Finally, some figures does not correctly show the EISCAT logo, due to issues in the GUISDAP software and/or the Matlab version we used. We apologize for that.

5.2. Results: Part 1 - Standard field aligned experiments

5.2.1. Case 1: 31 March 2005

On 31 March 2005 (see Fig.5.2.1 for the color plots) we observed NEIAL events in the interval 0600-0700 UT, where the type-II ion outflow was short but intense. We found 6 dumps containing NEIALs out of a total of 562. The low occurrence frequency is probably due to the short duration of the ion outflow. We found two distinct NEIAL events: one during the interval 0623:12-0623:31 UT and the other during the interval 0626:43-06:26:49 UT. We analyzed the second one, since it was more intense. Its spectra are shown in Fig.5.2.2. The spectrum of each dump gives several information. The upper left panel shows the power received by the antenna at every altitude. A "bump" in the spectral power is a signature for the NEIAL event, while satellites are usually characterized by a much more enhanced and square-like shape. The bottom panels shows the actual spectra of the event at every altitude. Thus, the intensity of the lines is identified by the colors, where black means no signal, white means a saturation and the color map used is the same as in Fig.5.2.1. Note how the downshifted line is enhanced more and more often than the upshifted one, as it is usually the case for NEIAL events above 300 km.

First we analyzed the field aligned ion velocity to check if the NEIAL and the outflow started at the same altitude. Finding a NEIAL below an outflow would pose a problem for the hypothesis stating that ion outflows are a necessary condition for the onset of a NEIAL event. In this case we actually found a good agreement, as the top panel in Fig.5.2.3 shows. Regarding the temperatures (Fig.5.2.3, bottom panel), we found that the electron temperature was slightly lower than the average (but still enhanced with respect to the standard ionosphere without any NEIAL occurring) and that the temperature ratio

T_e/T_i altitude profile oscillated between 2 and 4, which is a relatively low value. It is possible however, that on a shorter integration time we would find higher temperature ratio. We tried with a 60 s integration time (the figure is not reported here) and we got very similar profiles, but this time the temperature ratio reached nearly 5 around 400 km altitude, which is interesting, since the NEIAL event became intense at that very altitude. Unfortunately, we had to keep the integration time above 60 s to get reliable results.

To investigate if the standard parameters went into a "preparation" phase before the NEIAL appeared, we plotted the ion velocity, electron density, temperatures and temperature ratio over time and at several altitudes, both with and without dumps containing NEIALs. This is useful in order to study what is happening in the vicinity of the NEIAL event we are focused on. We are going to show here only the results obtained without dumps containing NEIALs, since they are usually more precise, especially for the electron density, which is reported by the software as exceptionally enhanced if one does not remove the dumps containing NEIALs (on a side note, this is the very reason for the idea discussed in Appendix A).

Fig. 5.2.4 (top panel) shows the electron density over time. There is nothing special regarding NEIALs, except for the very weak enhancement visible at 612 km. The trend seems to show an increasing electron density, but this is somewhat expected, since we are in the morning and the Sun's radiation is going to enhance the ionization, as is clearly visible in Fig. 5.2.1. Surprisingly, things changes drastically if we look at the electron density in the E-region (bottom panel in Fig. 5.2.4): here it is absolutely clear that hard particle precipitation is correlated with NEIAL events. This result is in a very good agreement with other authors, e.g. *Rietveld et al.* (1991). However, as we shall see in the next observation, this is not a necessary condition for NEIAL occurrence.

Very interesting is also Fig. 5.2.5, which shows the field aligned ion velocity over time at several altitudes. It is clearly evident that the ion velocity in correspondence of NEIALs is enhanced for each altitude considered here, especially at lower altitudes. This seems to be a strong evidence for the close relation between ion outflows and NEIALs. There is, however, an issue in this very figure: around 0630 UT, which correspond to block 30 in the figure, the ion velocity was quite high, but no NEIAL occurred. This is a recurring matter: it is not impossible to find common features for NEIAL events, even *necessary* conditions, but we could not find any *sufficient* condition for their occurrence.

Finally, Fig. 5.2.6 shows electron and ion temperatures (top panel) and the temperature ratio T_e/T_i (bottom panel). We have a slight enhancement when NEIALs occurred, both in electron temperature and in temperature ratio (again as *Rietveld et al.* (1991) observed) at several altitudes, for instance at 413 km, 493 km, 551 km and, only in the electron temperature, at 612 km. However, in contrast to *Rietveld et al.* (1991), we did not observe any enhancement in the ion temperature, except for a slight increase at 612 km, which is in fact the reason for the lower temperature ratio at this particular altitude.

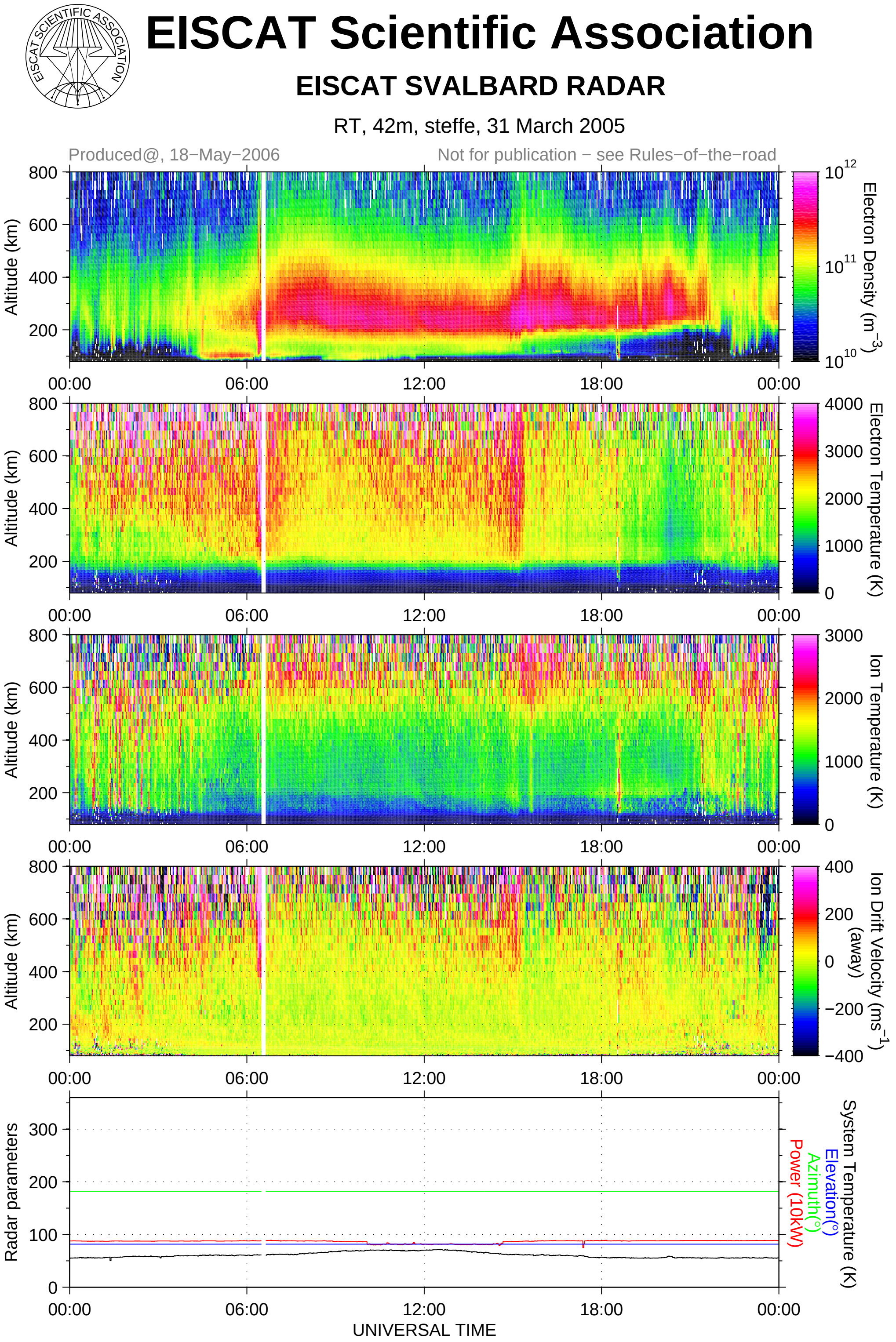

Figure 5.2.1.: Color plot showing electron density, electron temperature, ion temperature, ion velocity and radar parameters for the events observed on 31 March 2005. We analyzed the interval 0600-0700 UT. [from *EISCAT Scientific Association*, 2013]

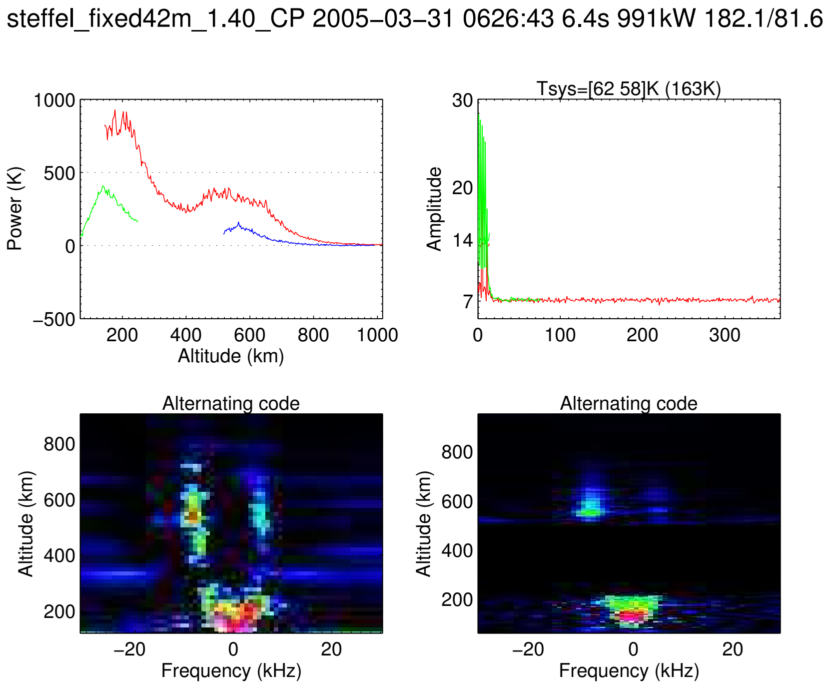

(a) 0626:43 UT

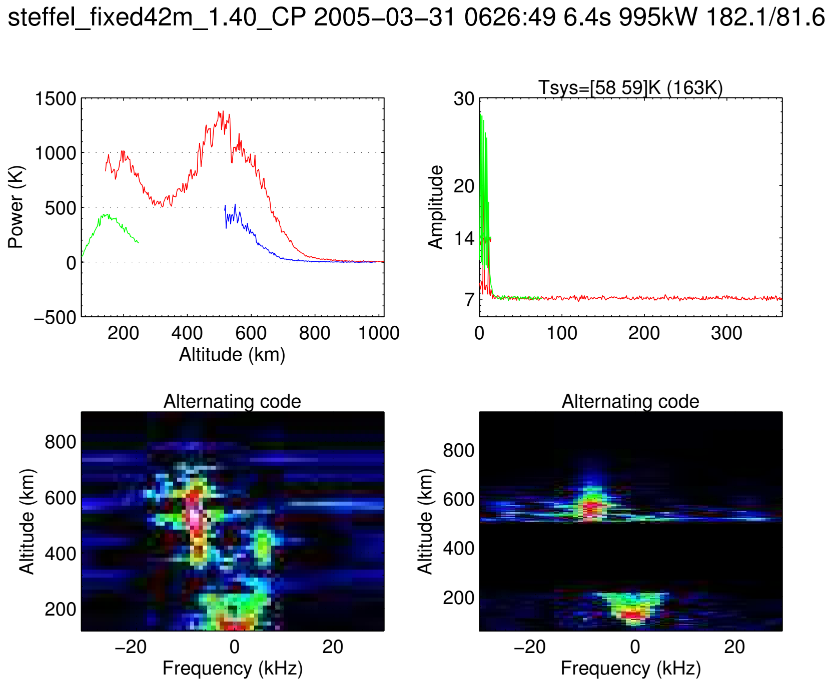

(b) 0626:49 UT

Figure 5.2.2.: Spectra of the NEIAL event occurring between 0626:43 and 0626:49 on 31 March 2005.

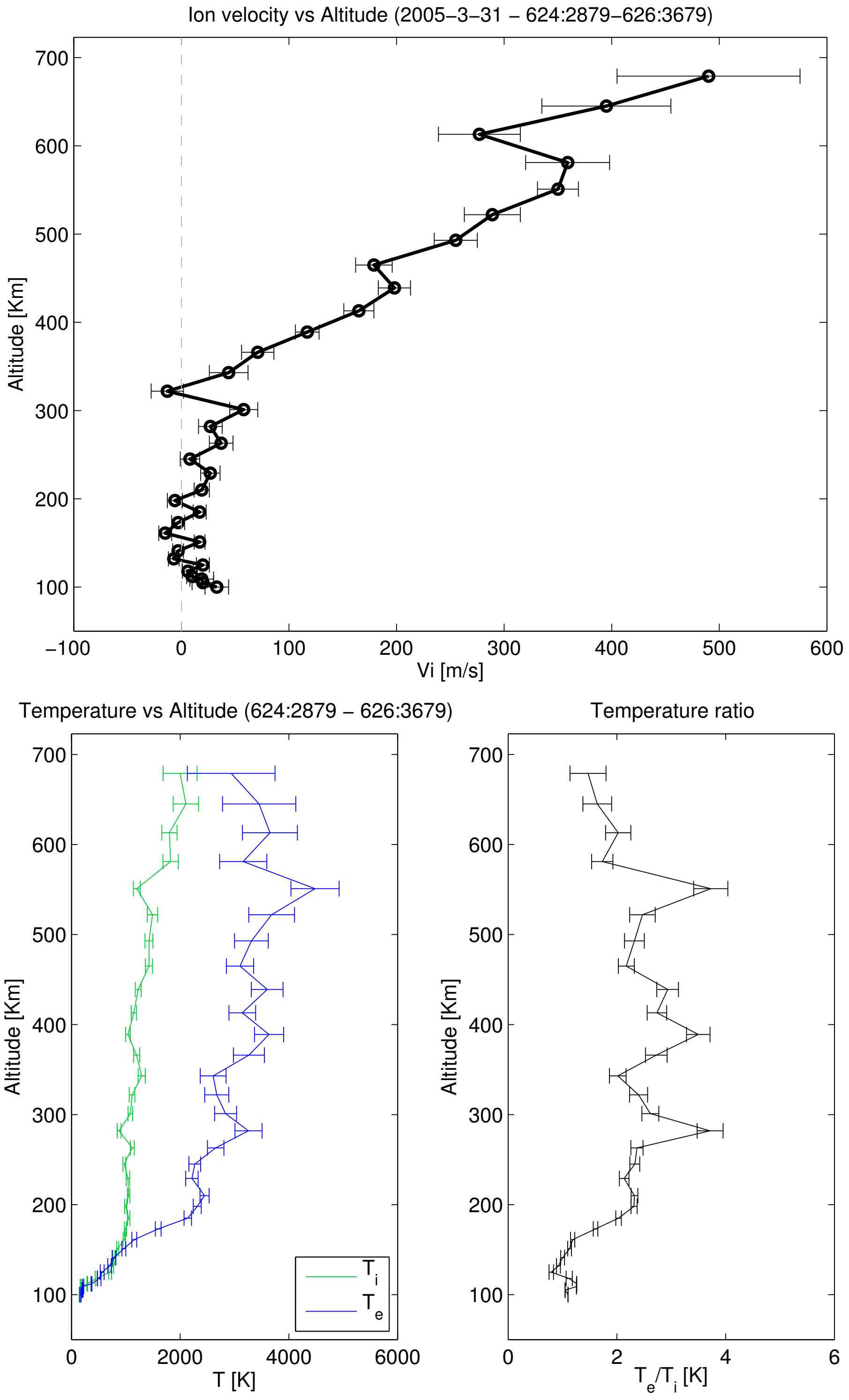

Figure 5.2.3.: Some ionospheric parameters evaluated with 120 s integration time between 0624:28 and 0626:36 UT on 31 March 2005. (Top panel) Ion field aligned velocity; (Bottom panel, left) Electron and ion temperatures; (Bottom panel, right) Temperature ratio T_e/T_i.

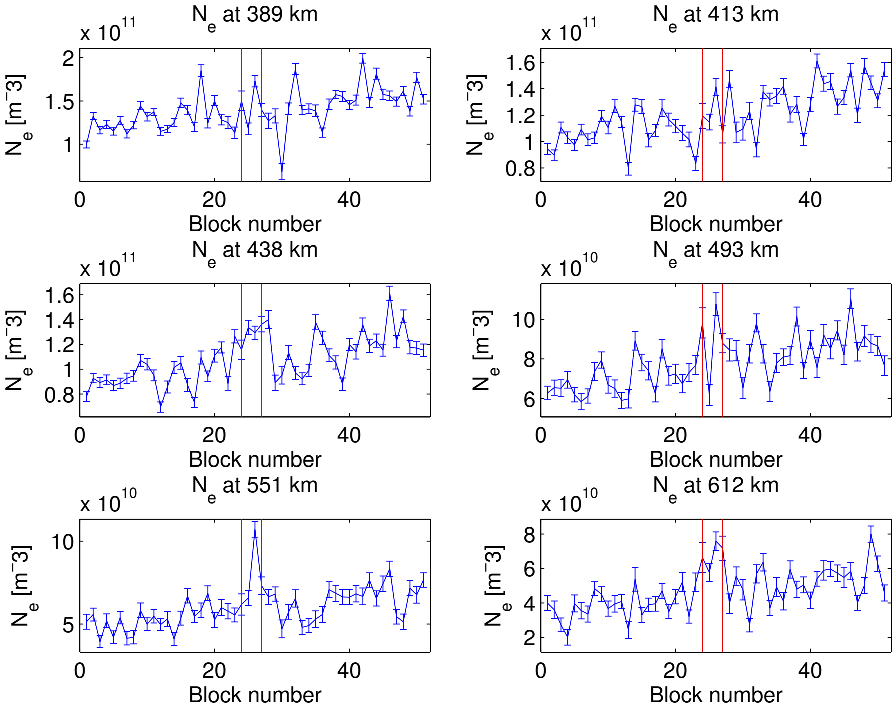

(a) Electron density (between 389 and 612 km)

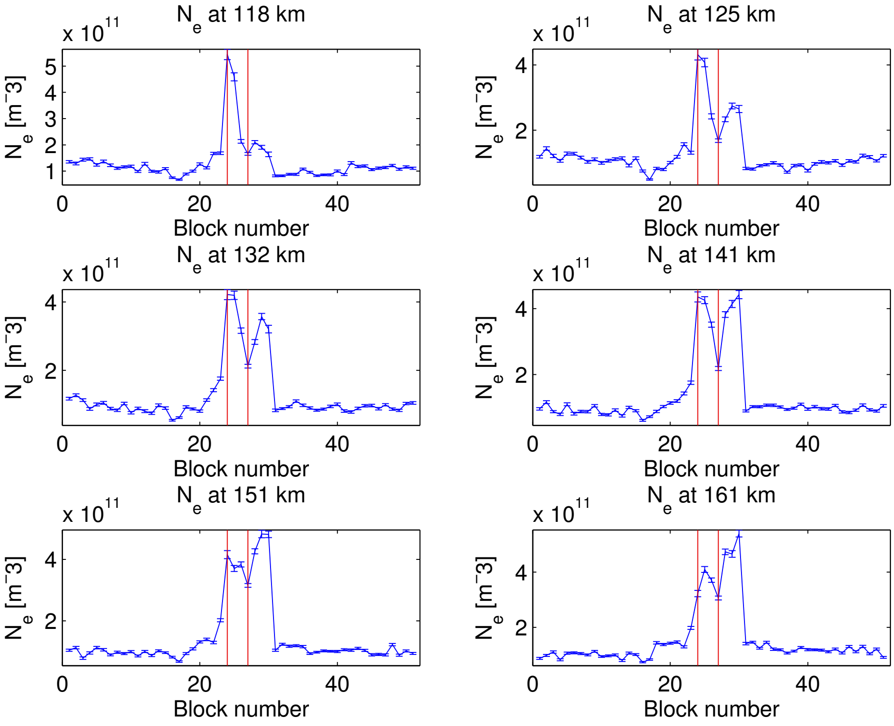

(b) Electron density (between 118 and 161 km)

Figure 5.2.4.: Electron density at high altitude (a) and in the E region (b) during the two NEIAL events occurring respectively between 0623:12 and 0623:30 UT and between 0626:43 and 06:26:49 UT on 31 March 2005. The red lines (blocks 24 and 27) indicate the NEIALs occurrence. Dumps containing NEIALs are removed from the analysis. The time interval shown is 0600-0659 UT. Integration time is 60 s.

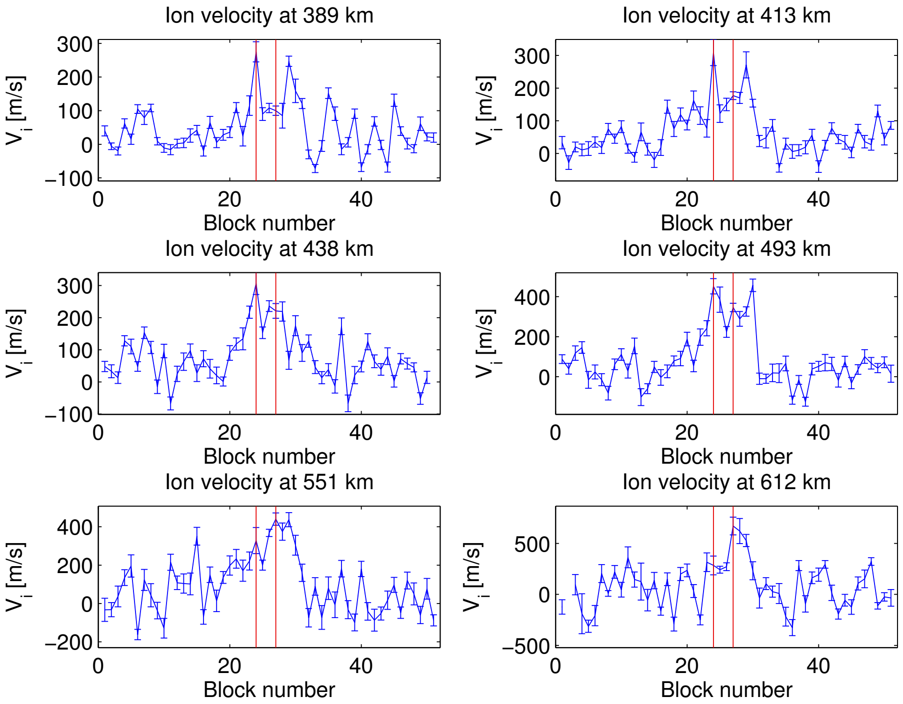

Figure 5.2.5.: Field aligned ion velocity during the two NEIAL events occurring respectively between 0623:12 and 0623:30 UT and between 0626:43 and 06:26:49 UT on 31 March 2005. The red lines (blocks 24 and 27) indicate the NEIALs occurrence. Dumps containing NEIALs are removed from the analysis. The time interval shown is 0600-0659 UT. Integration time is 60 s.

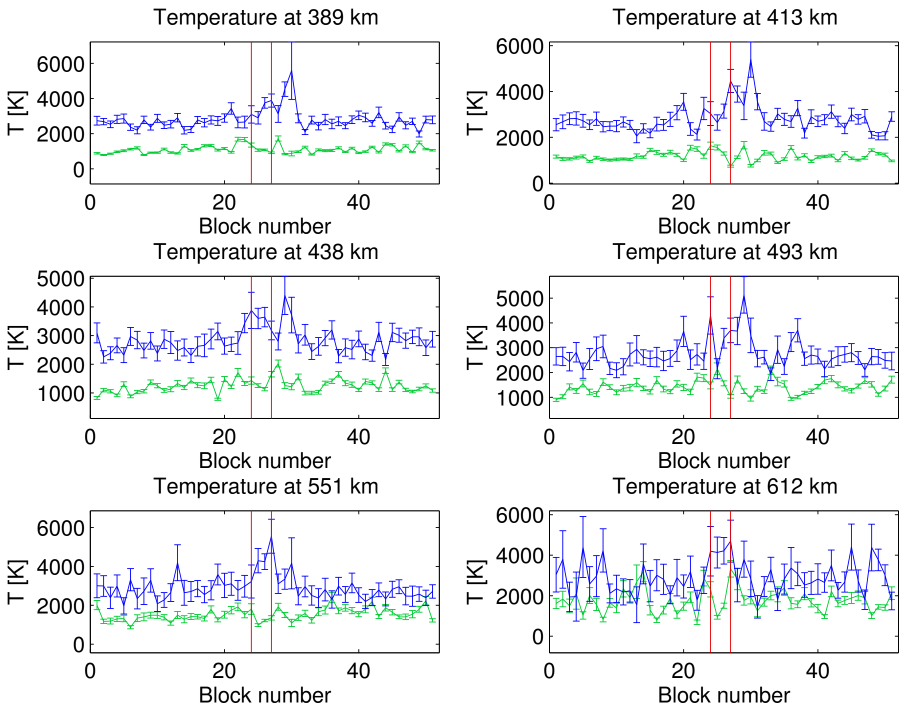

(a) Electron (blue) and ion (green) temperature

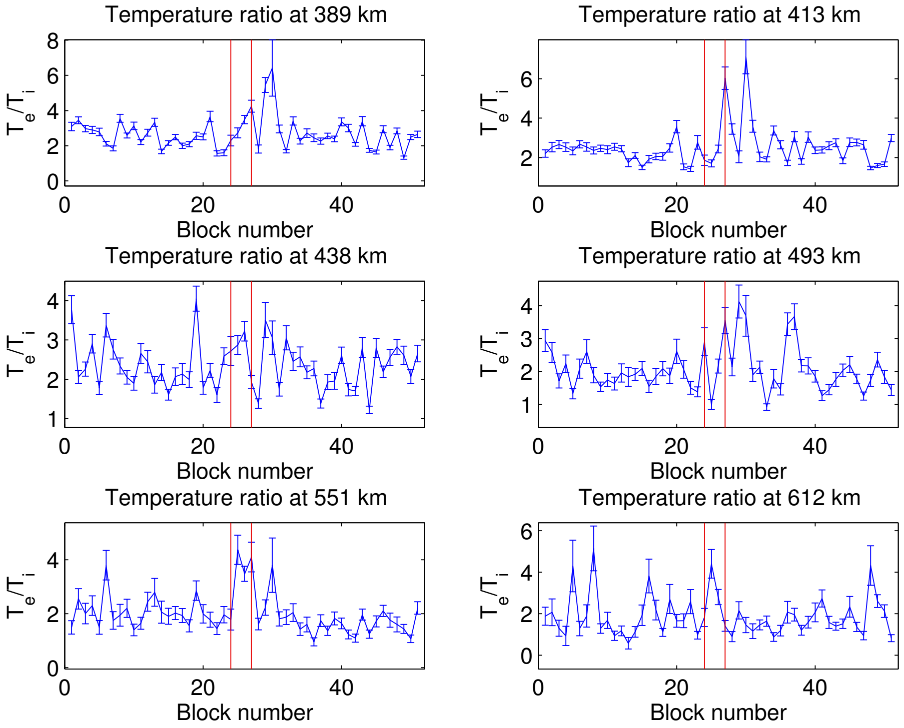

(b) Temperature ratio

Figure 5.2.6.: Electron and ion temperatures (a) and temperature ratio (b) during the two NEIAL events occurring between 0623:12 and 0623:30 UT and between 0626:43 and 06:26:49 UT on 31 March 2005. The red lines (blocks 24 and 27) indicate the NEIAL occurrence. Dumps containing NEIALs are removed from the analysis. The time interval shown is 0600-0659 UT. Integration time is 60 s.

5.2.2. Case 2: 22 May 2004

On 22 May 2004 we found many NEIAL events in the interval 0600-1230 UT. We found 55 dumps containing NEIALs out of a total of 3937. In addition, we found 3 dumps showing very weak enhancements, hence it was difficult to classify them as NEIAL events. We observed two different types of NEIAL: one associated with high ion temperatures at low altitude, the other without any enhancement in the ion temperature. In addition, both of them did not show any clear enhancement in the E region electron density, as opposed to the case discussed in sec. 5.2.1 (see Fig. 5.2.4). Fig. 5.2.7 shows ionospheric parameters for the interval 0600-1230 UT. It is possible to clearly see the four regions with enhancements in the ion temperature between 0630 and 0900 UT. Interestingly, all of them show a good correlation with both the ion velocity and the electron temperature enhancements. After 1000 UT, we found two NEIAL events with the enhancement occurring only in the electron temperature, as it is usually the case. Fig. 5.2.8 shows the same ionospheric parameters of Fig. 5.2.7, with the addition of ion flux, temperature ratio and NEIAL events.

For this case, we are going to compare results obtained at high altitude (topside ionosphere) and low altitude (E region). Fig. 5.2.9 shows the electron density; in this case we see a weak enhancement in the electron density at high altitudes, which is not corresponded by a similar trend in the E region. Hence there was no hard particle precipitation, but only soft particle precipitation around 400 km. Note that the behavior is the same both for the NEIAL events associated with an enhancement in the ion temperature and for the NEIAL events where only the electron temperature was enhanced.

We then looked at the temperatures. As shown in Fig. 5.2.10 (top panel), at high altitudes, the electron temperature is always slightly enhanced in correspondence with NEIAL events, while the ion temperature is weakly enhanced only for the events occurring both before 0900 UT (which correspond to the events at the left of block 100 in figure Fig. 5.2.10) and below 600 km altitude. However, as we mentioned, in the upper E region the temperatures show some peculiarity (see bottom panel of Fig. 5.2.10): several enhancements in the ion temperatures occurring together with the NEIAL events before block 100; the ion temperature enhancements gets as high as 3000 K, while the average ion temperature in E region is usually about 1000 K. The electron temperature, on the other hand, did not show any appreciable enhancement.

After this general analysis, we investigated in more detail two NEIAL events, one occurring at 0738:49 UT and belonging to the group where the ion temperature at low altitude was enhanced; the other occurring between 1023:05 and 1023:12 UT and belonging to the group where no enhancement in the ion temperature was observed. We chose them because they were the most powerful of each group.

As Fig. 5.2.11 shows, this event was not preceded by any build-up, but suddenly appeared with both lines enhanced between 300 and 600 km and the downshifted line enhanced more than the upshifted one. We found that the ion velocity (Fig. 5.2.12, top panel) was not very high before the NEIAL event. Furthermore, it gets positive only above 400 km altitude, while the ion acoustic lines are significantly enhanced already at 300 km (as it clearly shows the power profile in Fig. 5.2.11). This is surprising, since we expect that NEIALs are embedded in the outflow, and this seems not really to be the case. However, we must take into account the fact that we are actually analyzing the ionosphere 128 s before the NEIAL event and this can be problematic, as we explained in the introduction of this chapter. The bottom panel of Fig. 5.2.12 shows information about the temperatures. Again we did not find anything special about them and the temperature ratio is even less than 3 at every altitude (and we know that a higher temperature ratio lowers the threshold for the onset of the instabilities). This event, however, has a property that we can turn to be an advantage: it lasts less than 6.4 seconds, i.e. only one dump. This means that we can try to center our integration period on the event, instead of looking at what happened just before (the dump containing the NEIAL will of course be removed from the analysis). The results regarding ion velocity and temperatures are shown in Fig. 5.2.13, where we used a 64 s integration time and we had to remove values above 500 km altitude due to very large errors. The situation does not change a lot. We still have relative low ion velocities and low temperature ratios. It is interesting to note, however, that the ion velocity becomes positive around 300 km altitude, which is 100 km lower than the preceding analysis and closer to the NEIAL starting altitude. We believe that with a smaller integration time they would show a better agreement.

We can now point our attention to the event which occurred between 1023:05 and 1023:12 UT. Looking at the spectra in Fig. 5.2.14, we see that the NEIAL grew up fast and reached a high power at 1023:12 UT. Fig. 5.2.14b shows a low altitude NEIAL around 150 km, similar to other cases already reported by *Rietveld et al.* (1991) and *Ogawa et al.* (2011). From our study, it seems that they appear only when very powerful events take place and the upshifted line is usually more enhanced. However, since our work is not statistical, we do not dare to draw definitive conclusions on this subject. As a matter of fact, statistical studies, conducted by e.g. *Ogawa et al.* (2011), showed that only half of the NEIALs occurring in the E region were accompanied by ion acoustic enhancements in the F region.

The ion velocity (Fig. 5.2.15, top panel) was not strongly enhanced, but the NEIAL is totally embedded into it, except for the enhanced upshifted line in the upper E region. However, looking at the spectra shown in Fig. 5.2.14, we see that there is an evident variation in NEIAL morphology in just 6.4 s. This poses a serious concern when we need to decide where the NEIAL started: is it starting at around 500 km like it seems to suggest the enhanced downshifted line in Fig. 5.2.14a, or is it starting at 400 km as shown by the enhanced upshifted line in Fig. 5.2.14b? When we encountered such a situation (quite often, actually) we took as the starting altitude the one corresponding to the most enhanced line in the most powerful spectrum, which, in this case, is 400 km. However, when NEIAL events last for tens of seconds, with quick changes in consecutive spectra, it is not so easy to set a definite starting altitude.

The ion and electron temperature altitude profiles together with the temperature ratio T_e/T_i for the event occurring between 1023:05 and 1023:12 UT are shown in the bottom panel of Fig. 5.2.15. While there is not anything special at high altitudes, we got two very important results about the NEIAL occurring in the upper E region:

1. The NEIAL occurred *together* with the type-II outflow, but it is not *embedded* into it.
2. The temperature ratio is *lower* than 1 at the altitude where the NEIAL event occurred.

The two above points were never satisfied for the NEIAL events occurring above 300 km.

This lead us to think that it is not so easy to discard the idea that two different mechanisms can generate the low altitude and the high altitude NEIALs.

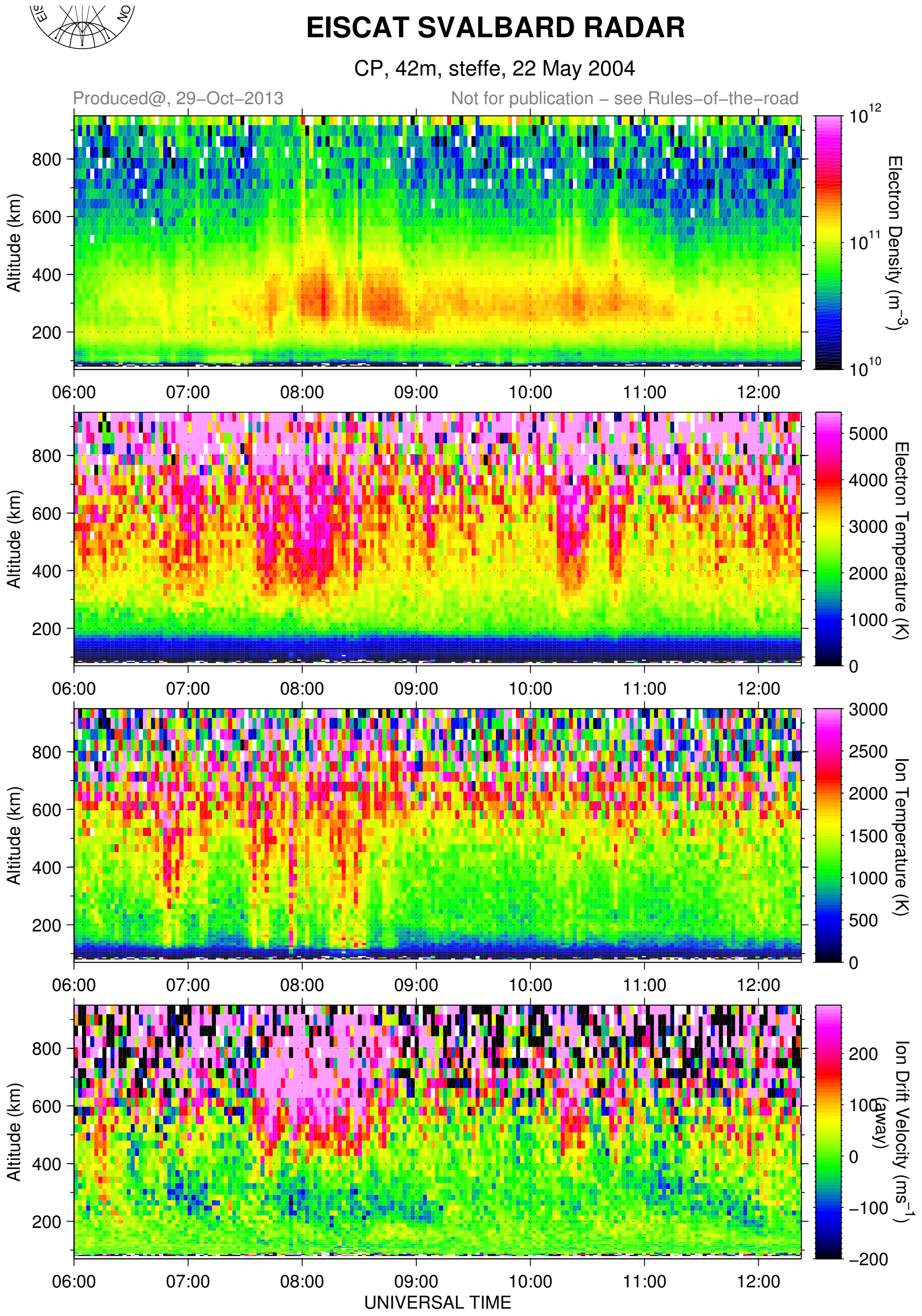

Figure 5.2.7.: Color plot showing electron density, electron temperature, ion temperature, ion velocity for the events observed on 22 May 2004 for the time interval 0600-1230 UT. We used a 128 s integration time.

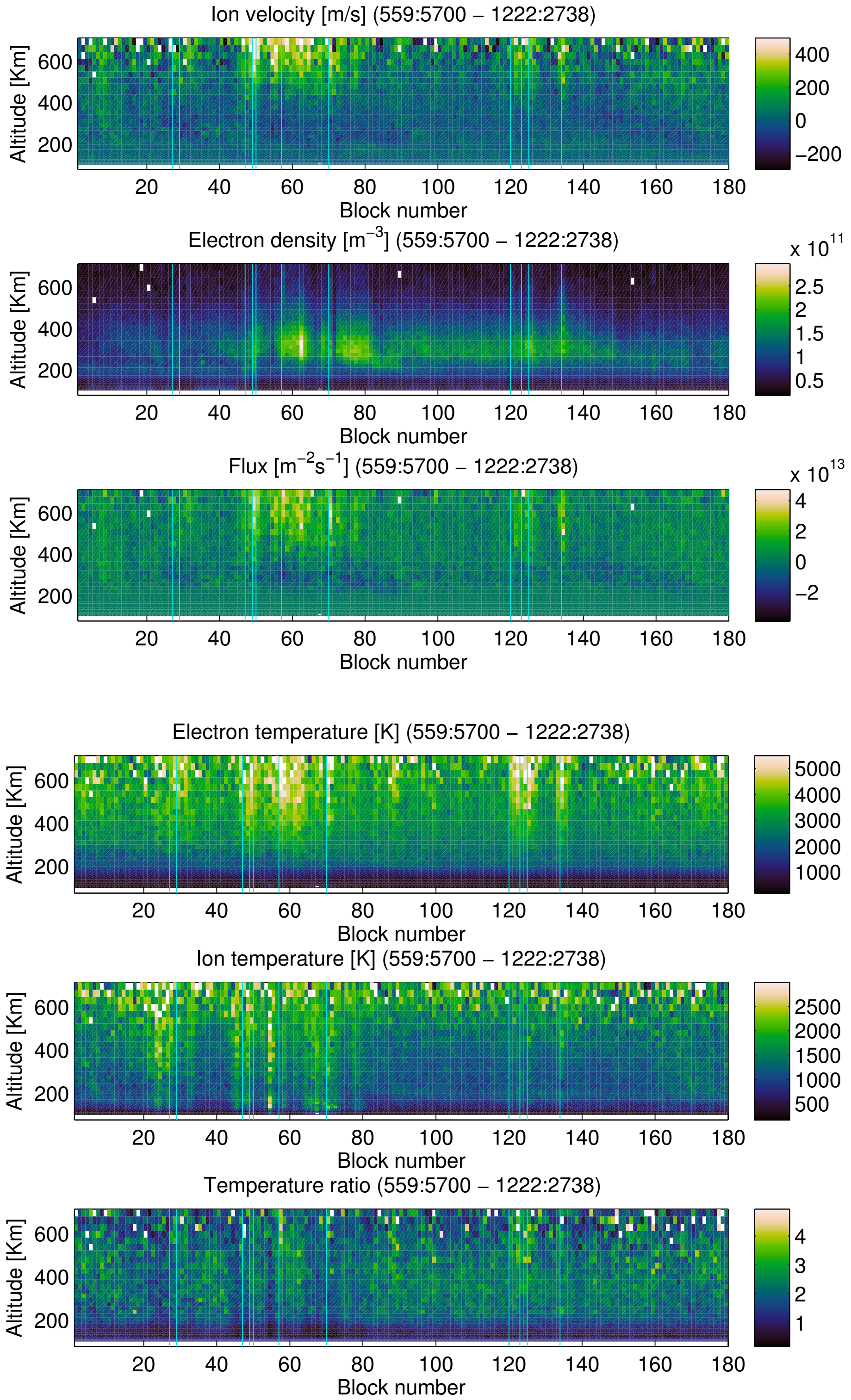

Figure 5.2.8.: Color plot showing ion velocity, electron density, flux, electron temperature, ion temperature, temperature ratio for the events observed on 22 May 2004 for the time interval 0600-1230 UT. Teal lines represent NEIAL events. We used a 128 s integration time.

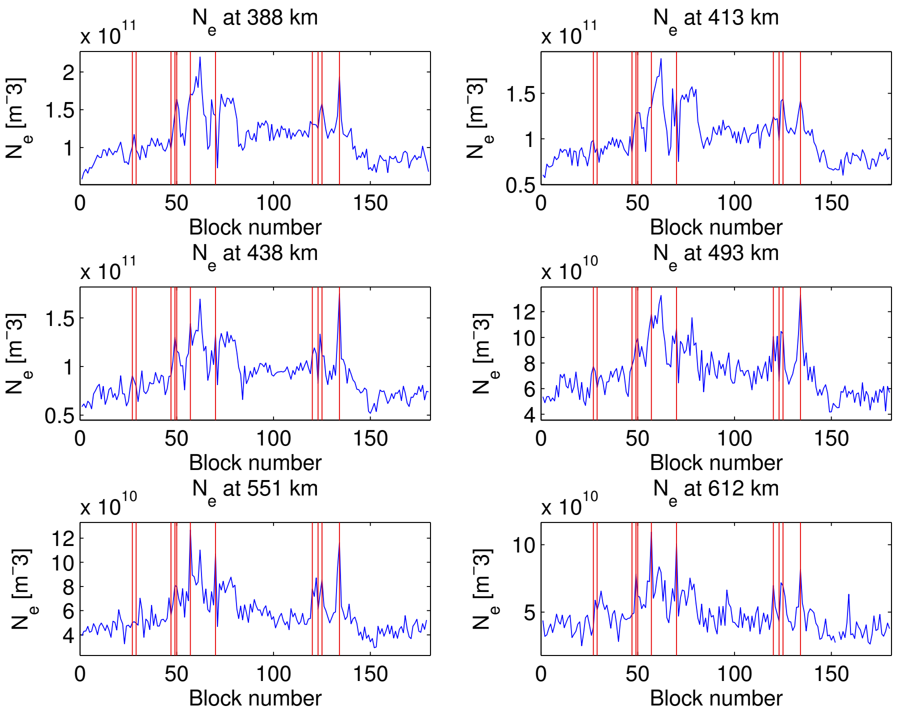

(a) Electron density (between 388 and 612 km)

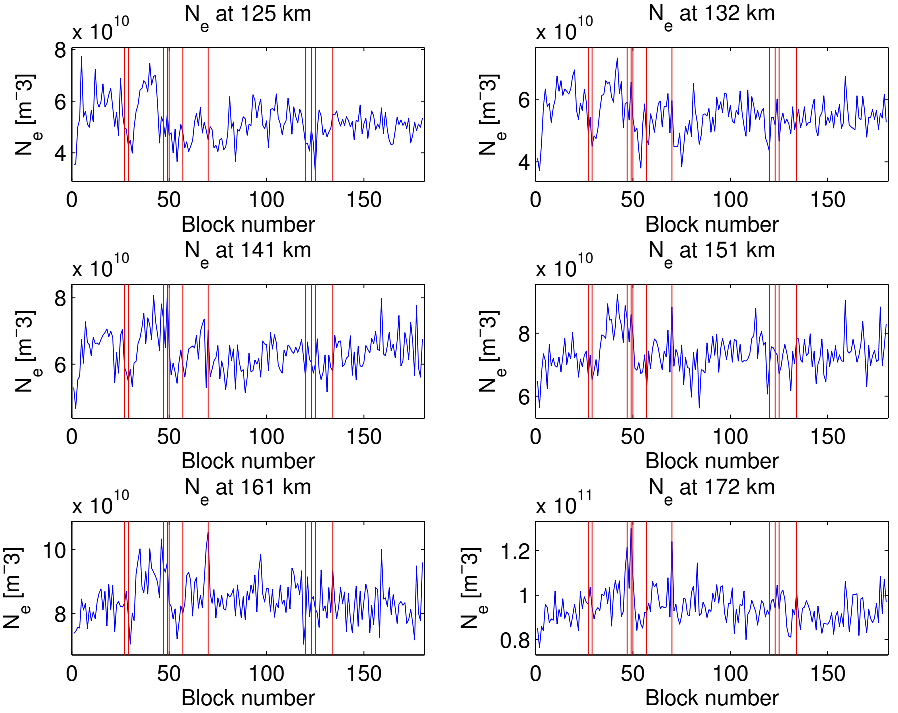

(b) Electron density (between 125 and 172 km)

Figure 5.2.9.: Electron density at high altitude (a) and in the E region (b) during several NEIAL events (indicated by red lines) occurring on 22 May 2004. Dumps containing NEIALs are removed from the analysis. The time interval shown is 0600-1230 UT. Integration time is 128 s. For better readability the error bars are not shown in this figure, but we removed all the values with errors larger than 50%.

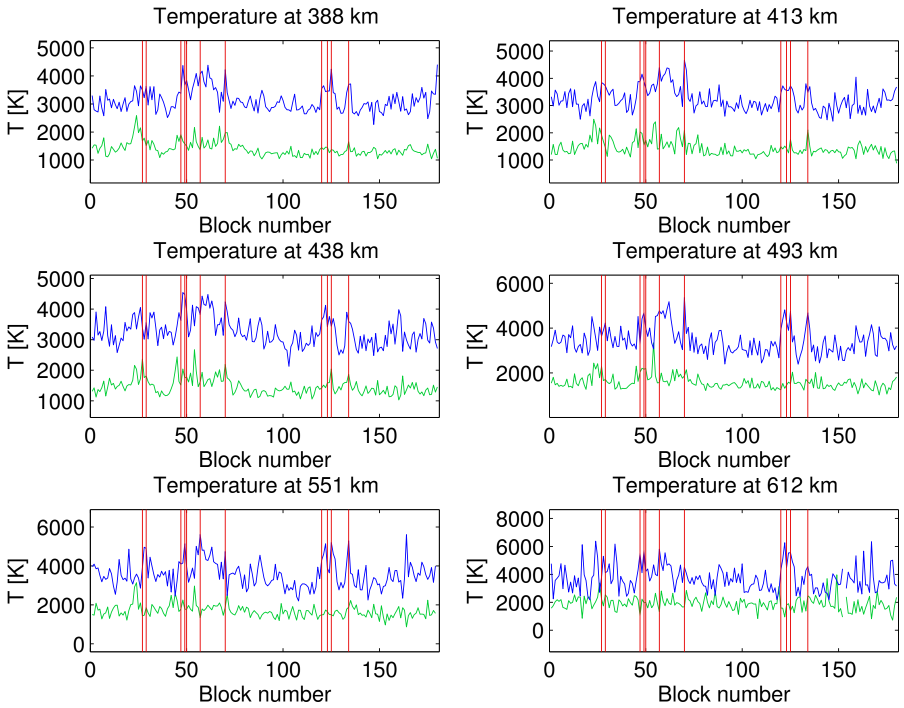

(a) Temperature (between 388 and 612 km)

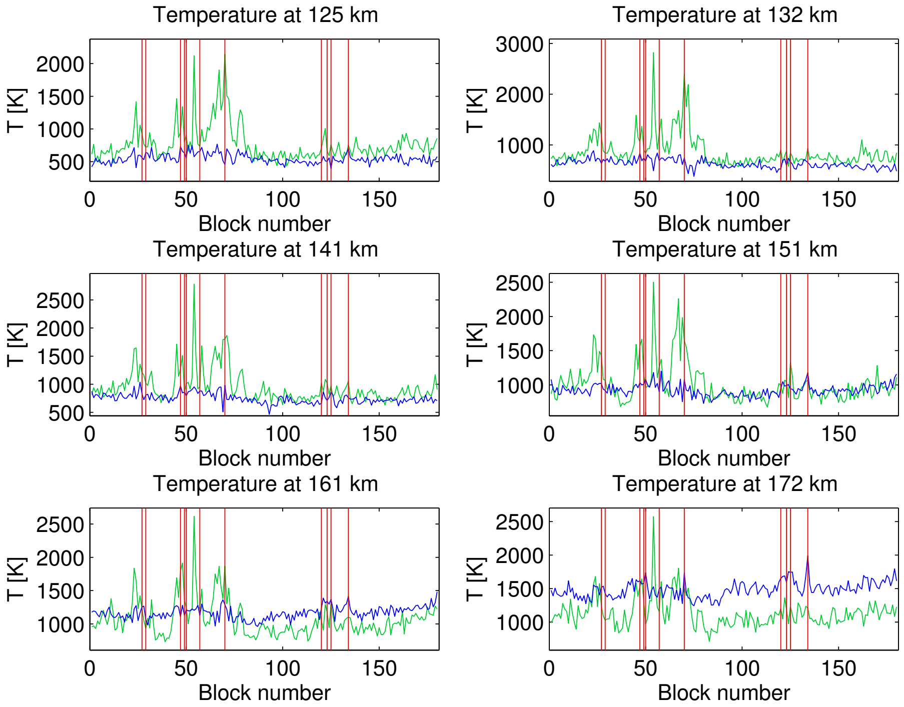

(b) Temperature (between 388 and 612 km)

Figure 5.2.10.: Electron (blue) and ion (green) temperature at high altitude (a) and in the E region (b) during several NEIAL events (indicated by red lines) occurring on 22 May 2004. Dumps containing NEIALs are removed from the analysis. The time interval shown is 0600-1230 UT. Integration time is 128 s. For better readability the error bars are not shown in this figure, but we removed all the values with errors larger than 50%.

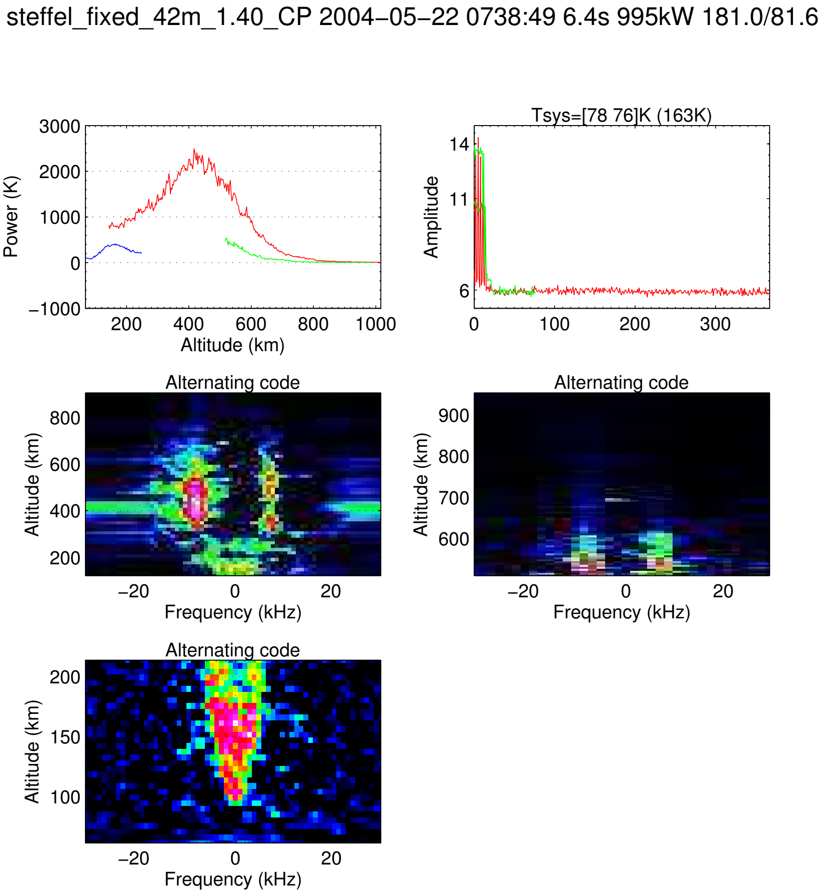

Figure 5.2.11.: Spectra of the NEIAL event occurring at 0738:49 UT on 22 May 2004.

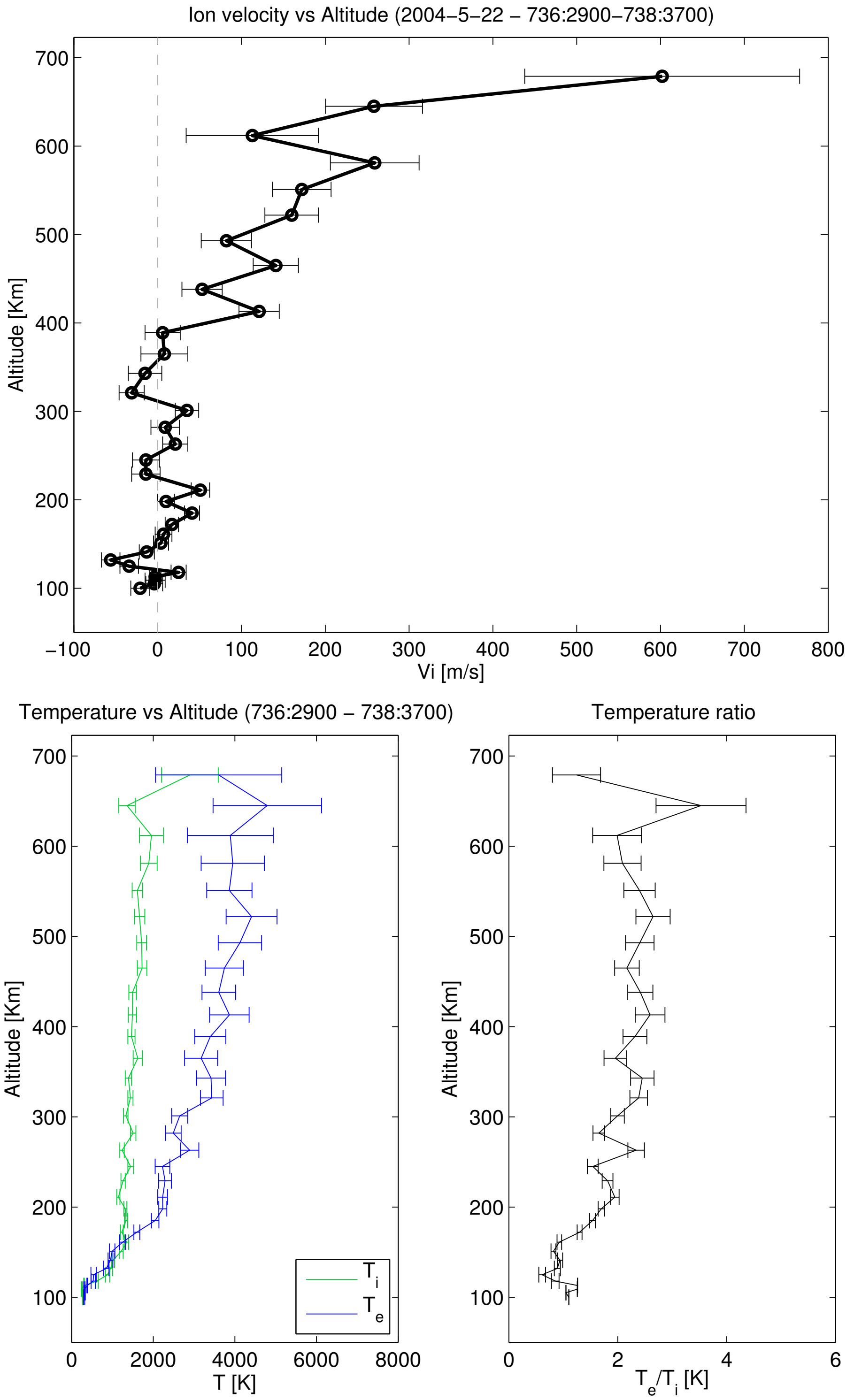

Figure 5.2.12.: Some ionospheric parameters evaluated with 128 s integration before the NEIAL event occurring at 0738:49 UT on 22 May 2004. (Top panel) Ion velocity; (Bottom panel, left) Electron and ion temperatures; (Bottom panel, right) Temperature ratio T_e/T_i.

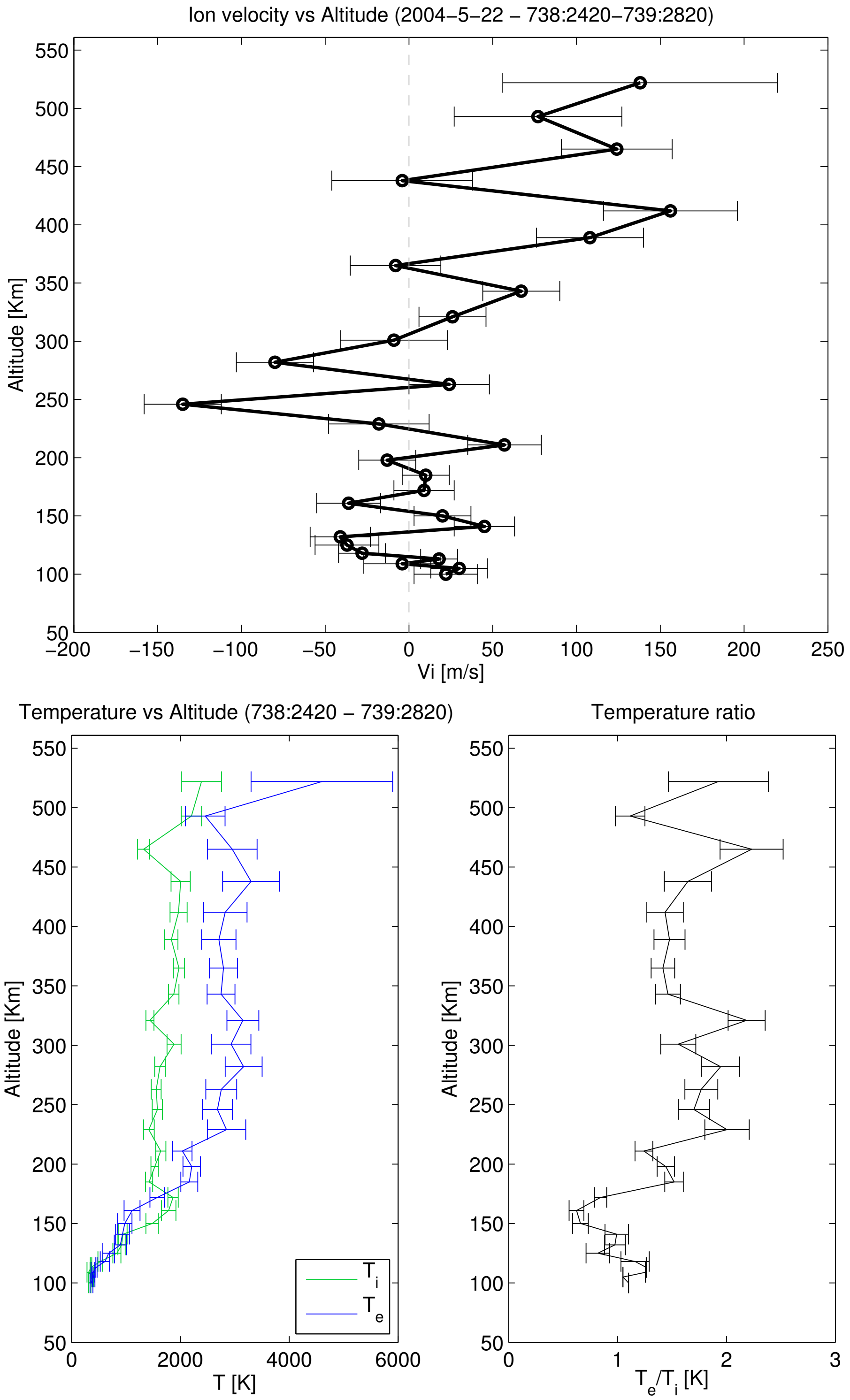
Ion velocity vs Altitude (2004−5−22 − 738:2420−739:2820)

Temperature vs Altitude (738:2420 − 739:2820)

Temperature ratio

Figure 5.2.13.: Some ionospheric parameters evaluated with 64 s centered on the NEIAL event occurring at 0738:49 UT on 22 May 2004. (Top panel) Ion velocity; (Bottom panel, left) Electron and ion temperatures; (Bottom panel, right) Temperature ratio T_e/T_i.

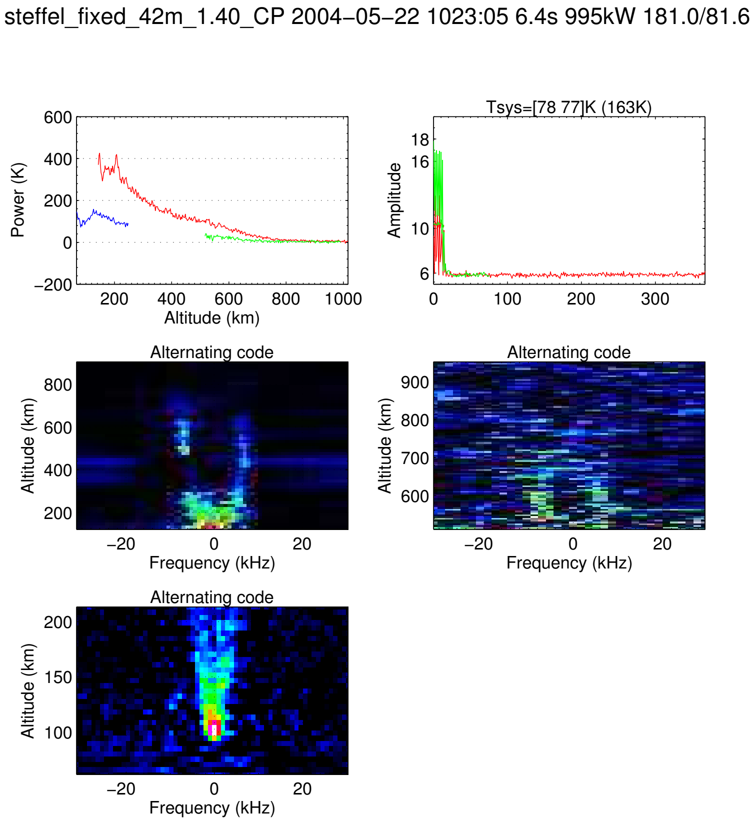

(a) 1023:05

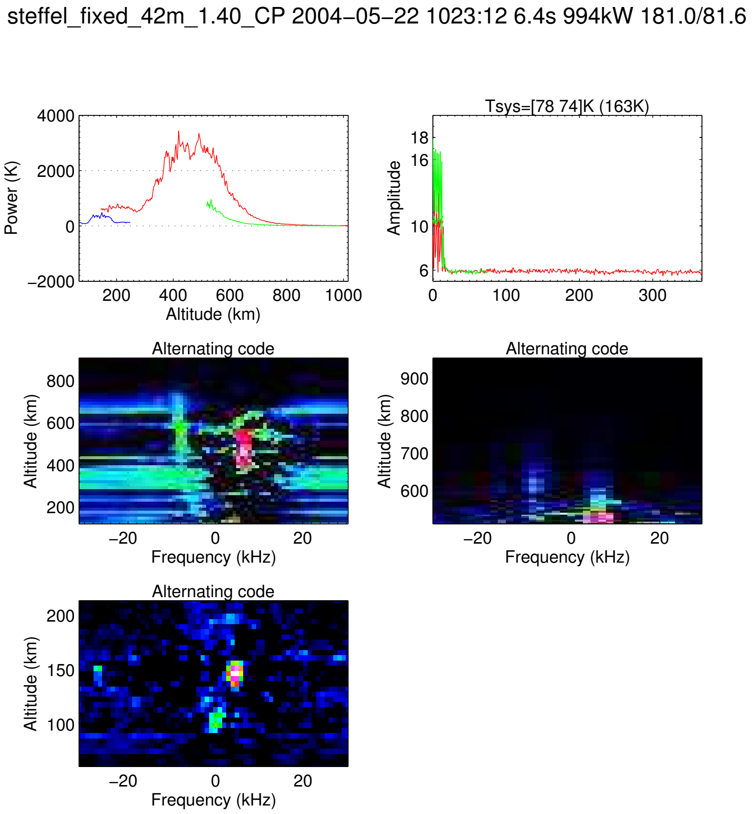

(b) 1023:12

Figure 5.2.14.: Spectra of the NEIAL event occurring between 1023:05 and 1023:12 UT on 22 May 2004.

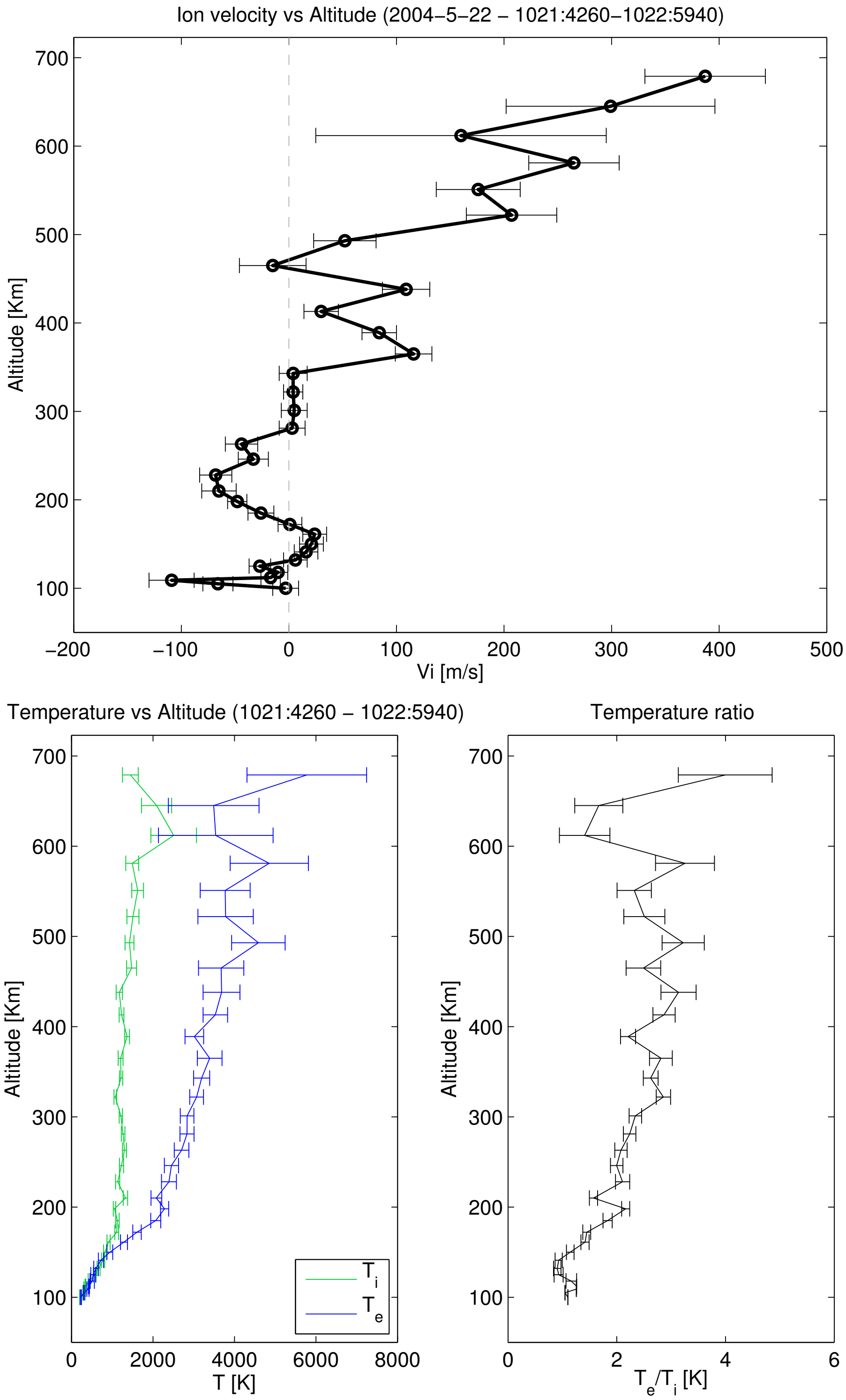
Ion velocity vs Altitude (2004−5−22 − 1021:4260−1022:5940)

Temperature vs Altitude (1021:4260 − 1022:5940)

Temperature ratio

Figure 5.2.15.: Some ionospheric parameters evaluated with 128 s integration before for the NEIAL event occurring between 1023:05 and 1023:12 UT on 22 May 2004. (Top panel) Ion velocity; (Bottom panel, left) Electron and ion temperatures; (Bottom panel, right) Temperature ratio T_e/T_i.

5.3. Results: Part 2 - The *Steffe CP-2* experiment

The steffe CP-2 is a multiposition experiment run at the ESR (EISCAT Svalbard Radar). The ESR runs the steffe CP-2 experiment with the 42m dish antenna field aligned and the 32m dish moving through 3 different positions. We analyzed only the 42m, since it is field aligned and more interesting for this work. However, as we mentioned in sec. 5.1, the 42m antenna was on for a minute and off for the successive one. Hence we had to pick carefully the events we wish to analyze in order to avoid NEIAL events overlapping on an on-off boundary.

5.3.1. Case 1: 9 June 2004

On 9 June 2004 (Fig. 5.3.1) we observed outflows in the intervals: 0800-1000 UT, 1200-1300 UT, 1600-1800 UT. We found NEIALs during each of them, specifically:

Time	*0800-0859*	*0900-0959*	*1200-1259*	*2000-2059*
	0820:03	**0911:21 - 0911:28**	1236:16	2033:42 - 2033:48
	0849:48 - 0850:08	0912:38	1246:49	2035:31
		0921:10	1246:56	
		0927:34		
		0929:55 - 0930:08		

Table 5.1.: All NEIAL events occurring in the specified time intervals. The bold intervals are events which were discussed here.

We got 20 data dumps containing NEIALs out of a total of 1693.

We analyzed the NEIAL event occurring between 0911:21 and 0911:28 UT, whose spectrum is shown in Fig. 5.3.2. The event started at about 350 km altitude. We have both lines enhanced, with the downshifted line enhanced from 350 km to more than 800 km and with the upshifted line strongly enhanced around 500 km in the first dump (a), while in the successive dump (b) the upshifted line was always weaker than the downshifted one.

The first panel in Fig. 5.3.3 shows the field aligned ion velocity. We found a positive velocity already at 350 km and above 400 km we saw a constant, sustained acceleration. We conclude that in this case the two events are related and that the NEIAL starts at the same altitude as the outflow.

We analyzed also the electron and ion temperatures altitude profiles (Fig. 5.3.3). It is interesting to look at the temperature ratio, which never exceeded the value of 3. This value is usually considered the threshold for the onset of the ion-ion instability, and a high temperature ratio is thought to be a facilitating condition for the onset of the other instabilities as well. It is probable that the higher temperature ratio was smoothed out by the long integration time. We plotted the electron density variation as a function of time (Fig. 5.3.4, panel (a)), to see if we could find any signature of the NEIAL event during the period preceding it. We plotted also ion velocity, electron temperature, ion temperature and temperature ratio (Fig. 5.3.5) to search for any useful information. We compared 6 altitudes and we could not find any strong evidence for the subsequent onset of a NEIAL event.

We found however an interesting feature regarding the temperature; the electron and ion temperature time profile shows a surprising anti-correlation, which is clearly visible e.g. at 612 km altitude in Fig. 5.3.5. This is not an isolated case, but we could not find any distinctive or recurring physical background where this anti-correlation occurs. It is difficult to imagine a physical mechanisms acting in such a way to heat the ions and cool the electrons (or vice versa) in a relatively short time scale of some tens of seconds. We believe we can exclude coding error, since all it is needed to get the electron temperature is to multiply the ion temperature by the temperature ratio, and both these parameters are given by the incoherent scatter analysis. In section sec. 5.4 we propose a possible explanation for this issue.

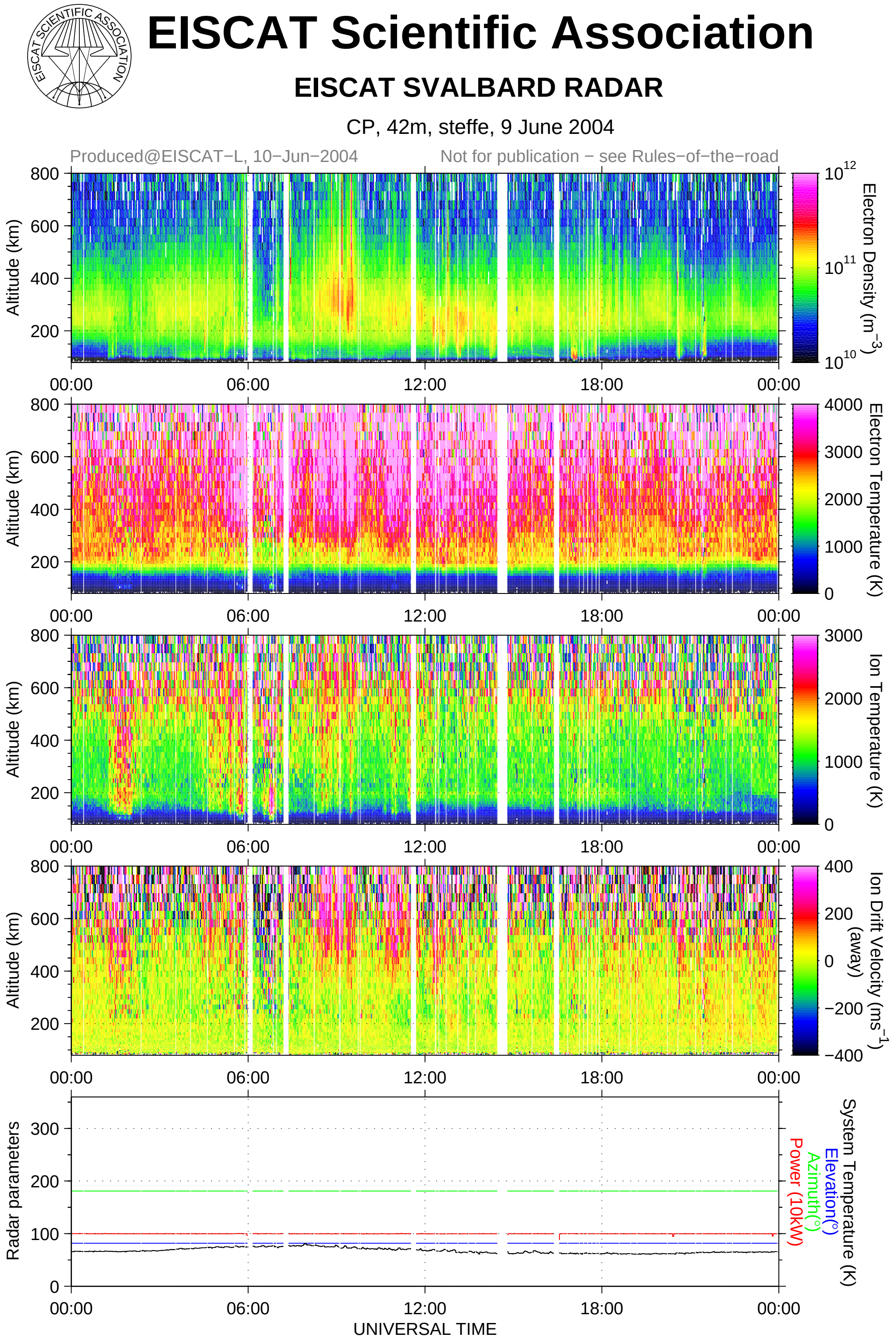

Figure 5.3.1.: Color plot showing electron density, electron temperature, ion temperature, ion velocity for the events observed on 9 June 2004. We analyzed the intervals 0800-1000 UT, 1200-1300 UT, 1600-1800 UT, [from *EISCAT Scientific Association*, 2013]

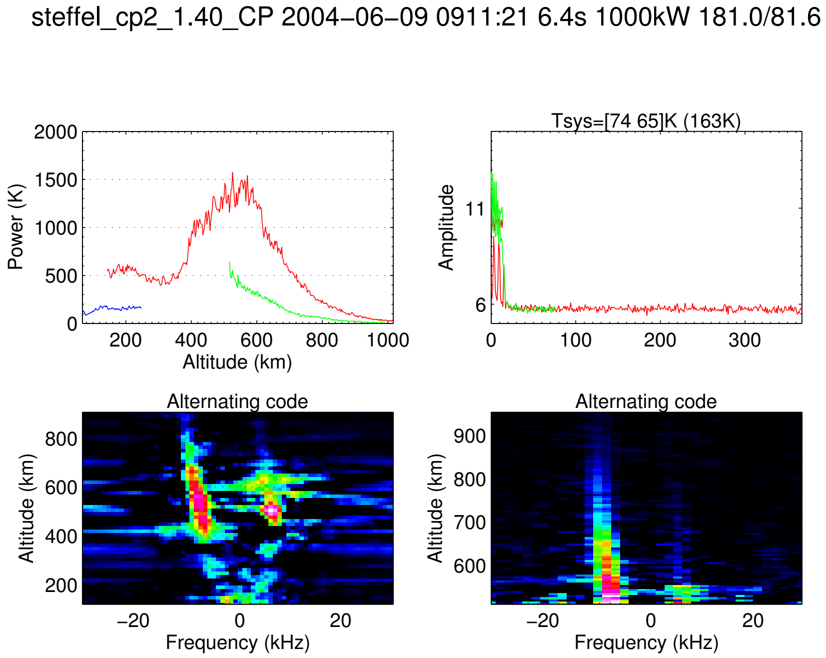

(a) 0911:21

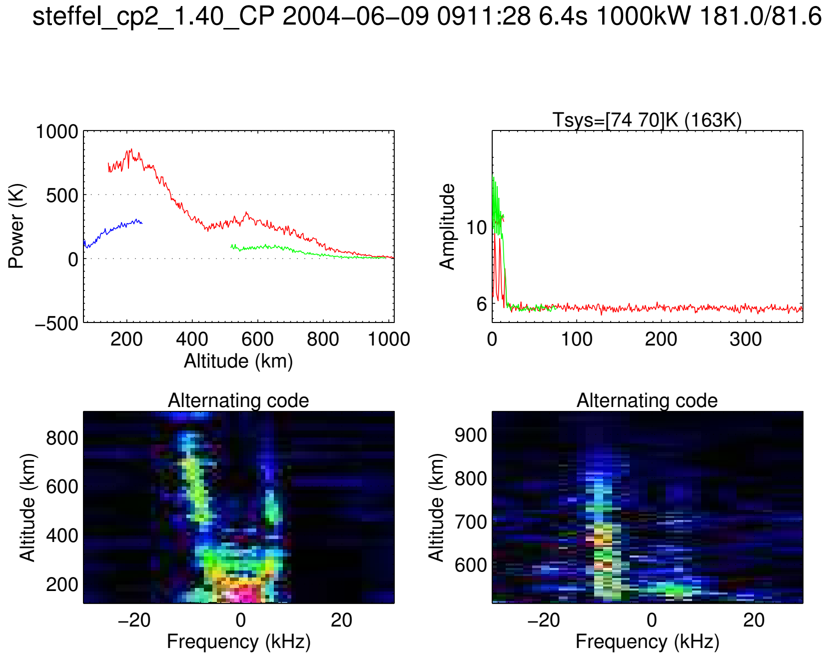

(b) 0911:28

Figure 5.3.2.: Spectra of the NEIAL event occurring between 0911:21 and 911:28 UT on June 2004.

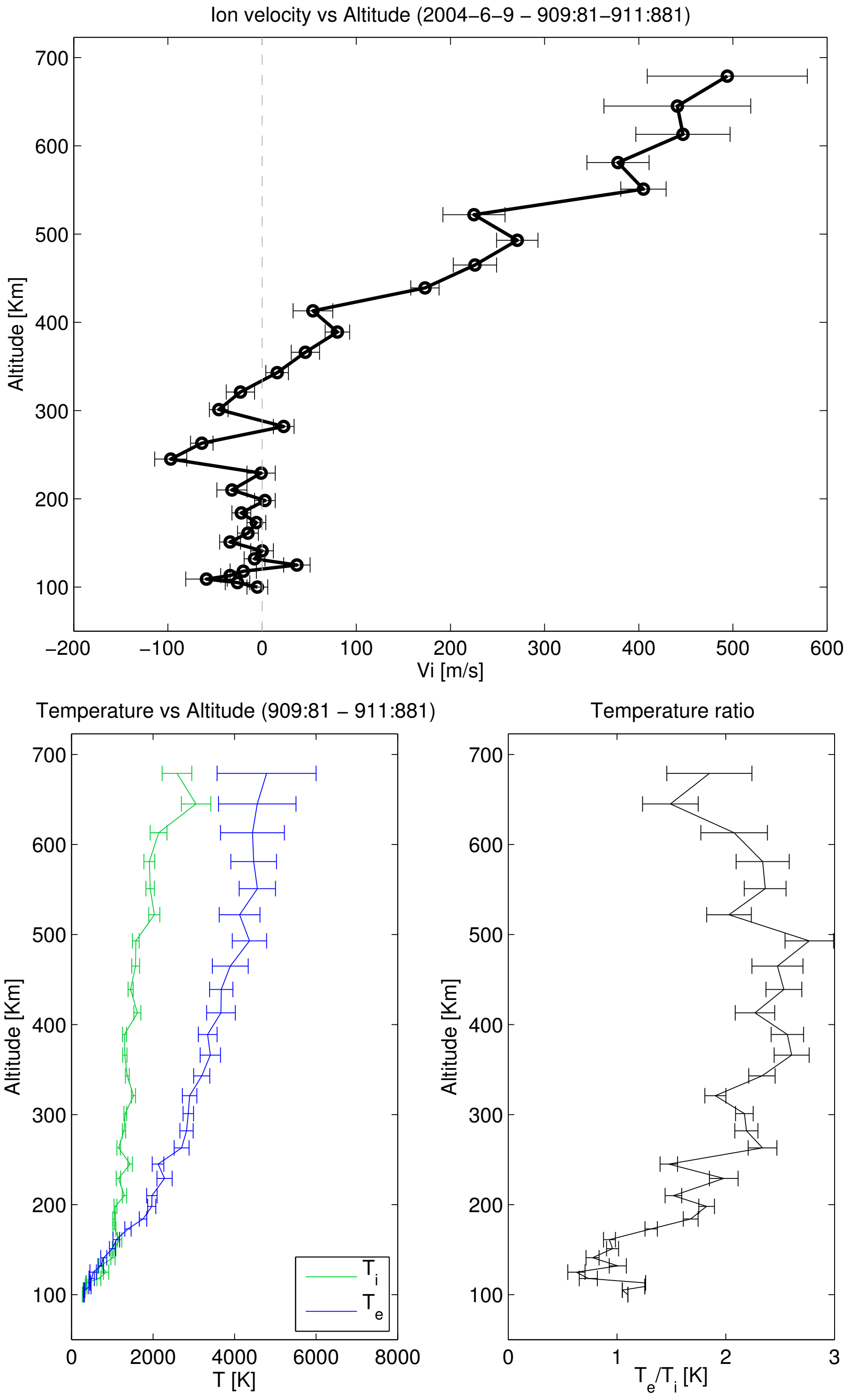

Figure 5.3.3.: Some ionospheric parameters evaluated with 120 s integration between 0909:00 and 0911:08 UT on 9 June, 2004. (Top panel) Ion velocity; (Bottom panel, left) Electron and ion temperatures; (Bottom panel, right) Temperature ratio T_e/T_i.

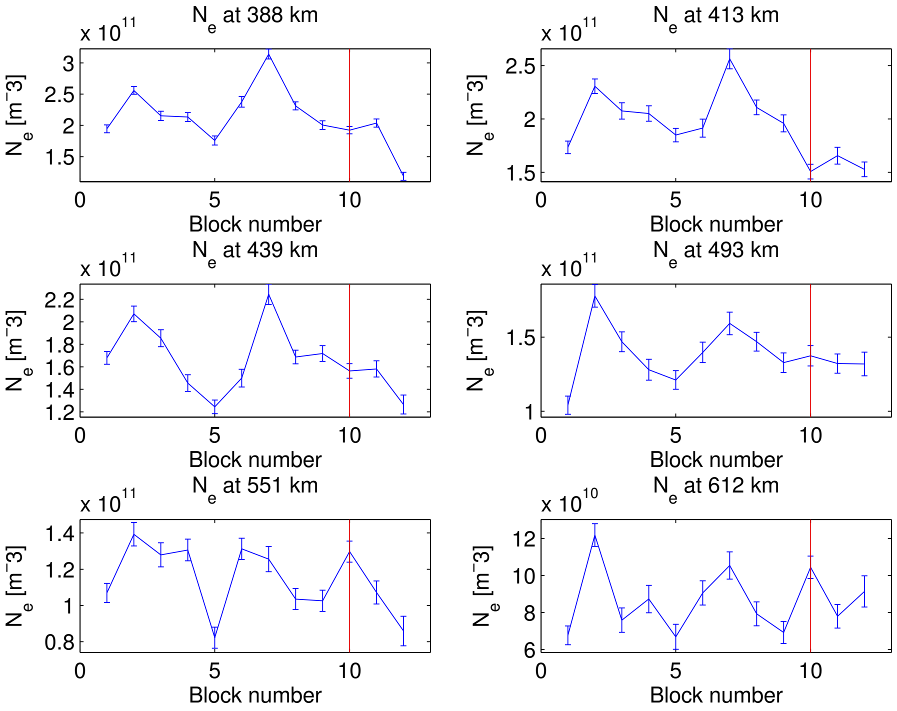

(a) Electron density

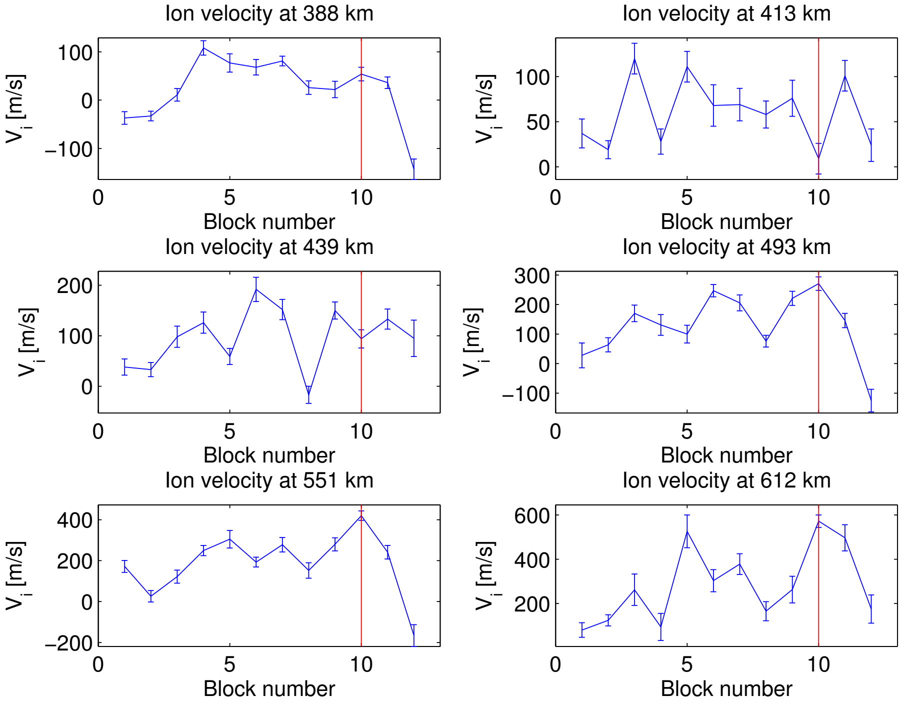

(b) Ion velocity

Figure 5.3.4.: Electron density (a) and ion velocity (b) during the NEIAL event at 0911:28 UT on 9 June 2004. The red line indicates the NEIAL occurrence. Dumps containing NEIALs are removed from the analysis.

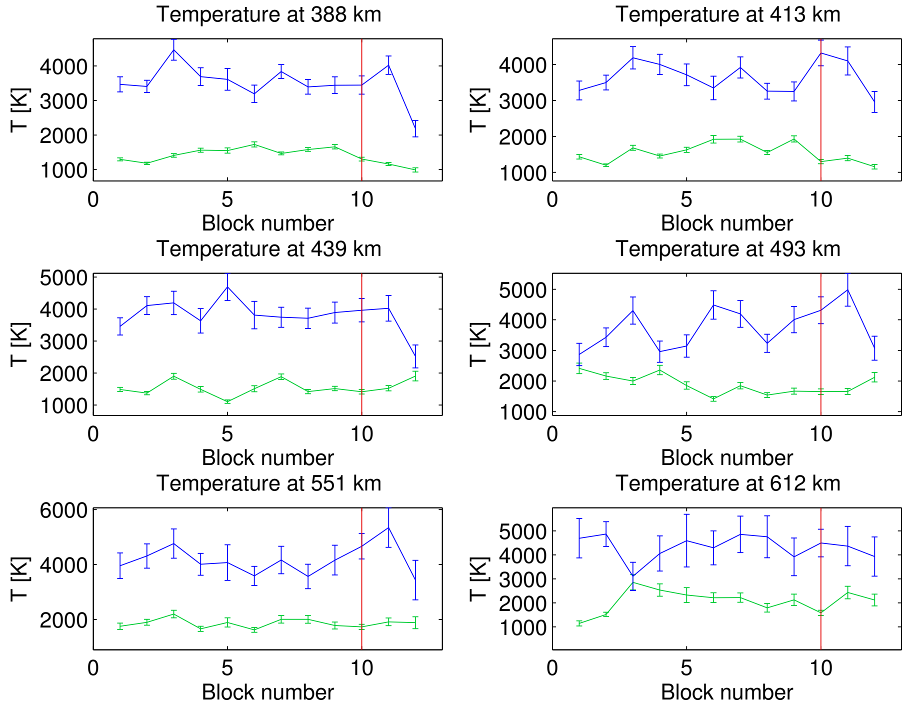

(a) Electron and ion temperature

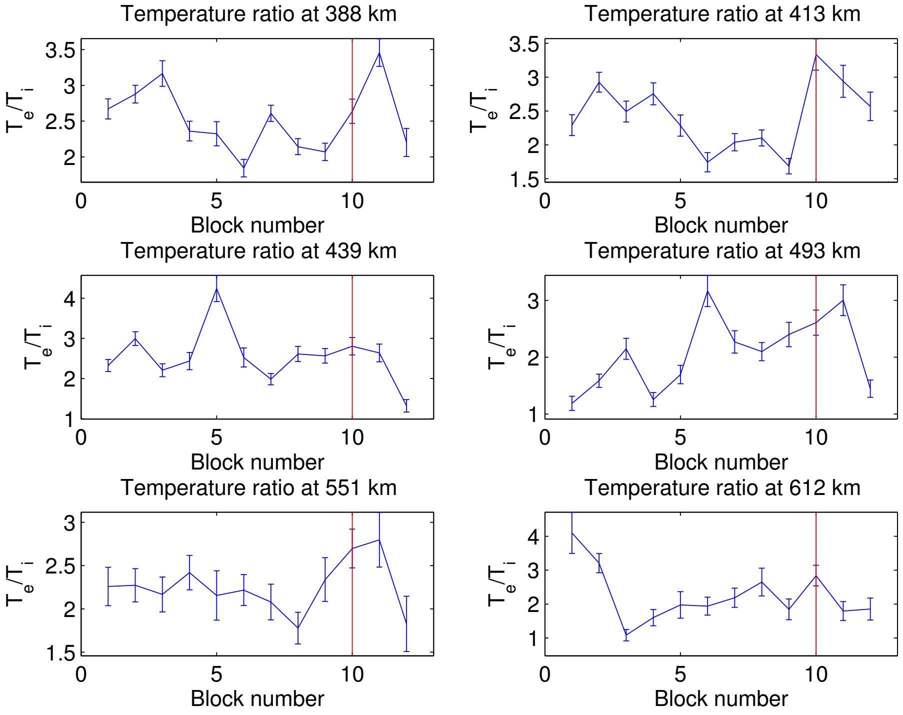

(b) Temperature ratio

Figure 5.3.5.: Electron and ion temperatures (a) and temperature ratio (b) during the NEIAL event at 0911:28 UT on 9 June 2004. Electron temperature is in blue, ion temperature is in green. The red line indicates the NEIAL occurrence. Dumps containing NEIALs are removed from the analysis.

5.3.2. Case 2: 16 June 2005

On 16 June 2005 we observed outflows in the interval 0900-1400 UT, and we found NEIAL events. We also analyzed the interval 1800-2200 UT (where no outflow was present) in order to check if NEIALs could occur without ion outflow. We did not find any NEIAL event in this 4 hours interval, which of course does not mean that NEIALs could not occur without ion outflow. However, there is no clear observation of NEIAL events not associated with ion outflow, and our short 4 hour analysis is in agreement with this.

In the following table we summarize the NEIAL events.

Time	*0900-0959*	*1000-1059*	*1100-1159*
	0940:13-0940:19		1149:36
	0944:04 - 0944:10		1150:27

Time	*1200-1259*	*1300-1359*
	1202:50	**1259:54-1300:52**
	1238:34-1238:47	1302:02-1302:37
		1302:40-1302:59
		1304:29-1304:55

Table 5.2.: All NEIAL events occurring in the specified time intervals. The bold intervals are events which were discussed here.

Fig. 5.3.6 shows only the interval 0900-1400 UT, which presents some interesting features:

- Two clear outflow events (one around 0930 UT and the other after 1200 UT) separated by a downflow event occurring in the time interval between the two upflows. The data were too noisy to perform a reliable analysis of the parameters during the downflow, however we checked for NEIALs event and we did not find any.
- The electron temperature is enhanced in the 0900-1400 UT interval, which is compatible with a type-II ion outflow scenario, except for the very low altitude enhancements around 100 km altitude, corresponding perhaps to an energetic particle precipitation. But it is the ion temperature profile which is unusual in this period, since it is strongly enhanced especially between 100 and 200 km altitude. We still regarded the ion outflow events as type-II, albeit the ion temperature profile does not appear to be unaffected as *Wahlund et al.* (1992b) suggested.
- The NEIAL events seem to occur preferably at the edge of the structure. We found NEIALs in the middle hours of the 0900-1400 UT time interval, however, the most enhanced ion acoustic lines were found around 0940 UT, 1230 UT and 1300 UT. Especially the NEIAL event lasting from 1259:54 until 1300:52 UT was one of the longest we ever observed. In addition, as reported in the table above, the time interval 1259:54-1306:50 UT was rich of dumps containing NEIALs: 26 out of 36.

We analyzed a total of 2528 dumps and we found that 36 of them contained NEIALs.

First we analyzed the event occurring between 0940:13 and 0940:19 UT, whose spectra are shown in Fig. 5.3.7. It has a very interesting feature: at 413 km altitude the temperature ratio T_e/T_i is less than 1, which means that it is difficult to consider the NEIAL event accompanied by a pure type-II ion outflow, although at all other altitude ranges the temperature ratio is always larger than unity. This feature is evident in Fig. 5.3.8. Albeit it is tempting to relate this event to a type-I ion outflow (or to a hypothetically type-III ion outflow, which could be defined as an outflow where both the electron and ion temperatures are enhanced), we must consider two aspects:

1. the temperature ratio is always larger than one, except at the mentioned altitude of 413 km, as it is shown in Fig. 5.3.8
2. the unusual and large enhancement in the ion temperature is predominant at lower altitudes (100-200 km, see Fig. 5.3.6), where we did not find neither NEIALs nor outflows.

Therefore we tend to discard this ion outflow as a type-I and rather consider it as a special case of a type-II.

We also tried to analyze the event occurring between 1259:54 and 1300:52 UT. Unfortunately, the data were not good enough to get reliable results. It is however interesting to look at the spectra of this event. They are shown in Fig. 5.3.11. From this sequence it seems that there is not a gradual increase in power until a maximum, followed by a decrease. What we observe here is a sort of “flaming”, where the intensity of the NEIAL events varies almost randomly.

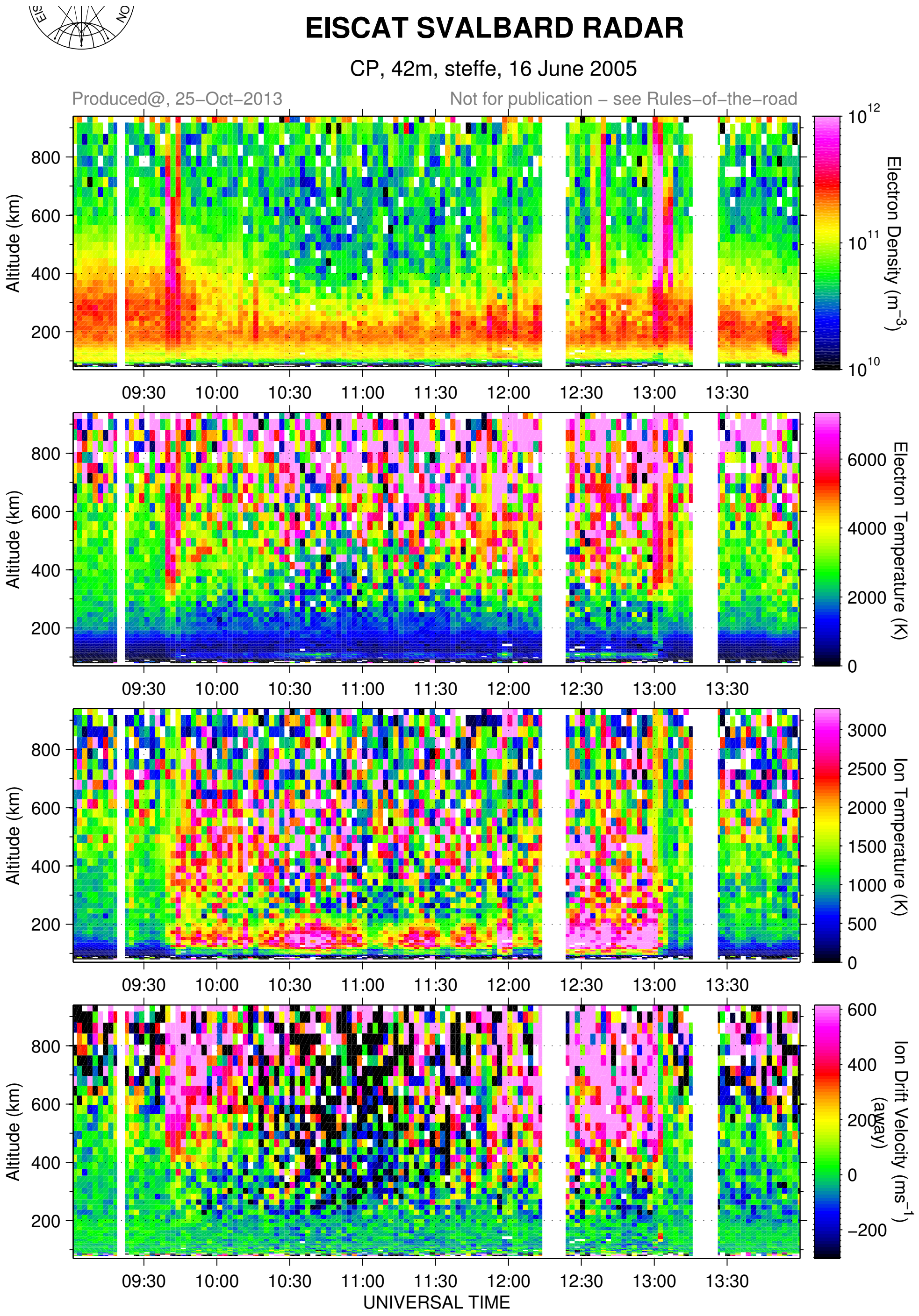

Figure 5.3.6.: Color plot showing electron density, electron temperature, ion temperature, ion velocity for the events observed on 16 June 2005, between 0900 and 1400 UT. We used a 128 s post-integration. Note that for this figure we did not remove the dumps containing NEIALs. However, we removed them afterward in order to carry out the analysis.

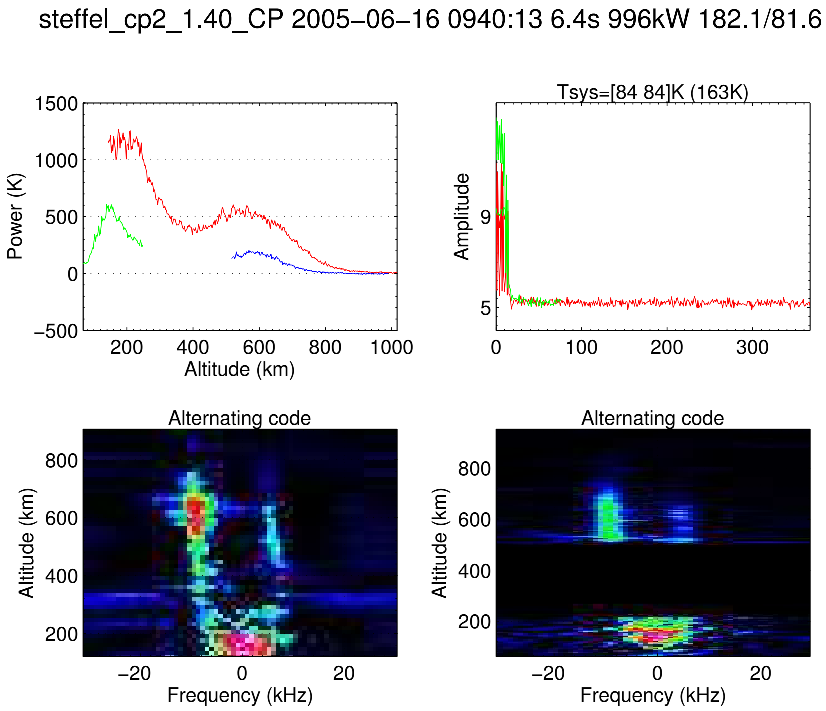

(a) 0940:13

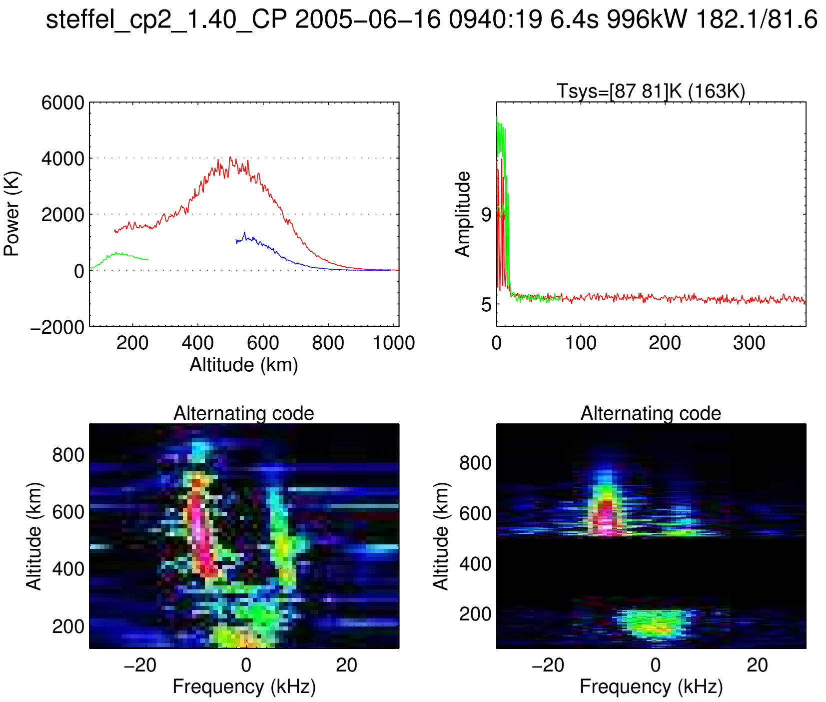

(b) 0940:19

Figure 5.3.7.: Spectra of the NEIAL event occurring between 0940:13 and 0940:19 UT on 16 June 2005.

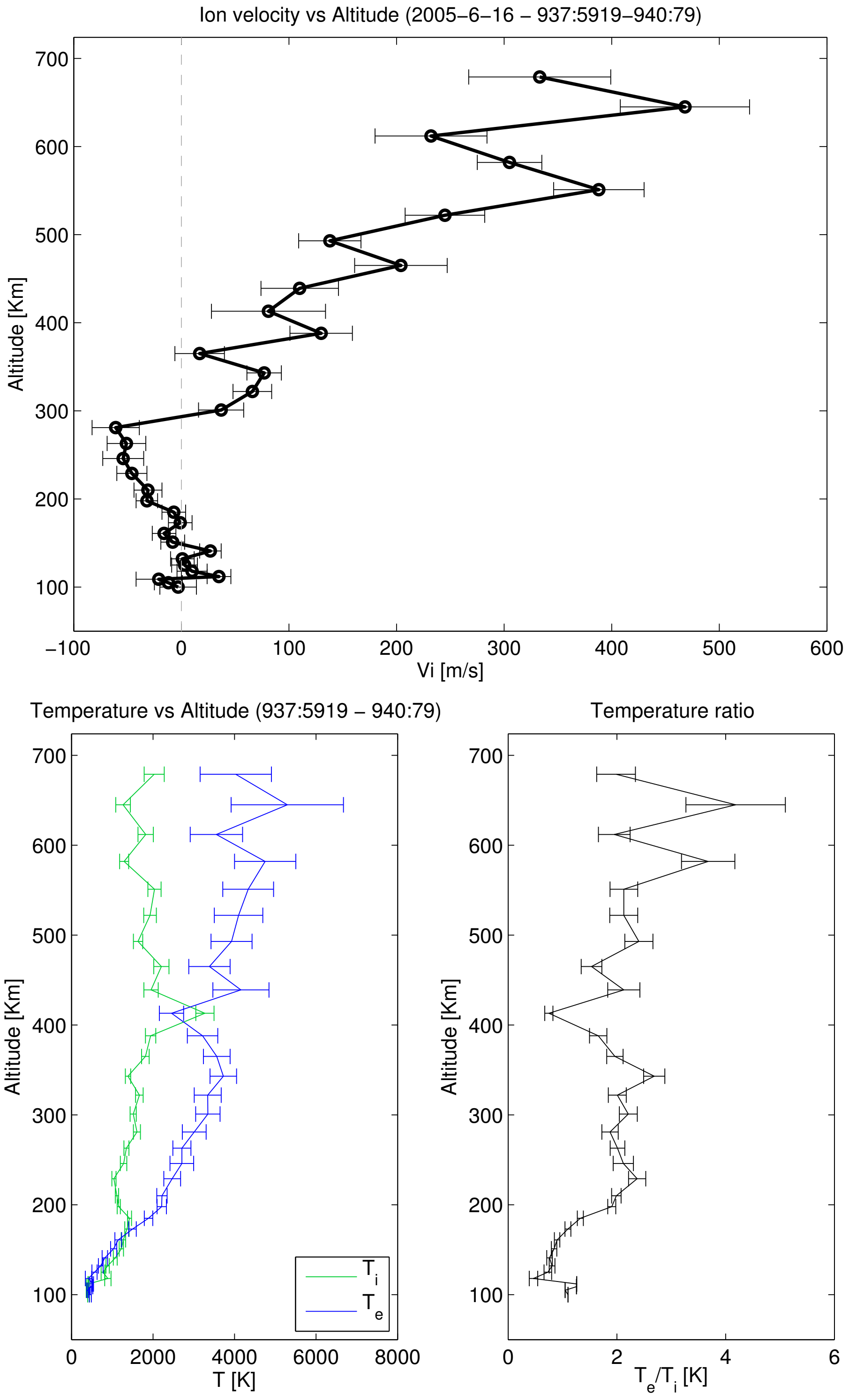

Figure 5.3.8.: Some ionospheric parameters evaluated with 128 s integration just before the NEIAL event occurring at 0940:13 UT on 16 June 2005. (Top panel) Ion velocity; (Bottom panel, left) Electron and ion temperatures; (Bottom panel, right) Temperature ratio T_e/T_i.

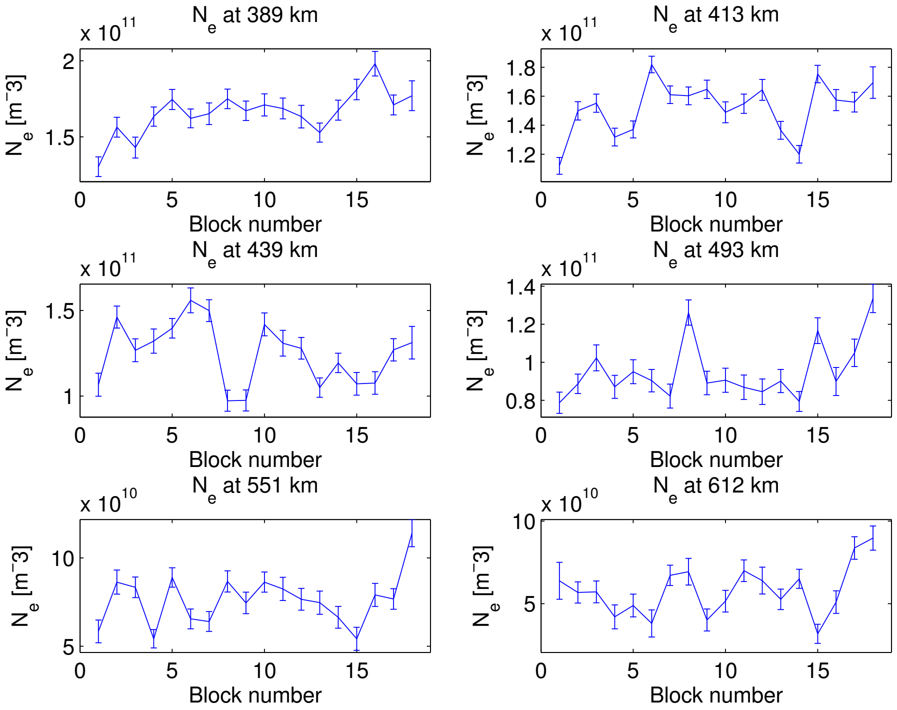

(a) Electron density

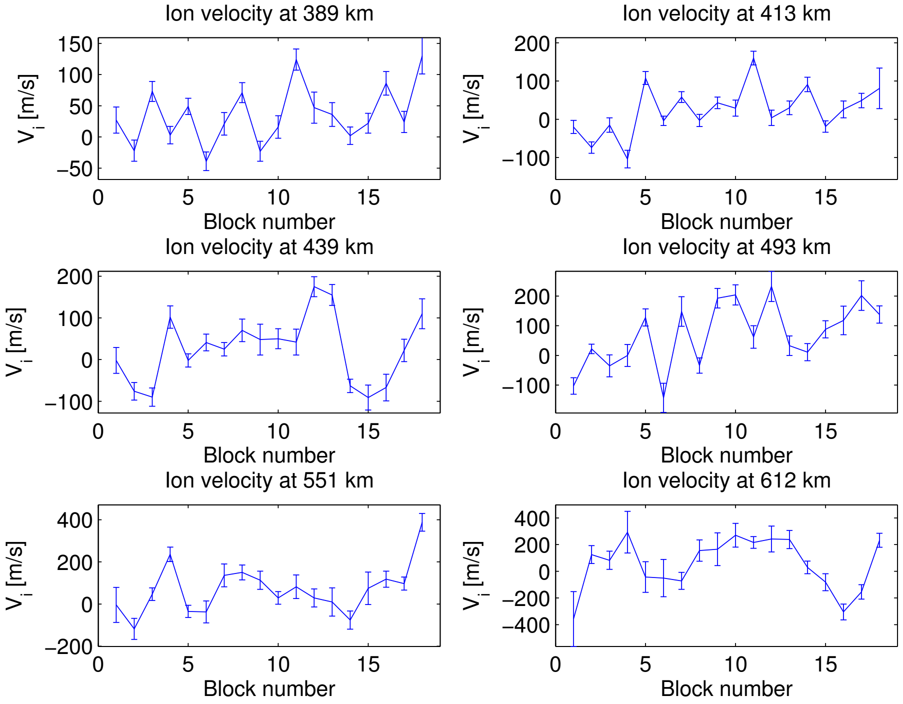

(b) Ion velocity

Figure 5.3.9.: Electron density (a) and ion velocity (b) just before the NEIAL event occurring at 0940:13 UT on 16 June 2005.

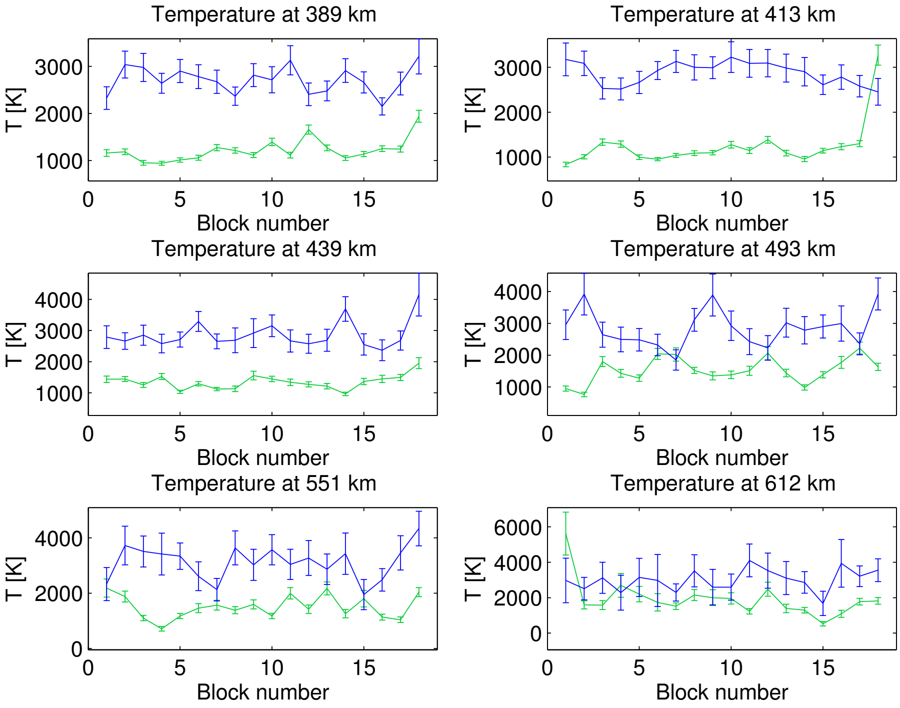

(a) Electron and ion temperature

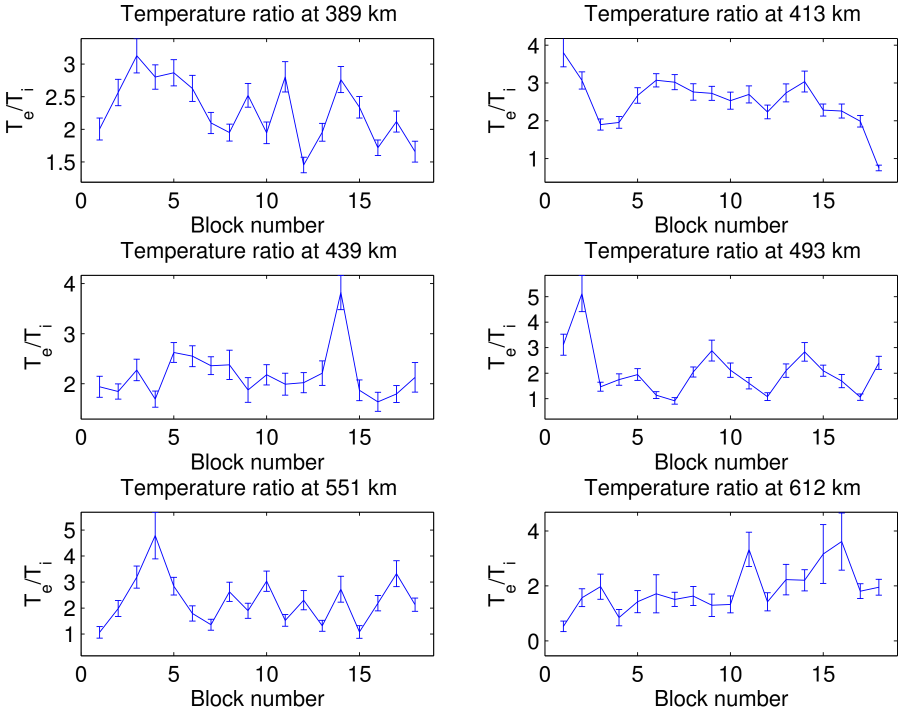

(b) Temperature ratio

Figure 5.3.10.: Electron and ion temperatures (a) and temperature ratio (b) just before the NEIAL event occurring at 0940:13 UT on 16 June 2005. Electron temperature is in blue, ion temperature is in green.

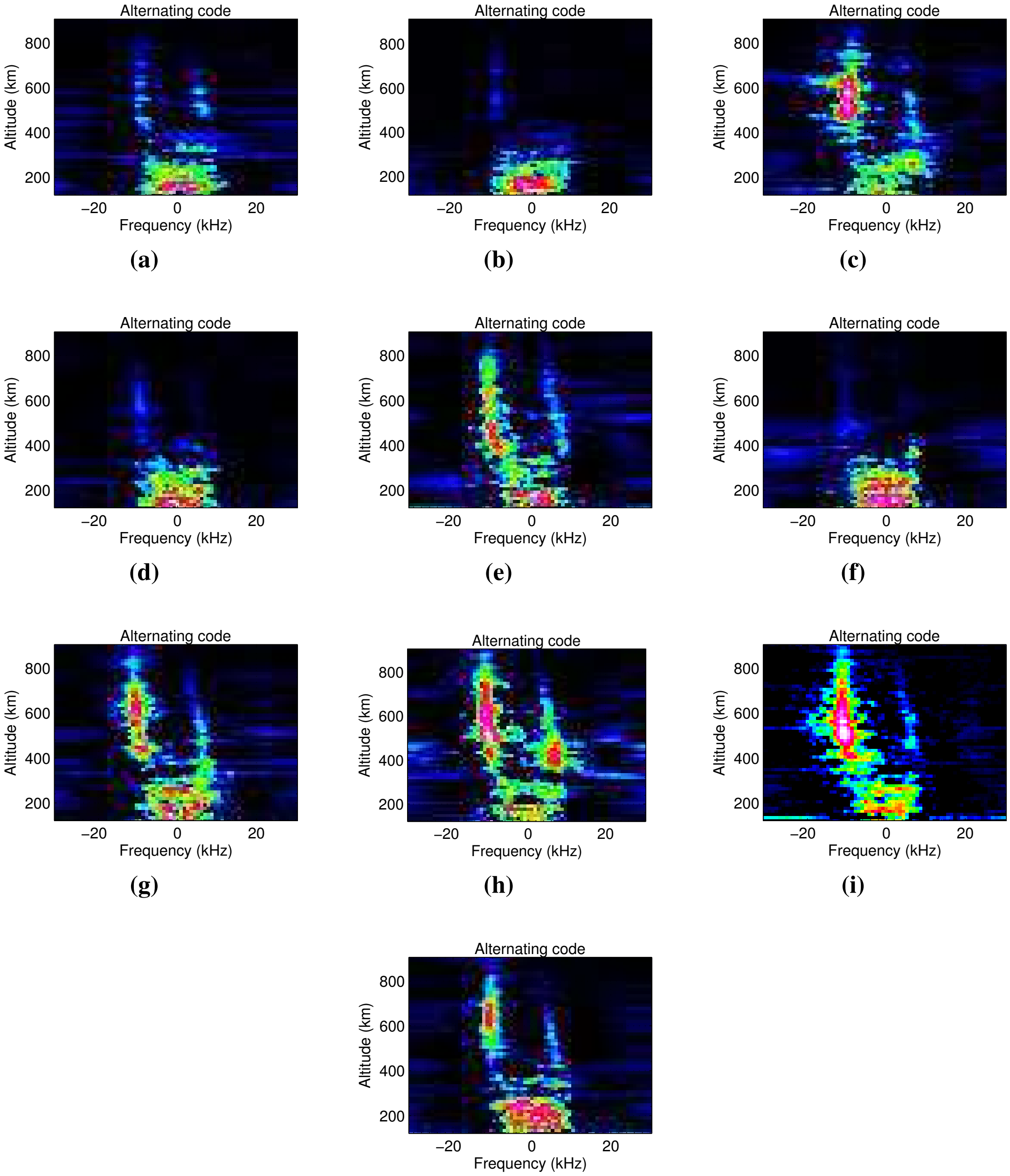

(a) (b) (c) (d) (e) (f) (g) (h) (i) (j)

Figure 5.3.11.: Spectra of the NEIAL event occurring between 1259:54 and 1300:52 UT on 16 June 2005.

5.3.3. Case 3: 10th September 2005

On 10 September 2005 we observed NEIAL events embedded into ion outflows with some peculiarity that we want to report. Fig. 5.3.6 shows electron density, electron temperature, ion temperature, field aligned ion velocity and some radar parameters. We analyzed every data dump between 0300 and 1400 UT; out of 3292 data dumps we found 46 dumps containing NEIALs. The low percentage is probably due to the fact that the outflows did not cover all of the data dumps; it would probably increase if one considers only dumps containing outflows. Note that there were 13 additional data dumps that were difficult to classify as containing NEIALs, since they did not show the typical power enhancement, although they showed clear (albeit weak) enhancements in the ion acoustic lines.

Tab. 5.3 summarizes NEIAL events we found in the time interval 0300-1500 UT.

Time	*0300-0359*	*0400-0459*	*0500-0559*	*0600-0659*	*0700-0759*
			0537:19	0603:20-0603:33	0728:08-0728:27

Time	*0800-0859*	*0900-0959*	*1000-1059*	*1100-1159*
			1038:07	1107:59-1108:05
			1044:18-1044:43	1114:10-1114:29
			1055:17-1055:49	1114:55-1115:08

Time	*1200-1259*	*1300-1359*	*1400-1459*
	1215:37-1215:44		
	1221:16-1221:36		
	1223:37-1223:44		
	1249:07-1249:20		
	1249:39-1249:45		
	1253:29-1253:42		

Table 5.3.: All NEIAL events occurring in the specified time intervals. The bold intervals are events which were discussed here.

The event that first caught our attention was the one occurring between 1055:17 and 1055:49 UT. It shows a huge power increase, the largest we observed in our entire data set. As it is shown in Fig. 5.3.13, it is very intense and fast growing, since we go from a standard ionospheric situation (Fig. 5.3.13a) to a full power NEIAL (Fig. 5.3.13b) in no more than 6.4 seconds. This would be in agreement with the hypothesis which regards NEIALs as a prompt event (see e.g. *Michell and Samara*, 2010), rather than a "building-up" event. However, as we shall see, we found events that differs from this view.

Fig. 5.3.14 shows ion velocity and temperature profiles obtained just before the event. The clear variability at various altitudes reflects the not so high quality of data, especially above 550 km. We could however get reasonably good values, which show that the ion outflow (Fig. 5.3.14, top panel) is occurring above 300 km, despite the relatively low values around 400 and 500 km. The problem is that, as it is shown in Fig. 5.3.14, that the NEIAL event is already occurring at 200-250 km. This would represent an issue for the hypothesis according to which the NEIAL event is embedded into the ion outflow. We think that, at least in this particular case, it is unlikely that the NEIAL is actually occurring below the outflow. It is probable that on a shorter timescale and during the NEIAL (if it would be possible to analyze it), the ion outflow would be already present on a lower altitude. Our opinion is also strengthened by the fact that, in almost all the events we analyzed, the NEIAL occurred above the ion outflow.

The temperature profiles (Fig. 5.3.14, lower panel) were standard for the type-II ion outflow event. We have observed a temperature ratio higher than 3 at some altitudes, but not in a continuous way. We did not manage to get good time profiles due to the many NEIALs and some satellite passing which occurred before our targeted event.

During our analysis we observed some "odd" spectra which were difficult to discard as due to satellite passing, noise or technical issues. As we mentioned at the beginning of this subsection, we observed many cases where the power seemed to be not enhanced, but the ion acoustic lines were clearly visible. One such example is shown in Fig. 5.3.15a. It is interesting to note that the ion acoustic lines are not continuous, but rather they form "spots", which in this particular case are located at around 400, 600 and 800 km. This is unusual, since the ion acoustic lines are mostly continuous in altitude when NEIAL events occur. A similar case is shown in Fig. 5.3.15b, where the spots are located between 450 and 700 km altitude. Common to all of these events is the tendency to observe the weak enhancement only in the downshifted line, while the upshifted line seems not to be affected at all. This is in agreement with the statistics, according to which the downshifted lines are more enhanced at higher altitudes (see for example *Lunde et al.*, 2007 and *Ogawa et al.*, 2011).

In addition to these isolated cases, there are "building-up" events that, again, does not become full NEIALs. Fig. 5.3.16 shows one of these cases: it seems that the NEIAL is slowly growing in time, but then, instead of showing a full enhancement in power, it just fades away. This behavior seems to be quite different from what one would expect from a prompt event. We tried to find an inverse proportional relation, such that the more powerful the NEIAL was, the more rapid they were growing. Unfortunately, this seems not to be the case, since many "not-so-spectacular" events are indeed prompt events, not showing any signs of a possible build-up. Furthermore, many of these cases had low signal-to-noise ratio and the analysis we attempted failed due to very large errors.

We would like to remark that all of these events occur sometimes close to standard NEIAL events, but they are always separated by at least one data dump, i.e. at least more than 6.4 s for the data sets we examined. That is why we considered them as isolated events.

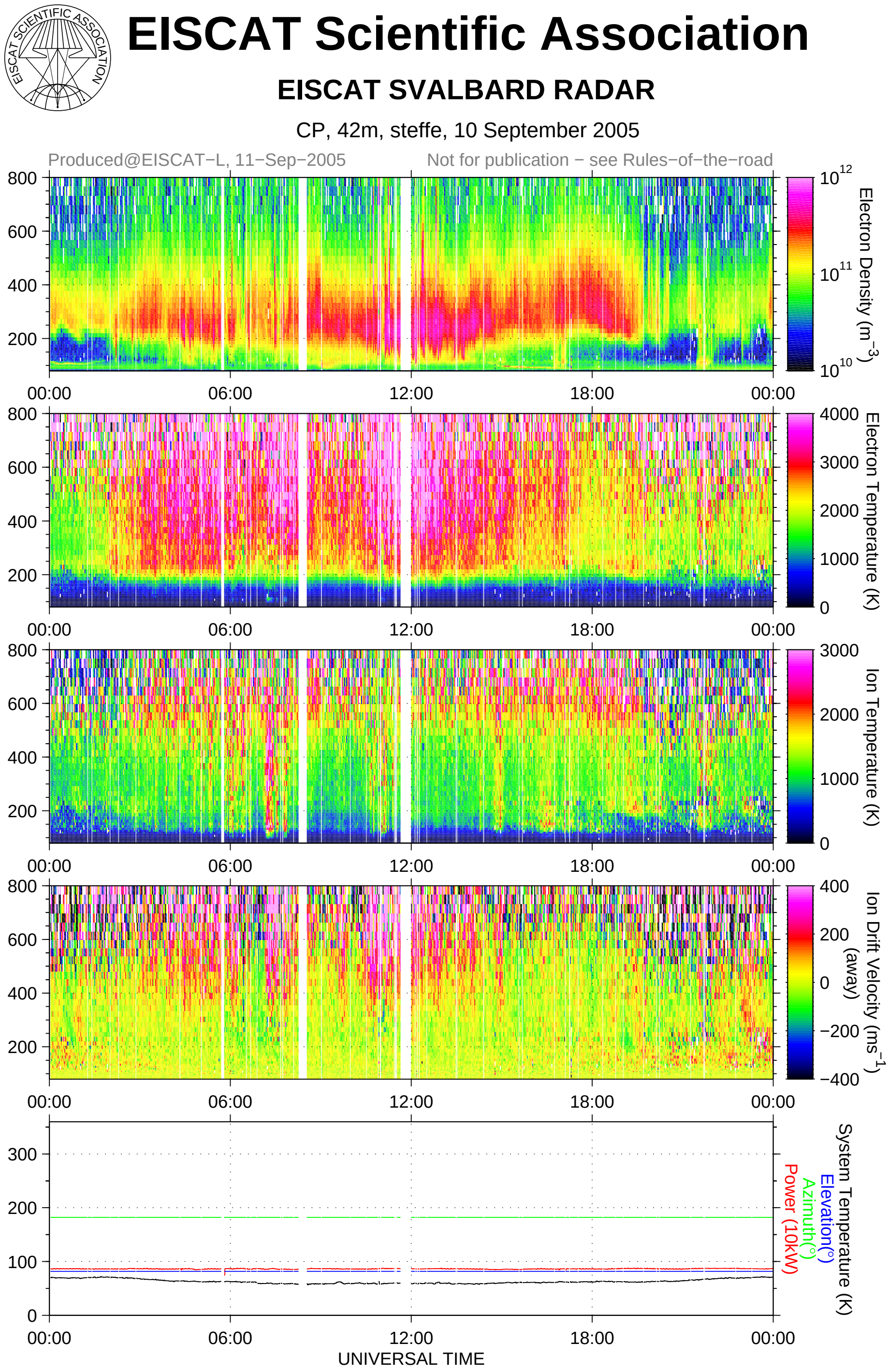

Figure 5.3.12.: Color plot showing electron density, electron temperature, ion temperature, ion velocity and radar parameters for the events observed on 10 September 2005, where a 128 s post-integration was used. [from *EISCAT Scientific Association* (2013)]

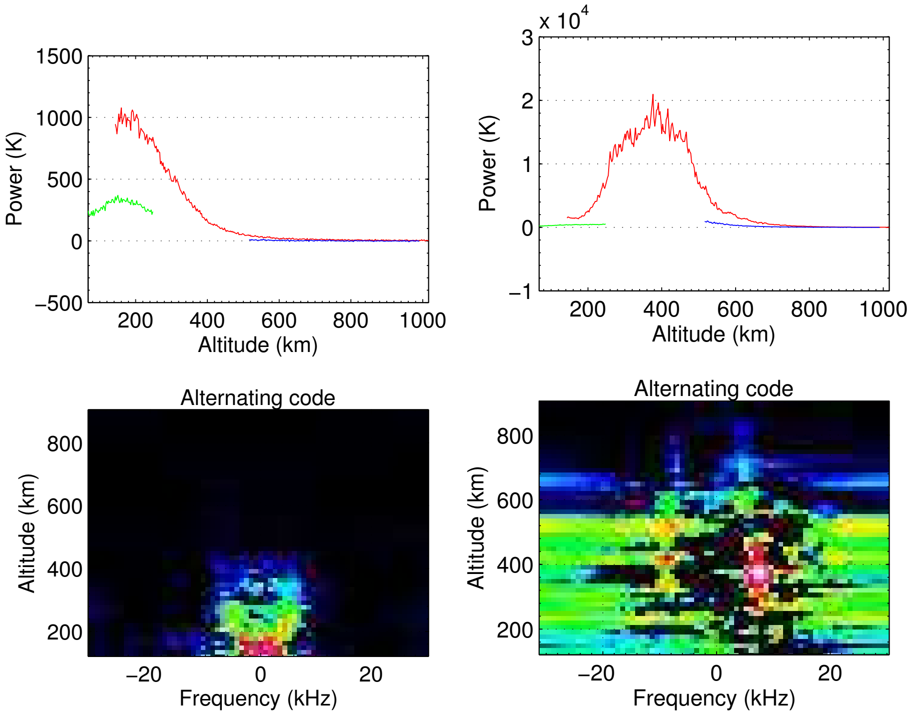

(a) 1055:17 **(b)** 1055:23

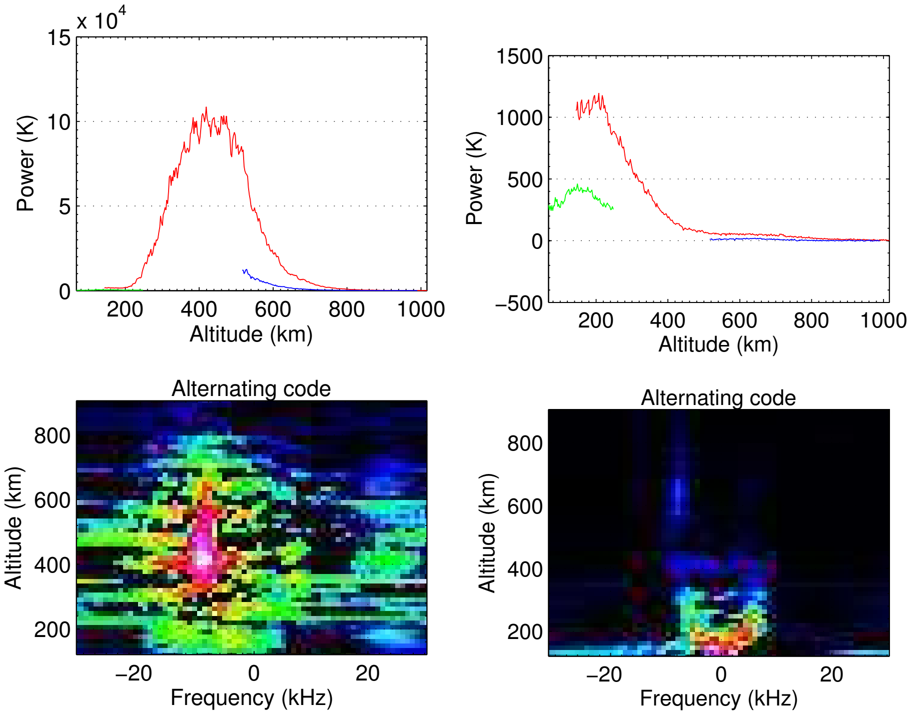

(c) 1055:30 **(d)** 1055:36

Figure 5.3.13.: Spectra of the NEIAL event occurring between 1055:17 and 1055:36 UT on 10 September 2005.

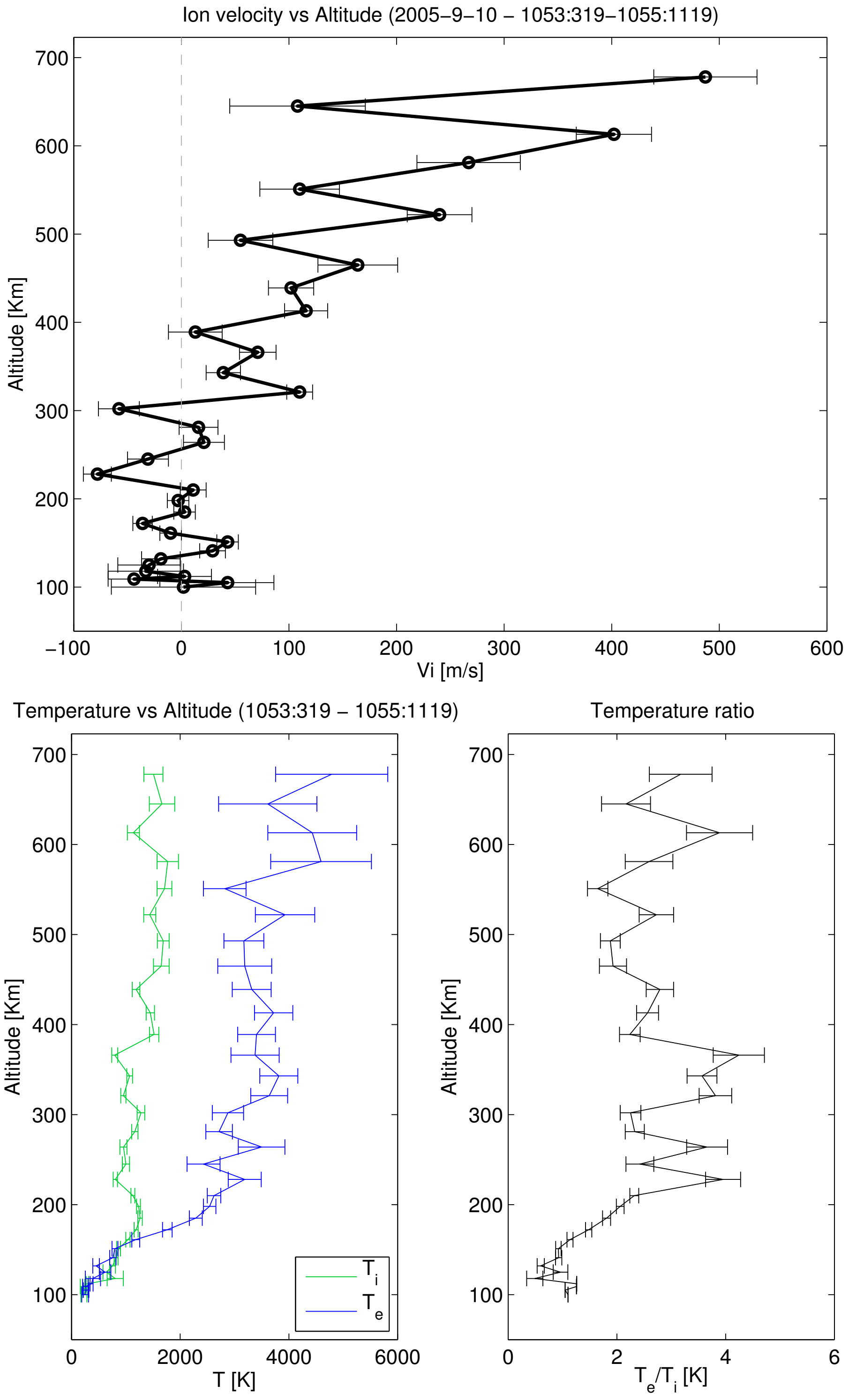

Figure 5.3.14.: Ionospheric parameters evaluated with 128 s integration just before the NEIAL event occurring between 1055:17 and 1055:36 UT on 10 September 2005. (Top panel) Ion velocity; (Bottom panel, left) Electron and ion temperatures; (Bottom panel, right) Temperature ratio T_e/T_i.

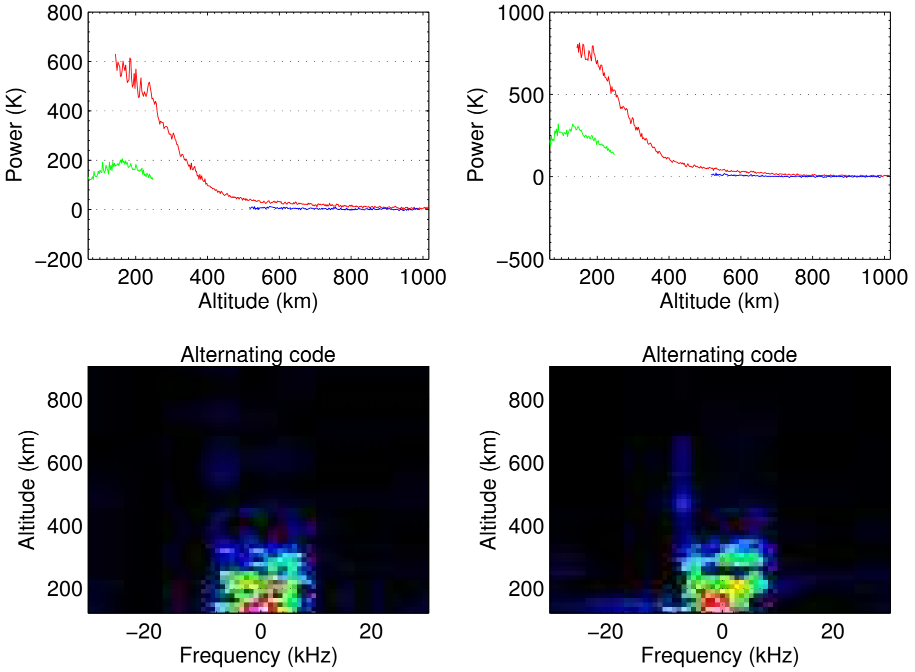

(a) 0605:41 **(b)** 1236:51

Figure 5.3.15.: Example of spectra showing weak ion acoustic lines enhancement occurring at (a) 0605:41 UT and (b) 1236:51 UT on 10 September 2005.

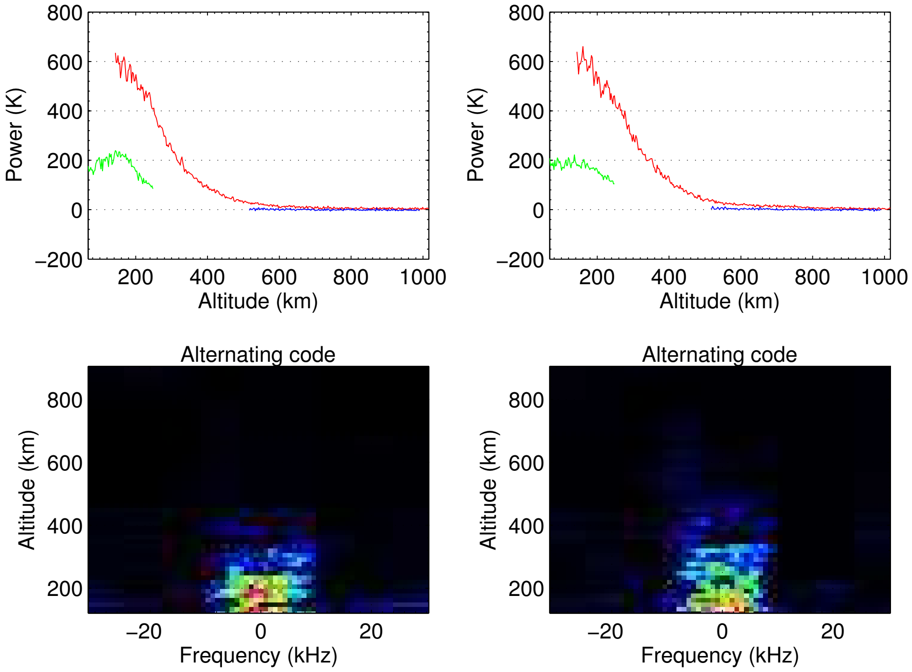

(a) 1106:04 **(b)** 1106:10

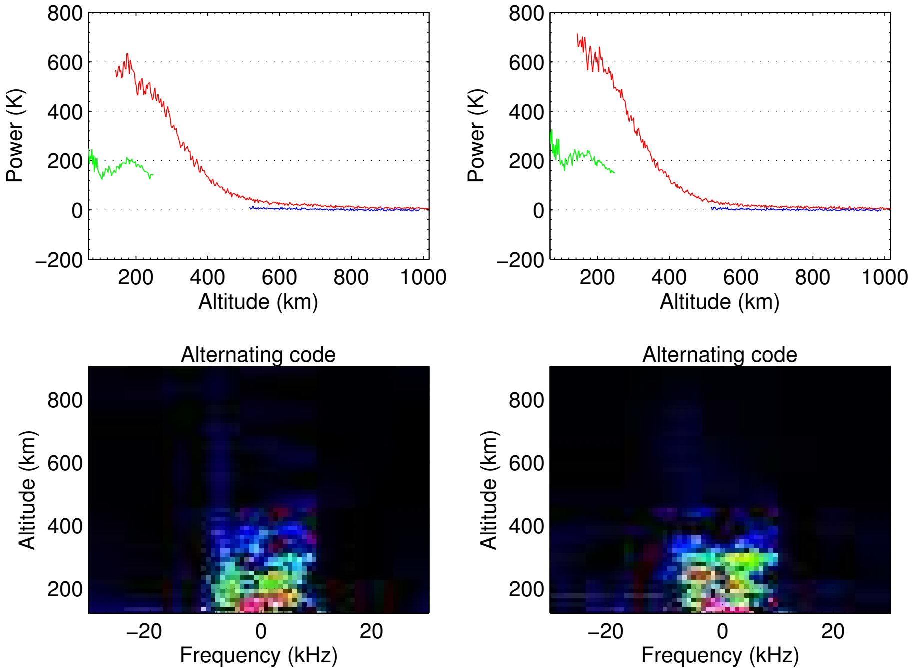

(c) 1106:16 **(d)** 1106:23

Figure 5.3.16.: Example of spectra showing weak ion acoustic lines enhancement occurring at four consecutive dumps between 1106:04 and 1106:23 UT on 10 September 2005.

5.4. Discussion

From the observations reported in this chapter, it is evident that NEIALs are a complex phenomenon. It is difficult to find properties which are valid for every event, and finding necessary conditions for NEIALs occurrence is even more problematic. Nevertheless, we tried to establish their most common features in our study.

NEIALs occur in association with ion outflows. More specifically, they occur mostly together with type-II ion outflows, i.e. when the temperature ratio T_e/T_i is higher than one and the electron temperature is enhanced. At present, we know only one case of NEIAL occurring together with a type-I outflow (*Argese*, 2013). There are, however, two different classes of NEIALs. In addition, it is very difficult to establish whether NEIAL events are correlated with the ion velocity magnitude and duration. In order to get better results on this topic, we need a statistical study. For example, on the basis of one year of data, *Ogawa et al.* (2011) suggested, as we explained in chapter 3, that NEIALs are more likely to occur when the outflows are more intense, i.e. when they have a higher flux (see Fig. 3.2.5). We hence plotted the flux for our observations to see if a correlation could be found; unfortunately, the errors were large and we had to increase the integration time past 120 s, thus making the analysis not applicable.

In a few cases we found outflows starting above the NEIAL events, which is an unexpected result. A continuous NEIAL event between 300 and 600 km associated with an outflow where the ion velocity is positive from 400 km would be affected by the outflow only between 400 and 600 km, while no relation with the outflow is present between 300 and 400 km. It is possible, nevertheless, that a shorter integration time would give similar starting altitudes. There is, however, a feature which can be interesting to explore. What we see as a continuous NEIAL in the RTG could actually be the overlapping at different altitudes (or at different times) of isolated ion acoustic enhancements which could have different generation mechanisms, one of them not requiring the NEIAL embedded into the outflow. We can ground this hypothesis using the fact that the mechanisms generating NEIALs could be embedded in the NEIAL itself, as *Forme et al.* (1995) suggested. In addition, in our work we actually found enhancements (albeit very weak) distributed as spots in the RTG (see, for instance, Fig. 5.3.15) and a low extension “real” NEIAL can be seen in Fig. 5.2.14a. Finally, the need of two different mechanisms acting together could be necessary for the explanation of NEIALs observed in the upper E region, as showed in Fig. 5.2.14.

As we said, we found two different types of NEIALs. They are not the same as *Forme et al.* (1995) found, but rather are the ones reported by *Lunde et al.* (2007) and *Ogawa et al.* (2011). The first type of NEIAL occurs at higher altitudes (above ~300 km), presents enhancement in both lines, often simultaneously, and the downshifted line is usually more enhanced than the upshifted line. This characteristics are in very good agreement with the descriptions given by *Lunde et al.* (2007) and *Ogawa et al.* (2011). In this case it is possible to apply the parametric decay of Langmuir waves and the ion-ion two stream theories when the events were occurring in the topside ionosphere (above 450-500 km). We often observe a weak particle precipitation, required for the parametric decay instability to occur, and, while the temperature ratio is seldom higher than 3 (which is considered the optimal value for the ion-ion instability to occur), it is very often above 2, hence compatible with the ion-ion instability. Furthermore, if we accept the reasonable assumption that with shorter integration times and analysis centered on the NEIAL event we would get higher temperature ratios, then it is very possible to give credit to the ion-ion instability theory. However, when the events occur at lower ionospheric altitudes (300-450 km) it is more difficult to use the ion-ion two stream instability theory because, as we explained in chapter 3 citing the work of *St.-Maurice et al.* (1996), at these altitude ranges the current driven instability would be already acting and in control of non-linear processes. If one could get the current density values, then it would have been possible to try to assess the validity of the current driven instability theory.

The second class of NEIALs occurs in the E region around 150 km. Such events have been reported by e.g. *Rietveld et al.* (1991) and *Ogawa et al.* (2011); we noticed that they occur together with the type-II ion outflow, but are not embedded into it. In addition, due to the low altitude, the temperature ratio can be relatively low: it is possible to find cases where $T_e/T_i \sim 1$, which is very hard for the theories to explain, since the instabilities are likely to occur for a higher temperature ratio value. In addition, we did not find any enhancement in the electron density and temperatures associated with this type of NEIAL. At this altitude, it is complicated to use both the ion-ion two stream instability (because we are further down in the boundary between E and F regions and hence too low for it to be valid) and the parametric decay of Langmuir waves, which requires soft particles precipitation. It is possible in this case that the current driven instability plays a role, but we would need to identify the electron population responsible for the electron-ion stream. In addition, although in the example we reported here only one of the ion acoustic lines is enhanced, we observed cases where both lines are enhanced, which makes difficult accepting this theory for all the NEIALs appearing in the upper E region, unless we assume two anti-parallel currents in a relatively small volume of space.

Ion temperature associated with NEIAL events occurring at high altitudes can show two different behaviors; in some cases it can be enhanced at upper E region altitudes, although no NEIAL occurs at such altitude; however, this seems to not affect the other parameters in the F region and topside ionosphere, where the NEIALs actually occur. The second behavior (which seems to be observed more often) consist in a relatively constant ion temperature at every altitude, resembling the definition given by *Wahlund et al.* (1992b) in their seminal paper about the type-II ion outflow, where they showed NEIALs occurring together with type-II ion outflows. Our observation are in good agreement with *Wahlund et al.* (1992b).

Electron temperatures show always an enhancement during type-II ion outflows, as observed by *Wahlund et al.* (1992b); sometimes we have observed a further enhancement in the electron temperature when close to a NEIAL event, however, we did not register the very high electron temperatures (as high as 6000 K) they found. This could be actually due to the low solar activity during the years we analyzed. Indeed, the years 2004 and 2005, where we found most of our data, were very close to the last solar minimum occurring around 2007 and hence many of our “best” events would just be below-average events on a very active year such as 2000.

We also found an unexpected anti-correlation between ion and electron temperatures, particularly evident in the CP-2 experiments but present in some other cases as well. We could not give any meaningful physical interpretation of this phenomenon, but it is difficult to discard it as a technical issue. What we think is the most plausible explanation is the following: the incoherent scatter radar measures only T_i and T_e/T_i. Thus, any fluctuation in the temperature ratio will be interpreted as a fluctuation both in T_e and T_i, but there is a higher probability that the two will be anti-correlated due to the very fact that T_e/T_i is a ratio and T_e is derived, not directly measured. Variations in T_e/T_i will produce a variation in the difference between T_e and T_i, i.e. $|T_e - T_i|$ will increase when T_e/T_i increases and will decrease when T_e/T_i decreases. Since a fluctuation in the temperature ratio can be actually seen as successive increases and decreases, it follows that we will see successive increases and decreases in $|T_e - T_i|$.

In addition to the two different types of “real” NEIALs, we observed some particular cases that deserve attention, such as the “failed NEIALs” showed in Fig. 5.3.15 and Fig. 5.3.16. If we consider the NEIALs as a prompt event with an “on-off” behavior, these observations are difficult to explain. However, we should be aware that all of the events of this kind we observed were actually embedded in a type-II ion outflow just as the standard events, and often they happened near the standard events (within seconds or minutes) and when we analyzed dumps not containing outflows we never found these events. We cannot however discard them as non-existent without outflows, since we analyzed about 10 hours of data not containing NEIAL on a total of more than 130 hours. A more statistically oriented study could discuss this matter in greater detail. In conclusions, our observations lead us to think that “real” and “failed” NEIAL events have probably a lot in common. It is possible, for instance, that what we observed as “failed” NEIALs are actually standard but very fast events whose power is then smoothed-out on a 6.4 seconds dump. Indeed, the works of *Grydeland et al.* (2003) and *Michell and Samara* (2010) suggest that the time scale of a NEIAL event can be less than 0.1 s.

The electron density exhibits some interesting features: often it is enhanced at the same altitudes as the NEIALs, which is an important clue about the particle precipitation, which in turn is believed to play an essential role for NEIALs’ generation mechanisms and it is thought to be important for ion outflow acceleration as well. The most interesting thing, however, is the presence of enhanced electron density in the E region altitude ranges, which can be related to the presence of hard particle precipitation. Since the parametric decay of Langmuir waves require soft particle precipitation, it is unlikely that this theory can explain the events reported for instance in Fig. 5.2.4, where we have a clear enhancement in low altitude electron density but no evident enhancement above 400 km. In addition, both the ion lines are enhanced (even though the upshifted is weaker) so it is difficult to apply the current driven instability. Moreover, the ion-ion two stream instability theory could find it difficult to explain the ion acoustic enhancements below 400 km as in the case shown in Fig. 5.2.2b. It is also possible that, on shorter time scales, the two ion lines would not be simultaneously enhanced, thus making the current driven instability applicable, provided that large current densities are present.

It is difficult to give a definitive answer regarding the validity of the theories using our data set. The lack of field aligned electric field and current densities measurements is an obstacle to assess the validity of the current driven instability, while the lack of data about different ion species and electron populations makes it difficult to apply the ion-ion two stream instability and the parametric decay of Langmuir waves, respectively. But the most serious problem we had is the long integration time. We could never keep it below

60 s and this is a lot longer than the duration of the average NEIAL. As *Grydeland et al.* (2003) and *Michell and Samara* (2010) showed, we need a lower integration time to better study what is happening close to a NEIAL event. However, even with a lower integration time, we would still be unable to get ionospheric parameters during the NEIAL due to the turbulence, a problem which is not surmountable with the incoherent scatter radar technique. Satellites and rockets can provide a valid help in this regard.

Since we used almost exclusively the ESR, which runs in the UHF band at 500 MHz, we cannot say anything about the higher frequency occurrence of NEIALs at VHF with respect to UHF frequencies, as reported e.g. by *Cabrit et al.* (1996). A broader statistical study is needed to give more information about this matter. Similarly, correlation with solar activity (e.g. NEIALs-sunspots correlation) is left out from our work, since it is necessary to have more homogeneous data (for instance, the same experiment mode and frequency) and perform a continuous observation for several years (the optimal would be for an entire 11-years solar cycle).

6. Conclusions and future works

Our results show that the NEIALs always occur in association with ion outflows. However, they are not always embedded into the ion outflow event. Throughout our analysis we observed three possible situations:

- Events where NEIALs are embedded into the ion outflow and start at about the same altitude
- Events where NEIALs start below the ion outflow
- Events where NEIALs are not embedded in the ion outflow

More in detail:

1. NEIAL events occurring above 300 km are always embedded into the ion outflows, which we assumed to be type-II ion outflow in each case, although, in some cases, it is possible to observe an enhancement in the ion temperature at lower altitudes, namely in the E region. The majority of NEIAL events above 300 km started at about the same altitude as the type-II ion outflow. Only occasionally, we observed NEIAL events which appeared to start below the outflows, however, a shorter integration time usually tends to lower the differences between the starting altitudes. Thus, this behavior can be due to the relative large integration time we needed to use in our analysis to overcome the lack of sufficient time resolution in the experiment.
2. NEIAL events in the upper E region can occur without being embedded in ion outflows, but in our data set they were associated with ion outflow and NEIALs occurring at higher altitudes. However, NEIAL events in the upper E region were quite rare in our data set, so we were not able to discuss them in a statistical way. More insights can be found in e.g. *Rietveld et al.* (1991), *Lunde et al.* (2007) and *Ogawa et al.* (2011).
3. We found two different types of background conditions when NEIALs can occur: the first is associated with enhanced electron temperatures mostly in the F region together with enhancements in the ion temperature (the latter especially in the E region); the second is associated with enhanced electron temperatures alone, as typical for type-II ion outflows.
4. We found a general good correlation between NEIALs and particle precipitation. On some occasions, the electron density was not clearly enhanced when NEIAL events occurred; in addition, we observed NEIALs in upper F region which showed very good correlation with electron density enhancements in the E region. We can conclude that particle precipitation is a necessary condition for NEIAL occurring, but it is not a sufficient condition.
5. The temperature ratio is always above 2 but seldom more than 3 for the NEIAL events occurring above 300 km, while $T_e/T_i \gtrapprox 3$ is usually considered the threshold

for the instabilities to occur. It is worth to note, however, that on shorter integration times the temperature ratio tends to increase at each altitude. Therefore, we believe that very close to the NEIAL event the temperature ratio can easily be above 3. For the events in the E region the temperature ratio is around 1, which is really low. It is possible, nevertheless, that a sudden increase in electron temperature very close to the NEIAL event will make the temperature ratio higher than 3. Alternatively, a different and unknown mechanism could trigger these events, but this seems to us less likely to occur.

6. There exist situations where the NEIALs seem to be slowly growing, but not always reaching a full intensity. In addition, we found some cases where the ion acoustic lines are very weakly enhanced, but no “real” NEIAL followed. In many of these cases the weak enhancements seem to be not continuously distributed in altitude, but rather “spotty”. We wonder if this particular morphology can be present also in the standard NEIALs, but are hidden by the rapid growing of the event.

These results are interesting for the NEIALs’ generation theories. While previous studies were directed towards assessing the validity of one and only one theory, our results tell us that each of the three mechanisms might prevail during their favorite conditions. For instance, the current driven instability theory (*Rietveld et al.*, 1991) have no altitude restriction, but needs very high current densities (which have been observed by e.g. *Neubert and Christiansen*, 2003) and cannot explain simultaneously enhanced ion acoustic lines. Since *Michell et al.* (2009) found that on shorter time scales simultaneously enhancements are less frequently occurring, the current driven instability can be very capable of explaining many NEIAL events. In addition, the presence of ion outflow and particle precipitation that we observed close to the NEIAL events are consistent with the theory proposed by *Rietveld et al.* (1991). Moreover, it is worth to note that the current driven instability is the only theory which is compatible with the events occurring in the upper E region. The ion-ion two stream instability theory (*Wahlund et al.*, 1992a), on the other hand, cannot be valid at lower altitudes, where collision frequency is high, i.e. we cannot employ it below 400 km. However, it is able to explain simultaneously enhancement in ion acoustic lines and the field aligned ion velocity we measured is of the same order of the thermal velocity, which is compatible with the requirement $v_{drift} \approx v_{thermal}$, together with soft particle precipitation and high electron temperatures, which we observed in tpye-II ion outflows. The tendency we observed, i.e. to have an increasing temperature ratio T_e/T_i as we get close to the NEIAL, is also important for assessing the ion-ion instability. Finally, the Langmuir decay theory (*Forme*, 1993 and *Forme*, 1999) can explain simultaneously enhanced ion acoustic lines and, in the version given by *Forme* (1999) can explain the feature consisting in mostly enhanced downshifted lines at higher altitudes. In order to trigger the instability, this theory requires soft particle precipitation, which we observed in our data set. Furthermore, it does not need high current densities as the current driven instability or, as the ion-ion two stream instability, two different ion populations, thus it can be perfectly valid above 400 km in the cases where these conditions are not met.

As it is evident, the most important issue with this work is the integration time, which is too long to get smooth behavior of ionospheric parameters very close to the NEIAL events. For instance, *Grydeland et al.* (2003) showed that the time scale for NEIAL events are about 200 ms and *Michell and Samara* (2010) identified NEIAL events on time scale of 12 ms. Unfortunately, in our work we had to use integration times of at least 60 s in order to get reliable ionospheric parameters. A new promising system which can be successfully used to refine and extend this work is the EISCAT 3D, whose predicted measurement improvements are between 10 and 50 times the actual EISCAT radars generation (*EISCAT Scientific Association*, 2013).

Additionally, a statistical study, similar to the one carried on by *Ogawa et al.* (2011), can give more information about the NEIAL morphology and the NEIAL occurrence frequency. A perhaps demanding task would be to follow the NEIAL and ion outflow processes for an entire solar cycle and see if there are significant differences in the coupling of the two processes when different solar conditions occur, e.g. at solar maximum and solar minimum.

Acknowledgments

First and foremost I would like to thank my supervisor, Prof. Unni Pia Løvhaug, for her continuous support and for many hours of interesting, fruitful and even fun discussions about all the topics we touched in this thesis. After this work, I feel I grew up not only as a student, but as a person as well, since it is my opinion that in life it is of greatest importance to have the inquiring mind, the curiosity and the enthusiasm of the scholar.

Although not in direct relation with this work, I would like to thank all the professors that I met here at UiT and taught me so many useful and interesting things, which had a sure influence on this work: Odd Erik Garcia, Torbjørn Eltoft, Harald Johnsen, Robert Jenssen, Cesar La Hoz, Ulf Peter Hoppe, Björn Gustavsson.

I want to thank also PHD students Hannah Vickers and Henry Pinedo for having always found time to help us when we got stacked with Matlab, RTG files and other technical stuff, and for suggestions about the best strategies to solve our problems.

I want to thank my family, because they have always believed in me and they have managed to let me feel close to them even at 4500 km away. A special thanks to Chiara Argese, for being the marvelous person she is.

Last but not least, I thank $C_8H_{10}N_4O_2$ (better known as *caffeine*), for keeping me awake, especially when outside was dark and cold.

Without all of you, this work would have never seen the light.

A. Identify NEIALs using electron density enhancements

In order to identify NEIAL events, we try to implement an idea of Prof. Björn Gustavsson. When a NEIAL occurs we measure a large enhancement in electron density. Note that it is just the *measured* electron density which is enhanced, actually we do not know what happens to the ionosphere parameters during a NEIAL event, since the incoherent scatter analysis fails in those cases. When the event ends, the electron density measured comes back to a standard value. We know from the theory that there is a limit for the decay rate of the electron density. In order to better understand the problem, we are going to derive the final relation for the electron density decay.

We start by considering the electron density continuity equation, neglecting any transport processes. In this case the equation can be written as:

$$\frac{\mathrm{d}n_e}{\mathrm{d}t} = q_e - l_e \tag{A.0.1}$$

where q_e and l_e are respectively the production and loss terms for electrons. In the F region the loss rate takes a so-called β-profile, namely $l_e = \beta n_e$, so that A.0.1 can be rewritten as:

$$\frac{\mathrm{d}n_e}{\mathrm{d}t} = q_e - \beta n_e \tag{A.0.2}$$

If the production $q_e = q_0$ is shut-off at a time $t = 0$, so that $q_e = 0$ when $t > 0$, the solution of the equation A.0.2 will be:

$$n_e = n_{e,0} \exp\left(-\beta t\right) \tag{A.0.3}$$

where $n_{e,0} = q_0/\beta$ is the density at $t = 0$.

In the E region the loss rate is proportional to n_e^2, hence the continuity equation is:

$$\frac{\mathrm{d}n_e}{\mathrm{d}t} = q_e - \alpha n_e^2 \tag{A.0.4}$$

Since NEIALs occur mostly in the F region, we used A.0.2 to describe the electron density. The factor β is:

$$\beta = \frac{k_1[\mathrm{N}^2] + k_2[\mathrm{O}^2]}{1 + \frac{k_1}{\alpha_1}\frac{[\mathrm{N}^2]}{n_e} + \frac{k_2}{\alpha_2}\frac{[\mathrm{O}^2]}{n_e}} \tag{A.0.5}$$

where the reaction rates in $\mathrm{m}^3\mathrm{s}^{-1}$ are (from *Brekke*, 2012, *Chen et al.*, 1978 and *Gustavsson and Eliasson*, 2008):

- $k_1 = 2\times10^{-18}$ for $O^+ + N_2 \longrightarrow NO^+ + N$
- $k_2 = 3.33\times10^{-18}\exp\left(3.72\frac{300}{T_f} - 1.78\frac{300}{T_f}\right)^2$ for $O^+ + O_2 \longrightarrow O_2^+ + O$ and where $T_f = \frac{T_i+T_n}{2}$ and T_n indicates neutral temperature, which is usually around 1000 K.
- $a_1 = 2.1\times10^{-13}\left(\frac{T_e}{300}\right)^{-0.85}$ for $NO^+ + e \longrightarrow N + O$
- $a_2 = 1.9\times10^{-13}\left(\frac{T_e}{300}\right)^{-0.5}$ for $O_2^+ + e \longrightarrow O + O$
- $a_r = 7.8\times10^{-14}\left(\frac{T_e}{300}\right)^{-0.5}$ for $O^+ + e \longrightarrow O + h\nu$

Now that we have all the necessary equations, we can think to use the electron density decay to identify NEIALs. In fact if we stop the production we will have the fastest time decay for electron density. Hence, if we observe a decay which is faster than what A.0.2 provide, we could conclude that the situation is unphysical, and therefore a NEIAL (which as we said makes the measured electron density greatly enhanced) could be occurring.

Unfortunately our tentative didn't succeed. The decay profiles we obtained were always slowest than the observations. We tried several altitudes and dumps containing NEIAL events. Fig. A.0.1 shows the electron density decay for a dump containing a NEIAL (top) and a standard dump with no NEIAL (bottom). It is evident that in both cases the observed electron density decays way faster than our numerical solutions (b) and (d) and theoretical solutions (a) and (c). Basically every dump was considered containing a NEIAL. The time constant $1/\beta$ was at least 10^3 bigger than what we needed, and that is way the calculated decay seems a straight line instead of an exponential decay. Apart from a mistake in the code, the principal reason of our failure could be a too strict assumption. For example, it is possible that transport terms (which we neglected) play a role in shaping the electron density decay. We probably need a more detailed model, including transport terms in the equation, in order to better face this very interesting matter.

For reference Fig. A.0.2 shows the electron density over time, NEIALS were present at blocks 27, 28, 29, 30. In this case we obviously did not remove the dumps containing NEIALs.

Here we list part of the Matlab function we use to implement the density decay, which is called from the main routine we used to analyze data (see Appendix B).

```
function neneial(ne,neerr,te,ti,tr,t,alt,halt,...
    plotvector,errorbars,neial_t,...
    starttime_h,starttime_m,endtime_h,endtime_m)
if plotvector(11)>0

time=0:0.1:6; %integration time

%densities
nN2=3.004E+13; %m^-3
%nN2=0;
nO2=1.318E+12; %m^-3

for a=32 %altitude vector (set a single number if want only one plot)
for j=[20] % Blocks containing NEIALs
    Te=te(a,j);
```

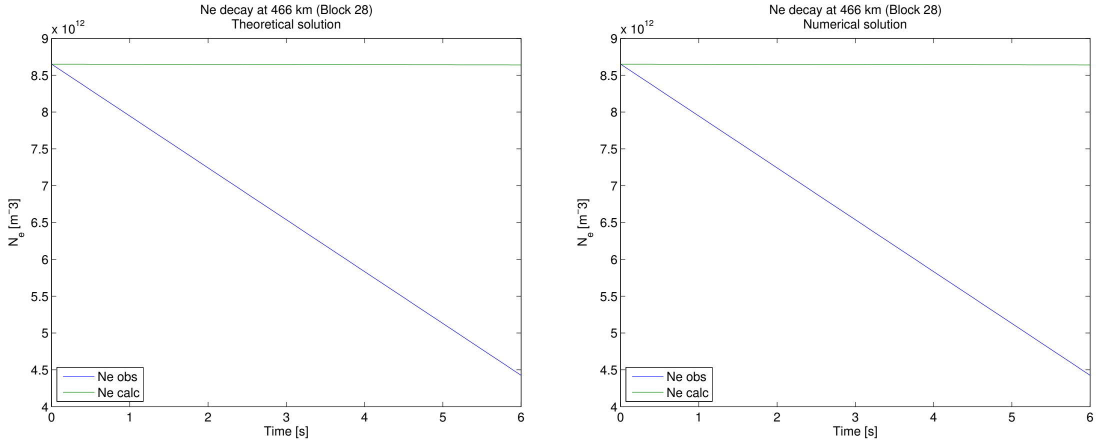

(a) Electron density decay after a NEIAL. Theoretical solution

(b) Electron density decay after a NEIAL. Numerical solution

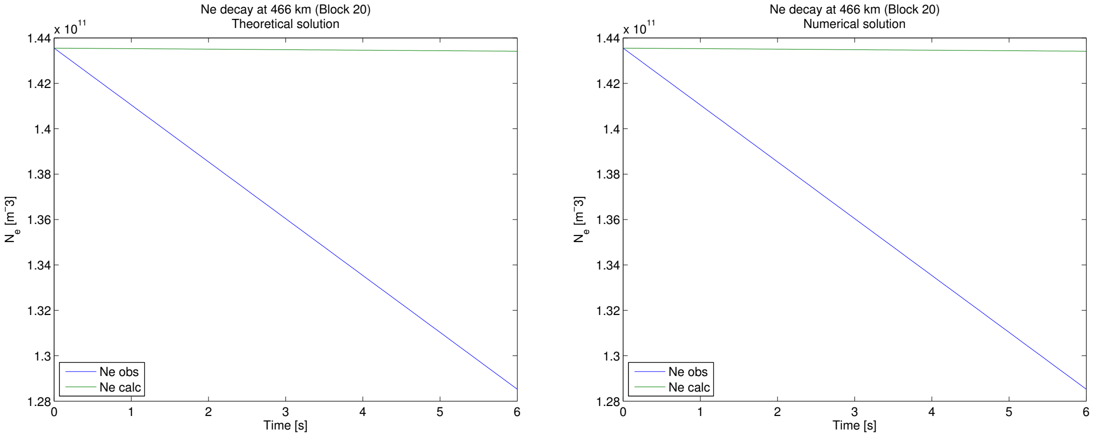

(c) Electron density after a NEIAL-free dump. Theoretical solution

(d) Electron density after a NEIAL-free dump. Numerical solution

Figure A.0.1.: Electron density decay after a block containing a NEIAL, obtained with a numerical (a) and a theoretical (b) approach. Comparison with a block containing no NEIALs, where (c) is the theoretical solution and (d) is the numerical one, shows almost no difference, which means that the calculated electron density decay is too slow.

```
    Ti=ti(a,j);
    Tn=937; %taken from the database
    Tr=tr(a,j);
    Tf=Ti/2+Tn/2;
    Ne=ne(a,j);

    %reaction rates (see Brekke, 2012, pag. 259)
    k1=2e-18; %O+ + N2 --> NO+ + N
    k2=2e-17.*(Tr/300).^(-0.4); %O+ + O2 --> O + O2+
    %The following k2 is supposed to be more precise
    %k2=3.33e-18.*exp(3.72.*300./Tf - 1.78.*(300./Tf).^2);
    a1=2.1e-13.*(Te/300).^(-0.85);
    a2=1.9e-13.*(Te/300).^(-0.5);
    ar=7.8e-14.*(Te./300)^(-0.5);
```

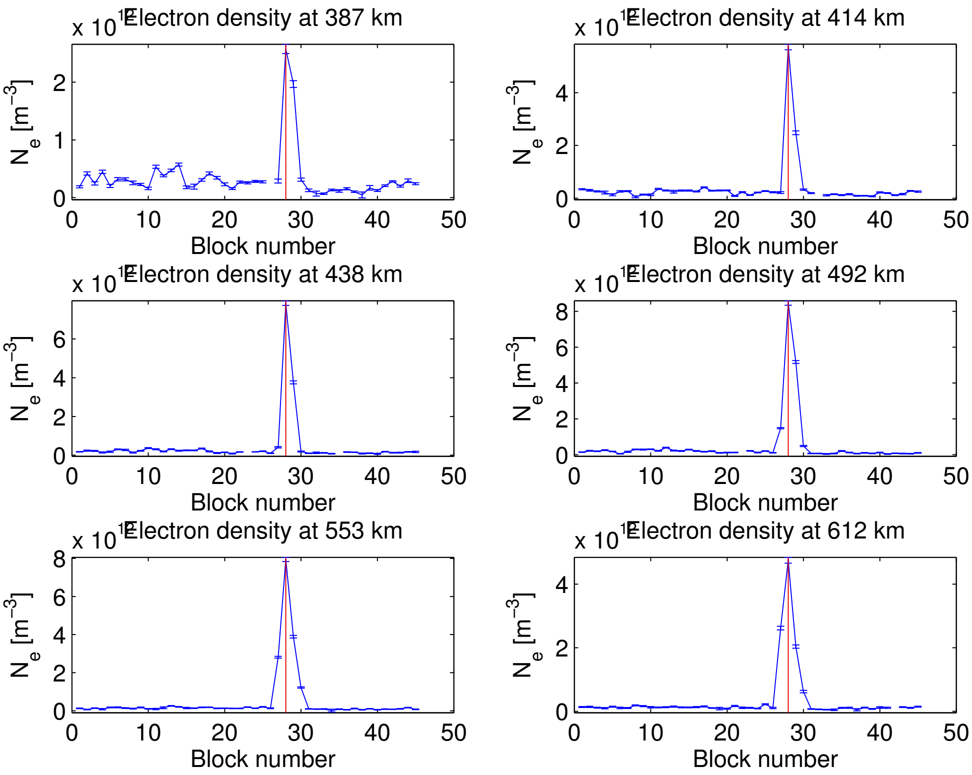

Figure A.0.2.: Electron density time profile. The red line indicates the strongest NEIAL event (block 28), which was used to evaluate the electron density decay for a NEIAL event. The same results were obtained for block 29, not reported here. Block 20 was used to evaluate electron density decay where no NEIAL occurred.

```
beta=(k1.*nN2+k2.*nO2)./...
    (1+ (k1./a1).*(nN2./ne(a,j)) + (k2./a2).*(nO2./ne(a,j)));
%beta=(k1.*nN2+k2.*nO2) %simpler beta
ne_c=ne(a,j).*exp(-beta.*time);

%solve diff eq numerically
[T N]=ode15s(@(time,ne1) odefun(time,ne1,beta),time,Ne);

%PLOTS
ne_int=interp1([0 6],[ne(a,j) ne(a,j+1)],time,'linear');

%Numerical solution
figure;plot(time,ne_int,T,N)
legend('Ne obs','Ne calc','Location','SouthWest');
xlabel('Time [s]');
ylabel('N_e [m^-3]');
title({sprintf('Ne decay at %d km (Block %d)',alt(a),j),...
    'Numerical solution'})
set(gcf, 'Position', get(0,'Screensize'));
strfig = sprintf('Electron density decay - Numerical (%d:%d - ...
   %d:%d)', starttime_h,starttime_m,endtime_h,endtime_m);
if plotvector(11)==2
    saveas(gcf,strfig,'png');
    saveas(gcf,strfig,'epsc');
end
```

```
    %Theoretical solution
    figure;plot(time,ne_int,time,ne_c);
    legend('Ne obs','Ne calc','Location','SouthWest');
    xlabel('Time [s]');
    ylabel('N_e [m^-3]');
    title({sprintf('Ne decay at %d km (Block %d)',alt(a),j),...
        'Theoretical solution'})
    set(gcf, 'Position', get(0,'Screensize'));
    strfig = sprintf('Electron density decay - Theoretical (%d:%d - ...
       %d:%d)', starttime_h,starttime_m,endtime_h,endtime_m);
    if plotvector(11)==2
        saveas(gcf,strfig,'png');
        saveas(gcf,strfig,'epsc');
    end
end
end

%PLOT ELECTRON DENSITY (for reference)
strfig = sprintf('Electron density (%d:%d - ...
   %d:%d)',starttime_h,starttime_m,endtime_h,endtime_m);
figure('Name',strfig)
sn=1;
for a=halt
subplot(3,2,sn);
if errorbars(1)==1
    errorbar(t,ne(a,:),neerr(a,:),'-b');
else
    plot(t,ne(a,:),'-b')
end
maxylim=max(ne(a,:))+max(neerr(a,:));
minylim=min(ne(a,:))-max(neerr(a,:));
set(gca,'YLim',[minylim maxylim])
set(gca,'XLim',[min(t)-1 max(t)+1])
%YL = get(gca,'ylim');
for j=1:length(neial_t)
    line([neial_t(j) neial_t(j)],[minylim maxylim], ...
        'LineStyle','-','Color',[0.9,0.0,0.0]);
end
title(sprintf('Electron density at %d km',alt(a)))
xlabel('Block number')
ylabel('N_e [m^{-3}]')
sn=sn+1;
end
set(gcf, 'Position', get(0,'Screensize'));
if plotvector(11)==2
saveas(gcf,strfig,'png');
saveas(gcf,strfig,'epsc');
end
end
end
```

B. Code

B.1. MATLAB scripts used to analyze NCAR files

The following Matlab scripts were used to extract parameters from NCAR ASCII data, which were created from raw data using `GUISDAP 8.7` software. Note that we used some external function, namely:

herrorbar.m to plot vertical profiles with horizontal error bars (http://www.mathworks.com/matlabcentral/fileexchange/3963-herrorbar)

pmkmp.m to use perceptually balanced color maps (http://www.mathworks.com/matlabcentral/fileexchange/28982-perceptually-improved-colormaps/content/pmkmp.m)

In the following we list first the main script (`AnalyseNcar.m`) and then the various functions called from it. In order to work, the main script requires that an NCAR ASCII file is already present (i.e. imported used the specific Matlab function). Alternatively, it is possible to import analyzed data set, together with the associated NEIAL times, previously saved as a `.mat` file. The saving is automatically done by the routine. More information about the functions are given in the code via comments (identified by the starting "%" symbol and green colored). The code was not optimized for every type of NCAR data, although we tried to write it in a way which is easily customizable and expandable. However, when the data are particularly bad (e.g. there are "holes" in the NCAR file) the script usually fails.

B.1.1. `AnalyseNcar.m` (main script)

```
%==============================================================
%AnalyseNCAR.m
%==============================================================
%Matlab script which take an EISCAT data NCAR ascii file as
%input (manual import using Matlab's 'Input data' function)
%and extract, analyse and plot relevant ionospheric parameters.
%It's possible to save plots in a .fig/.eps file and
%analysed data in a .mat file.
%===============================================================

%clean console screen
clc;

%%%%%%%%%%%%%%%%%%%%%%%%%%%
```

```
% MANUAL INPUT PARAMETERS %
%%%%%%%%%%%%%%%%%%%%%%%%%%%
%altitude vector for plots (use 6 elements vector)
%NOTE: adjust depending on experiment type
%halt=(28:1:33); %topside ionosphere
%halt=(12:1:17); %E-region
halt=[29 30 31 33 35 37];
%delete first n and last m values (e.g. because not useful/too noisy)
n=6;
m=7;

%max error allowed (set errmax to 0 if don't want to check)
%Ex: 0.5=50%
errmax=0;

%limits on parameters for the color plot
%set vector=[0 0] to have no limits
vilim=[-300 500];
nelim=[0 0];
telim=[100 8000];
tilim=[100 6000];
trlim=[0.1 5];

%plot errorbars (0=no 1=yes)
errorbars=[1 1];

%plotting vector (1=plot 2=plot&save)
plotvector=[2  2  2  0  0  0  0  0  0  2  0  0  2];
%plotvector=[0   0  0  2  2  2  2  0  2  0  0  0  0];
%index     [1  2  3  4  5  6  7  8  9  10 11 12 13]
%Structure:
%[1. ion velocity vs time
% 2. electron and ion temperatures vs time
% 3. temperature ratio te/ti vs time
% 4. ion velocity vs altitude
% 5. flux vs altitude
% 6. electron density vs altitude
% 7. temperatures vs altitude [PLOTS ONLY TE FOR MULTIBLOCK DATA]
% 8. electric field [WORKS ONLY FOR 1-BLOCK DATA!]
% 9. summury Ne Flux Vi [WORKS ONLY FOR 1-BLOCK DATA!]
% 10. color plots
% 11. NEIAL checking using ne variation [NEEDS NEIALS SPECTRA W ...
   6-sec INT TIME!]
% 12. Te estimates during NEIALs [NEEDS NEIALS SPECTRA W 6-sec INT ...
   TIME!][NOT IMPLEMENTED]
% 13. electron density vs time



%Automatically rename imported NCAR file to 'data'
%otherwise assume we have already loaded a mat data previously saved
%NOTE: in Matlab usually one should not use this eval() trick...
%Check if empty workspace
ncarname = who('-regexp','NCAR*');
dataname = who('-regexp','data*');
if isempty(ncarname) && isempty(dataname)
```

```
    disp('No data loaded!');clear;return;
end
if ~isempty(ncarname)
    ncarname = ncarname{1};
    data = eval(ncarname);
end

%restore backup if present
if exist('databak','var')
    data=databak;
end



%i=pulse number
%change if you want to start from a successive time
%TODO: implement choosing start time and end time
i=1;

%Automatically check NCAR file for step and range
%range of altitudes (for ex. ipy=31,steffe=45,tau0=52)
firstNaN=find(isnan(data(1:end,4)),1);
range=firstNaN-9;
st=find(~isnan(data(firstNaN:end,4)),1)+firstNaN-2;
if isempty(st)
    st=length(data);
end
step=st*(i-1); %(step between successive times)*(pulse number)
start=5; %starting row for altitude and value



%backup of original data (useful if need to split data blocks in ...
   separate variable)
databak=data;
% EX: if need to select only a particular block
% data1=data(1:st,:); %select first block
%data2=data(st+1:st*2,:); %select second block
%datalast=data(length(data)-st+1:length(data),:); %select last block
%data=data2; %use only first block as data
%data=datalast; %use only last block as data


%Look for NEIALs times, otherwise ask for vector containing them
%Ex. [x y z] --> Neials occurring at x, y and z timestep
if exist('neial_t','var')==0
    neial_t=input(sprintf('Insert neials timestep (0 for 1-block ...
       data): '));
    if neial_t==0
        neial_t=[];
    end
end


%SELECT DATE AND TIME
[starttime_h,starttime_m,...
```

```
    endtime_h,endtime_m,...
    date_y,date_m,date_d]=selDateTimes(data,start,step,st,range);



%data column numbers in NCAR file
calt=1; %column of altitude
cvo=10; %column of ion velocity
cvoerr=15; %column of ion velocity error
cti=7; ctierr=12; %ion temp
ctr=8; ctrerr=13; %temp ratio te/ti
cnel=6;cnelerr=11; %electron density
cneucl=3; %uncorrected electron density
cnr=5; %no/ne ratio



%select altitude and last altitude value
alt = data(start+step:start+range+step,calt);
lastalt = alt(end-m+1);
% %select altitude range for uncorrected log(ne)
%alt_neucl=data(range+10+st*(i-1):st+st*(i-1),calt);



%check if the chosen altitude are ok
while halt(end)>range || length(halt)>6 || ...
        halt(1)<=n || halt(end)>=(range+1)-(m-1) ||...
        ismember(0,halt)
    if ismember(0,halt)
        disp([find(alt), alt])
    end
    disp('Uncorrect altitude range (*halt* variable)')
    fprintf('Note:   range=%d   n=%d   m=%d\n',range,n,m)
    halt=input(sprintf('Insert correct *halt* vector or press 0 to ...
       see altitude vector: '));
end




% %select value (uncorrected log(ne))
%neucl=ucvalSelect(data,range,st,cneucl,n,m);

%select values
nel=valSelect(data,start,range,st,cnel,n,m);
nelerr=valSelect(data,start,range,st,cnelerr,n,m);
vo=valSelect(data,start,range,st,cvo,n,m);
voerr=valSelect(data,start,range,st,cvoerr,n,m);
ti=valSelect(data,start,range,st,cti,n,m);
tierr=valSelect(data,start,range,st,ctierr,n,m);
tr=valSelect(data,start,range,st,ctr,n,m);
trerr=valSelect(data,start,range,st,ctrerr,n,m);
nr=valSelect(data,start,range,st,cnr,n,m);

%delete NaN/unreliable values
```

```
[vo, voerr]=remBadValues(vo,voerr);
[ti, tierr]=remBadValues(ti,tierr);
[nel, nelerr]=remBadValues(nel,nelerr);
[tr, trerr]=remBadValues(tr,trerr);


%Evaluate other parameters
%conversion from logarithmic ne to usual ne
ne=10.^(nel*1e-3);
neerr=10.^(nelerr*1e-3);
%make tr varying between 0 and 1
tr=tr*1e-3;
trerr=trerr*1e-3;
%evaluate oxygen density
no=nr.*1e-3.*ne;
%evaluate flux
flux=no.*vo;
fluxerr=abs((no .* vo) .* (voerr./vo));
%%alternative flux (should be ok above 250-300 km)
% flux2=ne.*vo; %flux expressed as number of particeles*m^-2*s^-1
% fluxerr2=abs(ne .* vo) .* sqrt((neerr./ne).^2+(voerr./vo).^2);
%evaluate electron temperature
te=ti.*tr;
teerr=abs(ti .* tr) .* sqrt( (tierr ./ ti) .^ 2 + (trerr ./ tr) .^2 );


%Remove values with errors greater than errmax
[vo, voerr]=remBigErrs(vo,voerr,errmax);
[ti, tierr]=remBigErrs(ti,tierr,errmax);
[nel, nelerr]=remBigErrs(nel,nelerr,errmax);
[tr, trerr]=remBigErrs(tr,trerr,errmax);


%%%%%%%%%%%%%%%%%%
%     PLOTS      %
%%%%%%%%%%%%%%%%%%
%Set plots font size
set(0,'DefaultAxesFontSize',12)
set(0,'DefaultTextFontSize',12)

t=1:length(data)/st; %timestep vector

% ION VELOCITY vs TIME
plotVi(vo,voerr,t,alt,halt,...
    plotvector,errorbars,neial_t,...
    starttime_h,starttime_m,endtime_h,endtime_m)

%TEMPERATURES vs TIME
plotT(ti,tierr,te,teerr,t,alt,halt,...
    plotvector,errorbars,neial_t,...
    starttime_h,starttime_m,endtime_h,endtime_m)

%TEMP RATIO vs TIME
plotTr(tr,trerr,t,alt,halt,...
    plotvector,errorbars,neial_t,...
    starttime_h,starttime_m,endtime_h,endtime_m)
```

```
%ION VELOCITY vs ALTITUDE
plotViAlt(vo,voerr,data,st,alt,lastalt,...
    plotvector,neial_t,...
    date_y,date_m,date_d,starttime_h,starttime_m,endtime_h,endtime_m)

%FLUX vs ALTITUDE
plotFluxAlt(flux,fluxerr,data,st,alt,lastalt,...
    plotvector,neial_t,...
    starttime_h,starttime_m,endtime_h,endtime_m)

%ELECTRON DENSITY vs ALTITUDE
plotNeAlt(ne,neerr,data,st,alt,lastalt,...
    plotvector,neial_t,...
    starttime_h,starttime_m,endtime_h,endtime_m)

%TEMPERATURE vs ALTITUDE (plots only Te for multiblock data)
plotTAlt(te,teerr,ti,tierr,tr,trerr,data,st,alt,lastalt,...
    plotvector,neial_t,...
    starttime_h,starttime_m,endtime_h,endtime_m)

%ELECTRIC FIELD vs ALTITUDE
%Calculate Electric field
if plotvector(8)>0
[gradPi gradPe gradPierr gradPeerr efield efielderr]=...
    calcEfield(data,st,alt,ne,ti,te,neerr,teerr,tierr);
%Plot Electric Field and Pressure gradients
plotEfield(efield,efielderr,...
    gradPi,gradPierr,gradPe,gradPeerr,alt,lastalt,...
    plotvector,...
    starttime_h,starttime_m,endtime_h,endtime_m)
end

%SUMMARY PLOTS vs ALTITUDE (Flux, Vi, Ne)
plotFluxViNe(flux,vo,ne,alt,lastalt,...
    plotvector,...
    starttime_h,starttime_m,endtime_h,endtime_m)

%COLOR PLOTS (Ne, Vi, Flux)
plotColPlots(ne,flux,vo,te,ti,tr,vilim,nelim,telim,tilim,trlim,...
    t,alt,lastalt,plotvector,neial_t,...
    starttime_h,starttime_m,endtime_h,endtime_m)

%NEIALS CHECK USING ELECTRON DENSITY VARIATION
neneial(ne,neerr,te,ti,tr,t,alt,halt,...
    plotvector,errorbars,neial_t,...
    starttime_h,starttime_m,endtime_h,endtime_m)

%Te VARIATION DUE TO ELECTRON COOLING
teneial(te,ti,ne,no,t,alt,halt,...
    plotvector,errorbars,neial_t,...
    starttime_h,starttime_m,endtime_h,endtime_m)

%PLOT ELECTRON DENSITY VS TIME
plotNe(ne,neerr,t,alt,halt,...
    plotvector,errorbars,neial_t,...
```

```
    starttime_h,starttime_m,endtime_h,endtime_m)



%save Neials time and data mat files
save(sprintf('%d%d%d_--_%d_%d_-_%d_%d',date_y,date_m,date_d,...
starttime_h,starttime_m,endtime_h,endtime_m),'data');
if length(data)/st~=1
    save(sprintf('%d%d%d_--_%d_%d_-_%d_%d_neial_t',...
    date_y,date_m,date_d,...
    starttime_h,starttime_m,endtime_h,endtime_m),'neial_t');
end

%command to replace spaces and colons in namefiles with underscores
!rename "s/[ :]/_/g" *.eps && rename "s/[ :]/_/g" *.png
%Useful BASH script to convert eps in pdf (useful in some LaTeX ...
   environment)
!bash -c 'for i in `ls *.eps`;do `epstopdf $i`; done'
%move all figures and data in a folder (works only in a UNIX-like ...
   evironment)
!mkdir -p figs && mkdir -p figs/eps && mkdir -p figs/pdf;
!mv *.eps figs/eps; mv *.png *.mat figs; mv *.pdf figs/pdf;

%%clear variables if needed;
%clear
```

B.1.2. `calcEfield.m`

This function evaluates the electric fields using the electron and ion momentum equations. It gives large errors, so it was not used for our analysis.

```
function [gradPi gradPe gradPierr gradPeerr efield ...
   efielderr]=calcEfield(data,st,alt,ne,ti,te,neerr,teerr,tierr)
% SIMPLE CODE (maybe inaccurate)
kBoltz=1.28*1e-23; %Boltzmann's const
eplus=1.6*1e-19; %electron charge (abs value)
gradNe=diff(ne)./diff(alt.*1e3);
gradNe=[gradNe; gradNe(end)];
gradTi=diff(ti)./diff(alt.*1e3);
gradTi=[gradTi; gradTi(end)];
gradTe=diff(te)./diff(alt.*1e3);
gradTe=[gradTe; gradTe(end)];
gradPi=kBoltz.*(ne.*gradTi + ti.*gradNe);
gradPe=kBoltz.*(ne.*gradTe + te.*gradNe);
efield=-1./(ne.*eplus).*gradPe;
gradNeerr=zeros(length(gradNe),length(data)/st);
gradTierr=zeros(length(gradTi),length(data)/st);
gradTeerr=zeros(length(gradTe),length(data)/st);
gradPierr=zeros(length(gradPi),length(data)/st);
gradPeerr=zeros(length(gradPe),length(data)/st);
efielderr=zeros(length(efield),length(data)/st);
%error propagation (mathematical way)
```

```
for j=2:length(ne)
    gradNeerr(j,:)=abs(sqrt(neerr(j,:).^2 + ...
       neerr(j-1,:).^2)./(alt(j)*1e3-alt(j-1)*1e3));
    gradTierr(j,:)=abs(sqrt(tierr(j,:).^2 + ...
       tierr(j-1,:).^2)./(alt(j)*1e3-alt(j-1)*1e3));
    gradTeerr(j,:)=abs(sqrt(teerr(j,:).^2 + ...
       teerr(j-1,:).^2)./(alt(j)*1e3-alt(j-1)*1e3));
    gradPierr(j,:)=abs(kBoltz.*sqrt(...
        ( (ne(j,:).*gradTi(j,:)).^2 .* ((neerr(j,:)./ne(j,:)).^2 + ...
           (gradTierr(j,:)./gradTi(j,:)).^2) )+...
        ( (ti(j,:).*gradNe(j,:)).^2 .* ((tierr(j,:)./ti(j,:)).^2 + ...
           (gradNeerr(j,:)./gradNe(j,:)).^2) )));
    gradPeerr(j,:)=abs(kBoltz.*sqrt(...
        ( (ne(j,:).*gradTe(j,:)).^2 .* ((neerr(j,:)./ne(j,:)).^2 + ...
           (gradTeerr(j,:)./gradTe(j,:)).^2) )+...
        ( (te(j,:).*gradNe(j,:)).^2 .* ((teerr(j,:)./te(j,:)).^2 + ...
           (gradNeerr(j,:)./gradNe(j,:)).^2) )));
    efielderr(j,:)=abs((1./eplus).*(gradPe(j,:)./ne(j,:)) .* ...
        sqrt( (gradPeerr(j,:)./gradPe(j,:)).^2 + ...
           (neerr(j,:)./ne(j,:)).^2 ));
end
end
```

B.1.3. `neneial.m`

Evaluates the electron density decay over time (see Appendix A for an explanation of this technique)

```
function neneial(ne,neerr,te,ti,tr,t,alt,halt,...
    plotvector,errorbars,neial_t,...
    starttime_h,starttime_m,endtime_h,endtime_m)
if plotvector(11)>0

time=0:0.1:6; %integration time

%densities
nN2=3.004E+13; %m^-3
%nN2=0;
nO2=1.318E+12; %m^-3

for a=32 %altitude vector (set a single number if want only one plot)
for j=[20] % Blocks containing NEIALs
    Te=te(a,j);
    Ti=ti(a,j);
    Tn=937; %taken from the database
    Tr=tr(a,j);
    Tf=Ti/2+Tn/2;
    Ne=ne(a,j);

    %reaction rates (see Brekke, 2012, pag. 259)
    k1=2e-18; %O+ + N2 --> NO+ + N
    k2=2e-17.*(Tr/300).^(-0.4); %O+ + O2 --> O + O2+
```

```
    %The following k2 is supposed to be more precise
    %k2=3.33e-18.*exp(3.72.*300./Tf - 1.78.*(300./Tf).^2);
    a1=2.1e-13.*(Te/300).^(-0.85);
    a2=1.9e-13.*(Te/300).^(-0.5);
    ar=7.8e-14.*(Te./300)^(-0.5);

    beta=(k1.*nN2+k2.*nO2)./...
        (1+ (k1./a1).*(nN2./ne(a,j)) + (k2./a2).*(nO2./ne(a,j)));
    %beta=(k1.*nN2+k2.*nO2) %simpler beta
    ne_c=ne(a,j).*exp(-beta.*time);

    %solve diff eq numerically
    [T N]=ode15s(@(time,ne1) odefun(time,ne1,beta),time,Ne);

    %PLOTS
    ne_int=interp1([0 6],[ne(a,j) ne(a,j+1)],time,'linear');

    figure;plot(time,ne_int,T,N)
    legend('Ne obs','Ne calc','Location','SouthWest');
    xlabel('Time [s]');
    ylabel('N_e [m^-3]');
    title({sprintf('Ne decay at %d km (Block %d)',alt(a),j),...
        'Numerical solution'})
    set(gcf, 'Position', get(0,'Screensize'));
    strfig = sprintf('Electron density decay - Numerical (%d:%d - ...
       %d:%d)', starttime_h,starttime_m,endtime_h,endtime_m);
    if plotvector(11)==2
        saveas(gcf,strfig,'png');
        saveas(gcf,strfig,'epsc');
    end

    figure;plot(time,ne_int,time,ne_c);
    legend('Ne obs','Ne calc','Location','SouthWest');
    xlabel('Time [s]');
    ylabel('N_e [m^-3]');
    title({sprintf('Ne decay at %d km (Block %d)',alt(a),j),...
        'Theoretical solution'})
    set(gcf, 'Position', get(0,'Screensize'));
    strfig = sprintf('Electron density decay - Theoretical (%d:%d - ...
       %d:%d)', starttime_h,starttime_m,endtime_h,endtime_m);
    if plotvector(11)==2
        saveas(gcf,strfig,'png');
        saveas(gcf,strfig,'epsc');
    end
end
end
%PLOT ELECTRON DENSITY ()
strfig = sprintf('Electron density (%d:%d - ...
   %d:%d)',starttime_h,starttime_m,endtime_h,endtime_m);
figure('Name',strfig)
sn=1;
for a=halt
subplot(3,2,sn);
if errorbars(1)==1
    errorbar(t,ne(a,:),neerr(a,:),'-b');
else
```

```
    plot(t,ne(a,:),'-b')
end
maxylim=max(ne(a,:))+max(neerr(a,:));
minylim=min(ne(a,:))-max(neerr(a,:));
set(gca,'YLim',[minylim maxylim])
set(gca,'XLim',[min(t)-1 max(t)+1])
%YL = get(gca,'ylim');
for j=1:length(neial_t)
    line([neial_t(j) neial_t(j)],[minylim maxylim], ...
        'LineStyle','-','Color',[0.9,0.0,0.0]);
end
title(sprintf('Electron density at %d km',alt(a)))
xlabel('Block number')
ylabel('N_e [m^{-3}]')
sn=sn+1;
end
set(gcf, 'Position', get(0,'Screensize'));
if plotvector(11)==2
saveas(gcf,strfig,'png');
saveas(gcf,strfig,'epsc');
end
end
end
```

B.1.4. `odefun.m`

Simply definition of a differential equation to use in `neneial.m` (see also Appendix A)

```
function dnedt=odefun(t,Ne,beta)
    dnedt=-beta.*Ne;
end
```

B.1.5. `plotColPlots.m`

Generate color plots for electron density, ion temperature, electron temperature, temperature ratio, ion velocity and ion flux.

```
%COLOR PLOTS (Ne, Flux, Vi)
function ...
   plotColPlots(ne,flux,vo,te,ti,tr,vilim,nelim,telim,tilim,trlim,t,...
alt,lastalt,plotvector,neial_t,starttime_h,starttime_m,...
endtime_h,endtime_m)
if plotvector(10)>0

% % create palette with nl levels
% % cut=[];
% % nl=[];
% % if isempty(cut), cut=0; end
% % if isempty(nl)
```

```
% %  nl=size(get(gcf,'colormap'),1);
% % end
% % f=[0 0 0 0 0 1 2 2 2 2 2 2 2
% %    0 0 0 1 2 2 2 1 0 0 0 1 2
% %    0 1 2 1 0 0 0 0 0 1 2 2 2]'/2;
% % nc=size(f,1);
% % n=nc-cut;
% % b=round([0:n-1]/(n-1)*(nl-1))+1;
% % f=sin(interp1(b,f(1:n,:),1:nl)*pi/2);
% % f=tanh(interp1(b,f(1:n,:),1:nl))/tanh(1);
% % colormap(f);
map=pmkmp(256,'linearl');
%map=pmkmp(256);
%map='jet';

%COLORT PLOTS: Ne, Vo, FLUX
strfig=sprintf('Color plots (%d:%d - ...
    %d:%d)',starttime_h,starttime_m,endtime_h,endtime_m);
figure('Name',strfig)

%Electron density
str = sprintf('Electron density [m^{-3}] (%d:%d - ...
    %d:%d)',starttime_h,starttime_m,endtime_h,endtime_m);
subplot(3,1,2)
if nelim(2)~=0
    ne(ne>nelim(2))=NaN;
end
if nelim(1)~=0
    ne(ne<nelim(1))=NaN;
end
pcolor(t,alt,ne); shading flat;
colormap(map);colorbar();
YL = get(gca,'ylim');
YL(2)=lastalt;
set(gca,'ylim',[YL(1) YL(2)])
for j=1:length(neial_t)
    line([neial_t(j) neial_t(j)],[YL(1) YL(2)],...
        'LineStyle','-','Color',[0.0,0.9,0.9]);
end
title(str)
xlabel('Block number')
ylabel('Altitude [Km]')

%Flux
str = sprintf('Flux [m^{-2}s^{-1}] (%d:%d - ...
    %d:%d)',starttime_h,starttime_m,endtime_h,endtime_m);
subplot(3,1,3)
pcolor(t,alt,flux);shading flat;
colormap(map);colorbar();
YL = get(gca,'ylim');
YL(2)=lastalt;
set(gca,'ylim',[YL(1) YL(2)])
for j=1:length(neial_t)
    line([neial_t(j) neial_t(j)],[YL(1) YL(2)],...
        'LineStyle','-','Color',[0.0,0.9,0.9]);
end
```

```
title(str)
xlabel('Block number')
ylabel('Altitude [Km]')

%Ion velocity
str = sprintf('Ion velocity [m/s] (%d:%d - ...
    %d:%d)',starttime_h,starttime_m,endtime_h,endtime_m);
subplot(3,1,1)
if vilim(2)~=0
    vo(vo>vilim(2))=NaN;
end
if vilim(1)~=0
    vo(vo<vilim(1))=NaN;
end
pcolor(t,alt,vo);shading flat;
colormap(map);colorbar();
YL = get(gca,'ylim');
YL(2)=lastalt;
set(gca,'ylim',[YL(1) YL(2)])
for j=1:length(neial_t)
    line([neial_t(j) neial_t(j)],[YL(1) YL(2)],...
        'LineStyle','-','Color',[0.0,0.9,0.9]);
end
title(str)
xlabel('Block number')
ylabel('Altitude [Km]')

set(gcf, 'Position', get(0,'Screensize'))
if plotvector(10)==2
    saveas(gcf,strfig,'epsc2');
    set(gcf, 'Renderer', 'zbuffer')
    saveas(gcf,strfig,'png');
end



%COLOR PLOT: TEMPERATURES
strfig=sprintf('Color plots - Temperatures (%d:%d - ...
    %d:%d)',starttime_h,starttime_m,endtime_h,endtime_m);
figure('Name',strfig)

%Electron temperature
str = sprintf('Electron temperature [K] (%d:%d - ...
    %d:%d)',starttime_h,starttime_m,endtime_h,endtime_m);
subplot(3,1,1)
if telim(2)~=0
    te(te>telim(2))=NaN;
end
if telim(1)~=0
    te(te<telim(1))=NaN;
end
pcolor(t,alt,te);shading flat;
colormap(map);colorbar();
YL = get(gca,'ylim');
YL(2)=lastalt;
set(gca,'ylim',[YL(1) YL(2)])
```

```
for j=1:length(neial_t)
    line([neial_t(j) neial_t(j)],[YL(1) YL(2)],...
        'LineStyle','-','Color',[0.0,0.9,0.9]);
end
title(str)
xlabel('Block number')
ylabel('Altitude [Km]')

%Ion temperature
str = sprintf('Ion temperature [K] (%d:%d - ...
   %d:%d)',starttime_h,starttime_m,endtime_h,endtime_m);
subplot(3,1,2)
if tilim(2)~=0
    ti(ti>tilim(2))=NaN;
end
if tilim(1)~=0
    ti(ti<tilim(1))=NaN;
end
pcolor(t,alt,ti);shading flat;
colormap(map);colorbar();
YL = get(gca,'ylim');
YL(2)=lastalt;
set(gca,'ylim',[YL(1) YL(2)])
for j=1:length(neial_t)
    line([neial_t(j) neial_t(j)],[YL(1) YL(2)],...
        'LineStyle','-','Color',[0.0,0.9,0.9]);
end
title(str)
xlabel('Block number')
ylabel('Altitude [Km]')

%Temperature ratio
str = sprintf('Temperature ratio (%d:%d - ...
   %d:%d)',starttime_h,starttime_m,endtime_h,endtime_m);
subplot(3,1,3)
if trlim(2)~=0
    tr(tr>trlim(2))=NaN;
end
if trlim(1)~=0
    tr(tr<trlim(1))=NaN;
end
pcolor(t,alt,tr);shading flat;
colormap(map);colorbar();
YL = get(gca,'ylim');
YL(2)=lastalt;
set(gca,'ylim',[YL(1) YL(2)])
for j=1:length(neial_t)
    line([neial_t(j) neial_t(j)],[YL(1) YL(2)],...
        'LineStyle','-','Color',[0.0,0.9,0.9]);
end
title(str)
xlabel('Block number')
ylabel('Altitude [Km]')


set(gcf, 'Position', get(0,'Screensize'))
```

```
if plotvector(10)==2
    saveas(gcf,strfig,'epsc');
    set(gcf, 'Renderer', 'zbuffer')
    saveas(gcf,strfig,'png');
end
end
end
```

B.1.6. `plotEfield.m`

Generate field aligned electric field altitude profiles.

```
function ...
   plotEfield(efield,efielderr,gradPi,gradPierr,gradPe,gradPeerr,...
    alt,lastalt,plotvector,starttime_h,starttime_m,endtime_h,endtime_m)
if plotvector(8)>0
j=1;
str=sprintf('Electric field vs Altitude (%d:%d - ...
   %d:%d)',starttime_h,starttime_m,endtime_h,endtime_m');
figure('Name',str)
set(gcf, 'Position', get(0,'Screensize'));
subplot(1,2,1)
herrorbar(efield(:,j),alt,efielderr(:,j),'-k')
maxylim=lastalt+10;
%line([0 0],[0 maxylim],'LineStyle','--','Color',[0.7,0.7,0.7]);
set(gca,'YLim',[50 maxylim])
title(str)
xlabel('E [V/m]')
ylabel('Altitude [Km]')
subplot(1,2,2)
gradPiLines=herrorbar(gradPi(:,j),alt,gradPierr(:,j),'--k');
set(gradPiLines,'LineWidth',2)
set(gradPiLines(1),'LineStyle','none')
hold on
gradPeLines=herrorbar(gradPe(:,j),alt,gradPeerr(:,j),'-k');
set(gradPeLines,'LineWidth',1)
set(gradPeLines(1),'LineStyle','none')
maxylim=lastalt+10;
%line([0 0],[0 maxylim],'LineStyle','--','Color',[0.7,0.7,0.7]);
set(gca,'YLim',[50 maxylim])
gradPiGroup = hggroup;
gradPeGroup = hggroup;
set(gradPiLines,'Parent',gradPiGroup)
set(gradPeLines,'Parent',gradPeGroup)
set(get(get(gradPiGroup,'Annotation'),'LegendInformation'),...
    'IconDisplayStyle','on');
set(get(get(gradPeGroup,'Annotation'),'LegendInformation'),...
    'IconDisplayStyle','on');
legend('grad(P_i)','grad(P_e)')
title('Pressure gradient')
xlabel('[Pa/m]')
ylabel('Altitude [Km]')
    if plotvector(8)==2
```

```
        saveas(gcf,str,'png');
        saveas(gcf,str,'epsc');
    end
end
end
```

B.1.7. `plotFluxAlt.m`

If given only one block, it generates the altitude profile for the ion flux. If given more than one block, generates the altitude profile for each block and will plot in red color the altitude profile where the NEIAL took place, provided that the `.mat` file containing the NEIAL events times is present.

```
%FLUX vs ALTITUDE
function ...
   plotFluxAlt(flux,fluxerr,data,st,alt,lastalt,plotvector,neial_t,...
starttime_h,starttime_m,endtime_h,endtime_m)
if plotvector(5)>0
if length(data)/st~=1
str=sprintf('Flux vs Altitude (1-6) (%d:%d - ...
   %d:%d)',starttime_h,starttime_m,endtime_h,endtime_m');
figure('Name',str)
set(gcf, 'Position', get(0,'Screensize'));
sn=1;
for j=1:length(data)/st
    if mod(j-1,6)==0 && j~=1
        %save figure and creates a new one
        if plotvector(5)==2
        saveas(gcf,str,'png');
        saveas(gcf,str,'epsc');
        end
        str=sprintf('Flux vs Altitude (%d-%d) (%d:%d - ...
           %d:%d)',j,j+5,starttime_h,starttime_m,endtime_h,endtime_m');
        figure('Name',str)
        set(gcf, 'Position', get(0,'Screensize'));
        sn=1;
    end
    subplot(2,3,sn);
    if ismember(j,neial_t)
        herrorbar(flux(:,j),alt,fluxerr(:,j),'-r')
    else
        herrorbar(flux(:,j),alt,fluxerr(:,j))
    end
    maxylim=lastalt+10;
    line([0 0],[0 maxylim],'LineStyle','--','Color',[0.7,0.7,0.7]);
    set(gca,'YLim',[50 maxylim])
    title(sprintf('t=%d',j))
    xlabel('Flux [m^{-2}*s^{-1}]')
    ylabel('Altitude [Km]')
    sn=sn+1;
end
if plotvector(5)==2
```

```
    saveas(gcf,str,'png');
    saveas(gcf,str,'epsc');
end
else
j=1;
str=sprintf('Flux vs Altitude (%d:%d - ...
   %d:%d)',starttime_h,starttime_m,endtime_h,endtime_m');
figure('Name',str)
set(gcf, 'Position', get(0,'Screensize'));
h=herrorbar(flux(:,j),alt,fluxerr(:,j),'-ko');
set(h(2),'LineWidth',2);
maxylim=lastalt+10;
line([0 0],[0 maxylim],'LineStyle','--','Color',[0.7,0.7,0.7]);
set(gca,'YLim',[50 maxylim])
title(str)
xlabel('Flux [m^{-2}*s^{-1}]')
ylabel('Altitude [Km]')
    if plotvector(5)==2
        saveas(gcf,str,'png');
        saveas(gcf,str,'epsc');
    end
end
end
end
```

B.1.8. `plotNe.m`

Generates time plots of electron density at several altitudes, which can be customized in the main routine. It works better when more blocks are provided.

```
%ELECTRON DENSITY VS TIME
function plotNe(ne,neerr,t,alt,halt,plotvector,errorbars,neial_t,...
starttime_h,starttime_m,endtime_h,endtime_m)
if plotvector(13)>0
strfig = sprintf('Electron density (%d:%d - %d:%d)',...
starttime_h,starttime_m,endtime_h,endtime_m);
figure('Name',strfig)
sn=1;
for a=halt
subplot(3,2,sn);
if errorbars(1)==1
    errorbar(t,ne(a,:),neerr(a,:),'-b');
else
    plot(t,ne(a,:),'-b')
end
maxylim=max(ne(a,:))+max(neerr(a,:));
minylim=min(ne(a,:))-max(neerr(a,:));
set(gca,'YLim',[minylim maxylim])
set(gca,'XLim',[min(t)-1 max(t)+1])
%YL = get(gca,'ylim');
for j=1:length(neial_t)
    line([neial_t(j) neial_t(j)],[minylim maxylim], ...
```

```
        'LineStyle','-','Color',[0.9,0.0,0.0]);
end
title(sprintf('N_e at %d km',alt(a)))
xlabel('Block number')
ylabel('N_e [m^-3]')
sn=sn+1;
end
set(gcf, 'Position', get(0,'Screensize'));
if plotvector(1)==2
saveas(gcf,strfig,'png');
saveas(gcf,strfig,'epsc');
end
end
end
```

B.1.9. `plotNeAlt.m`

If given only one block, it generates the altitude profile for the electron density. If given more than one block, generates the altitude profile for each block and will plot in red color the altitude profile where the NEIAL took place, provided that the `.mat` file containing the NEIAL events times is present.

```
%ELECTRON DENSITY vs ALT
function plotNeAlt(ne,neerr,data,st,alt,lastalt,plotvector,neial_t,...
starttime_h,starttime_m,endtime_h,endtime_m)
if plotvector(6)>0
if length(data)/st~=1
str=sprintf('Electron density vs Altitude (1-6) (%d:%d - %d:%d)',...
starttime_h,starttime_m,endtime_h,endtime_m');
figure('Name',str)
set(gcf, 'Position', get(0,'Screensize'));
sn=1;
for j=1:length(data)/st
    if mod(j-1,6)==0 && j~=1
        %save figure and creates a new one
        if plotvector(6)==2
        saveas(gcf,str,'png');
        saveas(gcf,str,'epsc');
        end
        str=sprintf('Electron density vs Altitude (%d-%d) (%d:%d - ...
            %d:%d)',j,j+5,starttime_h,starttime_m,endtime_h,endtime_m');
        figure('Name',str)
        set(gcf, 'Position', get(0,'Screensize'));
        sn=1;
    end
    subplot(2,3,sn);
    if ismember(j,neial_t)
        herrorbar(ne(:,j),alt,neerr(:,j),'-r')
    else
        herrorbar(ne(:,j),alt,neerr(:,j))
    end
    maxylim=lastalt+10;
```

```
    %line([0 0],[0 maxylim],'LineStyle','--','Color',[0.7,0.7,0.7]);
    set(gca,'YLim',[50 maxylim])
    title(sprintf('t=%d',j))
    xlabel('N_e [m^{-3}]')
    ylabel('Altitude [Km]')
    sn=sn+1;
end
if plotvector(6)==2
    saveas(gcf,str,'png');
    saveas(gcf,str,'epsc');
end
else
j=1;
str=sprintf('Electron density vs Altitude (%d:%d - ...
   %d:%d)',starttime_h,starttime_m,endtime_h,endtime_m');
figure('Name',str)
set(gcf, 'Position', get(0,'Screensize'));
herrorbar(ne(:,j),alt,neerr(:,j),'-ko')
maxylim=lastalt+10;
%line([0 0],[0 maxylim],'LineStyle','--','Color',[0.7,0.7,0.7]);
set(gca,'YLim',[50 maxylim])
title(str)
xlabel('N_e [m^{-3}]')
ylabel('Altitude [Km]')
    if plotvector(6)==2
        saveas(gcf,str,'png');
        saveas(gcf,str,'epsc');
    end
end
end
end
```

B.1.10. `plotT.m`

Generates time plots of electron (blue) and ion (green) temperatures at several altitudes, which can be customized in the main routine. It works better when more blocks are provided.

```
%TEMP vs TIME
function ...
   plotT(ti,tierr,te,teerr,t,alt,halt,plotvector,errorbars,neial_t,...
starttime_h,starttime_m,endtime_h,endtime_m)
if plotvector(2)>0
strfig = sprintf('Temperature (%d:%d - %d:%d)',...
starttime_h,starttime_m,endtime_h,endtime_m);
figure('Name',strfig)
sn=1;
for a=halt
subplot(3,2,sn);
if errorbars(1)==1
    errorbar(t,ti(a,:),tierr(a,:),'LineStyle','-',...
    'Color',[0.0,0.8,0.2]);
```

```
    hold on;
    errorbar(t,te(a,:),teerr(a,:));
else
    plot(t,ti(a,:),'LineStyle','-','Color',[0.0,0.8,0.2])
    hold on;
    plot(t,te(a,:));
end
maxylim=max(max(ti(a,:)),max(te(a,:)))+...
max(max(tierr(a,:)),max(teerr(a,:)));
minylim=min(min(ti(a,:)),max(te(a,:)))-...
max(max(tierr(a,:)),max(teerr(a,:)));
set(gca,'YLim',[minylim maxylim])
set(gca,'XLim',[min(t)-1 max(t)+1])
%YL = get(gca,'ylim');
for j=1:length(neial_t)
    line([neial_t(j) neial_t(j)],[minylim maxylim], ...
        'LineStyle','-','Color',[0.9,0.0,0.0]);
end
title(sprintf('Temperature at %d km',alt(a)))
xlabel('Block number')
%ylabel({'T [K]';'electron=blue, ion=green'})
ylabel('T [K]')
sn=sn+1;
end
set(gcf, 'Position', get(0,'Screensize'));
% legend1=legend('T_i','T_e','Location','Northeast');
% set(legend1,'FontSize',6)
if plotvector(2)==2;
saveas(gcf,strfig,'png');
saveas(gcf,strfig,'epsc');
end
end
end
```

B.1.11. plotTAlt.m

If given only one block, it generates the altitude profile for the ion and electron temperatures together with the temperature ratio. If given more than one block, generates the electron temperature altitude profile for each block and will plot in red color the altitude profile where the NEIAL took place, provided that the `.mat` file containing the NEIAL events times is present.

```
%TEMPERATURE vs ALTITUDE (plots only Te for multiblock data)
function plotTAlt(te,teerr,ti,tierr,tr,trerr,data,st,alt,lastalt,...
plotvector,neial_t,starttime_h,starttime_m,endtime_h,endtime_m)
if plotvector(7)>0
if length(data)/st~=1
str=sprintf('Temperature vs Altitude (1-6) (%d:%d - ...
   %d:%d)',starttime_h,starttime_m,endtime_h,endtime_m');
figure('Name',str)
set(gcf, 'Position', get(0,'Screensize'));
sn=1;
```

```
for j=1:length(data)/st
    if mod(j-1,6)==0 && j~=1
        %save figure and creates a new one
        if plotvector(7)==2
        saveas(gcf,str,'png');
        saveas(gcf,str,'epsc');
        end
        str=sprintf('Temperature vs Altitude (%d-%d) (%d:%d - ...
            %d:%d)',j,j+5,starttime_h,starttime_m,endtime_h,endtime_m');
        figure('Name',str)
        set(gcf, 'Position', get(0,'Screensize'));
        sn=1;
    end
    subplot(2,3,sn);
    if ismember(j,neial_t)
        herrorbar(te(:,j),alt,teerr(:,j),'-r')
    else
        herrorbar(te(:,j),alt,teerr(:,j))
    end
    maxylim=lastalt+10;
    %line([0 0],[0 maxylim],'LineStyle','--','Color',[0.7,0.7,0.7]);
    set(gca,'YLim',[50 maxylim])
    title(sprintf('t=%d',j))
    xlabel('T_e [K]')
    ylabel('Altitude [Km]')
    sn=sn+1;
end
if plotvector(7)==2
    saveas(gcf,str,'png');
    saveas(gcf,str,'epsc');
end
else
j=1;
str=sprintf('Temperature vs Altitude (%d:%d - ...
    %d:%d)',starttime_h,starttime_m,endtime_h,endtime_m');
figure('Name',str)
set(gcf, 'Position', get(0,'Screensize'));
subplot(1,2,1)
tiLines=herrorbar(ti(:,j),alt,tierr(:,j),'-g');
set(tiLines,'LineStyle','-','Color',[0.0,0.8,0.2]);
%set(tiLines,'LineWidth',2)
hold on
teLines=herrorbar(te(:,j),alt,teerr(:,j),'-b');
tiGroup = hggroup;
teGroup = hggroup;
set(tiLines,'Parent',tiGroup)
set(teLines,'Parent',teGroup)
set(get(get(tiGroup,'Annotation'),'LegendInformation'),...
    'IconDisplayStyle','on');
set(get(get(teGroup,'Annotation'),'LegendInformation'),...
    'IconDisplayStyle','on');
legend('T_i','T_e','Location','SouthEast')
maxylim=lastalt+10;
%line([0 0],[0 maxylim],'LineStyle','--','Color',[0.7,0.7,0.7]);
set(gca,'YLim',[50 maxylim])
title(str)
```

```
xlabel('T [K]')
ylabel('Altitude [Km]')
subplot(1,2,2)
herrorbar(tr,alt,trerr,'-k')
xlabel('T_e/T_i [K]')
ylabel('Altitude [Km]')
title('Temperature ratio')
set(gca,'YLim',[50 maxylim])
    if plotvector(7)==2
        saveas(gcf,str,'png');
        saveas(gcf,str,'epsc');
    end
end
end
end
```

B.1.12. `plotTr.m`

Generates time plots of temperature ratio at several altitudes, which can be customized in the main routine. It works better when more blocks are provided.

```
%TEMPERATURE RATIO vs TIME
function plotTr(tr,trerr,t,alt,halt,plotvector,errorbars,neial_t,...
starttime_h,starttime_m,endtime_h,endtime_m)
if plotvector(3)>0
strfig = sprintf('Temperature ratio (%d:%d - %d:%d)',...
starttime_h,starttime_m,endtime_h,endtime_m);
figure('Name',strfig)
sn=1;
for a=halt
subplot(3,2,sn);
if errorbars==1
    errorbar(t,tr(a,:),trerr(a,:));
else
    plot(t,tr(a,:));
end
maxylim=max(tr(a,:))+max(trerr(a,:));
minylim=min(tr(a,:))-max(trerr(a,:));
set(gca,'YLim',[minylim maxylim])
set(gca,'XLim',[min(t)-1 max(t)+1])
%YL = get(gca,'ylim');
for j=1:length(neial_t)
    line([neial_t(j) neial_t(j)],[minylim maxylim], ...
        'LineStyle','-','Color',[0.9,0.0,0.0]);
end
title(sprintf('Temperature ratio at %d km',alt(a)))
xlabel('Block number')
ylabel('T_e/T_i')
sn=sn+1;
end
set(gcf, 'Position', get(0,'Screensize'));
if plotvector(3)==2
```

```
saveas(gcf,strfig,'png');
saveas(gcf,strfig,'epsc');
end
end
end
```

B.1.13. `plotVi.m`

Generates time plots of ion velocity at several altitudes, which can be customized in the main routine. It works better when more blocks are provided.

```
%ION VELOCITY VS TIME
function plotVi(vo,voerr,t,alt,halt,plotvector,errorbars,neial_t,...
starttime_h,starttime_m,endtime_h,endtime_m)
if plotvector(1)>0
strfig = sprintf('Ion velocity (%d:%d - %d:%d)',...
starttime_h,starttime_m,endtime_h,endtime_m);
figure('Name',strfig)
sn=1;
for a=halt
subplot(3,2,sn);
if errorbars(1)==1
    errorbar(t,vo(a,:),voerr(a,:),'-b');
else
    plot(t,vo(a,:),'-b')
end
maxylim=max(vo(a,:))+max(voerr(a,:));
minylim=min(vo(a,:))-max(voerr(a,:));
set(gca,'YLim',[minylim maxylim])
set(gca,'XLim',[min(t)-1 max(t)+1])
%YL = get(gca,'ylim');
for j=1:length(neial_t)
    line([neial_t(j) neial_t(j)],[minylim maxylim], ...
        'LineStyle','-','Color',[0.9,0.0,0.0]);
end
title(sprintf('Ion velocity at %d km',alt(a)))
xlabel('Block number')
ylabel('V_i [m/s]')
sn=sn+1;
end
set(gcf, 'Position', get(0,'Screensize'));
if plotvector(1)==2
saveas(gcf,strfig,'png');
saveas(gcf,strfig,'epsc');
end
end
end
```

B.1.14. `plotViAlt.m`

If given only one block, it generates the altitude profile for the ion velocity. If given more than one block, it generates the altitude profile for each block and will plot in red color the altitude profile where the NEIAL took place, provided that the `.mat` file containing the NEIAL events times is present.

```
%ION VELOCITY VS ALT
function plotViAlt(vo,voerr,data,st,alt,lastalt,...
    plotvector,neial_t,...
    date_y,date_m,date_d,starttime_h,starttime_m,endtime_h,endtime_m)
if plotvector(4)>0
if length(data)/st~=1
str=sprintf('Ion Velocity vs Altitude (1-6) (%d:%d - %d:%d)',...
    starttime_h,starttime_m,endtime_h,endtime_m');
figure('Name',str)
set(gcf, 'Position', get(0,'Screensize'));
sn=1;
for j=1:length(data)/st
    if mod(j-1,6)==0 && j~=1
        %save figure and creates a new one
        if plotvector(4)==2
        saveas(gcf,str,'png');
        saveas(gcf,str,'epsc');
        end
        str=sprintf('Ion Velocity vs Altitude (%d-%d) (%d:%d - ...
            %d:%d)',...
             j,j+5,starttime_h,starttime_m,endtime_h,endtime_m');
        figure('Name',str)
        set(gcf, 'Position', get(0,'Screensize'));
        sn=1;
    end
    subplot(2,3,sn);
    if ismember(j,neial_t)
        herrorbar(vo(:,j),alt,voerr(:,j),'-r')
    else
        herrorbar(vo(:,j),alt,voerr(:,j))
    end
    maxylim=lastalt+10;
    line([0 0],[0 maxylim],'LineStyle','--','Color',[0.7,0.7,0.7]);
    set(gca,'YLim',[50 maxylim])
    title(sprintf('t=%d',j))
    xlabel('Vi [m/s]')
    ylabel('Altitude [Km]')
    sn=sn+1;
end
if plotvector(4)==2
    saveas(gcf,str,'png');
    saveas(gcf,str,'epsc');
end
else
j=1;
str=sprintf('Ion velocity vs Altitude (%d-%d-%d - %d:%d-%d:%d)',...
    date_y,date_m,date_d,starttime_h,starttime_m,endtime_h,endtime_m');
```

```
figure('Name',str)
set(gcf, 'Position', get(0,'Screensize'));
h=herrorbar(vo(:,j),alt,voerr(:,j),'-ko');
set(h(2),'LineWidth',2);
maxylim=lastalt+10;
line([0 0],[0 maxylim],'LineStyle','--','Color',[0.7,0.7,0.7]);
set(gca,'YLim',[50 maxylim])
title(str)
xlabel('Vi [m/s]')
ylabel('Altitude [Km]')
    if plotvector(4)==2
        saveas(gcf,str,'png');
        saveas(gcf,str,'epsc');
    end
end
end
end
```

B.1.15. `remBadValues.m`

Removes values which are considered unreliable by the GUISDAP software analysis.

```
% Remove bad values
% value = value to check
% valueerr = error on value to check
function [value, valueerr]=remBadValues(value,valueerr)
%No data/known bad data received
valueerr(abs(value)==32767)=NaN;
value(abs(value)==32767)=NaN;
value(abs(valueerr)==32767)=NaN;
valueerr(abs(valueerr)==32767)=NaN;
%when error=32766 we are using assumed data, so set error=0
valueerr(valueerr==-32766)=0;
end
```

B.1.16. `remBigErrs.m`

Removes errors larger than a certain value, customizable in the main script.

```
% Remove errors greater then errmax
function [value, valueerr]=remBigErrs(value,valueerr,errmax)
if errmax~=0
    err=valueerr./value;
    valueerr(err>errmax)=NaN;
    value(err>errmax)=NaN;
end
end
```

B.1.17. `selDateTimes.m`

Selects date and times from the imported file, in order to use them in the plots.

```
function [starttime_h,starttime_m,...
    endtime_h,endtime_m,...
    date_y,date_m,date_d]=selDateTimes(data,start,step,st,range)
%select date and times
starttime_h = data(start-4+step,7);
starttime_m = data(start-4+step,8);
endtime_h = data(length(data)-st+range+start+1,11);
endtime_m = data(length(data)-st+range+start+1,12);
date_md=data(start-4+step,6);
digits=sscanf(strrep(num2str(date_md,4),'',''),'%1d');
if length(digits)==3
    date_m=digits(1);
    date_d=digits(2).*10+digits(3);
else
    date_m=digits(1).*10+digits(2);
    date_d=digits(3).*10+digits(4);
end
date_y=data(start-4+step,5);
end
```

B.1.18. `ucvalSelect.m`

Selects the uncorrected values from the NCAR ASCII file. It selects only electron density which is the only value of this type available in our data sets. We didn't use this feature in our work, so this function is commented in the main routine.

```
function value=ucvalSelect(data,range,st,cvalue,n,m)
value=zeros(st-range-10+1,length(data)/st);
for j=1:length(data)/st
    value(:,j)=data(range+10+st*(j-1):st+st*(j-1),cvalue);
    %delete first n and last m values
    %(not useful/too much noise/not interesting)
    value(1:n,j)=NaN;
    value(end-m+1:end,j)=NaN;
end
```

B.1.19. `valSelect.m`

Selects the values from the NCAR ASCII file columns, which corresponds to the ionospheric parameters measured by radars and derived by the GUISDAP analysis.

```
function value=valSelect(data,start,range,st,cvalue,n,m)
value=zeros(range+1,length(data)/st);
```

```
for j=1:length(data)/st
    value(:,j)=data(start+st*(j-1):start+range+st*(j-1),cvalue);
    %delete first n and last m values
    %(not useful/too much noise/not interesting)
    value(1:n,j)=NaN;
    value(end-m+1:end,j)=NaN;
end
end
```

B.2. Other useful Matlab scripts not related to the main routine

B.2.1. `convd.m`

This is a short but useful script we made to convert date in seconds and vice versa, which is useful when one wants to remove data dumps containing NEIALs (which are named after the number of seconds since the start of the year) knowing only the date and hour of the event.

```
function convd(date)
%calculate the number of second since beginning of the year and ...
   copy the
%result to the clipboard
%if provided with year and number of seconds will give date
%
%date=[day month year hour min sec]
%ex. date=[23 4 2007 9 10 34];
%or
%date=[year seconds]
%ex. date=[2001 1258226]

while length(date)~=6 && length(date)~=2
    disp('Input date error. Format allowed are:')
    disp('[day month year hour minute seconds]')
    disp('or')
    disp('[year seconds]')
    date=input(sprintf('Try to manually insert date: '));
end

if length(date)==6
    days=[31 28 31 30 31 30 31 31 30 31 30 31];
    %check for leap year
    if (mod(date(3),100)~=0 && mod(date(3),4)==0) || ...
       mod(date(3),400)==0
        days(2)=29;
    end
    sec=(date(1)-1)*86400 + ...
        date(4)*3600 + ...
        date(5)*60 + ...
        date(6) + ...
```

```
    sum(days(1:date(2)-1))*86400;
    fprintf('Number of seconds: %d \n',sec)
    clipboard('copy', sec)
end

if length(date)==2
    datestring=datestr(date(2)/86400+datenum(date(1),1,1));
    fprintf('Date: %s \n',datestring)
    clipboard('copy', datestring)
end

end
```

B.2.2. `fig2pdf.m`

This short script automatically converts Matlab figures in `.pdf` files, more suitable for using in some LaTeX environments. We use it to convert sequences of spectra containing NEIALs.

```
% change path to your .fig spectra files location
path='/home/max/Uni/analysis/...
steffel_fixed_42m_1.40_CP20040522...
/rtg/fig/img';
%change both the following line and the seq command in line 12
%to match the sequence of spectra needed
seq=7965:2:7965;
for i=seq
    openfig(sprintf('%s%d.fig',path,i));
    saveas(gcf,sprintf('img%d',i),'epsc');
    close();
end
!mkdir -p figs/spectra;
!for i in `seq 7965 1 7965`; do var=$(printf 'img%d.eps' $i); ...
   epstopdf $(echo $var);done;
!mv img*.pdf figs/spectra; rm img*.eps;
```

B.3. Customized routines to save RTG figures

B.3.1. Customized function in `remtg` routine

The standard RTG routine `remtg` doesn't have an option to save spectra to a local disk for successive analysis. This would result in a time consuming activity in order to manually check every spectrum. Hence we decided to slightly modify the `remtg` code to save `.fig` and `.png` files. We modified the function `spitspec.m` adding the following code at the end (just before the last `end`):

```
%save plot on file
%(change /home/max/tmp/rtg in the next two lines to what you need)
!mkdir -p /home/max/tmp/rtg
myFolder='/home/max/tmp/rtg';
filePattern = fullfile(myFolder,'*.png');
jpegFiles = dir(filePattern);
baseFileName = strcat('img',int2str(length(jpegFiles)+1));
fullFileName = fullfile(myFolder, baseFileName);
saveas(gcf,fullFileName,'png')
saveas(gcf,fullFileName,'fig')
```

This is not a highly efficient way of doing it, because it generates a file each time the function `updateplot` is called, which means that we generate e.g. 4 different files if we have 4 different windows for the same dump. On the bright side, it is a very small and harmless modification, which does not alter anything else in the code, thus in practice reducing to zero possible complications.

B.3.2. Linux BASH script to take screenshots

An alternative way to save a figure to disk, with the advantage of not touching the code at all, is to use a simple BASH script to take a screenshot. For example:

```
#!/bin/bash
#Save screenshots using scrot command
mkdir -p ~/Downloads/screenshots
i=1
while true; do
    #using scrot (faster)
    scrot -u ~/Downloads/screenshots/`printf %05d $i`.png

    #using imagemagick and xprop
    #activeWinLine=$(xprop -root | grep "_NET_ACTIVE_WINDOW(WINDOW)")
    #activeWinId=${activeWinLine:40}
    #import -window "$activeWinId" ~/Downloads/screenshots/`printf ...
       %05d $i`.png

    #using imagemagick and xdotool
    #import -window "$(xdotool getwindowfocus -f)" ...
       ~/Downloads/screenshots/$i.png

    sleep 0.9
    echo 'Screenshot number '`echo $i`' saved'
    let i++
done

exit 0
```

There are however many disadvantages if using such a solution. First of all, the computer screen must be always on, thus wasting a lot more energy. In addition, it is needed to manually set the time delay, it is not possible to save the `.fig` file, the image dimension is fixed and dependent on the screen resolution, therefore the resulting files are not of a good quality and hence not suited for an official publication.

C. Final notes

All the websites, references and Matlab external functions have been last accessed on 15 November 2013.

All the credit for the external routines and functions goes to their respective authors.

The code we wrote is free software: you can redistribute it and/or modify it under the terms of the GNU General Public License as published by the Free Software Foundation, either version 3 of the License, or (at your option) any later version.

Bibliography

André, M., and A. Yau (1997), Theories and observations of ion energization and outflow in the high latitude magnetosphere, *Space Science Reviews*, *80*(1-2), 27–48, doi:10.1023/A:1004921619885.

Argese, C. (2013), Type-i ion outflow from the high latitude ionosphere, Master's thesis, University of Tromsø.

Axford, W. I. (1968), The polar wind and the terrestrial helium budget, *Journal of Geophysical Research*, *73*(21), 6855–6859, doi:10.1029/JA073i021p06855.

Banks, P., and G. Kockarts (1973), *Aeronomy*, no. v. 2 in Aeronomy, Academic Press.

Bates, D., and T. Patterson (1962), Helium ions in the upper atmosphere, *Planetary and Space Science*, *9*(10), 599–605, doi:10.1016/0032-0633(62)90121-6.

Beynon, W. J. G., and P. J. S. Williams (1978), Incoherent scatter of radio waves from the ionosphere, *Reports on Progress in Physics*, *41*, 909–956, doi:10.1088/0034-4885/41/6/003.

Bjørnå, N. (2005), Lecture notes in radar diagnostic of space plasma.

Block, L. P., and C. G. Fälthammar (1968), Effects of field-aligned currents on the structure of the ionosphere, *Journal of Geophysical Research*, *73*(15), 4807–4812, doi:10.1029/JA073i015p04807.

Brekke, A. (2012), *Physics of the Upper Polar Atmosphere*, Springer.

Buneman, O. (1963), Excitation of field aligned sound waves by electron streams, *Phys. Rev. Letters*, *Vol: 10*, doi:http://dx.doi.org/10.1103/PhysRevLett.10.285.

Burchill, J. K., D. J. Knudsen, J. H. Clemmons, K. Oksavik, R. F. Pfaff, C. T. Steigies, A. W. Yau, and T. K. Yeoman (2010), Thermal ion upflow in the cusp ionosphere and its dependence on soft electron energy flux, *Journal of Geophysical Research: Space Physics*, *115*(A5), n/a–n/a, doi:10.1029/2009JA015006.

Cabrit, B., H. Opgenoorth, and W. Kofman (1996), Comparison between EISCAT UHF and VHF backscattering cross section, *Journal of Geophysical Research: Space Physics*, *101*(A2), 2369–2376, doi:10.1029/95JA02175.

Caton, R., J. L. Horwitz, P. G. Richards, and C. Liu (1996), Modeling of f-region ionospheric upflows observed by EISCAT, *Geophysical Research Letters*, *23*(12), 1537–1540, doi:10.1029/96GL01255.

Chappell, C. R., K. K. Harris, and G. W. Sharp (1970), A study of the influence of magnetic activity on the location of the plasmapause as measured by OGO 5, *Journal of Geophysical Research*, *75*(1), 50–56, doi:10.1029/JA075i001p00050.

Chen, A., R. Johnsen, and M. A. Biondi (1978), Measurements of the O++N2 and O++O2 reaction rates from 300 to 900 k, *The Journal of Chemical Physics*, *69*(6), 2688–2691, doi:10.1063/1.436917.

Chen, F. F. (1984), *Introduction to Plasma Physics and Controlled Fusion*, Springer.

Collis, P. N., L. Häggström, K. Kaila, and M. T. Rietveld (1991), Eiscat radar observations of enhanced incoherent scatter spectra; their relation to red aurora and field-aligned currents, *Geophysical Research Letters*, *18*(6), 1031–1034, doi:10.1029/91GL00848.

Davies, J., M. Lester, B. Jenkins, and R. Moffett (1995), Dayside ion frictional heating: EISCAT observations and comparison with model results, *Journal of Atmospheric and Terrestrial Physics*, *57*(7), 775–793, doi:10.1016/0021-9169(94)00051-O.

Davies, J. A., M. Lester, and I. W. McCrea (1997), A statistical study of ion frictional heating observed by EISCAT, *Annales Geophysicae*, *15*, 1399–1411, doi:10.1007/s00585-997-1399-x.

EISCAT Scientific Association (2013), https://www.eiscat.se.

Endo, M., R. Fujii, Y. Ogawa, S. C. Buchert, S. Nozawa, S. Watanabe, and N. Yoshida (2000), Ion upflow and downflow at the topside ionosphere observed by the EISCAT VHF radar, *Annales Geophysicae*, *18*, 170–181, doi:10.1007/s00585-000-0170-3.

Farley, D. T. (1963), A plasma instability resulting in field-aligned irregularities in the ionosphere, *Journal of Geophysical Research*, *68*(22), 6083–6097, doi:10.1029/JZ068i022p06083.

Fejer, J. A. (1979), Ionospheric modification and parametric instabilities, *Reviews of Geophysics*, *17*(1), 135–153, doi:10.1029/RG017i001p00135.

Forme, F., J.-E. Wahlund, H. Opgenoorth, M. Persson, and E. Mishin (1993), Effects of current driven instabilities on the ion and electron temperatures in the topside ionosphere, *Journal of Atmospheric and Terrestrial Physics*, *55*(4–5), 647–666, doi:10.1016/0021-9169(93)90011-M.

Forme, F. R. E. (1993), A new interpretation on the origin of enhanced ion acoustic fluctuations in the upper ionosphere, *Geophysical Research Letters*, *20*(21), 2347–2350, doi:10.1029/93GL02490.

Forme, F. R. E. (1999), Parametric decay of beam-driven langmuir wave and enhanced ion-acoustic fluctuations in the ionosphere: a weak turbulence approach, *Ann. Geophys.*, *17*(9), 1172–1181, doi:10.1007/s00585-999-1172-4.

Forme, F. R. E., and D. Fontaine (1999), Enhanced ion acoustic fluctuations and ion outflows, *Annales Geophysicae*, *17*(2), 182–189, doi:10.1007/s00585-999-0182-6.

Forme, F. R. E., D. Fontaine, and J. E. Wahlund (1995), Two different types of enhanced ion acoustic fluctuations observed in the upper ionosphere, *Journal of Geophysical Research: Space Physics*, *100*(A8), 14,625–14,636, doi:10.1029/94JA01093.

Foster, J. C., and P. J. Erickson (2000), Simultaneous observations of e-region coherent backscatter and electric field amplitude at f-region heights with the millstone hill UHF radar, *Geophysical Research Letters*, *27*(19), 3177–3180, doi:10.1029/2000GL000042.

Foster, J. C., C. del Pozo, K. Groves, and J.-P. St. Maurice (1988), Radar observations of the onset of current driven instabilities in the topside ionosphere, *Geophysical Research Letters*, *15*(2), 160–163, doi:10.1029/GL015i002p00160.

Fung, S. F., and R. A. Hoffman (1991), A search for parallel electric fields by observing secondary electrons and photoelectrons in the low-altitude auroral zone, *Journal of Geophysical Research: Space Physics*, *96*(A3), 3533–3548, doi:10.1029/90JA02244.

Ganguli, G., M. J. Keskinen, H. Romero, R. Heelis, T. Moore, and C. Pollock (1994), Coupling of microprocesses and macroprocesses due to velocity shear: An application to the low-altitude ionosphere, *Journal of Geophysical Research: Space Physics*, *99*(A5), 8873–8889, doi:10.1029/93JA03181.

Grydeland, T., C. La Hoz, T. Hagfors, E. M. Blixt, S. Saito, A. Strømme, and A. Brekke (2003), Interferometric observations of filamentary structures associated with plasma instability in the auroral ionosphere, *Geophysical Research Letters*, *30*(6), n/a–n/a, doi:10.1029/2002GL016362.

Grydeland, T., T. Hagfors, T. S. Trondsen, E. M. Blixt, U. P. Løvhaug, and C. La Hoz (2004), Interferometric radar observations of filamented structures due to plasma instabilities and their relation to dynamic auroral rays.

Gustavsson, B., and B. Eliasson (2008), HF radio wave acceleration of ionospheric electrons: Analysis of HF-induced optical enhancements, *Journal of Geophysical Research: Space Physics*, *113*(A8), n/a–n/a, doi:10.1029/2007JA012913.

Hagfors, T. (1995), Plasma fluctuations excited by charged particle motion and their detection by weak scattering of radio waves.

Horwitz, J. L., and T. E. Moore (1997), Four contemporary issues concerning ionospheric plasma flow to the magnetosphere, *Space Science Reviews*, *80*(1-2), 49–76, doi:10.1023/A:1004973603955.

Kagan, L. M., and J.-P. St.-Maurice (2005), Origin of type-2 thermal-ion upflows in the auroral ionosphere, *Annales Geophysicae*, *23*(1), 13–24.

Keating, J., F. Mulligan, D. Doyle, K. Winser, and M. Lockwood (1990), A statistical study of large field-aligned flows of thermal ions at high-latitudes, *Planetary and Space Science*, *38*(9), 1187–1201, doi:10.1016/0032-0633(90)90026-M.

Kindel, J. M., and C. F. Kennel (1971), Topside current instabilities, *Journal of Geophysical Research*, *76*(13), 3055–3078, doi:10.1029/JA076i013p03055.

Laqua, H. P. (2007), Electron bernstein wave heating and diagnostic, *Plasma Physics and Controlled Fusion*, *49*(4), R1, doi:10.1088/0741-3335/49/4/R01.

Liu, C., J. L. Horwitz, and P. G. Richards (1995), Effects of frictional ion heating and soft-electron precipitation on high-latitude f-region upflows, *Geophysical Research Letters*, *22*(20), 2713–2716, doi:10.1029/95GL02551.

Lockwood, M., J. Waite, J. H., T. E. Moore, C. R. Chappell, and J. F. E. Johnson (1985), A new source of suprathermal o(+) ions near the dayside polar cap boundary, *Journal of Geophysical Research*, *90*, 4099–4116, doi:10.1029/JA090iA05p04099.

Loranc, M., and J. P. St. Maurice (1994), A time-dependent gyro-kinetic model of thermal ion upflows in the high-latitude f region, *Journal of Geophysical Research: Space Physics*, *99*(A9), 17,429–17,451, doi:10.1029/93JA01852.

Løvhaug, U., and T. Flå (1986), Ion temperature anisotropy in the auroral f-region as measured with EISCAT, *Journal of Atmospheric and Terrestrial Physics*, *48*(9–10), 959–971, doi:10.1016/0021-9169(86)90069-3.

Lunde, J., B. Gustavsson, U. P. Løvhaug, D. A. Lorentzen, and Y. Ogawa (2007), Particle precipitations during NEIAL events: simultaneous ground based observations at svalbard, *Ann. Geophys.*, *25*(6), 1323–1336, doi:10.5194/angeo-25-1323-2007.

Makita, K., C.-I. Meng, and S.-I. Akasofu (1988), Latitudinal electron precipitation patterns during large and small IMF magnitudes for northward IMF conditions, *Journal of Geophysical Research: Space Physics*, *93*(A1), 97–104, doi:10.1029/JA093iA01p00097.

Michell, R. G., and M. Samara (2010), High-resolution observations of naturally enhanced ion acoustic lines and accompanying auroral fine structures, *Journal of Geophysical Research: Space Physics*, *115*(A3), n/a–n/a, doi:10.1029/2009JA014661.

Michell, R. G., K. A. Lynch, C. J. Heinselman, and H. C. Stenbaek-Nielsen (2009), High time resolution PFISR and optical observations of naturally enhanced ion acoustic lines, *Ann. Geophys.*, *27*(4), 1457–1467, doi:10.5194/angeo-27-1457-2009.

Mishin, E. V., and V. Fiala (1995), Radiation of whistlers by the ion-acoustic turbulence in the ionosphere, *Journal of Geophysical Research: Space Physics*, *100*(A10), 19,695–19,700, doi:10.1029/95JA01628.

Neubert, T., and F. Christiansen (2003), Small-scale, field-aligned currents at the top-side ionosphere, *Geophysical Research Letters*, *30*(19), n/a–n/a, doi:10.1029/2003GL017808.

Nygrén, T. (1996), *Introduction to Incoherent Scatter Measurements*, Invers.

Ogawa, Y., S. C. Buchert, R. Fujii, S. Nozawa, and A. P. van Eyken (2009), Characteristics of ion upflow and downflow observed with the european incoherent scatter svalbard radar, *Journal of Geophysical Research: Space Physics*, *114*(A5), n/a–n/a, doi:10.1029/2008JA013817.

Ogawa, Y., S. C. Buchert, I. Häggström, M. T. Rietveld, R. Fujii, S. Nozawa, and H. Miyaoka (2011), On the statistical relation between ion upflow and naturally enhanced ion-acoustic lines observed with the EISCAT svalbard radar, *Journal of Geophysical Research: Space Physics*, *116*(A3), n/a–n/a, doi:10.1029/2010JA015827.

Rietveld, M., P. Collis, A. vanEyken, and U. Løvhaug (1996), Coherent echoes during EISCAT UHF common programmes, *Journal of Atmospheric and Terrestrial Physics*, *58*(1–4), 161–174, doi:10.1016/0021-9169(95)00027-5.

Rietveld, M. T., P. N. Collis, and J.-P. St.-Maurice (1991), Naturally enhanced ion acoustic waves in the auroral ionosphere observed with the EISCAT 933-MHz radar, *Journal of Geophysical Research: Space Physics*, *96*(A11), 19,291–19,305, doi:10.1029/91JA01188.

Robinson, R. M., R. R. Vondrak, K. Miller, T. Dabbs, and D. Hardy (1987), On calculating ionospheric conductances from the flux and energy of precipitating electrons, *Journal of Geophysical Research: Space Physics*, *92*(A3), 2565–2569, doi: 10.1029/JA092iA03p02565.

Rosenbluth, M. N., and N. Rostoker (1962), Scattering of electromagnetic waves by a nonequilibrium plasma, *Physics of Fluids*, *5*(7), 776–788, doi:doi:10.1063/1.1724446.

Schunk, R. (2000), Theoretical developments on the causes of ionospheric outflow, *Journal of Atmospheric and Solar-Terrestrial Physics*, *62*(6), 399–420, doi:10.1016/S1364-6826(00)00017-1.

Schunk, R., and A. Nagy (2004), *Ionospheres: Physics, Plasma Physics, and Chemistry*, Cambridge atmospheric and space sciences series, Cambridge University Press.

Sedgemore-Schulthess, F., and J.-P. St.-Maurice (2001), Naturally enhanced ion-acoustic spectra and their interpretation, *Surveys in Geophysics*, *22*(1), 55–92, doi:10.1023/A:1010691026863.

Seo, Y., J. L. Horwitz, and R. Caton (1997), Statistical relationships between high-latitude ionospheric f region/topside upflows and their drivers: DE 2 observations, *Journal of Geophysical Research: Space Physics*, *102*(A4), 7493–7500, doi:10.1029/97JA00151.

Shelley, E. G., R. G. Johnson, and R. D. Sharp (1972), Satellite observations of energetic heavy ions during a geomagnetic storm, *Journal of Geophysical Research*, *77*(31), 6104–6110, doi:10.1029/JA077i031p06104.

St-Maurice, J.-P., and R. W. Schunk (1979), Ion velocity distributions in the high-latitude ionosphere, *Reviews of Geophysics*, *17*(1), 99–134, doi:10.1029/RG017i001p00099.

St.-Maurice, J.-P., W. Kofman, and D. James (1996), In situ generation of intense parallel electric fields in the lower ionosphere, *Journal of Geophysical Research: Space Physics*, *101*(A1), 335–356, doi:10.1029/95JA02586.

Torr, M. R., J. C. G. Walker, and D. G. Torr (1974), Escape of fast oxygen from the atmosphere during geomagnetic storms, *Journal of Geophysical Research*, *79*(34), 5267–5271, doi:10.1029/JA079i034p05267.

Tsunoda, R. T., R. C. Livingston, J. F. Vickrey, R. A. Heelis, W. B. Hanson, F. J. Rich, and P. F. Bythrow (1989), Dayside observations of thermal-ion upwellings at 800-km altitude: An ionospheric signature of the cleft ion fountain, *Journal of Geophysical Research: Space Physics*, *94*(A11), 15,277–15,290, doi:10.1029/JA094iA11p15277.

Tsytovich, V. N. (1967), Nonlinear effects in a plasma, *Soviet Physics Uspekhi*, *9*(6), 805, doi:10.1070/PU1967v009n06ABEH003226.

Wahlund, J.-E., F. R. E. Forme, H. J. Opgenoorth, M. a. L. Persson, E. V. Mishin, and A. S. Volokitin (1992a), Scattering of electromagnetic waves from a plasma: Enhanced ion acoustic fluctuations due to ion-ion two-stream instabilities, *Geophysical Research Letters*, *19*(19), 1919–1922, doi:10.1029/92GL02101.

Wahlund, J. E., H. J. Opgenoorth, I. Häggström, K. J. Winser, and G. O. L. Jones (1992b), EISCAT observations of topside ionospheric ion outflows during auroral activity: Revisited, *Journal of Geophysical Research: Space Physics*, *97*(A3), 3019–3037, doi: 10.1029/91JA02438.

Yau, A. W., and M. André (1997), Sources of ion outflow in the high latitude ionosphere, *Space Science Reviews*, *80*(1-2), 1–25, doi:10.1023/A:1004947203046.

Yeh, H.-C., and J. C. Foster (1990), Storm time heavy ion outflow at mid-latitude, *Journal of Geophysical Research: Space Physics*, *95*(A6), 7881–7891, doi:10.1029/JA095iA06p07881.

Nomenclature

ε_0	permittivity of free space
k_B	Boltzmann constant
K_P	estimated planetary K-index
m_j	particle mass (either ion or electron)
n_0	background electron density
X_e	physical quantity X relative to electrons
X_i	physical quantity X relative to ions
BBELF	broad-band extremely low frequency
CME	coronal mass ejection
ESR	Eiscat Svalbard radar
EUV	extra ultra violet
FAC	field aligned current
IMF	interplanetary magnetic field
ISR	incoherent scatter radar
MHD	magnetohydrodynamic
MLT	magnetic local time
NBZ	northward z-component of the interplanetary magnetic field
NEIALs	naturally enhanced ion-acoustic lines
RTG	real time graph
UHF	ultra low frequency
VLF	very low frequency

UNIVERSITY OF TROMSØ